UNIVERSIDAD COMPLUTENSE DE MADRID

FACULTAD DE CIENCIAS FÍSICAS

Departamento de Física de Materiales

TESIS DOCTORAL

Medidas de transporte térmico de materiales termoeléctricos mediante la técnica fotoacústica: del material en volumen a la nanoescala

Thermal transport measurements of thermoelectric materials by the photoacoustic technique : from bulk to nano

MEMORIA PARA OPTAR AL GRADO DE DOCTOR

PRESENTADA POR

Begoña Abad Mayor

Directora

Mª Soledad Martín González

Madrid, 2017

UNIVERSIDAD COMPLUTENSE DE MADRID

FACULTAD DE CIENCIAS FÍSICAS

DEPARTAMENTO DE FÍSICA DE MATERIALES

MEDIDAS DE TRANSPORTE TÉRMICO DE MATERIALES TERMOELÉCTRICOS MEDIANTE LA TÉCNICA FOTOACÚSTICA: DEL MATERIAL EN VOLUMEN A LA NANOESCALA

THERMAL TRANSPORT MEASUREMENTS OF THERMOELECTRIC MATERIALS BY THE PHOTOACOUSTIC TECHNIQUE: FROM BULK TO NANO

Memoria presentada por

Begoña Abad Mayor

Para optar al grado de Doctora en Ciencias Físicas por la Universidad Complutense de Madrid

Directora

Dra. Mª Soledad Martín González

INSTITUTO DE MICROELECTRÓNICA DE MADRID

CONSEJO SUPERIOR DE INVESTIGACIONES CIENTÍFICAS

Este trabajo doctoral ha sido realizado en el Instituto de Microelectrónica de Madrid (IMM), perteneciente a la Agencia Estatal Consejo Superior de Investigaciones Científicas (CSIC). Ha sido dirigido por la Dra. Mª Soledad Martín González.

La realización de esta tesis doctoral ha sido posible gracias a la financiación del proyecto europeo ERC StG NanoTEC 240497 y el proyecto nacional PHOMENTA MAT2011-27911.

A mi familia

Acknowledgements

I would like to thank Marisol for her continuous guidance, encouragement and advice. I am very grateful for being given the opportunity to do my PhD in her laboratory. I have been so lucky to have a supervisor who cares so much about my work.

Grateful thanks to all people of thermoelectric devices group where this thesis was developed: Pablo, Jaime, Jon, Juanjo, Liliana, Marina, David, Jaime Andrés, Miguel y Alejandra. My special thanks to Olga for all her support and collaboration throughout this PhD thesis. It is been a relief to know she would be there for me whenever I needed it. Special thanks to Cris, for her friendship and support. Special thanks also to Marta, living this adventure with her was a treasure for me. Thanks to all the people from the IMM.

I would like to thank many people related with my short abroad stays: Yoshikazu Shinohara and Hiroshi Kawakami, who gave me the opportunity to work with them at the Institute for Materials Science (NIMS) in Tsukuba (Japan). I am very grateful to Tim Sands, who helped me to receive me at Purdue University. During this time, I had access to Xianfan Xu laboratory and there I learned many key details for the development of this thesis. Thanks to Bivas from Purdue University too. Special thanks to Theo, Diana and Adam from Rensselaer Polytechnic Institute, who did their best to help me in this thesis.

I would like to thank to all people that were near to me during this time: frikisicos group, cañas girls, Alma and Andra, Ali and Ángela and the girls from the school, in special Nuria.

Finally, I would like to thank to my family. This thesis would not have been possible without you.

Agradecimientos

En primer lugar, quería agradecer a Marisol por su continua guía, apoyo y consejo durante el transcurso de esta tesis. Estoy muy agradecida de que me diese la oportunidad de hacer la tesis en su laboratorio. He sido muy afortunada de tener una directora que se preocupa tanto de mi trabajo.

Muchas gracias a mi grupo de dispositivos termoeléctricos donde realicé mi tesis: Pablo, Jaime, Jon, Juanjo, Liliana, Marina, David, Jaime Andrés, Miguel y Alejandra. A Olga quería agradecerle su presencia y colaboración, especialmente en esta última etapa. Ha sido un gran alivio saber que ella estaba ahí para lo que necesitara. En especial gracias a Cris por su amistad y apoyo incondicional. Un gracias enorme para Marta también, haber vivido esta aventura con ella tiene un valor incalculable. Gracias a todas las personas del IMM.

Me gustaría agradecer a todas las personas relacionadas con de mis estancias en el extranjero: Yoshikazu Shinohara y Hiroshi Kawakami, que me dieron la oportunidad de trabajar con ellos en el Instituto de Ciencia de Materiales (NIMS) en Tsukuba (Japón). Tengo mucho que agradecer a Tim Sands que me dio la oportunidad de realizar una estancia en la Universidad de Purdue, durante la cual tuve acceso al laboratorio del Xianfan Xu. Allí pude aprender muchos detalles clave en el desarrollo de la tesis. También gracias a Bivas de la Universidad de Purdue. Gracias especialmente a Theo, Diana y Adam del Instituto Politécnico Rensselaer, por haberme ayudado en todo lo que estaba en su mano.

Me gustaría agradecer a todas las personas que han estado cerca de mí: al grupo de los frikisicos, a las chicas de las cañas, a Alma y Andra, Ali y Ángela y a las chicas del colegio, en especial, a Nuria.

Finalmente me gustaría agradecer a mi familia, porque esta tesis no habría podido ser posible sin vosotros.

Contents

Abstract

The aim of this PhD work was the implementation of the photoacoustic technique, a powerful tool to determine the thermal diffusivity of materials. This thesis can be divided in two fundamental sections: i) the set-up design, implementation, and calibration; and ii) thermal property measurements of different material types with applications in thermoelectricity.

The main motivation to implement this technique lays on the importance of the thermal properties in a wide variety of applications from thermal management in electronics, space industry, or medicine; to energy conversion by means of the thermoelectric effects. The thermoelectricity is the ability of the materials to convert temperature differences into electricity and *vice versa*, so that any waste heat could be recovered and utilized. The efficiency of these materials is directly related to the electrical conductivity and the Seebeck coefficient and inversely related to the thermal conductivity. The thermal conductivity characterization is then critical to evaluate a material as a promising thermoelectric candidate. Moreover, the thermoelectric efficiency has been proved to be enhanced by the reduction of thermal conductivity through the increasing of phonon scattering due to nanosize effects. Therefore, the determination of the thermal properties of these nanostructures materials becomes crucial. For that purpose, non-contact heating methods are being developed, which allows for the thermal contact resistances to be avoided, which is one of the main drawbacks of many thermal property measurement techniques. Non-contact heating techniques are usually based on photothermal phenomenon, where heating is generated by an incident radiation. In the case of the photoacoustic technique, an incident modulated radiation impinges on the sample so that its surface is heating and cooling and hence, the air in contact with it expands and contracts as a consequence of this periodically heating. From this effect, acoustic waves are created and detected by a microphone. The signal coming from the microphone is then compared with the laser incident signal and from the phase shift the thermal properties of the material can be extracted with a proper theoretical model.

This thesis is divided in six chapters. In the first chapter, an introduction to thermoelectricity and a review of the non-contact methods to measure the thermal conductivity are presented. In the second chapter, the experimental methodologies used to fabricate and characterize the thermoelectric materials under study are explained. Chapter 3 is devoted to the photoacoustic technique from the optimization of the different elements of the experimental setup to an exhaustive study about its stability, reproducibility and detection limits. In the fourth chapter, bulk reference materials are measured in order to prove the validity of the technique for

this type of materials. Then, two different systems are studied: a) zinc oxide doped with nickel oxide nanoparticles and b) polyaniline blended with graphene nanoplatelets. The physical explanation of the obtained thermoelectric measurements is given. Chapter five explains the capability of the photoacoustic setup to measured multilayered materials is shown. Different types of structures from films (Si-Ge or Te), to porous structures (porous alumina), or to nanowires embedded into alumina matrix (Bi_2Te_3 and Sb_2Te_3) are analyzed. Finally, chapter sixth summarizes the most important conclusions of this PhD work.

Resumen

El objetivo de este trabajo de doctorado consistió en la implementación de la técnica fotoacústica, una herramienta muy poderosa para determinar la difusividad térmica de los materiales.

Esta tesis puede dividirse en dos secciones principales: i) el diseño del montaje, implementación y calibración, y ii) medidas de las propiedades térmicas de diferentes tipos de materiales con aplicaciones en la termoelectricidad.

La mayor motivación para implementar esta técnica se basa en la importancia de las propiedades térmicas en una amplia variedad de aplicaciones desde gestión térmica en electrónica, industria espacial o medicina, hasta conversión de energía mediante el efecto termoeléctrico. La termoelectricidad consiste en la habilidad de los materiales de convertir diferencias de temperaturas en electricidad y viceversa, de modo que el calor residual podría ser recuperado y reutilizado. La eficiencia de estos materiales está directamente relacionada con la conductividad eléctrica y el coeficiente Seebeck, e inversamente relacionada con la conductividad térmica. La caracterización de la conductividad térmica es por tanto crítica para evaluar a un material como un candidato prometedor en la termoelectricidad. Además, ha sido comprobado cómo la eficiencia termoeléctrica mejora por la reducción de la conductividad térmica debida a la dispersión de fonones por el efecto del tamaño nanométrico. Por consiguiente, la determinación de las propiedades térmicas de estos materiales nanoestructurados es crucial. Para este propósito se han desarrollado métodos de calentamiento de no contacto, los cuales permiten evitar las resistencias térmicas de contacto, uno de los grandes inconvenientes de muchas de las técnicas de medida de propiedades térmicas. Las técnicas de calentamiento en modo no-contacto se basan normalmente en el fenómeno fototérmico, donde el calor es generado por una radiación incidente. En el caso de la técnica fotoacústica, una radiación incidente modulada incide en la muestra por lo que la superficie se calienta y enfría y por tanto, el aire en contacto se expande y contrae como consecuencia de este calentamiento periódico. Debido a este efecto, se crean ondas acústicas que son detectadas mediante un micrófono. La señal proveniente del micrófono se compara con la señal del láser incidente y a partir del desfase entre ambas se pueden obtener las propiedades térmicas del material mediante un modelo teórico apropiado.

Esta tesis está dividida en seis capítulos. En el primero se presenta una introducción de la termoelectricidad y una revisión de los métodos de no-contacto para medir la conductividad térmica. En el segundo capítulo se explican los métodos experimentales utilizados para fabricar y caracterizar los diferentes materiales termoeléctricos estudiados. En el capítulo 3 se centra en

la técnica fotoacústica desde la optimización de los diferentes elementos del montaje experimental a un estudio exhaustivo sobre su estabilidad, reproducibilidad y límites de detección. En el capítulo 4, se recogen las medidas de diferentes materiales en volumen para comprobar la validez de la técnica y obtener una explicación física de las medidas termoeléctricas. Se han estudiado dos tipos de sistemas diferentes: a) óxido de zinc dopado con nanopartículas de óxido de níquel, y b) nanoplaquetas de grafeno embebidas en una matriz de polianilina. En el capítulo 5, se muestra la capacidad del montaje fotoacústico de medir materiales multicapas. Se analizaron diferentes tipos de estructuras desde películas (Si-Ge o Te) a estructuras porosas (alúmina porosa) o nanohilos embebidos dentro de una matriz de alúmina (Bi_2Te_3 y Sb_2Te_3). Finalmente, el capítulo 6 resume las conclusiones más importantes de este trabajo doctoral.

Chapter 1:

Introduction, background and objectives

In this Chapter, the main motivations of the thesis work are explained. The chapter starts with a brief introduction about thermoelectricity and the necessity of characterizing the efficiency of thermoelectric materials. Then, a short overview about the thermal conductivity is presented. Afterwards, the state-of-the-art of the non-contact thermal conductivity measurements techniques is given. Then, an introduction to the photoacoustic technique (the technique developed under this PhD work) is explained in more detail; the historical background, basis concepts, experimental setup and applications are exposed. Finally, the objectives and the organization of this thesis are pointed out.

1.1 Motivation

Thermal conductivity and diffusivity along with heat capacity and thermal expansion are among the most important thermal properties of solid materials. Characterization of these properties is critical for new materials, in bulk or nanostructures, which is emerging at fast peace and has a variety of applications from energy production (thermoelectricity) and thermal management of electronics to space industry and medicine. On the other hand, thermal characterization, especially measurement of thermal conductivity and diffusivity is typically not a simple task. The challenges can be especially difficult when attempting to measure nanostructured materials, such as thin film or nanowires. For instance, during the measurement of thermal conductivity or diffusivity, the specimen is locally heated and the thermal response is recorded at various locations away from the heated spot. The thermal property is then extracted by interpreting the experimental temperature data based on the theoretical analysis of the heat transfer inside the material. Depending on the particularities of the experimental setup, the heat transfer can be affected by heat losses or thermal contact resistances, which may become dominant in nanoscale samples and difficult to predict accurately. Optical heating methods are typically based on photothermal phenomenon, where heating is produced by absorbed incident radiation. Thus, contact resistance from a heat source is avoided.

This thesis is focused on the design, development and implementation of a thermal property measurement technique based on an optical heating method, the photoacoustic effect, which is able to measure many different types of materials, from bulk materials (3D) to nanowires (1D) at room temperature. The capabilities and limitations of the technique are established. Examples of the different materials measured by this technique are given: ZnO nanostructured pellets, standard bulk references, thick and thin films on different type of substrates, nanowire arrays embedded into anodic aluminum, and skeletal anodic alumina oxide membranes.

1.2 Thermoelectricity

Nowadays, the search for alternative energy resources is mandatory due to the high and increasing demand of electricity for human consume and the scarcity of fossil-fuel reserves. Apart from investigating new clean energy resources, a great effort is being done to improve the efficiency of the current energy system. The importance of this field of research lays on the fact that most of the energy produced in our society is lost as wasted heat, mainly in electrical power generation and during its transport. Generally speaking, two-thirds of the energy production is lost as heat[1]. In order to confront this situation, thermoelectric materials are being researched to take advantage of that wasted heat. These materials are able to convert a temperature difference into electrical energy and *vice-versa* so that a more sustainable world is likely by improving this type of technology.

The thermoelectricity is based on three different physics phenomena. The Seebeck effect consists of the generation of a voltage difference within a material causing by a temperature gradient. The Peltier effect, which is the inverse effect, generates a temperature difference when an electrical current goes through this material. Finally, the Thomson effect is described as the heat absorbed or emitted by a conductor when is subjected to a temperature gradient and an electrical current is passing through it.

Thermoelectricity is implemented in our daily life by means of thermoelectric devices which form the thermoelectric modules. Figure 1.1 shows the two operation modes used by a thermoelectric device: refrigeration and power generation modes. In both cases two different semiconductor materials are joint so that an n-type leg (conduction by free electrons) is connected electrically in series and thermally in parallel with a p-type leg (conduction by free holes). The cooling mode, also called Peltier cooler, needs an electrical current flowing through the module so that heat transfer takes place from one side to the other thanks to the Peltier effect. On the contrary, in the power generation mode a temperature difference is able to generate an electric voltage from the Seebeck effect.

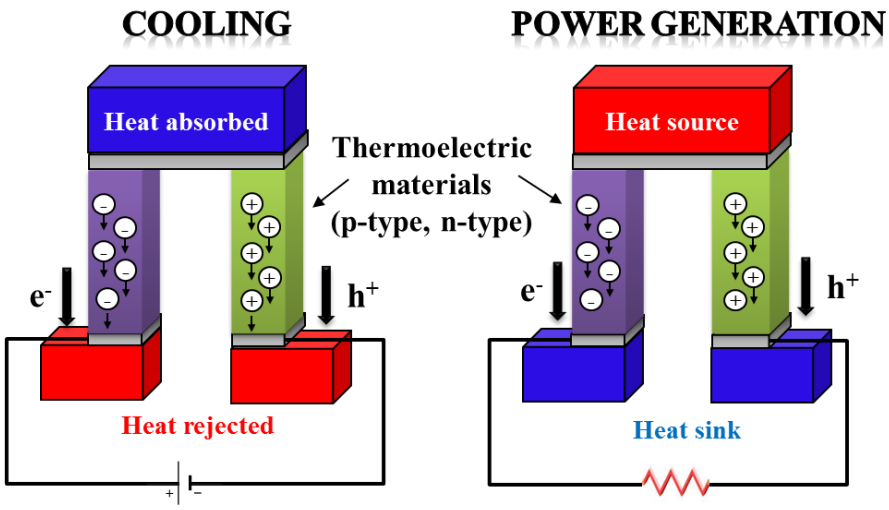

Figure 1.1. Thermoelectric device: cooling and power generation modes.

As an example, a thermoelectric generator was employed in the New Horizons spacecraft which recently collected Pluto images (July 2015) [2]. The power generation was produced by modules made of both n-type and p-type pellets of silicon-germanium (SiGe) which take advantage of the heat produced from a radioactive decay of the plutonium 238 to convert it into usable electricity.

The efficiency of this type of materials is related to the figure of merit by means of,

$$\eta(\%) = 100 \cdot \left(\frac{T_H - T_C}{T_H}\right) \frac{\sqrt{1+zT}-1}{\sqrt{1+zT}+(T_H/T_C)} \tag{1.1}$$

where T_H and T_C are the hot and cold sides and zT is the thermoelectric figure of merit which is in turns expressed as,

$$zT = \frac{S^2 \cdot \sigma}{\kappa} \; T \tag{1.2}$$

where $S^2 \cdot \sigma$ is called power factor, *PF*. In the above formula, *S* is the thermoelectric power (Seebeck coefficient), σ is the electrical conductivity, κ is the thermal conductivity which includes the phononic, κ_{ph}, and electronic, κ_e, contributions and *T* is the absolute temperature [3]. A good thermoelectric material should present a high Seebeck coefficient and electrical conductivity with a low thermal conductivity. Nevertheless, the efficiency of thermoelectric materials keeps being low, so great efforts are being made to improve it. Numerous materials for different temperature ranges as well as diverse strategies are been studying to increase it with the purpose of making this technology as competitive as other clean energies.

Metals present a large electrical conductivity but a very low Seebeck coefficient and high thermal conductivity. On the contrary, insulators have a considerably high Seebeck coefficient and a low thermal conductivity but these advantages are cancelled out by a significantly low electrical conductivity. Therefore, semiconductors stand for the best thermoelectric materials since they present an optimum combination of the three properties that govern their efficiency, as Table I.1 summarizes.

Table I.1. Thermoelectric properties of the metals, semiconductors and insulators materials [4, 5].

Property	Metals	Semiconductors	Insulators
Seebeck coefficient ($\mu V \cdot K^{-1}$)	~ 5	~ 200	~ 1000
Electrical conductivity $(\Omega \cdot cm)^{-1}$	~ 10^6	~ 10^3	~ 10^{-12}
Thermal conductivity ($W \cdot m^{-1} \cdot K^{-1}$)	~ 100	~ 1-10	~ 0.2-2
Figure of merit Z (K^{-1})	~ $3 \cdot 10^{-6}$	~ $2 \cdot 10^{-3}$	~$5 \cdot 10^{-17}$

The explanation of the adequacy of the semiconductor materials as good thermoelectric candidates can be explained in terms of the carrier concentration. Figure 1.2 shows the compromise existing between the Seebeck coefficient and the electrical conductivity. The maximum power factor typically arises at carrier concentrations ranging from 10^{19} to 10^{21} cm^{-3} depending on the material itself. However, it is necessary also to take the thermal conductivity into account. When doing that, the best figure of merit values are found also for heavily doped semiconductors, whose carrier concentration ranges approximately from 10^{19} to 10^{20} cm^{-3}. Figure 1.2 evidences the entanglement between the three properties. When the Seebeck coefficient is increased, a reduction in the electrical conductivity is produced due to a decrease in the carrier concentration. Conversely, if the electrical conductivity

increases, the electronic contribution of the thermal conductivity is also increased, as the Wiedemann-Franz law points out [6]. Improving the figure of merit becomes a very difficult task due to this entanglement.

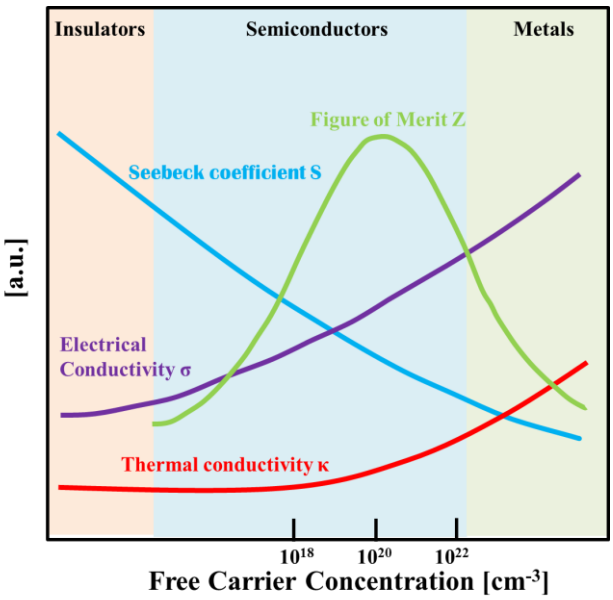

Figure 1.2. Figure of merit as a function of the carrier concentration. Figure adapted from reference [7].

Moreover, the efficiency of the thermoelectric materials also depends on the temperature range of operation (See Figure 1.3) Three different regimes can be found:

a) *Room temperature* (RT - 300 ºC): the most utilized materials are Bi_2Te_3 and its alloys and Sb_2Te_3. Also, $Bi_{1-x}Sb_x$ is used in the low temperature range [8].

b) *Mid-Temperatures*: (300 ºC – 700 ºC): the most common materials are found to be from group IV such as PbTe, GeTe, SnTe, among others.

c) *High temperatures*: (700 ºC – 1000 ºC): the most researched materials for both p-type and n-type components are SiGe as well as doped ZnO.

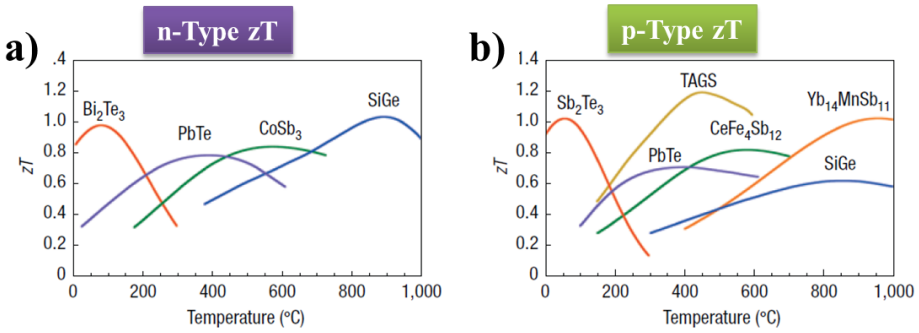

Figure 1.3. Figure of merit as a function of the temperature for different (a) n-type and (b) p-type materials. Graphs taken from reference [6].

Additionally, intensive studies have been carried out in organic materials. Intrinsically conductive polymers (ICP) have become promising materials due to their low thermal conductivity and relatively high electrical conductivity, especially when doping them [9] and blending them with different filler materials [10].

There are three different strategies to improve the overall figure of merit which are based on increasing of the power factor, $S^2\sigma$, or reducing the thermal conductivity, κ [11]:

- **New materials with complex bands structure**. The Seebeck coefficient would be increased while keeping the electric conductivity and the electronic contribution of the thermal conductivity.
- **Controlling the disorder within the materials to obtain electron-crystal phonon-glass behavior** [6]. For instance, Skutterudites and Clathrates play an important role in this sense since an increase of the electrical conductivity takes place at the same time as the phononic thermal conductivity is reduced by means of a *rattling effect* in this type of structures [12].
- **Nanostructuration of the materials** allows the reduction of the phononic thermal conductivity due mainly to the phonon scattering at the boundaries [13].

As this work is focused on the thermal conductivity measurements of many different materials after the design and implementation of the photoacoustic technique, this last strategy will be explored by means of the different found experimental results.

1.3 Thermal conductivity

In order to determine the efficiency of thermoelectric materials it is necessary to characterize the physical properties involved in the figure of merit. Therefore, developing experimental techniques to measure the Seebeck coefficient, electrical conductivity and thermal conductivity is as essential as the thermoelectric materials fabrication or the final thermoelectric device design. From these three magnitudes, the thermal conductivity is the most difficult one to determine, especially in the nanoscale regime.

The thermal conductivity is an intensive and intrinsic magnitude of materials which represents the ability of matter to conduct heat. Therefore, this parameter quantifies the capability of a substance to transfer the kinetic energy from its molecules to other adjacent molecules or substance, which is in contact to.

The thermal conductivity can be expressed as,

$$\kappa = -\frac{\vec{Q}}{\vec{\nabla}T} \tag{1.3}$$

where $\vec{Q}$ is the heat flux vector across an unit section of the material and $\vec{\nabla}T$ is the temperature gradient [14]. The thermal conductivity is, thus, a tensor since it depends on the direction within the material. However, it could be treated as a scalar magnitude for isotropic materials.

From a kinetic formalism point of view, the thermal conductivity in solids is found to be [14],

$$\kappa = \frac{1}{3} C v l \tag{1.4}$$

where C is the heat capacity, v is the particles velocity and l is the particle mean free path. As the thermal conductivity is a summation of many contributions from electrical carriers, lattice waves (phonons), among other excitations, Eq. 1.4 can be generalized to,

$$\kappa = \frac{1}{3}\sum_{\alpha} C_\alpha v_\alpha l_\alpha \tag{1.5}$$

In the above expression, the subscript α is related to the type of excitation which contributes to the thermal conductivity. This expression can be utilized to estimate the order of magnitude of different materials which are summarized in Figure 1.4.

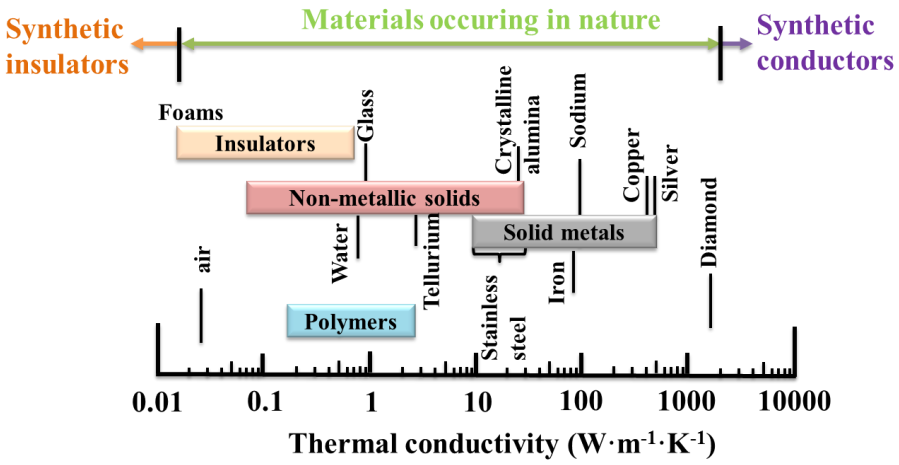

Figure 1.4. Thermal conductivity of different materials. Reference adapted from [15].

In metals, electrons carry most of the heat whereas in semiconductors and insulators, phonons transport that heat. Both electrons and phonons can be scattered from defects (e.g. charged impurities, neutral impurities, dislocations, etc.) and surfaces and boundaries. Moreover, electrons can be scattered by phonons and other electrons and phonons can also be scattered from other phonons and

electrons (which is called "*phonon drag*"). These scattering mechanisms determine the overall thermal conductivity in any type of structure [14].

1.4 Review of Non-contact methods to measure thermal conductivity

In general, the techniques employed to measure thermal properties can be categorized based on the time dependence of the thermal response as steady-state methods or transient methods as seen in Figure 1.5 (a).

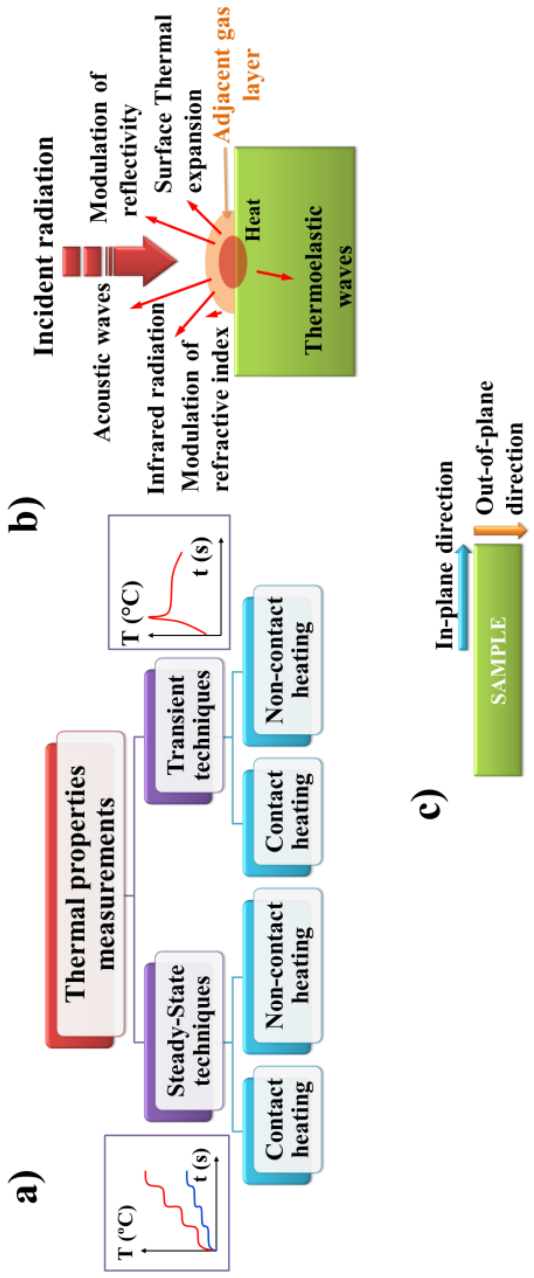

Figure 1.5. (a) Classification of the thermal conductivity and diffusivity measurement techniques, (b) thermal effects associated with incident radiation absorbed by a surface and (c) main measurement directions in a standard sample.

For instance, in steady-state techniques the heat is applied uniformly across a sample of uniform cross-section, the temperature is measured at both ends of the sample and the thermal conductivity is determined by applying a one-dimensional heat transfer model and knowing the sample dimensions [16-21]. On the other hand, transient methods study the thermal response as a function of time when heating the material [22, 23]. The experimental setup and the data reduction of the steady-state techniques are usually simpler than the transient techniques. However, the steady-state measurements are more time-consuming and are extremely sensitive to heat losses through convection, radiation and conduction.

Thermal properties characterization techniques are also classified depending on the heating procedure as contact and non-contact methods. In the former, the sample is heated by direct contact and the heating source can be either a microprobe as in Scanning Thermal Microscopy [24-27], a thin-film electrical resistor deposited directly onto the surface of the sample as in 3ω [28, 29], a bolometer [30], pulse heating [31] and micro-bridge methods [25, 32], or an external resistor in the case of hot disk [33], or many of the steady-state setups [10]. These techniques have been used for measuring different kinds of structures such as bulk, thick and thin films or nanowire arrays. However, when measuring thermal conductivity of single nanowires, microchips are typically employed [34-38]. The main common disadvantage of these techniques is the thermal contact resistance between the heat source and the sample, which makes it challenging to perform an accurate measurement mainly when measuring nanostructures like nanowires or thin film whose low thermal resistance can be easily overwhelmed by contact thermal resistance. On the contrary, dimensions of the bulk samples can be tuned in order to have a larger thermal resistance. Besides the thermal contact resistance, the complex microfabrication of the thin film electrical resistor or microchip is a major drawback in the sample preparation.

In contrast, non-contact methods are typically based on photothermal phenomenon, where heating is produced by absorbed incident radiation. Thus, contact resistance from a heat source is avoided. These techniques are of interest due to the simplicity of sample preparation and the absence of contact thermal resistances. Since it is difficult to establish accurately the amount of heat absorbed in the sample, the non-contact methods generally make use of a transient or modulated response, and the transport property determined experimentally is typically thermal diffusivity or effusivity. The thermal diffusivity, α, indicates how fast a material responds to a temperature change and it is related to the thermal conductivity, κ, by,

$$\kappa = \alpha \cdot C_p \cdot \rho \tag{1.6}$$

where ρ is the density and C_p is the specific heat. On the other hand, the thermal effusivity describes the capability of a material to exchange heat with its surrounds and is given by,

$$e = \sqrt{k \cdot C_p \cdot \rho} \tag{1.7}$$

Therefore, the main disadvantage of these methods arises from the necessity of knowing both density and specific heat in order to calculate the thermal conductivity. However, these properties can be determined by other methods such as differential scanning calorimetry (DSC) for specific heat measurement or pycnometry for density measurements. Oftentimes, when characterizing thermal transport properties of nanostructures, the density and specific heat are often considered similar to bulk [14, 39]. This assumption should be used with caution as it could lead to errors, since changes on phonon dispersion can affect the specific heat [40].

Although most of the non-contact techniques are based on optical heating, the measurement approach for thermal properties may be widely different depending on the thermal-sensitive phenomena employed in the detection scheme. Thermal emission [41], thermal expansion of the sample [42], refractive index changes [43], and acoustic waves [44] are some examples of the effects that can be caused by the optical heating and used for temperature measurement as schematically represented in Figure 5 (b). Most of the techniques make use of 1D heat transfer models, which allows obtaining the thermal conductivity or diffusivity in the out-of-plane direction, i.e., perpendicular to the surface of the sample. However, different experiments and analysis can be performed in order to obtain the in-plane thermal conductivity or diffusivity which corresponds to the value in the direction parallel to the surface of the sample as depicted in Figure 1.5 (c). This fact is of great importance in order to take into account the anisotropy of materials.

Regardless of the detection approach used, these techniques can be divided in two main groups: time-domain and frequency-domain [14]. The time-domain methods are based on the analysis of the thermal response as a function of time, such as, for example, decay in the sample temperature after pulse heating. In contrast, the frequency-domain is governed by an incident modulated radiation, which generates a periodic signal whose amplitude and phase dependence on frequency are analyzed. Besides these categories, additional methods employing non-contact optical heating for thermal conductivity measurement involve the investigation of the sample response to a continuous incident radiation. Among these, in Micro-Raman method the sample surface temperature increase is determined from the relation of the Stokes and anti-Stokes shift peaks when illuminating with a continuous wavelength [21]. In microphotoluminescence the sample is heated by a continuous laser causing a temperature increment gauged by studying the photoluminescence and then related to the thermal conductivity by knowing the optical power applied [45]. Apart from the optical heating methods, an additional non-contact method for thermal properties characterization is the thermal microprobe technique. This employs a Joule heated microprobe, which acts as a heating source,

brought in the close proximity of the sample, and takes advantage of the quasi-ballistic air conduction through the nanometer size air gap between the probe and sample surface [46].

Time-domain and frequency-domain techniques will be deeply reviewed since the photoacoustic technique is found to be among the frequency-domain methods.

1.4.1 Time-Domain techniques

The time-domain techniques used to measure the thermal conductivity are based on the analysis of the time-dependent thermal response of a material when this is heated by a pulsed laser beam. The time-domain signals, similar to frequency-domain signals, contain more information about the thermal properties of the sample since the transient response has multiple frequency components. However, the signal analysis presents higher noise in comparison with the frequency modulation techniques which typically use phase lock-in detection [14].

1.4.1.1 Time-Domain Thermoreflectance (TDTR)

1.4.1.1.1 Principle of the TDTR and historical background

The thermoreflectance technique was first proposed by Eesley in 1983 [47, 48]. Time-domain thermoreflectance method employs the so called "pump and probe" experimental setup, schematically shown in Figure 1.6 (a). In this setup, a pump laser, absorbed by the sample under investigation, produces a transient change in temperature. In turn, this causes a change in surface reflectivity, which is sensed with the help of the probe laser. Thus, the sample must be covered by a thin metallic layer, highly reflecting at the wavelength of the probe laser. The change in reflectivity, ΔR, of metallic materials is typically proportional to the temperature change (ΔT) through the thermoreflectance coefficient, k [49],

$$\frac{\Delta R}{R} = \left(\frac{1}{R}\frac{\partial R}{\partial T}\right)\Delta T = k\Delta T \tag{1.8}$$

Figure 6 (a) illustrates the typical time dependence of the temperature increase. During illumination, the heat is absorbed by the metallic film and its temperature increases, followed by a decrease, which depends on the thermal properties of the sample underneath the absorber.

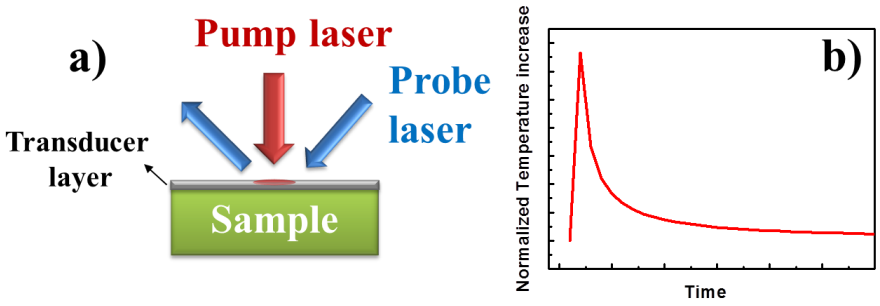

Figure 1.6. (a) Schematic of the pump and probe laser setup and (b) Temperature response as a function of time after a single-pulse.

1.4.1.1.2 TDTR Experimental setup

The experimental setup of TDTR is shown in Figure 1.7 and consists of an ultra-fast mode-locked pulse laser, with a frequency on the order of tens of MHz, producing a repetition rate in the nanoseconds range. This laser is split into a pump and a probe beams with the help of a beam splitter. The probe is then delayed with respect to the pump via a mechanical stage from 300 ms to 1 ps [50].

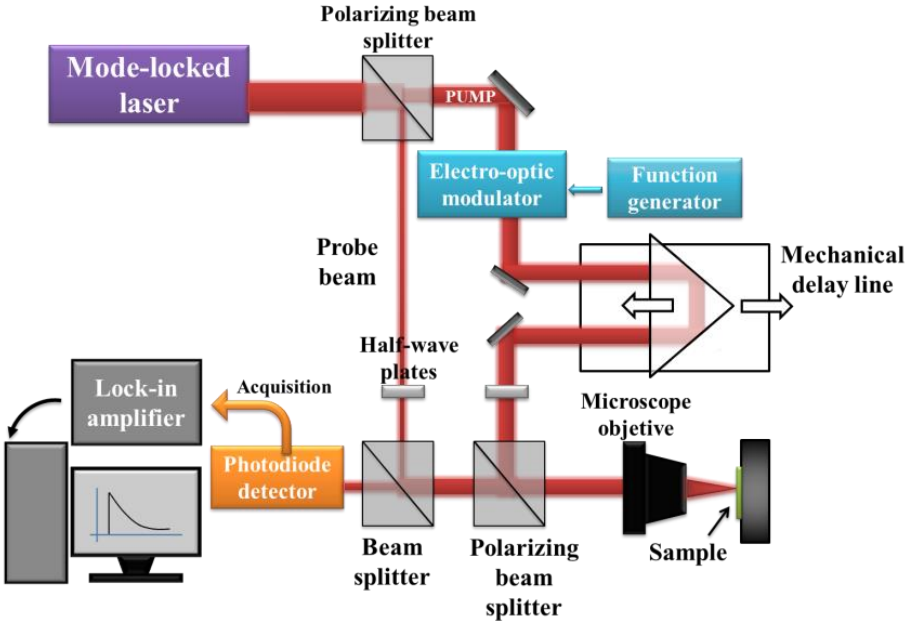

Figure 1.7. Time-Domain Thermoreflectance experimental setup.

The pump laser is modulated at a reference frequency which allows the lock-in detection whereas the probe laser remains unmodulated as shown in Figure 1.8 (a) and (b), respectively. When the pump and the probe lasers present the same repetition rate, the method is known as homodyne optical sampling which allows high time resolution [50]. The periodic heating produces a temporary increase in surface temperature which decays fast, depending on thermal properties of the sample. The pulsed probe beam, delayed with respect to the pump beam, is reflected by the sample surface and detected by a photodiode at each time delay. This probe laser is responsible for the detection of the

temperature decay, which is proportional to the change in reflectivity of the surface metallic layer. The time delay represents the time at which the temperature is probed and is key in data reduction since the lock-in detection can sense the amplitude and phase of the sinusoidal wave formed at each time delay as shown in Figure 1.8 (c). The real and imaginary parts or the in-phase (V_{in}) and out of phase (V_{out}) components of the wave are detected and used to extract the thermal properties. For clarity the detection scheme is shown in Figure 1.8.

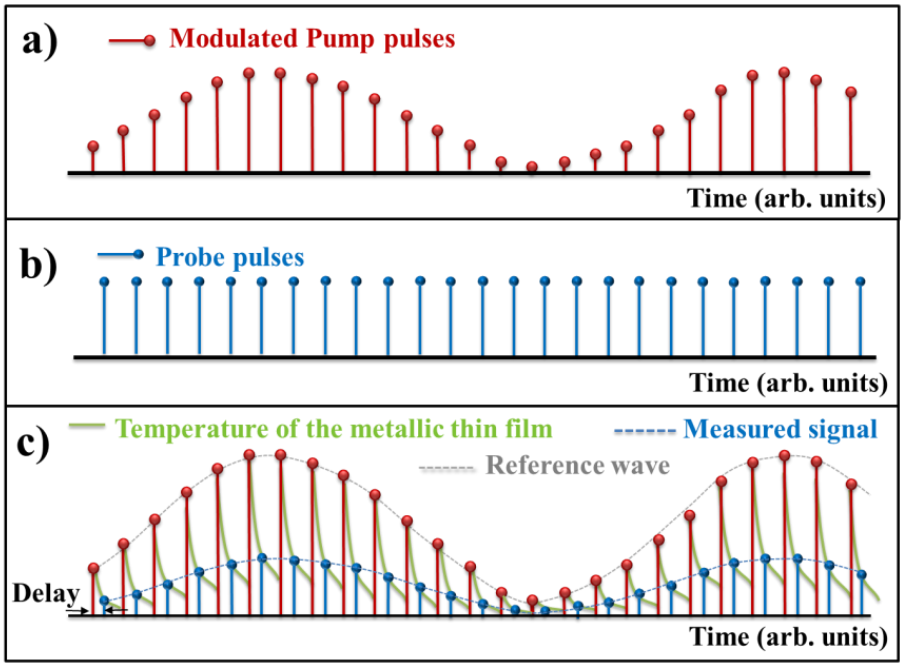

Figure 1.8. Homodyne optical sampling by TDTR with pump frequency modulation and probe delay. (a) The modulated pump beam, (b) Unmodulated probe beam and (c) Pump laser that heats the surface of the sample and creates a temperature profile. The probe laser which is time delayed which respect to the pump laser, is reflected off surface so that a sinusoidal wave is created and measured for different time delays.

This technique can be used without pump beam modulation [43, 51, 52]. However, accuracy is increased if an electric-optic or acoustic-optic modulator is used to modulate sinusoidally the pump beam (Figure 1.8 (a)) because frequency lock-in can then be employed in the detection of probe beam. This allows to eliminate the noise that arises from pump laser scattered light and background light and hence, the signal to noise ratio is increased, which is important as the change in reflectivity is small.

The mode-locked laser can be emitted as nanosecond, picosecond or femtosecond pulse. The pulse length sets the spatial resolution of the experiment because the thermal penetration length must be larger than the pulse length [14]:

$$\tau < \frac{l^2}{3\alpha} \tag{1.9}$$

In the above expression, l is the thickness of the sample, α is the thermal diffusivity and τ is the pulse duration. Thus, shorter pulses allow for studying thinner samples. For example, for a thin

film of 100 nm and thermal diffusivity of the order of 10^{-5} $m^2 \cdot s^{-1}$ (between metal and semiconductor materials), the pulse duration should be lower than 1 ns in order to avoid heat dissipation into the substrate which would require accounting for both the interface thermal resistance and the thermal properties of the substrate in data reduction.

1.4.1.1.3 TDTR theoretical model and data reduction procedure

The derivation of the expression for TDTR temperature rise has been carried out by many in both time [53, 54] and frequency [55] domains. Since the thermal diffusion length through the sample is smaller than the pump laser spot size [53] the thermal analysis is based on one-dimensional heat conduction, considering a Gaussian shaped periodic heat source on the surface.[55] The experimental signal detected by the lock-in amplifier, $V_f(t)$, is related to the temperature increase via:

$$\frac{V_f(t)}{V_0} = \frac{Q}{2}\frac{\Delta R(t)}{R} \tag{1.10}$$

where R is the reflectivity of the sample, $\Delta R(t)$ is the reflectivity change which is related to the temperature change by Eq. 1.8 , V_0 is the average voltage output of the detector, t is the probe beam time delay and Q is the quality factor of the resonant circuit. V_f includes both the in-phase (or real; V_{in}) and out of phase (or imaginary; V_{out}) signal components measured. Cahill used the ratio between the in-phase and out-of-phase component of the recorded voltage to extract the thermal conductivity of the material [55].

One of the limitations of TDTR technique is the necessity to ensure smooth sample surface to minimize diffuse reflections. In addition, a quantitative analysis of the data for times lower than 50 ps is difficult to carry out, one of the reason being that the thermal equilibrium between electrons and phonons may not hold on this time scale. On the other hand, measurements at very long time delays are not convenient since changes in the radius of the probe beam may occur by changing the length of its optical path and the model considers a constant probe spot [55].

1.4.1.1.4 Applications of TDTR and recent developments of the techniques

Originally, this method was developed for measurement the out-of-plane thermal conductivity of thin films or superlattices. Cross-plane thermal conductivity is typically difficult to measure in such structures even when they are freely suspended, because the small thickness limits the magnitude of thermal gradients that can be established cross-plane. However, thermal characterization can be carried out with TDTR for film on substrate configuration, without any interference from the substrate because of the picosecond time resolution[43, 53, 56-58]. More recently, this technique was modified to allow for characterization of nanowire arrays [59], as well as thermal interface resistances [60-62]. Heat conduction across a monolayer or a few layers of graphene was also investigated with TDTR [63]. It has

also been applied to emerging materials, such as characterization of thermal conductivity of silicon phononic crystals in the out-of-plane direction [13].

While TDTR method is more straightforwardly implemented for measurement of cross-plane thermal conductivity because the pump probe's short pulse causes very little lateral heat spreading, developments that allow for in-plane direction measurement have been also reported [64, 65].

Other studies explored the possibility to extract extended thermal or non-thermal information from TDTR measurements, For instance, Oyake *et al.*[66] studied the possibility to use gold nano-islands as heat absorbers for investigating the mean free path of the phonons in materials with low thermal conductivity. The nano-islands were necessary because it is not possible to reduce the pump laser spot to nanoscale range due to diffraction effects. Moreover, the study of the tiny peaks in the thermal decay, called acoustic echoes, which are created by the pump laser, have been employed to determine the film thickness and acoustic properties like the sound velocity [67, 68].

1.4.1.2 Laser flash

1.4.1.2.1 Principle of laser flash and historical background

The laser flash technique was developed in 1961 by Parker *et al.* [69], and currently it is one of the main techniques for measuring thermal properties of solid materials above room temperature [69, 70]. It relies on heating the sample optically on one side with a laser pulse and detecting the temperature change of the other side with infrared (IR) camera or a small thermocouple. Front heating and front detection configuration can be an alternative [71].

Laser flash technique is usually employed for measuring bulk materials [72], although it has been used for material other configurations such as nanowires embedded into a template [56], or thin film on substrate [73, 74]. For the later, the effect of the substrate and the interface thermal resistance between the film and the substrate is taken into account in the heat conduction model used for data reduction [51].

1.4.1.2.2 Experimental setup

Figure 1.9 shows a schematic of the experimental setup. In order to facilitate the absorption of the uniform, short-duration pulse incident onto the sample's surface, a layer of black paint is coated on both faces of translucent or transparent samples. Black paint is also added on the back side to enhance emissivity and enable more accurate temperature reading when IR camera is used for detection.

The typical temperature response obtained following a heating pulse is shown in Figure 1.10, which exemplifies the temperature change on the back of the sample as function of time. The thermal diffusivity is obtained by fitting the experimental data with a theoretical model.

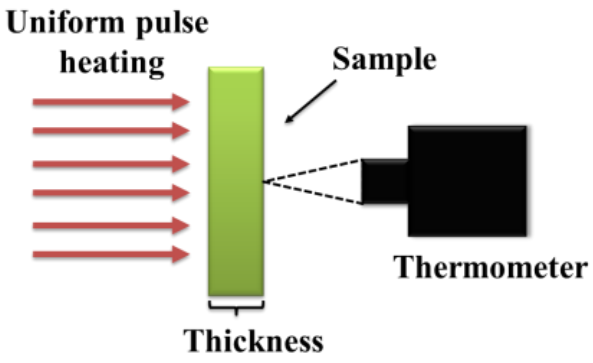

Figure 1.9. Laser flash experimental setup.

1.4.1.2.3 Theoretical model and data reduction procedure

Parker *et al.* [69] developed a solution of the one dimensional heat equation for the temperature increase of the rear face of the sample when the front face is heated by a short laser pulse. Two methods where proposed to obtain the thermal diffusivity.

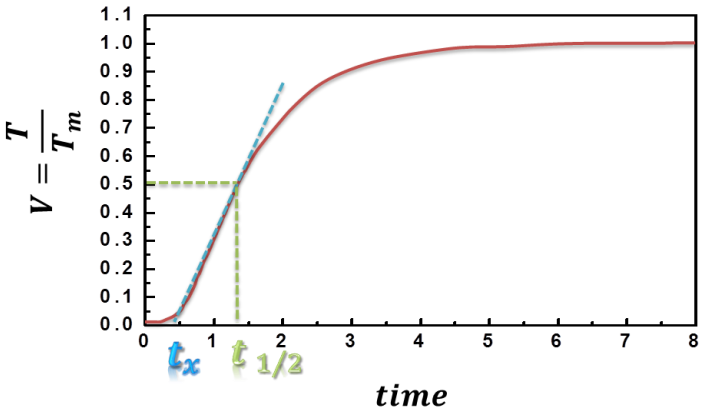

Figure 1.10. Sample response after a pulse of light.

The half-rise time method developed by Parker *et al.* [69] is the most commonly employed for determining the thermal diffusivity of the sample. Using this approach, the thermal diffusivity is given by,

$$\alpha = 1.38\frac{l^2}{\pi^2 t_{1/2}} \tag{1.11}$$

where $t_{1/2}$ is the time needed for the back-surface to reach one-half of the maximum temperature rise reached, as illustrated in Figure 1.10.

Another way to extract the thermal diffusivity is by extrapolating the linear regime of the temperature increase in Figure 1.10 until it intercepts the axis, at a time t_x. Based on this, the thermal diffusivity is determined as [69],

$$\alpha = 0.48\frac{l^2}{\pi^2 t_x} \tag{1.12}$$

Both approaches are developed on the basis that heat transfer inside the sample measured is one-dimensional. To meet this condition, the laser pulse width must be short enough so that it can be considered negligible when compared to the heat diffusion process characteristic time, the front surface of the sample must be uniformly heated by the incident laser beam, the sample must be adiabatically insulated, homogeneous, uniform in geometry and opaque to the wavelength of the incident laser beam. Experimental errors may arise due to difficulties in meeting these requirements. Radiative and convective heat losses from the sample can also affect the measurement so that they can be corrected by accounting for heat losses using models which take into account both convection and radiation like Cowan´s [75] method or Clark and Taylor´s [76] model, which only considers radiation losses. There are other sources of errors, such as the effect of Planck's law on emitted radiation which is usually avoided by calibrating the radiation detector [77], the response time, when an IR detector is used for temperature measurement and the uncertainty in the thickness of the sample. When a thermocouple is used for temperature measurement the thermal contact resistance between the thermocouple and the sample is also a source of experimental error. However, experimental uncertainties lower than 5 % have been reported [78].

Among the limitations of the technique, it is worth noting that the relation between the thermal diffusivity and the thickness of a sample plays an important role when measuring bulk samples. In general, the pulse width has to be much shorter than the time response. However, for thin and highly conductive samples, this assumption is no longer valid. For this reason, there is a thickness limitation depending on the thermal conductivity of the samples, which is directly related with the minimum pulse width that the setup can use[79]; otherwise one must correct for the actual laser pulse width in very thin samples in the model for data reduction [80].

1.4.1.2.4 Applications and other developments

This technique is widely used and commercial equipment has been developed by multiple companies, such as Linseis and Netzsch, able to perform out-of-plane thermal diffusivity measurements in the temperature ranges from -125 °C to 2800 °C.

When using an infrared camera for temperature measurement, the technique is also known as pulsed photothermal radiometry and is has been employed to extract the thermal diffusivity of films whose thicknesses are in the range of microns [81].

Efforts for extending this technique focused on the measurements in the in-plane direction in order to measure samples with anisotropic thermal properties have been made[74, 82-84]. For example, Tiwari *et al.* [82] developed an extension of laser flash by measuring the thermal response of the sample at different distances between the thermocouple in the rear face and the laser spot in the front face.

Other developments include extending the technique to measure inhomogeneous samples, such as fiber-reinforced composites, graded materials [85], and free standing carbon nanotubes measurements [86], among others.

1.4.1.3 Transient thermal grating (TTG)

1.4.1.3.1 Principle of TTG and historical background

Transient thermal grating was first proved by Eichler *et al.*[87] in 1973 who measured the thermal diffusivity in the in-plane direction of a solid sample for the first time. This technique relies on the diffraction pattern produced by the interference of two laser beams with the same wavelength and pulses of the order of nanoseconds to picoseconds which irradiate the surface of the sample under study at an angle θ on the sample surface. As a consequence, a sinusoidal intensity pattern is created on the surface of the sample whose spatial period is in the micrometer scale range and varies with the angle θ. As the thermal expansion is faster than the pulse duration, surface acoustic waves are created by thermally elastic stress induced by the radiation. Those waves propagate along the direction parallel to the surface of the sample forming standing waves. Due to the spatially modulated temperature distribution a photothermal grating emerges. Both the spacing of this thermal grating and the wavelength of the acoustic waves are the same as the spacing of the intensity pattern so that it can be modulated by the angle of incidence of the two pump laser beams. As Figure 1.11 shows, the thermal grating can be detected by the diffraction of a probe beam whose time relaxation time is related with the thermal diffusivity of the sample under study [88].

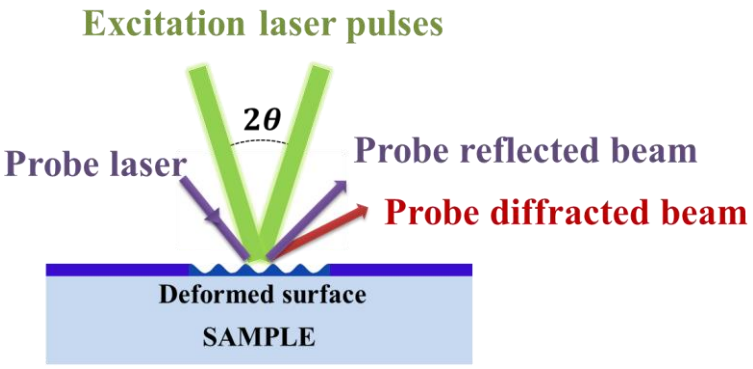

Figure 1.11.Surface thermal grating depiction.

This method does not require coating the sample with a metal layer, which makes the sample preparation easier, the measurements more accurate and not prone to error associated with metal layer thickness and thermal contact. Moreover, the data fitting is much simpler since metal layer parameters are avoided. On the other hand, the lack of a metal layer can be troublesome when measuring semiconducting materials whose energy carriers could be affected by the light [89]. Similar to thermal grating, concentration grating of the excited energy carriers can be created and affects the signal. However, this contribution used to be negligible since the time scale where this phenomena takes place greatly differs from the time scale of thermal grating [89], i.e., the carrier grating normally decays more rapidly than the thermal grating.

1.4.1.3.2 Experimental setup

Figure 1.12 (a) shows the typical transient thermal grating setup. An excitation laser beam is divided in two parts and crossed on the sample surface thus, creating the intensity pattern and the subsequent thermal grating. A probe laser is used to sense this phenomenon so that its diffracted beam due to the thermal grating is detected by a photomultiplier. Figure 1.12 (b) shows the decay of the thermal grating given by the intensity of the diffraction beam as a function of time, which follows an exponential relation. The experimental setup can adopt two configurations: reflection or transmission. In the second case, the sample must be transparent to the probe laser.

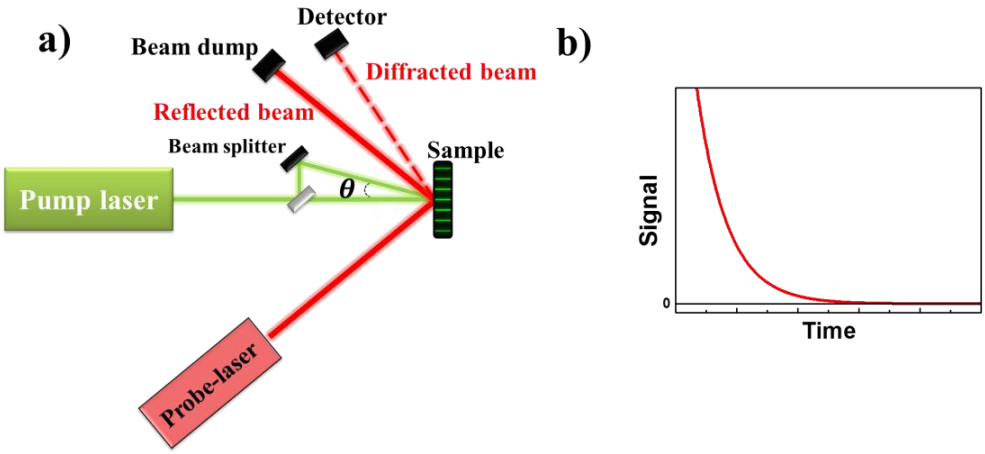

Figure 1.12. (a) Reflection configuration of the transient thermal grating setup sketch and (b) signal detected.

1.4.1.3.3 Theoretical model and data reduction procedure

Time-dependent and spatially periodic variations in the complex refractive index of the material take place when exciting the sample with two laser beams due to distribution of the light intensity created by their interference at each specific angle. [88]

The heat diffusion equation with appropriate boundary and initial conditions must be solved to determine the temperature variation at the surface of the sample needed to fit the thermal grating decay

[89]. The thermal diffusivity in the out-of-plane direction only influences the amplitude factor of the temperature decay, and the thermal diffusivity in the in-plane direction determines the temperature profile of the decay, which makes this method especially sensible to the in-plane thermal diffusivity measurements. This spatially periodic distribution of the temperature gives rise to a spatial distribution of the refractive index, which acts as a phase grating of the probe laser. For the first diffraction order, the relation between the temperature distribution and the diffracted beam efficiency is given by [88],

$$\eta(t) = K[g(t)]^2 \tag{1.13}$$

where *K* is time-independent constant and *g(t)* is the time dependent component of the temperature distribution, so there is a square-dependence of the intensity on the temperature and thus, the intensity of the diffracted beam also decays exponentially with the relaxation time.

The limitations of this technique include the low efficiency of the diffraction probe beam, which is normally overcome by the heterodyne detection. However, there are also difficulties in the heterodyne detection where it is necessary to avoid time delays between the probe and reference beams pulses and both must be collinear [90]. The experimental uncertainty is typically calculated from the standard deviation from several measurements, as 10 - 15 % [89].

1.4.1.3.4 Applications and other developments

This technique has permitted different studies such as the thermal diffusivity in the in-plane direction of bulk materials [87, 88, 91] and other kind of structures such as 5 μm thick single crystal PbTe [92], polymide films [93] or diamond crystals [94]. In-plane thermal conductivity anisotropy of GaAs/AlAs superlattices was measured by this technique, while the out-of-plane component was characterized with TDTR described above [89]. This technique has also allowed to prove some theoretical calculations previously performed in silicon, corroborating a non-diffusive thermal transport in the in-plane direction of freestanding silicon membranes in the range of microns [95]. Collins *et al.* [96] studied the influence of the size of the grating period in the phonon transport thus, establishing a new dependence of the relaxation time when the grating spacing is lower than the phonon mean free path, i.e., in the ballistic regime.

Marshall *et al*. studied the thermal diffusivity in Y-Ba-Cu-O thin films deposited on MgO [97] and later on the thermal boundary resistance between both layers [98]. Other studies have been carried out in order to study the temperature distribution on both a film and the corresponding substrate by a new model called the eigenfunction expansion method, which allows to calculate the thermal properties of both layers [99]. The technique was greatly improved by the development of the heterodyne detection. A reference beam is introduced in order to get an interference with the diffracted probe beam whose intensity has a very good signal to noise ratio [90, 100].

1.4.1.4 Pulsed photothermal displacement techniques

The pulsed phothothermal displacement techniques are based on the study of the thermal properties from a surface deformation of the sample caused by a heating pulse. The main advantage of this technique falls on the possibility of studying the surface temperature by a single pulse of the pump beam as well as the thermal properties associated with the thermal expansion generated by this temperature increment of the surface.

1.4.1.4.1 Pulsed photothermal mirror technique

1.4.1.4.1.1 Principle of pulsed photothermal mirror technique and historical background

The pulsed photothermal mirror technique was proposed by Astrath *et al.* [101] in 2007. This method is a type of photothermal displacement technique where a pump probe heats the sample, producing a mechanical distortion on the surface, which depends on sample's thermal expansion coefficient and thermal properties of the underneath layers. A probe laser is used to sense the wavefront distortion as shown in Figure 1.13 (a). In this technique a single pulse heats the sample and causes subsequent deformation due to thermal expansion. As sample surface is deformed, the probe beam is focused or defocused as a function of the expansion coefficient of the specimen which is known as the thermal mirror effect (TM) where the distorted surface acts as a concave or convex mirror [101, 102]. By analyzing the change in the intensity profile of the central portion of the beam in the far field, the thermal diffusivity can be extracted by means of a mathematical model based on the heat diffusion and thermoelastic equations [102].

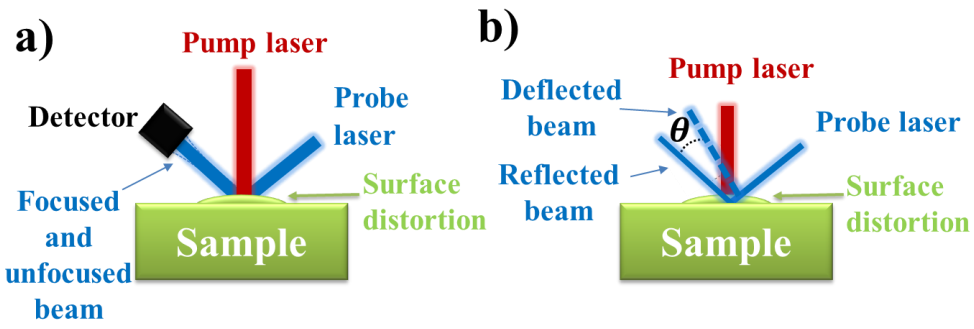

Figure 1.13. Schematic representation of the photothermal displacement techniques. a) photothermal mirror technique and b) Photothermal deflection method.

1.4.1.4.1.2 Experimental setup

Figure 1.14 shows the experimental setup where a nanosecond pulsed laser is commonly used as pump beam which heats the sample and a probe laser almost collinear to the pump beam which is the responsible for the detection of the thermal response of the sample by means of a photomultiplier.

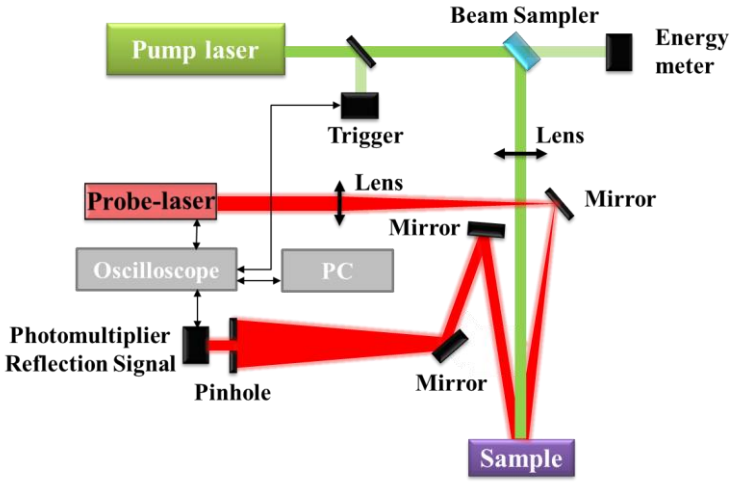

Figure 1.14. Pulsed photothermal mirror technique setup.

In order to ensure a good absorbance of the incident radiation, the sample should be opaque with an extremely low roughness, which can be achieved by surface polishing.

The response time depends on the thermal diffusivity of the sample ranging from hundreds of microseconds to milliseconds [102]. Thus, a regular photomultiplier, whose response time is less than 2 μm, is fast enough to perform the measurement.

1.4.1.4.1.3 Theoretical model and data reduction procedure

All the energy coming from the pump laser is absorbed by the sample and converted into heat, which diffuses through the sample. The thermal expansion gives rise to a surface distortion which follows the temperature rise distribution. The surface deformation can be seen as an optical element which affects the probe reflected beam by changing its intensity profile which is measured in the far field. The sample can be considered as semi-infinite and the heat is propagated in one-dimensional way in the cross-plane direction of the sample. The temperature increase on the surface of the sample can be determined from the heat diffusion equation [103] and appropriate boundary conditions.

On the other hand, the temperature change causes a surface deformation that can be described by the Navier-Stokes thermoelastic equation in the quasi-static approximation. The surface displacement of the sample is obtained from both expressions.

The surface deformation behaves as an optical element which induces a phase shift to the reflected probe beam. The intensity profile of the probe laser is related to this phase shift which in turn is related to the surface displacement [101, 102]. From the measured intensity of the probe beam, the thermal diffusivity can be extracted. The data reduction procedure relies on the knowledge of the Poisson's ratio, surface reflectivity, density and specific heat.

1.4.1.4.1.4 Applications and other developments

The pulsed photothermal mirror technique has been used to study the thermal diffusivity in the out-of-plane direction of different materials such as opaque materials [102] or optical glasses [104], where the limit of semi-infinite and finite media is also established as a function of the of the bulk optical absorption coefficient as well as the thickness of the sample. Moreover, this technique has also been used to measure the convective heat transfer coefficient on the solid-fluid interface [105]. Astrath *et al.* [101] measured the thermal diffusivity of low absorbing materials.

1.4.1.4.2 Pulsed photothermal displacement technique

1.4.1.4.2.1 Principle of pulsed photothermal displacement technique and historical background

The pulsed photothermal displacement technique (PTDT) was firstly proposed by Karner *et al.* in 1985 [106]. In this method a pump probe pulse impinges on a sample so that the surface of the sample experiences a deformation given by the thermal expansion due to the temperature increment. This distortion is sensed by a probe laser as shown in Figure 1.13 (b) which is deflected by the deformation of the surface and detected by a position sensitive detector. The angle between the deflected and reflected beam contains information about the thermal properties of the sample.

1.4.1.4.2.2 Experimental setup

Figure 1.15 shows and sketch of the experimental setup of the pulsed photothermal displacement technique. A pump laser pulse is used to excite the sample and the probe beam is responsible for the thermal expansion of the surface detection by a position detector which records the signal as a function of time.

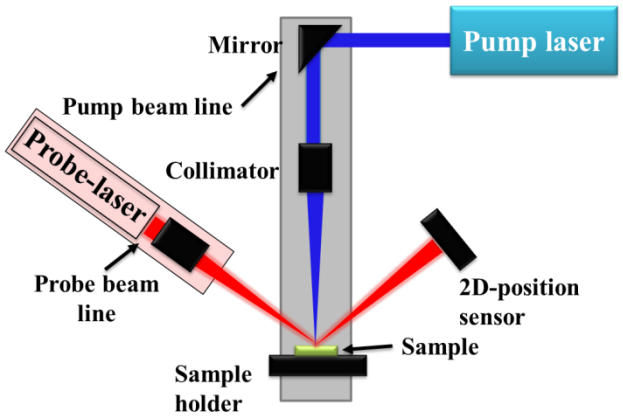

Figure 1.15. Pulsed photothermal displacement method setup

1.4.1.4.2.3 Theoretical model and data reduction procedure

The theory of the pulsed photothermal displacement method was developed by Li in 1989 [107]. The deflection of the probe beam is given by an angle and the photothermal displacement signal which is in relation with the solution of the equation for thermoelastic deformation in the quasistatic approximation from stress-free boundary conditions [108] and the solution of the heat diffusion equation subjected to adiabatic boundary conditions where heat does not flow out of the sample during the measurement.

1.4.1.4.2.4 Applications and other developments

This technique has been used for measuring the thermal diffusivity of solid materials like GaAs [108, 109] or InGaAs/AlGaAs multiple quantum wells[108]. Cheng and Zhang discussed the theory of the PTDT method for semiconducting materials by taking into account the photogenerated carriers [110]. In 2003 Xu *et al.* [111] developed a new system for the detection of the pulsed photothermal displacement based on optical birefringence interferometer .

Table 1.II. Summary of the time-domain techniques for measuring the thermal properties of different structures together with the advantages, disadvantages and uncertainties.

Time-Domain techniques				
Time-Domain Thermoreflectance (TDTR)				
	What measures?	**Advantages**	**Drawbacks**	**Uncertainty**
	Thermal conductivity: a) Out-of-plane b) In-plane	-No contact resistances -Nanometer scale depth resolution. -Information about the thickness and microstructure -Good sensitivity to thermal interfaces and conductivities of submicron thin films.	- Smooth surfaces - Extensive postprocessing - Metallization - Complex experimental setup - ρ and Cp needed	~10 %
Laser flash				
	What measures?	**Advantages**	**Drawbacks**	**Uncertainty**
	Thermal diffusivity of mainly bulk materials in the out-of-plane direction	-No contact resistances - Easy data reduction -High or low temperatures -Low amount of energy needed to heat the sample -Provide thermal diffusivity and heat capacity	- Thickness limitation - ρ and C_p needed - Thin films more complicated - Black painting - Big sizes	~ 5 – 10 %
Transient thermal grating				
	What measures?	**Advantages**	**Drawbacks**	**Uncertainty**
	Thermal diffusivity in the in-plane direction	- No contact resistances - In-plane measurements - No sample prerpation - Non-invasive	- Semiconductor materials are difficult to be measured - Low efficiency of the diffration pattern - ρ and Cp needed	~ 10-15 %
Pulsed photothermal displacement techniques				
	What measures?	**Advantages**	**Drawbacks**	**Uncertainty**
	Thermal diffusivity in the out-of-plane direction	- No contact resistances - Non-invasive	- Knowledge of the Poisson's ratio, surface reflectivity, ρ and Cp needed - Extremely low roughness needed	~ 15 %

1.4.2 Frequency-domain techniques

Frequency-based techniques are based on a modulated heating from a laser which is focused on the surface of a sample. The periodic heat diffuses through the sample producing thermal waves and a periodic temperature distribution. The thermal penetration depth, μ, defined as the distance at which the thermal wave is damped down to *1/e* (around 37 %), is a function of the modulated frequency,

$$\mu = \sqrt{\frac{\alpha}{\pi f}} \tag{1.14}$$

where α is the thermal diffusivity and f is the modulated frequency. Based on this parameter, a critical frequency can be defined for which the penetration depth is equal to the film thickness. If the

frequency of the signal is higher (lower) than critical frequency the sample is said to be thermally thick (thin). By sweeping the heating signal across a wide range of frequencies, the heated region can be focused next to the surface, which allows for two-dimensional spreading, or can be forced to be one dimensional across the sample of the film, allowing for a more comprehensive characterization of the materials under study.

1.4.2.1 Frequency-domain reflectance method (FDTR)

1.4.2.1.1 Principle of FDTR and historical background

FDTR was originally proposed by Schmidt and colleagues in 2008 [112]. In contrast to the TDTR technique, the FDTR is based on a continuous wave (CW) illumination, which removes the multiple time scales associated with pulse-lasers in TDTR methods. Both implementations are similar, but in the case of FDTR the pump laser is modulated and the thermoreflectance signal is recorded at a fixed time delay between the probe and pump pulse laser. Thus, unlike TDTR, FDTR does not require a moving stage, which eliminates undesired contributions from the delay stage movement. However, the sensitivity of the TDTR is highly dependent on the modulation frequency which has to be selected before the experiment [113]. FDTR is primarily used to measure the thermal conductivity of thin films and bulk samples for an extensive variety of materials since it allows a great resolution of the thermal penetration length [112].

1.4.2.1.2 Experimental setup

Figure 1.16 shows a sketch of the typical setup. The high power (> 100 mW) CW pump laser is modulated, so that it periodically heats the surface of the sample. A low power (5-10 mW) CW laser beam, which acts as a probe, is directed on the sample and its reflection detected. Based on the measured changes in the reflected probe laser beam, changes in on surface reflectivity can be assessed, from which temperature variation of the sample using Eq. 1.8. The phase shift between the pump and the probe lasers, which is recorded by a lock-in amplifier, is normally the observable of interest, since the amplitude is affected by the frequency response of the detector, setup wires and properties of the optical components in the beam path.

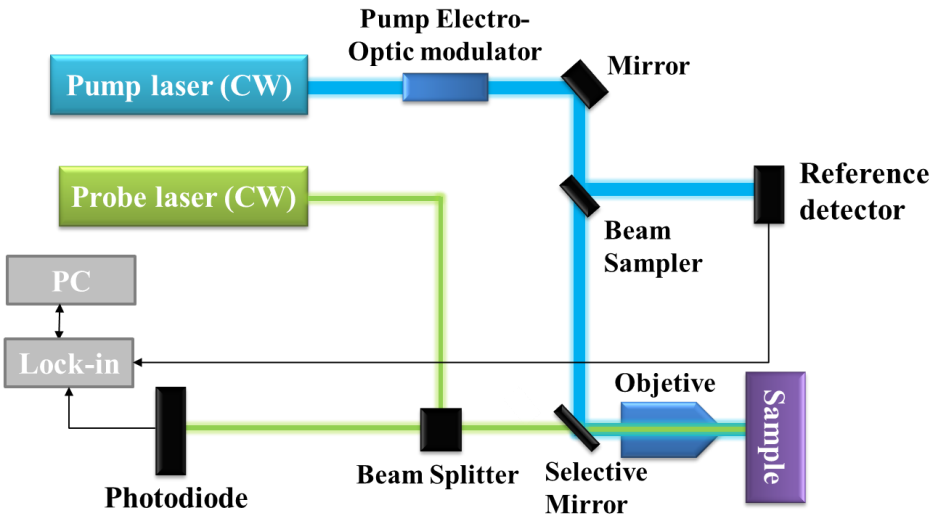

Figure 1.16. Frequency-Domain Thermoreflectance experimental setup.

As in the case of TDTR, in FDTR it is necessary to include a metal transducer which acts as a heater, and which experiences large changes in reflectivity with temperature at the wavelength of interest, as explained earlier in Section 1.4.1.1.1.

In order to perform an analysis of the size effects on thermal transport, for example to investigate the phonon transport mechanism in thin films, high frequencies are applied to the pump beam, which can range from 200 kHz to 200 MHz [114]. On the other hand, this technique has been also used as a method to determine the heat capacity of both bulk and thin films and the in-plane and out-of-plane thermal conductivity [112, 115].

1.4.2.1.3 Theoretical model of FDTR and data reduction procedure

As discussed earlier, the pump laser focused on the sample generates a periodic temperature change through the sample, which is detected by changes in probe beam reflectivity. The theoretical model of the heat transfer through a single film on substrate and their interface has been previously presented [54, 112]. From this solution, the amplitude and phase shift can be analyzed and fitted, which are recorded by the lock-in amplifier.

1.4.2.1.4 Applications and other developments

FDTR has been typically used to measure the thermal conductivity of both bulk and thin films along with interface thermal conductances [113, 115-117], but also other parameters such as conductance of self-assembled monolayer junctions formed between metal leads with mismatched phonon spectra [118] or thermal conductivity accumulation functions [114, 119].

A number of modified implementations of FTDR also exist. Regner *et al.* [114] used a novel heterodyne detection to avoid ambient and coherent noise by employing another electro-optical

modulator which modulates the probe beam after being reflected from the sample surface. However, Ramu *et al.*[120] have developed a new heat transfer model for the FDTR experiment comprised of two different channels for phonons with mean free path higher (quasi-ballistic channel) or lower (diffusive channel) than a threshold which explained the results obtained by Regner *et al.* [120], suggesting that FDTR has limited capabilities for studying of the accumulation function of bulk matter. Other interesting developments involve the modification of TDTR data into the similar expressions with the one used in FDTR. Thus, the high resolution and great signal to noise ratio of the TDTR are combined with the advantages provided by the heat model associated with the FDTR, allowing the study of signals obtained at very high frequencies where the TDTR is prone to effects of electron superdiffusion in the transducer film [121]. Finally, Yang *et al.* [122] developed a technique based on FDTR which allows for mapping with micrometer resolution of the in-plane and out-of-plane thermal conductivity, heat capacity, thermal interface resistance and thickness of films.

1.4.2.2 Photothermal emission/photothermal radiometry method

1.4.2.2.1 Principle of Photothermal emission method and historical background

The photothermal emission method, photothermal radiometry, lock-in thermography or infrared thermography was introduced in 1979 by Kanstad and Nordal [123]. This technique is based on the photothermal effect, where a surface emits more infrared radiation when heated. In this method, an incident modulated radiation heats periodically the surface of a sample which is covered normally with a thin layer to absorb the heat. The periodic radiation causes periodic fluctuations of temperature of the surface of the sample which are dictated by the material placed underneath the covered layer, which are recorded by an IR detector. By comparing the phase shift between the original signal, i.e., the modulated laser beam and the temperature variation, the thermal properties can be extracted[55, 124, 125]. This technique can be also used in the rear configuration, where the thermal emission from the rear surface of the sample is recorded by the IR camera, a setup very similar to laser flash technique [126]. In this case, it is necessary to deposit a black layer on both surfaces of the sample in order to improve the absorption of the laser and the backside infrared emission.

1.4.2.2.2 Experimental setup

A sketch of the experimental setup used in the photothermal radiometry technique is shown Figure 1.17 in both front (a) and rear (b) configurations. In this setup the intensity modulated radiation impinges onto the sample and the infrared radiation emitted by the front face is directed and focused onto an infrared detector. (see Figure 1.17 (a)). The specular reflected beam is typically collected by a beam dump. Visible radiation is blocked by using a Ge detector window with the proper spectral range. Finally, the collected signal is pre-amplified and fed to a lock-in amplifier which measures the amplitude and phase.

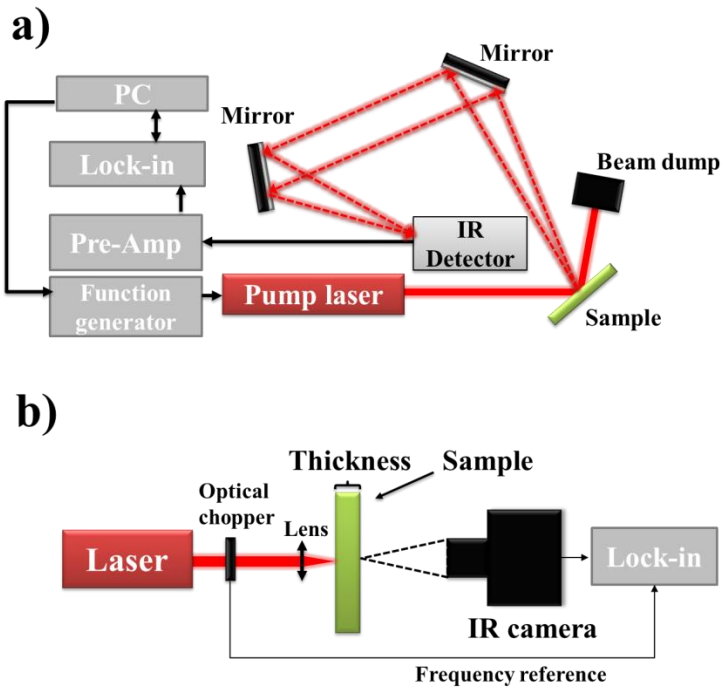

Figure 1.17. Photothermal emission setup (a) front and (b) rear configurations.

The experimental measurements must take into account the experimental phase shift that the setup introduces in the system and can distort the final signal. For that aim, a calibration is typically performed by measuring the phase shift between the original laser beam and the specular reflected beam [127].

1.4.2.2.3 Theoretical model and data reduction procedure

When the sample surface is heated with a laser, the infrared radiation emitted by the sample is phase shifted with respect to the incident radiation. The phase shift depends on the thermal transport that takes place in the sample and its thermal properties. Specifically, it encodes information about the thermal diffusivity of the sample, that can be extracted by fitting the data to a one-dimensional heat transfer model where the phase shift, $\Delta\varphi$, is proportional to the square root of the frequency as provided that $l > \mu$ [128, 129],

$$\Delta\varphi = \sqrt{\frac{l^2\pi}{\alpha}}\sqrt{f} \tag{1.15}$$

where l is the thickness of the sample and α is the thermal diffusivity. Measurement of multilayered structures is also possible by applying a multilayered model [130].

1.4.2.2.4 Applications and other developments

This technique has been employed to measure the out-of-plane thermal diffusivity of a diversity of materials, including multiwall carbon nanotubes in the axial direction [127], hybrid organic-inorganic films[131] or vanadium-doped magnesium nanostructures [130]. The thermal diffusivity of Bi_2Te_3 nanowires embedded in an alumina matrix was measured in the direction perpendicular to the nanowire axis [129] along with other low conductive materials [132]. The experimental uncertainty is found to be in the vicinity of 10 % for most works [133].

Recent improvements of this technique include extending the model to extract the optical absorption coefficient of both homogeneous solids and multi-layered solids at the same time as the thermal diffusivity measurements [134, 135] as well as the effective infrared optical absorption coefficient of solid samples [136]. Simultaneous measurement of thermal diffusivity and the thermal conductivity relative to a reference sample is also possible [128]. In the case of semiconducting materials, the recombination parameters can be extracted by studying the photothermal signal as a function of the modulation frequency [137]. The rear configuration has been mainly used to measure bulk samples [138], but it also serves to measure the in-plane thermal diffusivity of free standing thin films [133].

1.4.2.3 Photothermal Beam deflection (PBD) or "mirage method"

1.4.2.3.1 Principle of PBD and historical background

The Photothermal Beam deflection (PBD) technique, also called "mirage method", was firstly proposed in 1980 by Boccara *et al.*[139]. This technique is based on the deflection of a probe beam tangential to the surface due to changes in the refractive index of the gas layer adjacent to the surface (mirage effect) induced by a temperature change caused by a pump laser. The pump beam is typically modulated so that the heat diffusion through the sample and the temperature surface depends on the frequency modulation. A gradient in the refractive index causes the deflection, which depends on both the optical absorption coefficient and the thermal properties of the sample. From the deflection beam signal the thermal diffusivity in the out-of-plane direction can be extracted.

1.4.2.3.2 PBD Experimental setup

Figure 1.18 shows the experimental setup of the PBD technique. The pump laser heating the sample is modulated. A position sensitive detector is used to sense the deflection of the probe beam caused by the thermal response of the gas layer in the proximity of the sample. The detector is connected to a lock-in amplifier which compares the phase of the recorded signal with the reference one from the pump laser.

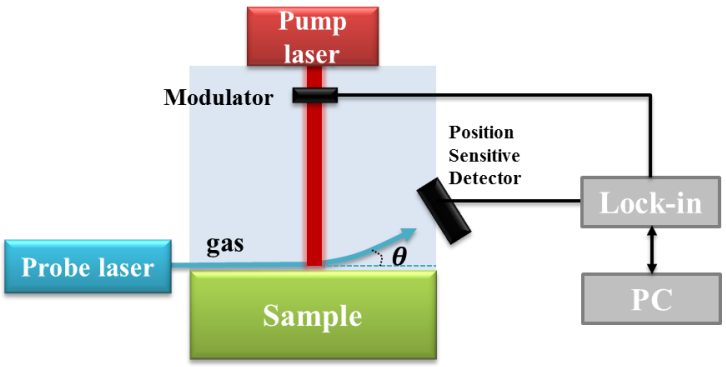

Figure 1.18. Photothermal beam deflection sketch.

1.4.2.3.3 Theoretical model and data reduction procedure

A complete description of the theoretical models used in data fitting of the PBD technique can be found elsewhere [140]. Considering a simple one dimensional model, the probe laser beam parallel to the surface of the sample is deflected by an angle [141] related to the temperature of the gas layer which is obtained by solving the heat diffusion equation for each layer (gas, sample and backing material) when the sample is periodically heated by a Gaussian beam and taking into account the appropriate boundary conditions for each layer, i.e., temperature continuity at the sample surfaces and heat flow continuity [142]

The thermal diffusivity can be extracted from the slope of the linear relationship between the first non-central zero crossings of the real part of the transversal deflection versus the inverse of the frequency root square which is known as crossing method [143]. Thermal diffusivity can be also extracted by the phase method in which the thermal diffusivity value is obtained from the slope of the linear relation between the transversal deflection phase signal versus the offset between the pump and probe lasers [144].

1.4.2.3.4 Applications and other developments

This technique has been used to measure the thermal diffusivity in the out-of-plane direction of bulk materials [145, 146], thick films [147] as well as thin films or multilayers [148]. Wong *et al.* [149] derived a solution of the mirage signal suitable to take into account the effect of the substrate in measurements where a thin film is deposited on a substrate. Low thermal diffusivity samples which are difficult to measure due to the high damping of the thermal wave profile have been also measured [150]. Bertolotti *et al.*[151] developed three new experimental setups in order to measure large sizes samples like semiconductor wafers. The experimental uncertainty was reported to be approximately 10-15 %.

1.4.2.4 Photothermal displacement techniques (PTDT)

1.4.2.4.1 Principle of PTDT and historical background

In 1983 Olmstead *et al.*[152] developed the photothermal displacement technique (PTDT) in order to extract thermal and optical properties of solids. The modulated radiation can also cause a thermal expansion in the sample which can be detected by different techniques, such as the deflection of a probe laser or interferometry. These techniques are widely used mainly for samples whose thermal expansion coefficient is high enough to generate a detectable signal, like polymers, to measure their thermal diffusivity of bulk and thin films and thermal boundary resistance between the film and the substrate.

In this method an intensity modulated pump laser beam impinges onto the sample along the normal direction, whereas a probe laser is incident to the surface at an oblique angle as shown in Figure 1.19. When the pump laser is off, the probe beam angle is reflected from the surface at an angle equal to the incident angle. When the pump probe is switched on, the angle of the reflected probe laser changes because the surface of the sample undergoes mechanical distortion caused by the heating [42].

1.4.2.4.2 Experimental setup

A sketch of the experimental setup is shown in Figure 1.19. A pump laser is modulated by means of a mechanical chopper, driven by a reference signal from a lock-in amplifier. This modulated signal is guided to the sample, where is absorbed by its surface. At the same time, the probe laser is directed onto the sample surface at an oblique angle. Because the sample is heated periodically, the probe beam is deflected as a function of the surface of the sample deformation. This deflection is sensed by means of a position sensitive detector, as depicted in Figure 1.19. Finally, the lock-in amplifier provides amplitude and phase data of the measured signal.

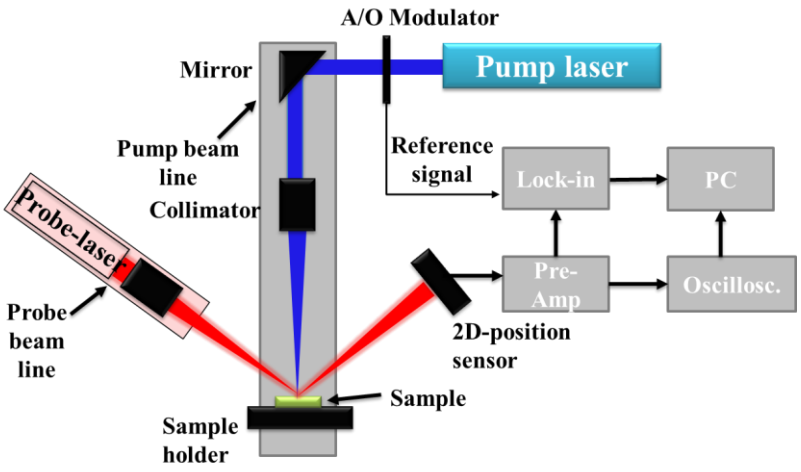

Figure 1.19. Photothermal displacement method experimental setup.

1.4.2.4.3 Theoretical model and data reduction procedure

The analysis of this technique is similar to that of the pulsed photothermal mirror technique, which combines heat diffusion equation with a Gaussian beam as a heat source and thermoelastic Navier-Stokes equation for a slab [42, 152]. After solving these equations the solution, the slope of the vertical displacement is derived, as seen elsewhere [42, 152]. This is a complex solution which can be described as a sum of the in-phase and out-of-phase components with respect to the reference pump laser signal. The actual measurement that is taken from the lock-in amplifier is given by the arctangent of the ratio between both components. This phase angle is measured as a function of the modulated frequency and can be fitted by knowing some laser and sample parameters such as the sample thickness, optical absorption coefficient, Poisson ratio or the pump beam radius.

1.4.2.4.4 Applications and other developments

The photothermal displacement technique has been employed to measure the out-of-plane thermal diffusivity of materials. Ogawa *et al.* [42] measured free-standing polymer thin films. Hu *et al.* [153] developed a model that allows measuring film on a substrate. This technique has been used also as a tool for surface profiling of materials with a vertical resolution of approximately 0.1 μm [154]. Penco *et al.*[155] developed a modified version of PTDT, based on a Michelson interferometer, where the sample under study substitutes one of the mirrors. A CW laser heats the surface of the sample and in response to this, the surface undergoes a thermal expansion, which modifies the optical path of a laser beam reflected by it. Since the Michelson interferometer is extremely sensible to distance changes, it can be used to determine the thermal properties from this thermal expansion. This interferometric method was used to measure the out-of-plane thermal diffusivity of silicon bulk and silicon thin film, as well as the thermal interface resistance between the substrate and the film many decades ago by Kuo *et al.* [156]. It was also used to measure the thermal diffusivity of ferrites [157]. The thermal diffusivity uncertainty was reported to be approximately 15 – 20 % [153].

1.4.2.5 Pyroelectric calorimetry (PC)

1.4.2.5.1 Principle of PC and historical background

The pyroelectric effect, which was discovered in the 18th century, is the ability of some materials to temporally induce a voltage when they are heated or cooled. In that sense, pyroelectric calorimetry uses a laser beam as a heat source which can be a single pulsed or modulated beam and a pyroelectric temperature detector to sense the thermal induced response [158]. The pyroelectric sensors have the capability of transforming a temperature gradient into an electric signal with fast and stable dynamic responses at temperatures below the Curie temperature. By studying the thermal response, the thermal properties of the sample can be obtained [159, 160]. This kind of detection ensures signal to

noise ratios better than 102-103, so that it can be considered as an accurate technique to determine thermal parameters of materials. This technique can operate in various configurations like front and rear detection, with different sources of information, amplitude and phase of the signal, at different frequency ranges or thicknesses of the samples depending on the particular study which is being developing.

1.4.2.5.2 Experimental setup

The photopyroelectric calorimetry experimental setups are shown in Figure 1.20. An intensity modulated laser impinges onto a pyroelectric sensor in the case of back illumination or directly onto the sample in the in front configuration. In either case, the sample is in good contact with the pyroelectric sensor. The thermal induced response, which encodes the thermal properties of the sample, is transduced by the pyroelectric sensor. The sensor is typically for a thick film of PVDF foils [158, 161, 162] or $LiTaO_3$ [163], and produces a voltage which is amplified and sent to the lock-in amplifier.

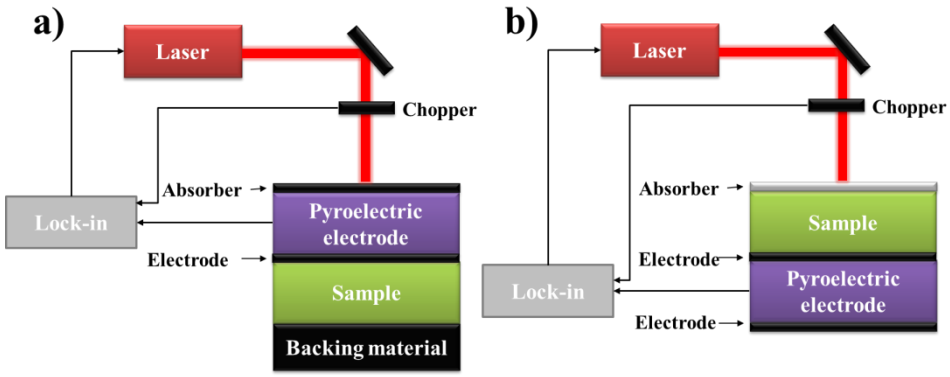

Figure 1.20. (a) Back and (b) Front configurations of a pyroelectric calorimetry setup.

1.4.2.5.3 Theoretical model and data reduction procedure

The generated voltage detected by the pyroelectric sensor is related to the pyroelectric coefficient, the thickness, the dielectric constant of the sensor and the average temperature fluctuation across the film sensor [159]. This thermal gradient can be calculated by solving the heat diffusion equation with a heat source given by a Gaussian beam distribution and taking into account the proper boundary conditions of heat-flux and temperature continuity across the layers [159].

The data reduction needed to extract the thermal properties of the materials is performed by analyzing either the amplitude of the phase shift between the reference signal associated with the laser modulation and the sensed signal as a function of the modulation frequency.

1.4.2.5.4 Applications and other developments

This technique has been used to measure the out-of-plane thermal diffusivity of bulk [159, 164] and thin films [158]. It has been also adapted for measurement of both heat capacity and thermal diffusivity simultaneously[161, 165]. Moreover, this technique has been employed as an accurate method to determine thermal properties of liquids [162, 166]. Different uncertainties have been reported, ranging between 5 - 20 % [158, 167].

1.4.2.6 Photothermoelectric technique

1.4.2.6.1 Principle of and historical background

In this technique a square wave modulated laser incident onto the sample is absorbed at the surface, producing a temperature rise with a dc and ac components, which propagates through the thickness of the sample. The temperature change is detected on the backside by a thermoelectric junction formed between the sample surface and a sharp tip.

The amplitude and phase of the ac thermoelectric voltage produced in response to temperature fluctuation are recorded by a lock-in amplifier. With this technique both in-plane and out-of-plane thermal diffusivities can be measured. In-plane thermal diffusivity is determined based on the ac temperature rise at the back surface measured as a function of distance from the heating spot. The out-of-plane thermal diffusivity is determined by carrying out a frequency sweep for a fixed location of the junction, typically right across the heating spot.

A main advantage of this technique is its capability of measuring both in-plane and out-of-plane thermal properties [168]. Moreover, the experimental setup, especially the detection part, is significantly simpler than that of others techniques which need high precision optical equipment. However, non-conductive and non-absorbing samples must be coated with additional layers, and knowing the properties of these layers is required for making accurate theoretical predictions.

1.4.2.6.2 Experimental setup

The experimental setup used in this method is similar to the laser flash set up. However, instead of a pulsed laser, a modulated laser beam with Gaussian intensity profile is used to periodically heat the front face of the sample as shown in Figure 1.21. For transparent samples, the surface must be coated with a layer optically thick at the wavelength of the incoming light [169]. Thermal waves across the sample are generated and detected by a fine thermocouple junction formed by back face of the sample and a sharp metallic tip of a wire probe. If the surface of the sample is not conductive, a metallic thin film has to be deposited in order to ensure the electrical contact. The thermocouple circuit is closed by another wire electrically connected to the back face of the sample at least several

thermal diffusion depths far from the heating spot. Because the heating is performed by an on-off laser beam, an ac temperature signal is generated, which is superimposed on a dc component. The dc signal is detected by a thermocouple to record the measurement temperature range, whereas the ac component is sensed by the thermocouple junction and sent to the lock-in amplifier. The diameter of the sharp wire probe must be as small as possible in order to avoid the heat loss and minimize the time response of the probe. The ac detected signal is the Seebeck voltage and the ac temperature rise can be determined directly if the Seebeck coefficient of the back surface and the sharp layer are known.

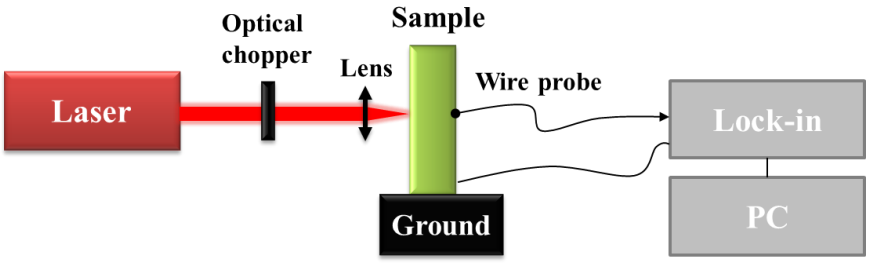

Figure 1.21. Photo-thermoelectric experimental setup.

1.4.2.6.3 Theoretical model and data reduction procedure

The data reduction is based on fitting the experimentally measured temperature rise (typically its phase) to temperature predictions based on a heat diffusion model solved in cylindrical coordinates. If the sample is coated with absorbing and conductive layers on its top and bottom surfaces, respectively, these layers must be taken into account. Assuming than the absorbing layer is optically thick, and applying the proper boundary condition to the continuity of the heat flux and the temperature rise at each interface for both out-of-plane and in-plane configurations, the solutions can be obtained with the help of Hankel transformations. These solutions can be found elsewhere [169].

This model neglects heat losses due to convection and radiation since the measurements are typically performed under vacuum conditions and temperature raise above ambient is small (a few degrees or less). Moreover, it also neglects heat losses through the probe.

1.4.2.6.4 Applications and other developments

The technique has been used for measuring thermal diffusivity of alumina templates[168], aligned CNT arrays [170], and bismuth [171] and bismuth telluride nanowire arrays embedded onto alumina templates [172]. The uncertainty of the thermal diffusivity measured by this technique strongly depends on the thickness uncertainty so that it ranges from 10-20 % [169].

Table 1.III summarizes the advantages, disadvantages and uncertainties of each frequency-domain technique as well as the main parameter (thermal conductivity or diffusivity) in the in-plane or out-of-plane direction that is measured.

Table 1.III. Summary of the frequency-domain techniques for measuring the thermal properties of different structures together with the advantages, disadvantages and uncertainties.

Frequency-Domain techniques				
Frequency-Domain Thermoreflectance (FDTR)				
	What measures?	**Advantages**	**Drawbacks**	**Uncertainty**
	Thermal conductivity: a) Out-of-plane b) In-plane	- No contact resistances - Bulk, thin films - Nanometer scale - Easier implementation than TDTR	- Metallization - Smooth surfaces - Hard post-procesing - ρ and Cp needed	~10 %
Photothermal emission method				
	What measures?	**Advantages**	**Drawbacks**	**Uncertainty**
	Thermal diffusivity in the out-of-plane direction	- No contact resistances - Recombination parameters semiconductor calculation - Possible to determine the in-plane thermal diffusivity	- ρ and Cp needed - Mainly bulk materials - Metallization - Precise alignment of the optical elements	~10 %
Photothermal beam deflection ("mirage method")				
	What measures?	**Advantages**	**Drawbacks**	**Uncertainty**
	Thermal diffusivity in the out-of-plane direction	- No contact resistances - Non-invasive - No sample preparation - Bulk and thin films - Simple experimental setup	- ρ and Cp needed - Complex model	~ 10-15 %
Photothermal displacement techniques				
	What measures?	**Advantages**	**Drawbacks**	**Uncertainty**
	Thermal diffusivity in the out-of-plane direction	- No contact resistances - Bulk and thin films - Vertical resolution of approximately 0.1 μm	- High thermal expansion coefficient - Poisson's ratio, surface reflectivity, ρ and Cp needed - Low roughness needed	~ 15 – 20 %
Pyroelectric calorimetry				
	What measures?	**Advantages**	**Drawbacks**	**Uncertainty**
	Thermal diffusivity in the out-of-plane direction	- High signal to noise ratios - Simple setup - Non-invasive	- Mainly bulk materials - Mechanical contact with the detector - ρ and Cp needed	~ 5 – 20 %
Photothermoelectric technique				
	What measures?	**Advantages**	**Drawbacks**	**Uncertainty**
	Thermal diffusivity a) Out-of-plane b) In-plane	- No contact resistances - In-plane and out-of-plane measurement - Simple detection scheme	- Non-conductive and non-absorbing samples must be coated - Properties of these layers are required for theoretical predictions - ρ and Cp needed	~ 10 – 20 %
Photoacoustic technique				
	What measures?	**Advantages**	**Drawbacks**	**Uncertainty**
	- Thermal diffusivity and thermal conductivity - Out-of-plane	- No contact resistances - Non-invasive - All type of materials and structures - Simple detection scheme	- Limited by the frequency range of the microphone. - Metallization - ρ and Cp needed	Depending on the model and the thickness and conductance: ~ 10%

1.5 Photoacoustic technique

1.5.1 Principle of and historical background

The photoacoustic (PA) effect was discovered by Alexander Graham Bell in 1880 with the photophone invention [173]. This effect is based on the production of acoustic waves when an incident modulated radiation impinges on a sample which is placed inside of a closed space. Specifically, an

incident modulated radiation periodically heats the sample and subsequently causes the air in contact with the surface to expand and contract as would do in a thermal piston [44].

Nowadays, the number of publications in the last 30 years has increased considerably, as seen in Figure 1.22, probably due to the improvements in the lasers and detection techniques, as in most research fields. The main fields of photoacoustic applications involve biology and medicine. In biomedicine, Photoacoustic imaging is being used as a hybrid biomedical imaging modality because optical absorption is closely associated with physiological properties. The magnitude of the photoacoustic signal reveals physiologically specific optical absorption contrast. 2D and 3D images of the targeted areas can then be formed [174-176].

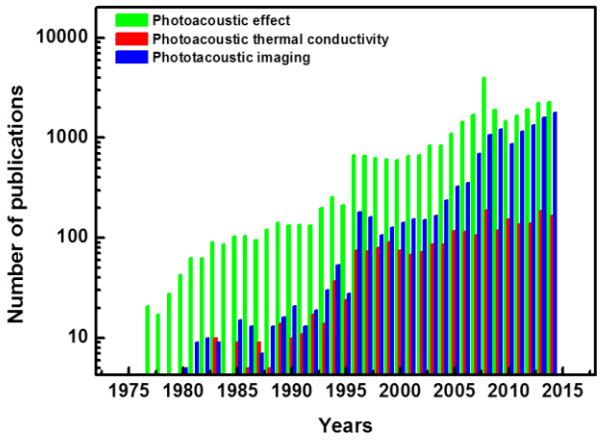

Figure 1.22. Number of publications as a function of the year for three different keywords.

In our case, the main application is in relation with the material characterization, and how the thermal properties of different materials can be studied. In 1976 Rosencwaig and Gersho developed a model with the theory of the photoacoustic effect with solids.[44] As explained above, any light absorbed by solid is converted, in part or in whole, into heat by non-radiative de-excitation processes within the solid. They formulated a one-dimensional model of the heat flow in the cell resulting from the absorbed light energy. They considered a simple cylindrical cell where the sample is mounted, so that its front surface is exposed to the gas (air) within the cell and its back surface is against a poor thermal conductor, backing material.

The photoacoustic signal is obtained from the complex temperature variation calculated from the heat equation for each component and taking into account the boundary conditions between each layer [44].

1.5.2 Experimental setup

The apparatus is schematically illustrated in Figure 1.23. A photoacoustic cell is typically a cylindrical cavity designed so that a 1D heat transfer model can be applied when analyzing the generation of the acoustic signal. This model is applied provided that the thermal diffusion length of the gas is much lower than the cell radius [177]. The photoacoustic cell is closed by a window and the sample. A microphone is used to sense the acoustic waves, which is connected to a lock-in amplifier.

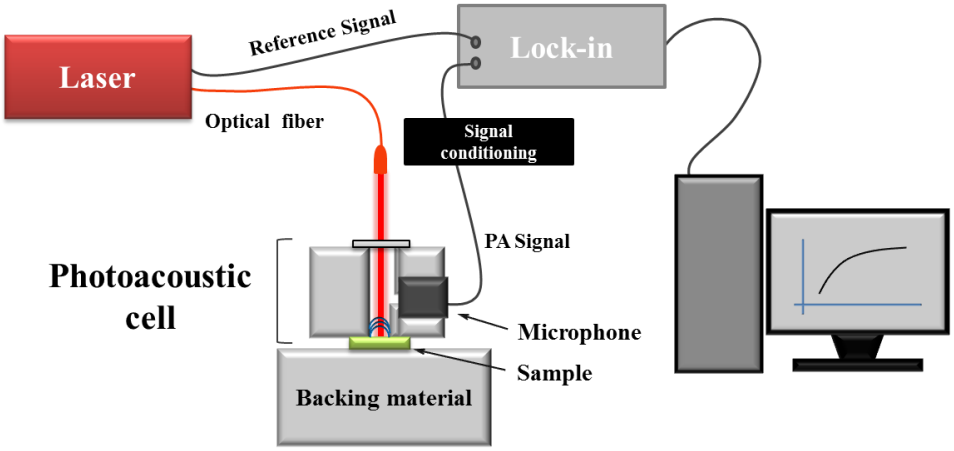

Figure 1.23. Photoacoustic technique setup

1.5.3 Theoretical model and data reduction procedure

The theory of the PA effect in solids was developed by Rosencwaig and Gersho who solved the heat diffusion equation for each layer: backing material, solid sample and the gas layer using the appropriate boundary conditions, and for illumination with a modulated uniform Gaussian beam. The spatially averaged temperature of the gas within this layer given by [44],

$$\overline{\phi(t)} \cong \left(\frac{1}{2\sqrt{2}\pi}\right)\theta exp\left[j\left(\omega t - \frac{1}{4}\pi\right)\right] \tag{1.16}$$

where θ is the complex amplitude of the temperature at the solid gas boundary ($x=0$), ω is the angular frequency and j is the imaginary unit. The gas layer acts as a thermal piston due to the periodic heating whose expansion is given by the ideal gas law,

$$\delta x(t) = 2\pi\mu_g \frac{\overline{\phi(t)}}{T_0} \tag{117}$$

where μ_g is the thermal diffusion length in the gas, and T_0 is the room temperature. The increment of pressure associated with this displacement can be expressed as:

$$\delta P(t) = \frac{\gamma P_0}{l_g}\delta x(t) \tag{1.18}$$

where $P_0$is the ambient pressure, γ is the ratio of the specific heats and l_g is the gas column length.

The full expression of the photoacoustic signal is somewhat difficult to interpret because of the complicated expression of the temperature variation. However, physical insight may be gained by examining special cases where the expression becomes relatively simple. They grouped these cases according to the optical opaqueness of the solids. We can distinguish two groups, optically transparent samples and optically opaque. Moreover, these groups can be divided into thermally thick or thermally thin, so that finally we obtain 6 groups of samples. The PA signal is ultimately governed by the magnitude of the thermal diffusion length (given by Eq. 1.14) of the solid and its dependence on frequency.

The experimental signal is perturbed by the photoacoustic cell contribution as well as some parasitic signal from the electronics so that a normalization procedure must be carried out in order to remove the cell influence. For multilayer samples, the signal is normalized with the help of a reference sample by using a multilayer model developed by Hu *et al.* where the samples are illuminated in the front configuration (see Figure 1.24 (a)) [178]. In the case of bulk samples, the normalization can be carried out by measuring in front (see Figure 1.24 (a)) and rear configurations (See Figure 1.24 (b)) and applying the phase lag method [179, 180].

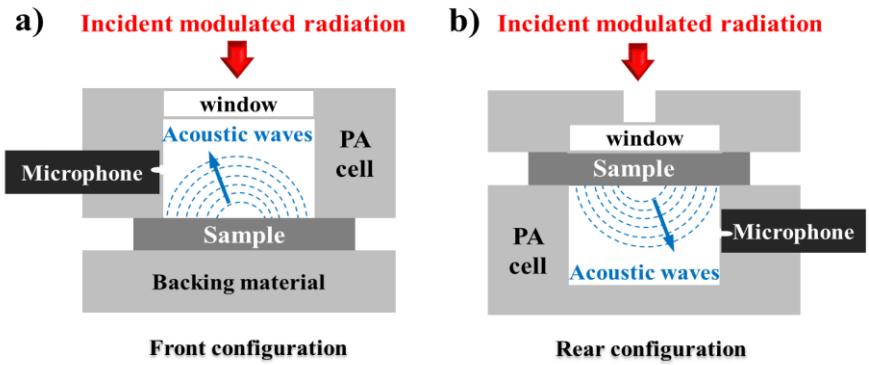

Figure 1.24. Schematic of the two main measurement modes (a) front and (b) rear configuration.

1.5.4 Applications and other developments

A number of modifications and improvements have been reported for this technique. In 1977 Aamodt *et al*[181]. study the dependence of PA spectrometer sensitivity on the physical dimensions of the cell because the amplitudes of the pressure fluctuations in the gas depend on the incident light intensity, thermal properties of both, sample and gas and the details of the thermal diffusion processes responsible for the heat flow. McDonald and Wetsel extended the theory of PA effect to include the contribution of mechanical vibration of the sample, which was described as acoustic coupling between heat diffusion and acoustic waves equations [182]. This effect is important for liquids, which present high thermal expansion coefficient, and for transparent samples, because the acoustic coupling is higher

when the absorption coefficient is reduced. Later, Cesar *et al.* studied the photoacoustic signal of a solid, taking into account the surface thermal resistance of the sample [183]. Then, Quimby *et al.* in 1980 developed a one dimensional theory of the PA effect in solids, which is valid provided that the thermal diffusion length of the gas is much lower than the radius of the sample.[177] This study considerably simplifies the mathematical treatment. In the same year, Fernelius studied the two-layer samples, where each layer had different optical and thermal properties [184]. Poulet studied the quantitative PAS applied to thermally thick samples where the theoretical variations of the modulus and of the phase of the PA signal were compared to the experimental results for a wide range of very or moderately absorbing materials.[185] Three years later, Korpiun and Buchner demonstrated the isochoric character of the PA effect [186]. Rousset *et al.* developed a model which takes into account the thermoelastic bending, which is the thermal expansion along the thickness of the sample due to a thermal gradient induced in that direction [187]. This can occur when measuring solid samples especially in the rear configuration. Other works improved the data reduction and the thermal diffusivity extraction by considering phenomena, thermal diffusion and thermoelastic bending [188, 189].

Many works have been done but in 1999 a generalized theory of photoacoustic effect in multilayer material was developed for Hu *et al.*[178] This work is the one which we are interested in since one of our main objectives is the thermal conductivity measurements of multilayered materials. The PA technique has been used to measure the thermal diffusivity or thermal conductivity in the out-of-plane direction of bulk materials[179, 190-192], thick films [39, 193, 194], thin films[191, 195], porous samples[196-198] or nanowire arrays [199, 200]. This technique is also suitable to measure the thermal resistance between layers [201].

1.6 Objectives

The main objective of this thesis is the implementation of the photoacoustic technique as a tool to determine the thermal properties of any type of structure, from bulk materials towards nanoengineered materials.

The first objective set out is the design and optimization of the experimental setup as well as the optimization of its operations modes. For that purpose, the design of the photoacoustic cell, laser beam characterization and the instrumentation and microphone election have to be carried out. Once the system is optimized, a deep study of the stability and reproducibility as well as the detection limits and uncertainty of the technique will be carried out in order to perform measurements as accurate as possible.

The second objective is related to the actual measurements of the thermal diffusivity of bulk materials. To that aim, both front and rear configuration measurements must be used to normalize the phase shift. The experimental conditions for each type of sample will be studied. The versatility and reliability of this technique will be checked by measuring many different reference samples. Once the system is found to be properly properly, the thermal properties of two types of bulk samples will be studied: a) inorganic samples like zinc oxide (ZnO) doped with nickel oxide (NiO) nanoparticles (with different sizes and NiO concentrations) sintered by Spark Plasma Sintering (SPS), and b) polyaniline (PANI) blended with graphene nanoplatelets (GNPs) in different proportions.

The third objective consists on proving the versatility of the technique to measure films (thin and thick), porous structures like non-filled anodic aluminum oxide (AAO) membranes (with different pore diameters prepared under different conditions) and a novel template developed in our lab, the so called 3D-AAO which has not been measured before. For that a model to understand its thermal conductivity will be developed. Finally, the thermal properties of the filled AAO templates will be investigated. The goal of measuring the filled AAO templates lays on the extraction of the thermal conductivity a single nanowire by using the one dimensional theory.

The fourth objective is to advance in the understanding of how nanostructuration affects the thermal properties of thermoelectric materials.

With all this measurements we will show the possibility of using this technique to measure the thermal conductivity of all type of samples morphology and the limitations of the technique in each case as well as to develop a better understanding of the thermal properties of materials when nanoengineered.

1.7 Organization of the Thesis

This thesis is comprised of six chapters:

Chapter 1 explains the main motivation of this thesis and gives a brief introduction about the thermoelectricity along with the main transport properties required to characterize the efficiency of this type of materials, especially, the thermal conductivity. Afterwards, this chapter also reviews the state of the art of the optical heating techniques for measuring thermal diffusivity and conductivity, finishing with a description of the experimental technique used in this PhD work, the photoacoustic technique.

Chapter 2 is divided in two different parts. Firstly, the fabrication techniques used to prepare the materials studied during this thesis are described. Secondly, the characterization techniques used to study the fabricated materials are also presented.

Chapter 3 contains the photoacoustic technique implementation. It includes a wide explanation about each of the elements of the experimental setup that we have developed during this PhD work: the main instrumentation components and the design and the election of the acoustics and optics elements. Also, this chapter includes a deep study of the signal to noise ratio, stability and reproducibility of the measurement for different materials under diverse experimental conditions. Finally, the detection limits of the technique are also studied.

In Chapter 4, the cross-plane thermal diffusivity of different bulk materials is presented. For that purpose, measurements in front and rear configurations are optimized and a calibration of many different reference samples, which cover a wide range of thermal diffusivity values, are showed. Once the experimental setup was proved to be properly working, different studies were performed. Zinc oxide pellets fabricated by ball milling and spark plasma sintering with different concentration of NiO nanoparticles and different ZnO particle size were studied. Finally, a study of the thermoelectric properties of samples composed of a conductive polymer, polyaniline (PANI), blended with graphene nanoplatelets (GNP) is also shown.

Chapter 5 describes the operation of the photoacoustic experimental setup when measuring films, porous structures and nanowires embedded into porous alumina membranes. Measurements of some reference samples demonstrated that the setup worked properly by comparing the results with those samples measured in other labs and by other techniques. Afterwards, different studies of diverse materials are presented. The thermoelectric properties of electrodeposited tellurium thick films are studied. Moreover, the thermal conductivity of SiGe thin films grown by sputtering are presented. The thermal conductivity of empty anodic aluminum oxide (AAO) membranes with both ordinary

longitudinal pores and with a tridimensional structure is investigated. Finally, the thermal conductivity of Bi_2Te_3 and Sb_2Te_3 nanowires inside the previous AAO templates is also explored.

Finally, Chapter 6 summarizes the main conclusions of this PhD work.

1.8 References

1. Lave, L.; Savitz, M.; Berry, R.; Brown, M.; Cohen, L.; Craford, M.; Decotis, P.; Degraffenreidt, J.; Geller, H.; Goldstein, D., The National Academies Press. In Washington DC, 2009.
2. Fountain, G. H.; Kusnierkiewicz, D. Y.; Hersman, C. B.; Herder, T. S.; Coughlin, T. B.; Gibson, W. C.; Clancy, D. A.; DeBoy, C. C.; Hill, T. A.; Kinnison, J. D.; Mehoke, D. S.; Ottman, G. K.; Rogers, G. D.; Stern, S. A.; Stratton, J. M.; Vernon, S. R.; Williams, S. P., The New Horizons spacecraft. *Space Science Reviews* **2008,** *140*, 23-47.
3. Rowe, D. M., CRC Thermoelectrics Handbook: Macro to Nano. In *CRC Press*, Rowe, D. M., Ed. 2005.
4. Wood, C., Materials for thermoelectric energy conversion. *Reports on Progress in Physics* **1988,** *51*, 459-539.
5. Lide, D. R., CRC Handbook of Chemistry and Physics. In Press, C., Ed. Boca Raton, 2005.
6. Snyder, G. J.; Toberer, E. S., Complex thermoelectric materials. *Nat Mater* **2008,** *7*, 105-114.
7. Dughaish, Z., Lead telluride as a thermoelectric material for thermoelectric power generation. *Physica B: Condensed Matter* **2002,** *322*, 205-223.
8. Tang, S.; Dresselhaus, M. S., Electronic properties of nano-structured bismuth-antimony materials. *Journal of Materials Chemistry C* **2014,** *2*, 4710-4726.
9. Maiz, J.; Muñoz Rojo, M.; Abad, B.; Wilson, A. A.; Nogales, A.; Borca-Tasciuc, D. A.; Borca-Tasciuc, T.; Martín-González, M., Enhancement of thermoelectric efficiency of doped PCDTBT polymer films. *RSC Advances* **2015,** *5*, 66687-66694.
10. Abad, B.; Alda, I.; Diaz-Chao, P.; Kawakami, H.; Almarza, A.; Amantia, D.; Gutierrez, D.; Aubouy, L.; Martin-Gonzalez, M., Improved power factor of polyaniline nanocomposites with exfoliated graphene nanoplatelets (GNPs). *Journal of Materials Chemistry A* **2013,** *1*, 10450-10457.
11. Martín-González, M.; Caballero-Calero, O.; Díaz-Chao, P., Nanoengineering thermoelectrics for 21st century: Energy harvesting and other trends in the field. *Renewable and Sustainable Energy Reviews* **2013,** *24*, 288-305.
12. Sales, B. C.; Mandrus, D.; Chakoumakos, B. C.; Keppens, V.; Thompson, J. R., Filled skutterudite antimonides: Electron crystals and phonon glasses. *Physical Review B* **1997,** *56*, 15081-15089.
13. Hopkins, P. E.; Reinke, C. M.; Su, M. F.; Olsson, R. H.; Shaner, E. A.; Leseman, Z. C.; Serrano, J. R.; Phinney, L. M.; El-Kady, I., Reduction in the Thermal Conductivity of Single Crystalline Silicon by Phononic Crystal Patterning. *Nano Letters* **2011,** *11*, 107-112.
14. Tritt, T. M., Thermal Conductivity: Theory, properties and applications. In Tritt, T. M., Ed. 233 Spring Street, New York, New York 10013, 2004.
15. http://www.akts.com/time-to-maximum-rate-adiabatic/runaway-reactions-akts-thermal-safety-software.html.
16. Beck, A., A steady state method for the rapid measurement of the thermal conductivity of rocks. *Journal of Scientific Instruments* **1957,** *34*, 186.
17. Dettmer, E. S.; Romenesko, B. M.; Charles, H. K., Jr.; Carkhuff, B. G.; Merrill, D. J., Steady-state thermal conductivity measurements of AlN and SiC substrate materials. *Components, Hybrids, and Manufacturing Technology, IEEE Transactions on* **1989,** *12*, 543-547.
18. Sass, J. H.; Stone, C.; Munroe, R. J., Thermal conductivity determinations on solid rock — a comparison between a steady-state divided-bar apparatus and a commercial transient line-source device. *Journal of Volcanology and Geothermal Research* **1984,** *20*, 145-153.
19. Khorunzhii, I.; Gabor, H.; Job, R.; Fahrner, W. R.; Denisenko, A.; Brunner, D.; Peschek, U., Steady-state thermal conductivity measurements of super-hard materials. *Measurement* **2002,** *32*, 163-172.
20. Moon, J.; Weaver, K.; Feng, B.; Gi Chae, H.; Kumar, S.; Baek, J.-B.; Peterson, G. P., Note: Thermal conductivity measurement of individual poly(ether ketone)/carbon nanotube fibers using a steady-state dc thermal bridge method. *Review of Scientific Instruments* **2012,** *83*, 016103.
21. Stoib, B.; Filser, S.; Stötzel, J.; Greppmair, A.; Petermann, N.; Wiggers, H.; Schierning, G.; Stutzmann, M.; Brandt, M. S., Spatially resolved determination of thermal conductivity by Raman spectroscopy. *Semiconductor Science and Technology* **2014,** *29*, 124005.

22. Gustafsson, S. E., Transient plane source techniques for thermal conductivity and thermal diffusivity measurements of solid materials. *Review of Scientific Instruments* **1991,** *62*, 797-804.
23. Healy, J. J.; de Groot, J. J.; Kestin, J., The theory of the transient hot-wire method for measuring thermal conductivity. *Physica B+C* **1976,** *82*, 392-408.
24. Gomès, S.; Assy, A.; Chapuis, P. O., Scanning thermal microscopy: A review. *physica status solidi (a)* **2015,** *212*, 477-494.
25. Cahill, D. G.; Goodson, K.; Majumdar, A., Thermometry and Thermal Transport in Micro/Nanoscale Solid-State Devices and Structures. *Journal of Heat Transfer* **2001,** *124*, 223-241.
26. Borca-Tasciuc, T., Scanning probe methods for thermal and thermoelectric property measurements. *Annual Review of Heat Transfer* **2013,** *16*.
27. Wilson, A. A.; Rojo, M. M.; Abad, B.; Perez, J. A.; Maiz, J.; Schomacker, J.; Martin-Gonzalez, M. S.; Borca-Tasciuc, D.-A.; Borca-Tasciuc, T., Thermal Conductivity Measurements of High and Low Thermal Conductivity Films Using a Scanning Hot Probe Method in the 3[small omega] Mode and Novel Calibration Strategies. *Nanoscale* **2015**.
28. Cahill, D. G., Thermal conductivity measurement from 30 to 750 K: the 3ω method. *Review of Scientific Instruments* **1990,** *61*, 802-808.
29. Lu, L.; Yi, W.; Zhang, D. L., <equation>3ω</equation> method for specific heat and thermal conductivity measurements. *Review of Scientific Instruments* **2001,** *72*, 2996-3003.
30. Völklein, F., Thermal conductivity and diffusivity of a thin film SiO2 Si3N4 sandwich system. *Thin Solid Films* **1990,** *188*, 27-33.
31. Okuda, M.; Ohkubo, S., A novel method for measuring the thermal conductivity of submicrometre thick dielectric films. *Thin Solid Films* **1992,** *213*, 176-181.
32. Davami, K.; Weathers, A.; Kheirabi, N.; Mortazavi, B.; Pettes, M. T.; Shi, L.; Lee, J.-S.; Meyyappan, M., Thermal conductivity of ZnTe nanowires. *Journal of Applied Physics* **2013,** *114*, 134314.
33. Gustavsson, M.; Karawacki, E.; Gustafsson, S. E., Thermal conductivity, thermal diffusivity, and specific heat of thin samples from transient measurements with hot disk sensors. *Review of Scientific Instruments* **1994,** *65*, 3856-3859.
34. Völklein, F.; Reith, H.; Schmitt, M. C.; Huth, M.; Rauber, M.; Neumann, R., Microchips for the Investigation of Thermal and Electrical Properties of Individual Nanowires. *Journal of Elec Materi* **2010,** *39*, 1950-1956.
35. Hochbaum, A. I.; Chen, R.; Delgado, R. D.; Liang, W.; Garnett, E. C.; Najarian, M.; Majumdar, A.; Yang, P., Enhanced thermoelectric performance of rough silicon nanowires. *Nature* **2008,** *451*, 163-167.
36. Lee, E. K.; Yin, L.; Lee, Y.; Lee, J. W.; Lee, S. J.; Lee, J.; Cha, S. N.; Whang, D.; Hwang, G. S.; Hippalgaonkar, K.; Majumdar, A.; Yu, C.; Choi, B. L.; Kim, J. M.; Kim, K., Large thermoelectric figure-of-merits from SiGe nanowires by simultaneously measuring electrical and thermal transport properties. *Nano Letters* **2012,** *12*, 2918-2923.
37. Roh, J. W.; Jang, S. Y.; Kang, J.; Lee, S.; Noh, J. S.; Kim, W.; Park, J.; Lee, W., Size-dependent thermal conductivity of individual single-crystalline PbTe nanowires. *Applied Physics Letters* **2010,** *96*.
38. Zhou, F.; Szczech, J.; Pettes, M. T.; Moore, A. L.; Jin, S.; Shi, L., Determination of transport properties in chromium disilicide nanowires via combined thermoelectric and structural characterizations. *Nano Letters* **2007,** *7*, 1649-1654.
39. Manzano, C. V.; Abad, B.; Muñoz-Rojo, M.; Koh, Y. R.; Hodson, S. L.; Martinez, A. M. L.; Xu, X.; Shakouri, A.; Sands, T. D.; Borca-Tasciuc, T.; Martín-González, M., Anisotropy effect on the thermoelectric properties of highly oriented electrodeposited Bi2Te3 films. *Scientific Reports* **2015,** *accepted*.
40. Chen, G., Phonon heat conduction in nanostructures1. *International Journal of Thermal Sciences* **2000,** *39*, 471-480.
41. Garcia, J.; Mandelis, A.; Farahbakhsh, B.; Lebowitz, C.; Harris, I., Thermophysical properties of thermal sprayed coatings on carbon steel substrates by photothermal radiometry. *Int J Thermophys* **1999,** *20*, 1587-1602.

42. Ogawa, E. T.; Hu, C.; Ho, P. S., Thermal diffusivity measurement of polymeric thin films using the photothermal displacement technique. I. Free-standing film case. *Journal of Applied Physics* **1999,** *86*, 6018-6027.
43. Paddock, C. A.; Eesley, G. L., Transient thermoreflectance from thin metal films. *Journal of Applied Physics* **1986,** *60*, 285-290.
44. Rosencwaig, A.; Gersho, A., Theory of the photoacoustic effect with solids. *Journal of Applied Physics* **1976,** *47*, 64-69.
45. Liu, X.; Wang, R.; Jiang, Y.; Zhang, Q.; Shan, X.; Qiu, X., Thermal conductivity measurement of individual CdS nanowires using microphotoluminescence spectroscopy. *Journal of Applied Physics* **2010,** *108*, 054310.
46. Zhang, Y.; Castillo, E. E.; Mehta, R. J.; Ramanath, G.; Borca-Tasciuc, T., A noncontact thermal microprobe for local thermal conductivity measurement. *Review of Scientific Instruments* **2011,** *82*, 024902.
47. Eesley, G. L., Generation of nonequilibrium electron and lattice temperatures in copper by picosecond laser pulses. *Physical Review B* **1986,** *33*, 2144-2151.
48. Eesley, G. L., Observation of Nonequilibrium Electron Heating in Copper. *Physical Review Letters* **1983,** *51*, 2140-2143.
49. Favaloro, T.; Bahk, J.-H.; Shakouri, A., Characterization of the temperature dependence of the thermoreflectance coefficient for conductive thin films. *Review of Scientific Instruments* **2015,** *86*, 024903.
50. Pernot, G.; Michel, H.; Vermeersch, B.; Burke, P.; Lu, H.; Rampnoux, J.-M.; Dilhaire, S.; Ezzahri, Y.; Gossard, A.; Shakouri, A. In *Frequency-Dependent Thermal Conductivity in Time Domain Thermoreflectance Analysis of Thin Films*, MRS Proceedings, 2011; Cambridge Univ Press: 2011; pp mrss11-1347-bb07-07.
51. Baba, T., Analysis of One-dimensional Heat Diffusion after Light Pulse Heating by the Response Function Method. *Japanese Journal of Applied Physics* **2009,** *48*, 05EB04.
52. Norris, P. M.; Caffrey, A. P.; Stevens, R. J.; Klopf, J. M.; McLeskey Jr, J. T.; Smith, A. N., Femtosecond pump–probe nondestructive examination of materials. *Review of Scientific Instruments* **2003,** *74*, 400-406.
53. Capinski, W. S.; Maris, H. J.; Ruf, T.; Cardona, M.; Ploog, K.; Katzer, D. S., Thermal-conductivity measurements of GaAs/AlAs superlattices using a picosecond optical pump-and-probe technique. *Physical Review B* **1999,** *59*, 8105-8113.
54. Schmidt, A. J.; Chen, X.; Chen, G., Pulse accumulation, radial heat conduction, and anisotropic thermal conductivity in pump-probe transient thermoreflectance. *Review of Scientific Instruments* **2008,** *79*, 114902.
55. Cahill, D. G., Analysis of heat flow in layered structures for time-domain thermoreflectance. *Review of Scientific Instruments* **2004,** *75*, 5119-5122.
56. Chiritescu, C.; Mortensen, C.; Cahill, D. G.; Johnson, D.; Zschack, P., Lower limit to the lattice thermal conductivity of nanostructured Bi2Te3-based materials. *Journal of Applied Physics* **2009,** *106*, 073503.
57. Chiritescu, C.; Cahill, D. G.; Nguyen, N.; Johnson, D.; Bodapati, A.; Keblinski, P.; Zschack, P., Ultralow Thermal Conductivity in Disordered, Layered WSe2 Crystals. *Science* **2007,** *315*, 351-353.
58. Luckyanova, M. N.; Garg, J.; Esfarjani, K.; Jandl, A.; Bulsara, M. T.; Schmidt, A. J.; Minnich, A. J.; Chen, S.; Dresselhaus, M. S.; Ren, Z.; Fitzgerald, E. A.; Chen, G., Coherent Phonon Heat Conduction in Superlattices. *Science* **2012,** *338*, 936-939.
59. Persson, A. I.; Koh, Y. K.; Cahill, D. G.; Samuelson, L.; Linke, H., Thermal Conductance of InAs Nanowire Composites. *Nano Letters* **2009,** *9*, 4484-4488.
60. Costescu, R. M.; Wall, M. A.; Cahill, D. G., Thermal conductance of epitaxial interfaces. *Physical Review B* **2003,** *67*, 054302.
61. Monachon, C.; Weber, L., Influence of a nanometric Al2O3 interlayer on the thermal conductance of an Al/(Si, Diamond) interface. *Advanced Engineering Materials* **2015,** *17*, 68-75.
62. Cheaito, R.; Gaskins, J. T.; Caplan, M. E.; Donovan, B. F.; Foley, B. M.; Giri, A.; Duda, J. C.; Szwejkowski, C. J.; Constantin, C.; Brown-Shaklee, H. J.; Ihlefeld, J. F.; Hopkins, P. E., Thermal

boundary conductance accumulation and interfacial phonon transmission: Measurements and theory. *Physical Review B* **2015,** *91*, 035432.
63. Koh, Y. K.; Bae, M.-H.; Cahill, D. G.; Pop, E., Heat Conduction across Monolayer and Few-Layer Graphenes. *Nano Letters* **2010,** *10*, 4363-4368.
64. Feser, J. P.; Liu, J.; Cahill, D. G., Pump-probe measurements of the thermal conductivity tensor for materials lacking in-plane symmetry. *Review of Scientific Instruments* **2014,** *85*, 104903.
65. Zheng, X.; Cahill, D. G.; Zhao, J. C., Thermal Conductivity Imaging of Thermal Barrier Coatings. *Advanced Engineering Materials* **2005,** *7*, 622-626.
66. Oyake, T.; Sakata, M.; Shiomi, J., Nanoscale thermal conductivity spectroscopy by using gold nano-islands heat absorbers. *Applied Physics Letters* **2015,** *106*, 073102.
67. Thomsen, C.; Strait, J.; Vardeny, Z.; Maris, H. J.; Tauc, J.; Hauser, J. J., Coherent Phonon Generation and Detection by Picosecond Light Pulses. *Physical Review Letters* **1984,** *53*, 989-992.
68. Grahn, H. T.; Young, D. A.; Maris, H. J.; Tauc, J.; Hong, J. M.; Smith, T. P., Sound velocity and index of refraction of AlAs measured by picosecond ultrasonics. *Applied Physics Letters* **1988,** *53*, 2023-2024.
69. Parker, W. J.; Jenkins, R. J.; Butler, C. P.; Abbott, G. L., Flash Method of Determining Thermal Diffusivity, Heat Capacity, and Thermal Conductivity. *Journal of Applied Physics* **1961,** *32*, 1679-1684.
70. Han, L.; Van Nong, N.; Zhang, W.; Hung, L. T.; Holgate, T.; Tashiro, K.; Ohtaki, M.; Pryds, N.; Linderoth, S., Effects of morphology on the thermoelectric properties of Al-doped ZnO. *RSC Advances* **2014,** *4*, 12353-12361.
71. Ohta, H.; Shibata, H.; Kasamoto, T., Estimation of heat transfer of a front-heating front-detection laser flash method measuring thermal conductivity for silicate melts at high temperatures. *ISIJ International* **2006,** *46*, 434-440.
72. Akoshima, M.; Baba, T., Study on a Thermal-diffusivity Standard for Laser Flash Method Measurements. *Int J Thermophys* **2006,** *27*, 1189-1203.
73. Cai, A.; Yang, L.-p.; Chen, J.-p.; Xi, T.-g.; Xin, S.-g.; Wu, W., Thermal Conductivity of Anodic Alumina Film at (220 to 480) K by Laser Flash Technique. *Journal of Chemical & Engineering Data* **2010,** *55*, 4840-4843.
74. Ruoho, M.; Valset, K.; Finstad, T.; Tittonen, I., Measurement of thin film thermal conductivity using the laser flash method. *Nanotechnology* **2015,** *26*.
75. Cowan, R. D., Pulse method of measuring thermal diffusivity at high temperatures. *Journal of Applied Physics* **1963,** *34*, 926-927.
76. Clark III, L.; Taylor, R., Radiation loss in the flash method for thermal diffusivity. *Journal of Applied Physics* **1975,** *46*, 714-719.
77. Baba, T.; Ono, A., Improvement of the laser flash method to reduce uncertainty in thermal diffusivity measurements. *Measurement Science and Technology* **2001,** *12*, 2046.
78. Vozár, L.; Hohenauer, W., Uncertainty of Thermal Diffusivity Measurements Using the Laser Flash Method. *Int J Thermophys* **2005,** *26*, 1899-1915.
79. Lindemann, A.; Blumm, J.; Brunner, M., Current limitations of commercial laser flash techniques for highly conducting materials and thin films. *High Temperatures - High Pressures* **2014,** *43*, 243-252.
80. Larson, K. B.; Koyama, K., Correction for Finite-Pulse-Time Effects in Very Thin Samples using the Flash Method of Measuring Thermal Diffusivity. *Journal of Applied Physics* **1967,** *38*, 465-474.
81. Leung, W. P.; Tam, A. C., Thermal diffusivity in thin films measured by noncontact single-ended pulsed-laser-induced thermal radiometry. *Opt. Lett.* **1984,** *9*, 93-95.
82. Tiwari, A.; Boussois, K.; Nait-Ali, B.; Smith, D. S.; Blanchart, P., Anisotropic thermal conductivity of thin polycrystalline oxide samples. *AIP Advances* **2013,** *3*.
83. Kulkarni, A.; Gutleber, J.; Sampath, S.; Goland, A.; Lindquist, W. B.; Herman, H.; Allen, A. J.; Dowd, B., Studies of the microstructure and properties of dense ceramic coatings produced by high-velocity oxygen-fuel combustion spraying. *Materials Science and Engineering A* **2004,** *369*, 124-137.
84. Goli, P.; Ning, H.; Li, X.; Lu, C. Y.; Novoselov, K. S.; Balandin, A. A., Thermal properties of graphene-copper-graphene heterogeneous films. *Nano Letters* **2014,** *14*, 1497-1503.

85. Zajas, J.; Heiselberg, P., Determination of the local thermal conductivity of functionally graded materials by a laser flash method. *International Journal of Heat and Mass Transfer* **2013,** *60*, 542-548.
86. Lin, W.; Shang, J.; Gu, W.; Wong, C., Parametric study of intrinsic thermal transport in vertically aligned multi-walled carbon nanotubes using a laser flash technique. *Carbon* **2012,** *50*, 1591-1603.
87. Eichler, H.; Salje, G.; Stahl, H., Thermal diffusion measurements using spatially periodic temperature distributions induced by laser light. *Journal of Applied Physics* **1973,** *44*, 5383-5388.
88. Harata, A.; Nishimura, H.; Sawada, T., Laser-induced surface acoustic waves and photothermal surface gratings generated by crossing two pulsed laser beams. *Applied Physics Letters* **1990,** *57*, 132-134.
89. Luckyanova, M. N.; Johnson, J. A.; Maznev, A. A.; Garg, J.; Jandl, A.; Bulsara, M. T.; Fitzgerald, E. A.; Nelson, K. A.; Chen, G., Anisotropy of the Thermal Conductivity in GaAs/AlAs Superlattices. *Nano Letters* **2013,** *13*, 3973-3977.
90. Maznev, A. A., Optical heterodyne detection of laser-induced gratings. *Opt. Lett.* **1998,** *23*, 1319-1321.
91. Käding, O. W.; Skurk, H.; Maznev, A. A.; Matthias, E., Transient thermal gratings at surfaces for thermal characterization of bulk materials and thin films. *Applied Physics A Materials Science & Processing* **1995,** *61*, 253-261.
92. Johnson, J. A.; Maznev, A. A.; Bulsara, M. T.; Fitzgerald, E. A.; Harman, T. C.; Calawa, S.; Vineis, C. J.; Turner, G.; Nelson, K. A., Phase-controlled, heterodyne laser-induced transient grating measurements of thermal transport properties in opaque material. *Journal of Applied Physics* **2012,** *111*, 023503.
93. Rogers, J. A.; Yang, Y.; Nelson, K. A., Elastic modulus and in-plane thermal diffusivity measurements in thin polyimide films using symmetry-selective real-time impulsive stimulated thermal scattering. *Appl Phys A* **1994,** *58*, 523-534.
94. Tokmakoff, A.; Banholzer, W. F.; Fayer, M. D., Thermal diffusivity measurements of natural and isotopically enriched diamond by picosecond infrared transient grating experiments. *Appl Phys A* **1993,** *56*, 87-90.
95. Johnson, J. A.; Maznev, A. A.; Cuffe, J.; Eliason, J. K.; Minnich, A. J.; Kehoe, T.; Torres, C. M. S.; Chen, G.; Nelson, K. A., Direct Measurement of Room-Temperature Nondiffusive Thermal Transport Over Micron Distances in a Silicon Membrane. *Physical Review Letters* **2013,** *110*, 025901.
96. Collins, K. C.; Maznev, A. A.; Tian, Z.; Esfarjani, K.; Nelson, K. A.; Chen, G., Non-diffusive relaxation of a transient thermal grating analyzed with the Boltzmann transport equation. *Journal of Applied Physics* **2013,** *114*, 104302.
97. Marshall, C. D.; Fishman, I. M.; Fayer, M. D., Ultrasonic wave propagation and barrier-limited heat flow in thin films of YBa2Cu3O7-x. *Physical Review B* **1991,** *43*, 2696-2699.
98. Marshall, C.; Fishman, I.; Dorfman, R.; Eom, C.; Fayer, M., Thermal diffusion, interfacial thermal barrier, and ultrasonic propagation in YBa 2 Cu 3 O 7-x thin films: Surface-selective transient-grating experiments. *Physical Review B* **1992,** *45*, 10009.
99. Ju, H.-y.; Kuo, P.-k.; Zhang, S.-y., Transient thermal grating analyses of film/substrate structures by eigenfunction expansion method. *The European Physical Journal Special Topics* **2008,** *153*, 191-194.
100. Johnson, J. A.; Maznev, A. A.; Bulsara, M. T.; Fitzgerald, E. A.; Harman, T. C.; Calawa, S.; Vinels, C. J.; Turner, G.; Nelson, K. A., Phase-controlled, heterodyne laser-induced transient grating measurements of thermal transport properties in opaque material. *Journal of Applied Physics* **2012,** *111*.
101. Astrath, N. G. C.; Malacarne, L. C.; Pedreira, P. R. B.; Bento, A. C.; Baesso, M. L.; Shen, J., Time-resolved thermal mirror for nanoscale surface displacement detection in low absorbing solids. *Applied Physics Letters* **2007,** *91*.
102. Capeloto, O. A.; Lukasievicz, G. V. B.; Zanuto, V. S.; Herculano, L. S.; Souza Filho, N. E.; Novatski, A.; Malacarne, L. C.; Bialkowski, S. E.; Baesso, M. L.; Astrath, N. G. C., Pulsed photothermal mirror technique: Characterization of opaque materials. *Applied Optics* **2014,** *53*, 7985-7991.
103. Carslaw, H.; Jaeger, J., Heat in solids. In Clarendon Press, Oxford: 1959.

104. Zanuto, V. S.; Herculano, L. S.; Baesso, M. L.; Lukasievicz, G. V. B.; Jacinto, C.; Malacarne, L. C.; Astrath, N. G. C., Thermal mirror spectrometry: An experimental investigation of optical glasses. *Optical Materials* **2013,** *35*, 1129-1133.
105. Rebay, M.; Arfaoui, A.; Mebarki, G.; Ben Maad, R.; Padet, J., Improvement of the pulsed photothermal technique for the measurement of the convective heat transfer coefficient. *J. Therm. Sci.* **2010,** *19*, 357-363.
106. Karner, C.; Mandel, A.; Träger, F., Pulsed laser photothermal displacement spectroscopy for surface studies. *Applied Physics A Solids and Surfaces* **1985,** *38*, 19-21.
107. Li, B. C., Three-dimensional theory of pulsed photothermal deformation. *Journal of Applied Physics* **1990,** *68*, 482-487.
108. Bennis, G. L.; Vyas, R.; Gupta, R.; Ang, S.; Brown, W. D., Thermal diffusivity measurement of solid materials by the pulsed photothermal displacement technique. *Journal of Applied Physics* **1998,** *84*, 3602-3610.
109. Soltanolkotabi, M.; Bennis, G.; Gupta, R., Temperature dependence of the thermal diffusivity of GaAs in the 100–305 K range measured by the pulsed photothermal displacement technique. *Journal of Applied Physics* **1999,** *85*, 794-798.
110. Cheng, J. C.; Zhang, S. Y., Theoretical studies of pulsed photothermal phenomena in semiconductors. *Journal of Applied Physics* **1993,** *74*, 5718-5725.
111. Xu, X.; Zhang, S.; Kuo, P., Application of an optical birefringence interferometer to photothermal detection for characterizing thermal diffusivities. *Review of Scientific Instruments* **2003,** *74*, 639-641.
112. Schmidt, A. J.; Cheaito, R.; Chiesa, M., A frequency-domain thermoreflectance method for the characterization of thermal properties. *Review of Scientific Instruments* **2009,** *80*, 094901.
113. Zhu, J.; Tang, D.; Wang, W.; Liu, J.; Holub, K. W.; Yang, R., Ultrafast thermoreflectance techniques for measuring thermal conductivity and interface thermal conductance of thin films. *Journal of Applied Physics* **2010,** *108*.
114. Regner, K. T.; Sellan, D. P.; Su, Z.; Amon, C. H.; McGaughey, A. J. H.; Malen, J. A., Broadband phonon mean free path contributions to thermal conductivity measured using frequency domain thermoreflectance. *Nat Commun* **2013,** *4*, 1640.
115. Liu, J.; Zhu, J.; Tian, M.; Gu, X.; Schmidt, A.; Yang, R., Simultaneous measurement of thermal conductivity and heat capacity of bulk and thin film materials using frequency-dependent transient thermoreflectance method. *Review of Scientific Instruments* **2013,** *84*, 034902.
116. Malen, J. A.; Baheti, K.; Tong, T.; Zhao, Y.; Hudgings, J. A.; Majumdar, A., Optical Measurement of Thermal Conductivity Using Fiber Aligned Frequency Domain Thermoreflectance. *Journal of Heat Transfer* **2011,** *133*, 081601-081601.
117. Zhu, J.; Tang, D.; Wang, W.; Liu, J.; Yang, R. In *Frequency-domain thermoreflectance technique for measuring thermal conductivity and interface thermal conductance of thin films*, 2010 14th International Heat Transfer Conference, IHTC 14, 2010; 2010; pp 371-379.
118. Majumdar, S.; Sierra-Suarez, J. A.; Schiffres, S. N.; Ong, W.-L.; Higgs, C. F.; McGaughey, A. J. H.; Malen, J. A., Vibrational Mismatch of Metal Leads Controls Thermal Conductance of Self-Assembled Monolayer Junctions. *Nano Letters* **2015,** *15*, 2985-2991.
119. Regner, K. T.; Majumdar, S.; Malen, J. A., Instrumentation of broadband frequency domain thermoreflectance for measuring thermal conductivity accumulation functions. *Review of Scientific Instruments* **2013,** *84*.
120. Ramu, A. T.; Bowers, J. E., A compact heat transfer model based on an enhanced Fourier law for analysis of frequency-domain thermoreflectance experiments. *Applied Physics Letters* **2015,** *106*, 263102.
121. Collins, K. C.; Maznev, A. A.; Cuffe, J.; Nelson, K. A.; Chen, G., Examining thermal transport through a frequency-domain representation of time-domain thermoreflectance data. *Review of Scientific Instruments* **2014,** *85*, 124903.
122. Yang, J.; Maragliano, C.; Schmidt, A. J., Thermal property microscopy with frequency domain thermoreflectance. *Review of Scientific Instruments* **2013,** *84*, 104904.
123. Otto Kanstad, S.; Nordal, P.-E., Photoacoustic and photothermal spectroscopy — novel tools for the analysis of particulate matter. *Powder Technology* **1979,** *22*, 133-137.

124. Huxtable, S.; Cahill, D. G.; Fauconnier, V.; White, J. O.; Zhao, J. C., Thermal conductivity imaging at micrometre-scale resolution for combinatorial studies of materials. *Nature Materials* **2004,** *3*, 298-301.
125. Dilhaire, S.; Pernot, G.; Calbris, G.; Rampnoux, J. M.; Grauby, S., Heterodyne picosecond thermoreflectance applied to nanoscale thermal metrology. *Journal of Applied Physics* **2011,** *110*, 114314.
126. Hostetler, J. L.; Smith, A. N.; Norris, P. M., Thin-film thermal conductivity and thickness measurements using picosecond ultrasonics. *Microscale Thermophysical Engineering* **1997,** *1*, 237-244.
127. Wang, X.; Zhong, Z.; Xu, J., Noncontact thermal characterization of multiwall carbon nanotubes. *Journal of Applied Physics* **2005,** *97*, 064302.
128. Boué, C.; Holé, S., Infrared thermography protocol for simple measurements of thermal diffusivity and conductivity. *Infrared Physics & Technology* **2012,** *55*, 376-379.
129. Giri, L. I.; Tuli, S.; Sharma, M.; Bugnon, P.; Berger, H.; Magrez, A., Thermal diffusivity measurements of templated nanocomposite using infrared thermography. *Materials Letters* **2014,** *115*, 106-108.
130. Chen, X.; He, Y.; Zhao, Y.; Wang, X., Thermophysical properties of hydrogenated vanadium-doped magnesium porous nanostructures. *Nanotechnology* **2010,** *21*, 055707.
131. Wang, T.; Wang, X.; Zhang, Y.; Liu, L.; Xu, L.; Liu, Y.; Zhang, L.; Luo, Z.; Cen, K., Effect of zirconium (IV) propoxide concentration on the thermophysical properties of hybrid organic-inorganic films. *Journal of Applied Physics* **2008,** *104*, 013528.
132. Rémy, B.; Degiovanni, A.; Maillet, D., Measurement of the In-plane Thermal Diffusivity of Materials by Infrared Thermography. *Int J Thermophys* **2005,** *26*, 493-505.
133. Wolf, A.; Pohl, P.; Brendel, R., Thermophysical analysis of thin films by lock-in thermography. *Journal of Applied Physics* **2004,** *96*, 6306-6312.
134. Salazar, A.; Fuente, R.; Apinaniz, E.; Mendioroz, A.; Celorrio, R., Simultaneous measurement of thermal diffusivity and optical absorption coefficient using photothermal radiometry. II Multilayered solids. *Journal of Applied Physics* **2011,** *110*, 033516.
135. Fuente, R.; Apinaniz, E.; Mendioroz, A.; Salazar, A., Simultaneous measurement of thermal diffusivity and optical absorption coefficient using photothermal radiometry. I. Homogeneous solids. *Journal of Applied Physics* **2011,** *110*, 033515.
136. Pawlak, M.; Maliński, M., Simultaneous measurement of thermal diffusivity and effective infrared absorption coefficient in IR semitransparent and semiconducting n-CdMgSe crystals using photothermal radiometry. *Thermochimica Acta* **2015,** *599*, 23-26.
137. Mandelis, A.; Othonos, A.; Christofides, C.; Boussey-Said, J., Non-contacting measurements of photocarrier lifetimes in bulk-and polycrystalline thin-film Si photoconductive devices by photothermal radiometry. *Journal of Applied Physics* **1996,** *80*, 5332-5341.
138. Mendioroz, A.; Fuente-Dacal, R.; Apiñaniz, E.; Salazar, A., Thermal diffusivity measurements of thin plates and filaments using lock-in thermography. *Review of Scientific Instruments* **2009,** *80*, 074904.
139. Boccara, A. C.; Fournier, D.; Badoz, J., Thermo-optical spectroscopy: Detection by the "mirage effect". *Applied Physics Letters* **1980,** *36*, 130-132.
140. Mandelis, A., Absolute optical absorption coefficient measurements using transverse photothermal deflection spectroscopy. *Journal of Applied Physics* **1983,** *54*, 3404-3409.
141. Vargas, H.; Miranda, L. C. M., Photoacoustic and related photothermal techniques. *Physics Reports* **1988,** *161*, 43-101.
142. Salazar, A.; Sánchez-Lavega, A.; Fernández, J., Theory of thermal diffusivity determination by the ‘‘mirage’’ technique in solids. *Journal of Applied Physics* **1989,** *65*, 4150-4156.
143. Salazar, A.; Sánchez-Lavega, A.; Fernández, J., Thermal diffusivity measurements in solids by the "mirage" technique: Experimental results. *Journal of Applied Physics* **1991,** *69*, 1216-1223.
144. Bertolotti, M.; Li Voti, R.; Liakhou, G.; Sibilia, C., On the photodeflection method applied to low thermal diffusivity measurements. *Review of Scientific Instruments* **1993,** *64*, 1576-1583.
145. Liu, X. J.; Huang, Q. J.; Zhang, S. Y.; Luo, A. H.; Zhao, C. X., Thermal diffusivity of double perovskite Sr2MMoO6 (M = Fe, Mn and Co) and La doping effects studied by mirage effect. *Journal of Physics and Chemistry of Solids* **2004,** *65*, 1247-1251.

146. Ghrib, T.; Yacoubi, N.; Saadallah, F., Simultaneous determination of thermal conductivity and diffusivity of solid samples using the "Mirage effect" method. *Sensors and Actuators, A: Physical* **2007,** *135*, 346-354.
147. Roger, J. P.; Lepoutre, F.; Fournier, D.; Boccara, A. C., Thermal diffusivity measurement of micron-thick semiconductor films by mirage detection. *Thin Solid Films* **1987,** *155*, 165-174.
148. Gonzalez, E. J.; Bonevich, J. E.; Stafford, G. R.; White, G.; Josell, D., Thermal transport through thin films: Mirage technique measurements on aluminum/titanium multilayers. *Journal of Materials Research* **2000,** *15*, 764-771.
149. Wong, P. K.; Fung, P. C. W.; Tam, H. L.; Gao, J., Thermal-diffusivity measurements of an oriented superconducting-film\char21{}substrate composite using the mirage technique. *Physical Review B* **1995,** *51*, 523-533.
150. Wong, P. K.; Fung, P. C. W.; Tam, H. L., Low thermal diffusivity measurements of thin films using mirage technique. *Journal of Applied Physics* **1998,** *84*, 6623-6627.
151. Bertolotti, M.; Dorogan, V.; Liakhou, G.; Li Voti, R.; Paoloni, S.; Sibilia, C., New photothermal deflection method for thermal diffusivity measurement of semiconductor wafers. *Review of Scientific Instruments* **1997,** *68*, 1521-1526.
152. Olmstead, M. A.; Amer, N. M.; Kohn, S.; Fournier, D.; Boccara, A. C., Photothermal displacement spectroscopy: An optical probe for solids and surfaces. *Applied Physics A Solids and Surfaces* **1983,** *32*, 141-154.
153. Hu, C.; Ogawa, E. T.; Ho, P. S., Thermal diffusivity measurement of polymeric thin films using the photothermal displacement technique. II. On-wafer measurement. *Journal of Applied Physics* **1999,** *86*, 6028-6038.
154. Umeda, N.; Itoh, K.-i., Surface Profiling Using the Photothermal Displacement Method. *Japanese Journal of Applied Physics* **1990,** *29*, L1206.
155. Penco, E.; Sparvieri, N.; Bertolotti, M.; Ferrari, A.; Sibilia, C.; Suber, G., Thermal diffusivity measurements by an interferometric method on magnetic ceramic materials. *Materials Chemistry and Physics* **1987,** *17*, 399-403.
156. Kuo, B.; Li, J.; Schmid, A., Thermal conductivity and interface thermal resistance of Si film on Si substrate determined by photothermal displacement interferometry. *Appl Phys A* **1992,** *55*, 289-296.
157. Sparvieri, N.; Penco, E.; Sibilia, C.; Bertolotti, M.; Suber, G.; Ferrari, A., A laser interferometric method applied to thermal diffusivity measurements of ferrites. *Materials Letters* **1987,** *5*, 449-452.
158. Coufal, H.; Hefferle, P., Thermal diffusivity measurements of thin films with a pyroelectric calorimeter. *Appl Phys A* **1985,** *38*, 213-219.
159. John, P. K.; Miranda, L. C. M.; Rastogi, A. C., Thermal diffusivity measurement using the photopyroelectric effect. *Physical Review B* **1986,** *34*, 4342-4345.
160. Chirtoc, M.; Mihilescu, G., Theory of the photopyroelectric method for investigation of optical and thermal materials properties. *Physical Review B* **1989,** *40*, 9606-9617.
161. Menon, C. P.; Philip, J., Simultaneous determination of thermal conductivity and heat capacity near solid state phase transitions by a photopyroelectric technique. *Measurement Science and Technology* **2000,** *11*, 1744.
162. Balderas-López, J. A.; Mandelis, A., New Photopyroelectric Technique for Precise Measurements of the Thermal Effusivity of Transparent Liquids. *Int J Thermophys* **2003,** *24*, 463-471.
163. Dadarlat, D.; Streza, M.; Pop, M. N.; Tosa, V.; Delenclos, S.; Longuemart, S.; Sahraoui, A. H., Photopyroelectric calorimetry of solids. *Journal of Thermal Analysis and Calorimetry* **2010,** *101*, 397-402.
164. Rombouts, M.; Froyen, L.; Gusarov, A. V.; Bentefour, E. H.; Glorieux, C., Photopyroelectric measurement of thermal conductivity of metallic powders. *Journal of Applied Physics* **2005,** *97*, 024905.
165. Marinelli, M.; Murtas, F.; Mecozzi, M. G.; Zammit, U.; Pizzoferrato, R.; Scudieri, F.; Martellucci, S.; Marinelli, M., Simultaneous determination of specific heat, thermal conductivity and thermal diffusivity at low temperature via the photopyroelectric technique. *Appl Phys A* **1990,** *51*, 387-393.

166. Dadarlat, D.; Pop, M. N., Self-consistent photopyroelectric calorimetry for liquids. *International Journal of Thermal Sciences* **2012,** *56*, 19-22.
167. Dadarlat, D.; Pop, M. N., New front photopyroelectric methodology based on thickness scanning procedure for measuring the thermal parameters of thin solids. *Measurement Science and Technology* **2010,** *21*.
168. Borca-Tasciuc, D.-A.; Chen, G., Anisotropic thermal properties of nanochanneled alumina templates. *Journal of Applied Physics* **2005,** *97*, -.
169. Borca-Tasciuc, T.; Borca-Tasciuc, D. A.; Chen, G., Photo-Thermoelectric Technique for Anisotropic Thermal Diffusivity Measurements. *Components and Packaging Technologies, IEEE Transactions on* **2007,** *30*, 609-617.
170. Borca-Tasciuc, T.; Vafaei, S.; Borca-Tasciuc, D.-A.; Wei, B. Q.; Vajtai, R.; Ajayan, P. M., Anisotropic thermal diffusivity of aligned multiwall carbon nanotube arrays. *Journal of Applied Physics* **2005,** *98*, 054309.
171. Borca-Tasciuc, D.-A.; Chen, G.; Lin, Y.-M.; Rabin, O.; Dresselhaus, M. S.; Borshchevsky, A.; Fleurial, J.-P.; Ryan, M. A. In *Thermal Characterization of Nanowire Array in a-Al 2 O 3 Matrix*, MRS Proceedings, 2001; Cambridge Univ Press: 2001; p V2. 7.
172. Borca-Tasciuc, D.-A.; Chen, G.; Prieto, A.; Martín-González, M. S.; Stacy, A.; Sands, T.; Ryan, M.; Fleurial, J., Thermal properties of electrodeposited bismuth telluride nanowires embedded in amorphous alumina. *Applied Physics Letters* **2004,** *85*, 6001-6003.
173. Bell, A. G., The Photophone. *Science* **1880,** *1*, 130-134.
174. De La Zerda, A.; Zavaleta, C.; Keren, S.; Vaithilingam, S.; Bodapati, S.; Liu, Z.; Levi, J.; Smith, B. R.; Ma, T.-J.; Oralkan, O.; Cheng, Z.; Chen, X.; Dai, H.; Khuri-Yakub, B. T.; Gambhir, S. S., Carbon nanotubes as photoacoustic molecular imaging agents in living mice. *Nat Nano* **2008,** *3*, 557-562.
175. Wang, L. V., Multiscale photoacoustic microscopy and computed tomography. *Nat Photon* **2009,** *3*, 503-509.
176. Ntziachristos, V.; Ripoll, J.; Wang, L. V.; Weissleder, R., Looking and listening to light: the evolution of whole-body photonic imaging. *Nat Biotech* **2005,** *23*, 313-320.
177. Quimby, R. S.; Yen, W. M., On the adequacy of one dimensional treatments of the photoacoustic effect. *Journal of Applied Physics* **1980,** *51*, 1252-1253.
178. Hu, H.; Wang, X.; Xu, X., Generalized theory of the photoacoustic effect in a multilayer material. *Journal of Applied Physics* **1999,** *86*, 3953-3958.
179. Bento, A. C.; Mansanares, A. M.; Vargas, H.; Miranda, L. C. M., Photoacoustic measurement of the thermal diffusivity of anisotropic samples using the phase lag method. *Physics and Chemistry of Glasses* **1989,** *30*, 160-162.
180. Balderas-Lopez, J. A., Photoacoustic signal normalization method and its application to the measurement of the thermal diffusivity for optically opaque materials. *Review of Scientific Instruments* **2006,** *77*, 064902-4.
181. Aamodt, L.; Murphy, J.; Parker, J., Size considerations in the design of cells for photoacoustic spectroscopy. *Journal of Applied Physics* **1977,** *48*, 927-933.
182. McDonald, F. A.; Grover C. Wetsel, J., Generalized theory of the photoacoustic effect. *Journal of Applied Physics* **1978,** *49*, 2313-2322.
183. Cesar, C. L.; Vargas, H.; Meyer, J. A.; Miranda, L. C. M., Photoacoustic Effect in Solids. *Physical Review Letters* **1979,** *42*, 1570-1573.
184. Fernelius, N. C., Extension of the Rosencwaig-Gersho photoacoustic spectroscopy theory to include effects of a sample coating. *Journal of Applied Physics* **1980,** *51*, 650-654.
185. Poulet, P.; Chambron, J.; Unterreiner, R., Quantitative photoacoustic spectroscopy applied to thermally thick samples. *Journal of Applied Physics* **1980,** *51*, 1738-1742.
186. Korpiun, P.; Büchner, B., On the thermodynamics of the photoacoustic effect of condensed matter in gas cells. *Appl. Phys. B* **1983,** *30*, 121-129.
187. Rousset, G.; Lepoutre, F.; Bertrand, L., Influence of thermoelastic bending on photoacoustic experiments related to measurements of thermal diffusivity of metals. *Journal of Applied Physics* **1983,** *54*, 2383-2391.
188. Somer, A.; Camilotti, F.; Costa, G. F.; Bonardi, C.; Novatski, A.; Andrade, A. V. C.; Kozlowski, V. A.; Cruz, G. K., The thermoelastic bending and thermal diffusion processes influence

on photoacoustic signal generation using open photoacoustic cell technique. *Journal of Applied Physics* **2013,** *114*, 063503.
189. Bedoya, A.; Marin, E.; Mansanares, A. M.; Zambrano-Arjona, M. A.; Riech, I.; Calderon, A., On the thermal characterization of solids by photoacoustic calorimetry: Thermal diffusivity and linear thermal expansion coefficient. *Thermochimica Acta* **2015,** *614*, 52-58.
190. Balderas-Lopez, J. A., Self-normalized photoacoustic technique for thermal diffusivity measurements of transparent materials. *Review of Scientific Instruments* **2008,** *79*, 024901-6.
191. Wang, X.; Hu, H.; Xu, X., Photo-Acoustic Measurement of Thermal Conductivity of Thin Films and Bulk Materials. *Journal of Heat Transfer* **2000,** *123*, 138-144.
192. El-Brolossy, T. A.; Ibrahim, S. S., Photoacoustic measurement of thermal properties of polystyrene metal oxide composites. *Thermochimica Acta* **2010,** *509*, 46-49.
193. Abad, B.; Rull-Bravo, M.; Hodson, S. L.; Xu, X.; Martin-Gonzalez, M., Thermoelectric properties of electrodeposited tellurium films and the sodium lignosulfonate effect. *Electrochimica Acta* **2015,** *169*, 37-45.
194. Maiz, J.; Rojo, M. M.; Abad, B.; Wilson, A.; Nogales, A.; Borca-Tasciuc, D.-A.; Borca-Tasciuc, T.; Martin-Gonzalez, M. S., Enhancement of thermoelectric efficiency of doped PCDTBT polymer films. *RSC Advances* **2015**.
195. Pérez-Taborda, J.A.; Romero, J.J.; Abad, B.; Muñoz-Rojo, M.; Mello, A.; Briones, F.; Martín-González, M. S., Low thermal conductivity and improved thermoelectric performance of nanocrystalline Silicon Germanium films by sputtering. *Nanotechnology (under review)* **2016**.
196. Sheng, C. K.; Mahmood Mat Yunus, W.; Yunus, W. M. Z. W.; Abidin Talib, Z.; Kassim, A., Characterization of thermal, optical and carrier transport properties of porous silicon using the photoacoustic technique. *Physica B: Condensed Matter* **2008,** *403*, 2634-2638.
197. Abad, B.; Maiz, J.; Martín-González, M., Rules to determine thermal conductivity and density of Anodic Aluminum Oxide (AAO) membranes *Nano Research (under review)* **2016**.
198. Abad, B.; Maiz, J.; Caballero-Calero, O.; Ruiz, A.; Martín-González, M., Opening the door to engineering material thermal properties by three dimensional porous alumina. *Scientific Reports (under review)* **2016**.
199. Smith, M. K.; Singh, V.; Kalaitzidou, K.; Cola, B. A., Poly(3-hexylthiophene) nanotube array surfaces with tunable wetting and contact thermal energy transport. *ACS Nano* **2015,** *9*, 1080-1088.
200. Biswas, K. G.; Sands, T. D.; Cola, B. A.; Xu, X., Thermal conductivity of bismuth telluride nanowire array-epoxy composite. *Applied Physics Letters* **2009,** *94*, 223116-3.
201. Cola, B. A.; Xu, J.; Cheng, C.; Xu, X.; Fisher, T. S.; Hu, H., Photoacoustic characterization of carbon nanotube array thermal interfaces. *Journal of Applied Physics* **2007,** *101*, 054313-9.

Chapter 2: Experimental methodology

This chapter is divided into two parts. Firstly, the fabrication techniques used to obtain the different materials measured in this PhD work: anodic aluminum oxide membranes, nanowires, films and bulk samples are explained (Section 2.1). Secondly, the physico-chemical characterization performed on them to help us to understand their thermal conductivity properties.

2.1. Fabrication techniques

2.1.1 Anodic Aluminum Oxide membranes fabrication

2.1.1.1 Fabrication of the regular AAO membranes

The anodic aluminum oxide (AAO) membranes are alumina membranes grown by an electrochemical method, known as anodization, which induces the formation of aluminum oxide on an aluminum surface and under certain conditions pores that self-ordered. These membranes can be grown highly hexagonal pore order with high aspect ratio (since the pores diameters range from 8 nm to 530 nm and their lengths can reach hundreds of microns)[1-4].

The anodization process was performed in an electrochemical cell, where an aluminum substrate and a platinum mesh act as the anode and the cathode, respectively. The procedure used to fabricate highly ordered AAO membranes is known as the two-step anodization process[5]. An ultrapure aluminum foil (99.999%) from Advent Research Materials (England) with a thickness of 500 μm and a diameter of 1.6 cm was employed for the fabrication of each template. In order to carry out the AAO membrane fabrication, five steps can be distinguished: aluminum cleaning, electropolishing, the first anodization, chemical etching and the second anodization.

First, the aluminum foil is cleaned by sonication with different polarity solvents: acetone, water, isopropanol and ethanol. Afterwards, the sample is electropolished under 20 V for 4 minutes in a solution made of ethanol and perchloric acid (75:25) in order to reduce the aluminum roughness. Second, the first anodization is performed. Different parameters such as the temperature, the constant output voltage, the anodization time and the type and concentration of the electrolyte can be selected during this process depending on the desired characteristics of the AAO membrane. The formation of the pores takes place during this process, but in a non-ordered fashion with a huge size distribution. However, after a certain time, the interface between the barrier layer and the alumina becomes ordered. The time of the first anodization process determines the order of the membranes.

The third step consists on a chemical etching of the non-ordered porous alumina formed during the first anodization process in an aqueous solution of chromic oxide (CrO_3 1.8 wt. %) and phosphoric acid (H_3PO_4 7 wt. %), so that an ordered pattern in the aluminum surface is obtained.

Finally, a second anodization process is performed, where the previously ordered pattern act as nucleation points, so that the new pores start to grow already with a hexagonal arrangement. The time of the second anodization determines the pore's length.

The different parameters used for the fabrication of the AAO membranes are shown in Table 2.I. [1, 2, 4].

Table 2.I. Experimental parameters selected for the anodization in sulfuric, oxalic and phosphoric acid and the 2nd anodization time needed to obtain approximately 100 μm length AAO membranes.

Electrolyte	Acid Concentration	Voltage (V)	Temperature (ºC)	1st anodization time (h)	2nd anodization time (h)	Pore diameter (nm)
H_2SO_4 (ethylene glycol 50 wt.%)	10 wt.%	19	0	24	100	15
H_2SO_4	0.3 M	25	1-2	24	24	25
$H_2C_2O_4$	0.3 M	40	3-5	24	30	40
H_3PO_4 (0.01 M AlO_x)	1 wt. %	205	5	6	20	150

2.1.1.2 Fabrication of 3D AAO membranes

The first anodization of the 3D AAO membrane is the same as the one used for the AAO prepared in sulfuric acid (Table 2.I.). After removing the first alumina layer by chemical etching, a pulsed anodization between a mild anodization (MA) and hard anodization (HA) with constant voltages is performed [6-9]. In our case, the applied voltage remains constant during the MA steps whereas the current is the limiting parameter in the HA steps, so that the resulting AAO is selectively etched. Therefore, the aluminum oxide formed during the HA steps is partially eliminated in such a way that transversal nanochannels are created, and hence, the 3D porous network is established .

The AAO membranes used in this work were prepared by Dr. Jon Maiz at Instituto de Microelectrónica de Madrid (IMM-CNM), CSIC.

2.1.1.3 Widening pores process, aluminum removal and barrier layer etching

In order to cover a broader range of pore diameters AAO membranes, a widening of the pores is carried out by a controlled etching of the pore walls with a phosphoric acid solution whose concentration is 5 wt.% at 35 ºC. The etching time depends on the pore diameter desired for each AAO template.

The AAO membranes were used for both, measuring their thermal conductivity and as a template to grow nanowires by electrodeposition. In both cases, it is necessary to remove the remaining aluminum layer and open the pores which are in contact with this layer. Firstly, the aluminum substrate is chemically attacked by a solution composed of 3.6 g $CuCl_2$ + 50 ml HCl +100 ml H_2O at 0 ºC. Afterwards, the oxide barrier layer is eliminated by a chemical etching in a 10 wt.% phosphoric acid solution at 30 ºC during a certain time, depending on the AAO.

2.1.2 Electrochemical deposition

The electrodeposition is an electrochemical process where a reduction of the ions, which are present in a solution (known as electrolyte), are reduced onto a conductive substrate following the next reaction,

$$M^{n+} + ne^{-} \leftrightarrow M \tag{2.1}$$

The reaction is determined by the equilibrium or reduction potential. The reduction potential depends on the activities of the oxidized and reduced species as the Nernst equation explains,

$$E = E^{0} - \frac{R\,T}{n\,F} Ln \frac{a_M^{n+}}{a_M} \tag{2.2}$$

where E^0 is the standard potential, R is the ideal gas constant (8.314 J·mol^{-1}·K^{-1}), T is the absolute temperature, F is the Faraday constant (96485.339 C·mol^{-1}), and a_M^{n+} and a_M are the oxidized and reduced species activities, respectively.

During the electrodeposition two different processes take place: electron transfer, as deduced from Eq. 2.1, and mass transport due to the ions movement through the electrolyte. Moreover, there are three different phenomena related to the ions transport: migration, convection and diffusion. Ions migration is given by the driving force applied to the system, i.e., the electric field generated by the applied potential. The convection is related to a mechanical force given for example, by stirring. The diffusion phenomenon is associated to a concentration gradient. As the deposit is growing onto the working electrode, the amount of ions near to its surface is lower so that a concentration gradient is created between this surface and the bulk electrolyte.

The amount of deposited material on the working electrode during the electrodeposition process can be controlled by selecting the applied potential. Faraday´s law describes the relation between the mass of a substance deposited onto a conductive substrate, *m*, the molecular weight of the substance, *M*, the number of electrons involved in the reduction reaction, *n*, and the total charge which is the electric current, *I(t)*, integrated over time t :

$$m = \frac{M}{n\,F} \int_0^t I(t)dt \tag{2.3}$$

For the electrodeposition of the different materials presented in this dissertation, a conventional three-electrode electrochemical cell was employed. The working electrode (WE) is a conductive substrate which acts as a cathode. In this work, the WE consists of 5 nm of chromium and 150 nm of gold or platinum deposited by electron beam evaporation onto a silicon substrate (1 0 0). The counter electrode (CE) is an inert material, a platinum mesh in our case, which acts as anode. Finally, a reference electrode (RE) of Ag/AgCl (3M KCl) is used to control the applied potential.

Figure 2.1 shows a scheme of the typical electrochemical cell used for the different electrodeposition processes. All the films and nanowires prepared by electrodeposition during this thesis were prepared by a bi-potentiostat (Eco Chemie, Model AUT302.0) governed by the software Nova 1.8.

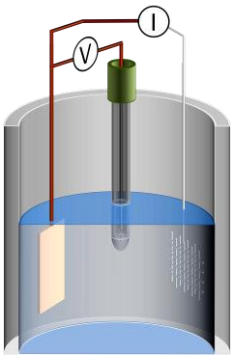

Figure 2.1. Scheme of the electrochemical cell used in this work.

The electrodeposition process can be carried out by controlling the applied potential, which is known as potentiostatic mode, or the applied electrical current, called galvanostatic mode.

The tellurium and bismuth telluride films were obtained at constant potential by using the potentiostatic mode, whereas the bismuth telluride and antimony telluride nanowires were prepared by pulsed electrodeposition between an applied potential and a zero current density, i.e., by alternating the potentiostatic and galvanostatic modes.

The characterization of the electrolyte/electrode system and the growth of the different materials have been carried out by using three electrochemical techniques: the cyclic voltammetry (CV), the chronoamperometry and chronopotentiometry. The CV allows the study of the different electrochemical processes that take place in the electrolyte and consequently, the determination of the reduction potential necessary to obtain the desired material.

These curves are obtained by measuring the electrical current that flows through the WE during a voltage sweep. In our case, the scan rate employed in all CVs was 0.01 $V \cdot s^{-1}$ and the start potential of the CVs is taken as the open circuit potential (OCP) which is the potential established between the WE and RE when there is no applied potential (open cell). Once the CV starts, the potential is swept towards the reduction/cathodic stage, i.e., potential more negatives than the OCP. The sweep direction is reversed at a certain potential and the potentials are swept towards the oxidation/anodic stage. The sweep direction is reversed again so that the scan finishes at the OCP, as shown in Figure 2.2.

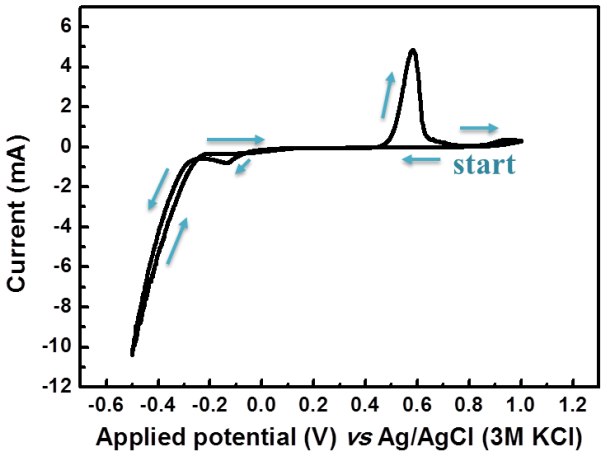

Figure 2.2. Cyclic voltammetry of a tellurium film onto a Platinum substrate.

When the reduction potential has been selected, a chronoamperometry is carried out to obtain the deposit. This curve consists in measuring the current density measured as a function of time during the chronopotentiostatic electrodeposition.

The bismuth telluride films and nanowires grown by electrodeposition without sodium lignosulfonate were prepared by Dr. Cristina V. Manzano. Alejandra Ruiz and Dr. Olga Caballero prepared bismuth telluride and antimony telluride with sodium lignosulfonate by electrodeposition. The PhD candidate prepared the tellurium films both with and without sodium lignosulfonate. All these growths were performed at Instituto de Microelectrónica de Madrid (IMM-CNM), CSIC.

2.1.3 Drop-casting

The non-doped films of poly [N-9'-heptadecanyl-2,7carbazole-alt-5,5-(4',7'-di-2-thienyl-2',1',3-benzothiadizole)] (PCDTBT) were prepared by drop casting. The polymer supplied by Solares Chem Inc. is dissolved in chloroform and drop casted into glass substrates previously cleaned with acetone.

These films were prepared by Dr. Jon Maiz at Instituto de Microelectrónica de Madrid (IMM-CNM), CSIC.

2.1.4 Sputtering

Sputtering is a process that involves a target bombardment with high energy ions, which produces the ejection of atoms from the target surface and their deposition in a substrate as a thin film[10]. The average amount of ejected atoms from the target per incident ion is known as the *sputter yield*, which depends on different factors such as the ion energy and incident angle, the ion and target atoms masses, among others. Due to the potential difference between the target which acts as a

cathode and the metal crown which is found around it, an electric discharge takes place so that the gas ionization is produced. As a consequence, a plasma, i.e., a gas of ionized particles, is generated. The gas molecules remain positively charged, in our case Ar^+, and are accelerated by the same electric field, which produced the electric discharge. The plasma is confined around the target due to the magnetic field created by the permanent magnets placed under the target. This confinement increases the process efficiency and only takes place when the incoming particles kinetic energy is much higher than conventional thermal energies ($\gg$ 1 eV).

The Silicon Germanium samples measured in this thesis were fabricated by a lab-made sputtering system. The target consists of a boron doped $Si_{0.8}Ge_{0.2}$ (99.999% purity) placed in a cylindrical magnetron cathode in a vertical configuration inside a vacuum chamber which reaches a base vacuum of 10^{-9} mbar, where ultrapure argon (99.9999%) is used as the sputtering atmosphere. Strontium titanate ($SrTiO_3$) and glass with an evaporated 25 nm gold layer were used as substrates. A DC source has been used to create sustained plasma, which allows $Si_{0.8}Ge_{0.2}$ samples growth in an Ar atmosphere.

These thin films were prepared by the PhD student Jaime Andrés Pérez Taborda by means of a system available in our group at Instituto de Microelectrónica de Madrid (IMM-CNM), CSIC.

2.1.5 Ball milling

Ball milling is a synthesis method in which the particle size is reduced by means of a grinding produced by the impact between the material and the balls or walls, thus, creating a powder of particle size lower than 100 nm. Depending on the hollow cylindrical shell revolutions, different state reactions can occur, which cannot be produced by other solid state methods.

The ZnO powders were prepared by ball milling. ZnO microparticles (Asturiana de Cinc SA, Spain) having and average particle size of 0.5 μm, named thereafter Regular ZnO, and ZnO-nanoparticles (Evonik, Germany) having and average particles size of 70 nm, named thereafter ZnO nano. As doping materials NiO-nanoparticles (ADParticles SL, Spain) having a primary particles size of 20 nm are used to modify the ZnO materials by wt. % addition of 0.01, 0.1, 1 and 3 in excess of NiO, Samples were dry milled following the nanodispersion method [11, 12]. This system is at Instituto de Cerámica y Vidrio (ICV), CSIC.

2.1.6 Spark Plasma Sintering (SPS)

Spark plasma sintering (SPS) is a pressure sintering process that involves electrical discharge between the air gaps of a powder material which generates briefly a high temperature plasma. The consolidation of the powder in a pellet is achieved by the uniaxial pressure along with the DC electrical current [13].

The mechanical properties of the materials obtained by this sintering process differ considerably from those sintered by conventional pressure methods. Moreover, SPS allows obtaining denser products of finer grain, quicker than usual processes keeping the nano-grain structure in a final pellet.

The ZnO pellets were prepared by SPS in a Dr. Sinter SPS-1050-CE (SPS Syntex Inc., Osaka, Japan). The ZnO and NiO-doped ZnO pellets were heated to 850 °C or 1100 ºC and held for 5 min and finally cooled to room temperature. The load applied to the samples was 40 MPa; all heating and cooling rates were 250 °C·min^{-1}. The processing of samples was performed under an Ar atmosphere to prevent damage of the graphite dies. For comparison purposes a standard sintering in air atmosphere is attempted for the samples by using a standard electric furnace up to 1400 ºC with a heating rate of 10 °C·min^{-1}.

The samples were prepared by D. Ángel de Pablos Pérez with the SPS system is at the Instituto de Cerámica y Vidrio (ICV), CSIC.

2.1.7 Mortar and pestle technique

This method is used to mix different materials. The mortar is a vessel where the material is placed so that a heavy tool, known as pestle, is used to crush and grind the material until getting a more homogeneous powder.

In this thesis, polyaniline blended with graphene nanoplatelets powders were obtained by this technique. An aqueous solution of anilinium salt (50 g, 37.4 mmol) was agitated for one hour at room temperature in order to completely dissolve the anilinium salt. Then, an aqueous solution (500 mL) of HCl (3 M, 2 mol) was incorporated. Afterward, an aqueous solution (500 mL) of the oxidant ammonium persulfate (153 g, 65.7 mmol) was also incorporated in the prior mix. The agitation of the solution was stopped one minute after adding the oxidizing agent. The polymerization reaction was completed by allowing the greenish colored solution to rest overnight at room temperature. The thick green product achieved was filtered and first cleaned with an acidic aqueous solution (4x1L) of 0.1 M HCl to eliminate the persulfate counter ion. Then, methanol (3x1L) was used to eliminate unwanted aniline oligomer. The purified polymer was then heated at 80 °C for two days to attain a green powder which is subsequently grounded with mortar and pestle so a finer powder is achieved. The PANI powder was blending with different weight percentages of the GNPs in a glass mortar and mechanically grounded to obtain a homogenous mixture.

The fabrication of the PANI/GNP powders were carried out by Dr. David Amantia in the Centro Tecnológico LEITAT in Barcelona.

2.1.8 Cold press

The cold press is a densification process of powder by pressure, whereby is possible to obtain dense pellets, [14] although not as dense as by SPS. In order to obtain these dense discs, the powders are pressed at several tons at room temperature to compact them.

In this PhD work, solid disks of PANI/GNP blends were obtained by pressing with 10 tons for 3 minutes onto 200 mg of the mixture in a 13 mm diameter pellet.

The fabrication of the PANI/GNP pellets was carried out by Dr. David Amantia in the Centro Tecnológico LEITAT in Barcelona.

2.1.9 Electron beam evaporation

The e-beam evaporation is a growth technique based on the heating of a target material until its sublimation by an incident electron beam supplied by a filament (in our case tungsten) when applying a large potential. The electrons are drawn from the filament and led and focused to the target by a magnet system. The sublimated target material is evaporated in the vacuum chamber and deposited on the desired substrate.

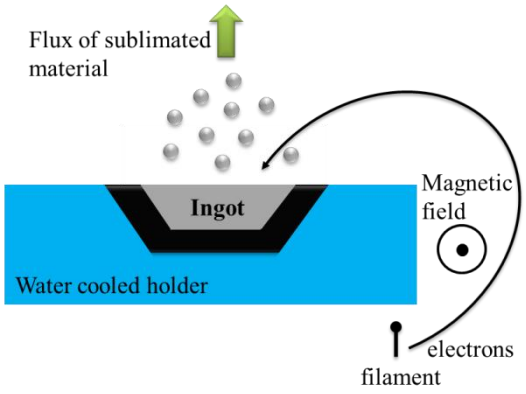

Figure 2.3. E-beam evaporation mechanism.

As explained above, the working electrode used in an electrodeposition process should be conductive. For this purpose, the Si wafer and the alumina membranes used as working electrodes are metallized by e-beam evaporation with different metal layers (see Table 2.II) Moreover the gold layer used the metal induced crystallization of SiGe films was also deposited by this procedure.

Table 2.II. Different metal layers have been evaporated on the substrates for the different materials studied in this thesis.

Sample	Substrate/Metal layers deposited by e-beam
Te films	Si / 5 nm Cr / 150 Pt
Bi_2Te_3 films without SLS	Si / 5 nm Cr / 150 Pt
Bi_2Te_3 films with SLS	Si / 5 nm Cr / 150 Au
Bi_2Te_3 and Sb_2Te_3 nanowires	AAO / 5 nm Cr / 150 Au
SiGe	AlN/ 25 nm gold Glass / 25 nm gold

Besides the working electrode preparation needed for the electrodeposition process, the e-beam evaporation technique was used to metallize the samples in order to measure their thermal conductivity, since it is necessary a metal layer which ensures the absorption of the laser on the surface of the sample. Photoacoustic technique requires an 80 nm titanium layer, whereas TDTR method needs a 70 nm aluminum layer.

The substrates and samples used during this thesis were all metallized with titanium by e-beam evaporation in the Instituto de Microelectrónica de Madrid (IMM-CNM), CSIC. The samples metallized with aluminum were prepared in Instituto de Sistemas Optoelectrónicos y Microtecnología (ISOM-UPM).

2.1.10 Mechanical polishing

Mechanical polishing is used to make the samples surface flatter and reduce the overall roughness [15]. The samples are polished by a disk plate with glasspapers. The sample is attached to a metallic holder by means of specific glue and positioned on the polishing machine arm. Polishing is achieved by the continuous spinning of the sample onto the glasspaper.

Nanowires embedded in alumina templates were polished by this process in order to remove any overgrown structure and achieve a flat surface with the tips of the nanowires at the alumina surface level. A polishing cloth along with alumina powders of different particle size, 1 µm, 0.5 µm and 0.03 µm, were used. The size of the alumina particles were gradually reduced from 1µm to 0.03 µm in such a way that a final roughness of less than 20 nm was achieved.

The polishing machine is at the clean room of the Instituto de Microelectrónica de Madrid (IMM-CNM), CSIC.

2.1.11 Films lift-off process

A conductive substrate is required in the electrodeposition technique. However, in order to avoid the influence of the conductive substrate when measuring the electrical properties of the films, a lift-off process was performed [16, 17]. This procedure allows the sample to be detached from the

substrate: a) the sample is glued to a piece of glass, when the glass is fixed to the sample, b) the whole block is introduced in liquid nitrogen. The difference between the thermal expansion coefficients of the film and the gold or platinum layer generates the lift-off.

2.1.12 Thermal treatments at reduction atmosphere

The thermal treatments were carried out in a system called Rapid Thermal Annealing (RTA). The sample is placed in a quartz ampoule and a controlled atmosphere is used for the treatments. In our case, a reductor atmosphere was achieved by using a mixture of 95% N_2 and 5% H_2 (formingas). The heating is performed by an infrared lamp which heats the sample rapidly and uniformly.

During this thesis, this system has been employed for the silicon germanium ex-situ annealing by the PhD student Marta Rull. The experimental equipment is available in our group at Instituto de Microelectrónica de Madrid (IMM-CNM), CSIC.

2.2 Characterization techniques

2.2.1 X-Ray diffraction (XRD)

The structural properties of the materials studied during this thesis have been analyzed by means of the X-Ray Diffraction (XRD). The equipment used was a Philips X´Pert four circle diffractometer with CuK_α X-Ray radiation.

When an X-ray beam interacts with a crystalline sample (periodic crystal), a coherent dispersion, called diffraction, is produced. The diffracted beam preserves the wavelength of the incident radiation and presents maxima intensity at specific space directions. These maxima are produced by the constructive interference of the coherently dispersed X-Rays and they are described by Bragg´s Law given by,

$$n\lambda = 2dsin\theta \tag{2.4}$$

where λ is the wavelength of incident radiation, d is the distance between the atomic planes within the crystal, n is an integer and θ is the angle between the incident wave and the scattering planes. According to Bragg´s law, constructive interference only occurs when the path difference between two waves is an entire multiple of the wavelength. Moreover, Bragg diffraction takes place when the incident electromagnetic radiation wavelength is comparable to the interplanar distance in the lattice of a crystalline sample.

All diffraction patterns of the films characterized in this thesis were performed in Bragg-Brentano configuration with steps of 0.02 ° with a time per step of 1s. In the case of the nanowires, the

scan step is also 0.02 ° but the time per step is 16 s in order to increase the signal to noise ratio. This system is available at the Instituto de Microelectrónica de Madrid (IMM-CNM), CSIC. The bismuth telluride films and nanowires without SLS XRD were performed by Dr. Cristina V. Manzano, whereas the XRD of films and nanowires grown with SLS were done by Dr. Olga Caballero. Finally, diffraction patterns of tellurium films were carried out by the PhD student Marta Rull Bravo.

2.2.2 Scanning Electron Microscopy (SEM)

The morphology characterization of the samples studied in this work was carried out by Field Emission Scanning Electron Microscopy (FE-SEM).

An electric field is applied to a filament located into a vacuum chamber so that electrons are drawn from it. The electron beam is focused and collimated to reach the surface of the sample by means of magnetic lens. When the electron beam hits the sample, several phenomena can occur: secondary electrons, backscattered electrons, X-Rays, among others, which provide different types of information. From secondary electrons, the morphology of the sample can be studied. The backscattered electrons are related to the atomic number of the elements present in the sample and from the X-Rays emission, a compositional study can be performed.

The different samples studied in this thesis were examined by three different systems. The tellurium, bismuth telluride films grown by electrodeposition and the PANI/GNP composites were characterized by a FE-SEM Philips XL305-FEG with 10 kV accelerating voltage. The anodic aluminum oxide membranes were studied by a Hitachi SU8000 with an accelerating voltage of 0.5 kV. A Field Emission-SEM Hitachi-S4700 (Hitachi High-Tech, Minato-ku, Tokyo, Japan) was employed to examine the zinc oxide pellets. Samples were ground then polished down to 0.25 ml diamond paste followed by polishing with OPS (colloidal silica suspension) for 5 h. Finally, they were chemically etched by using a water dilution of 5% HCl. These systems are set at Servicio Interdepartamental de Investigación (SIdI) of Universidad Autónoma de Madrid, Instituto de Ciencia y Tecnología de Polímeros (CSIC) and Instituto de Cerámica y Vidrio (ICV), respectively.

2.2.3 Energy-dispersive X-ray spectroscopy

Chemical composition of films and nanowires studied during this PhD work was analyzed by Energy-dispersive X-ray spectroscopy (EDX).

An elemental analysis can be performed by analyzing the X-Ray emission from a material when it is excited by a high energy electron beam from a scanning electron microscope. This excitation provokes the ejection of an electron from an inner shell so that an electron hole is created. Afterwards, an electron from an outer shell fills the hole by emitting X-Ray radiation due to the energy difference between both states. This radiation, which is detected by an energy-dispersive spectrometer,

is characteristic of each element thus allowing the determination of the chemical composition of the sample.

The equipment employed for this analysis was S-3000N and is found at the SiDI department (Servicio Interdepartamental de Investigación) of Universidad Autónoma de Madrid.

2.2.4 Raman spectroscopy

The Raman spectroscopy was employed to determine the vibrational and rotational properties, which can be used to identify molecules or elements of some of the studied materials and correlate them with the transport properties [18].

Raman spectroscopy is a non-destructive characterization technique used to study both organic and inorganic materials. It is based on the detection of the inelastic scattering suffered by the photons coming from a monochromatic source when reaching a material. Two different inelastic scattered photons can be distinguished depending on the wavelength of the scattered photons: Stokes and anti-Stokes when the output wavelength is higher and lower than that of the incident photon, respectively.

Raman spectra were measured by a LabRam HR Raman spectrometer (Horiba Jobin-Yvon) with a 532 nm wavelength Nd:YAG laser with an optical power of 8.5 mW in all the cases, in air and at room temperature. $Si_{0.8}Ge_{0.2}$ films were measured from 200 cm^{-1} to 600 cm^{-1} by Jaime Andrés Pérez Taborda. AAO samples were measured in the range from 300 cm^{-1} to 1300 cm^{-1} by Dr. Olga Caballero Calero.

This system is in our group at the Instituto de Microelectrónica de Madrid (IMM-CNM), CSIC.

2.2.5 Brunauer–Emmett–Teller (BET) technique

In order to measure the porosity of the anodic aluminum oxide membranes as well as the pore size distribution, the Brunauer-Emmett-Teller technique was employed.

The BET technique is based on the physic adsorption of an inert gas (nitrogen) on the solid surfaces of a sample in order to measure the specific surface area of a material [19]. A Barrett-Joyner-Halenda (BJH) method was used to determine the pore size distribution and the pore volume [20].

The porosity of a sample, *P*, can be evaluated once the pores volume, V_{pores}, and the volume of the solid, V_{solid}, are known by the next relation,

$$P = \frac{V_{pores}}{V_{pores} + V_{solid}} \tag{2.5}$$

The solid volume is calculated from the mass, *m*, and the density, ρ, of the sample measured by the Archimedes´ method since $\rho = m/V$ (see section 2.2.7). This procedure was carried out for the 25 nm pore diameter AAO membrane in order to check the ability of the porosity calculation by the SEM image analysis. Moreover, the porosity of 3D AAO membrane was also determined by this technique since it is not possible to analyze it by the SEM top-images.

This technique also allows the determination of the pore size distribution provided that the pore diameter ranges the mesoporosity (2-50 nm). These experiments were performed at the Instituto de Catálisis y Petroquímica, CSIC.

2.2.6 Differential Scanning Calorimetry (DSC)

The specific heat, C_p, of the different samples needed to calculate the thermal conductivity by the photoacoustic technique was measured by Differential Scanning Calorimetry (DSC). This technique measures the difference in the quantity of thermal energy necessary to rise the temperature of a sample and a reference as a function of the temperature. From this difference the specific heat capacity of the sample can be extracted.

The specific heat experiments were performed at Servicio Interdepartamental de Investigación (SIdI) of Universidad Autónoma de Madrid with a Discovery DSC from TA instruments in a temperature range from -10 ºC to 60 ºC.

2.2.7 Density measurement by Archimedes' method

Samples density measurements were carried out by the Archimedes' method with ethanol as the assisting liquid whose density (ρ_{et}) is well-known. A balance XS105DU from Mettler Toledo was employed to weigh the samples in air (W_{air}) and in ethanol (W_{et}). The skeletal density is finally assessed by employing the next equation,

$$\rho = \frac{W_{air}}{W_{air} - W_{et}} (\rho_{et} - \rho_{air}) + \rho_{air} \tag{2.6}$$

This procedure was employed to measure bulk samples, such as the AAO membranes or ZnO pellets prepared by SPS. Thin films cannot be characterized by this technique since it is necessary to take into account the substrate. The balance is available in our group at Instituto de Microelectrónica de Madrid (IMM-CNM), CSIC.

2.2.8 Profilometer measurements

The thickness of the films was measured by a profilometer Veeco Dektak Stylus. A mobile tip makes contact with the sample surface and scans it with a constant force. The tip is connected to a

measurement system which registers the vertical displacements during the sweep along the surface. This equipment was used to determine both the thickness and the roughness of the tellurium, bismuth telluride, PCDTBT and SiGe films. This system is available at Instituto de Microelectrónica de Madrid (IMM-CNM), CSIC.

2.2.9 Seebeck coefficient and electrical resistivity

The power factor, $PF = S^2 \cdot \sigma$, which is given by the product between the square of the Seebeck coefficient, S, and the electrical conductivity, σ, was measured by a commercial system LSR-3 Linseis in helium atmosphere by measuring simultaneously both magnitudes.

This system is able to measure both films and bulk materials in a temperature range from room temperature to 800 ºC. The sample is placed between two platinum electrodes as shown in figure 2.4. Two type-S (Platinum Rhodium - 10% /Platinum) thermocouples are used to sense both temperature and voltage along the sample. In the case of the Seebeck coefficient measurement, a heating power is applied to the lower platinum block so that a temperature gradient is created along the sample. This temperature difference, ΔT, is measured between the thermocouples which are in contact with the surface of the sample. The Seebeck voltage, ΔV, generated by the temperature gradient is also measured by the Pt wires of each thermocouple so that the Seebeck coefficient can be obtained by the next expression,

$$S_{rel} = \frac{\Delta V}{\Delta T} \tag{2.7}$$

where S_{rel} is the relative Seebeck coefficient which contains the influence of the probes. In order to calculate the absolute Seebeck coefficient, S_{abs}, it is necessary to take into account the Seebeck coefficient of the platinum wires, S_{Pt}, by means of the following relation,

$$S_{rel} = S_{abs} - S_{Pt} \tag{2.8}$$

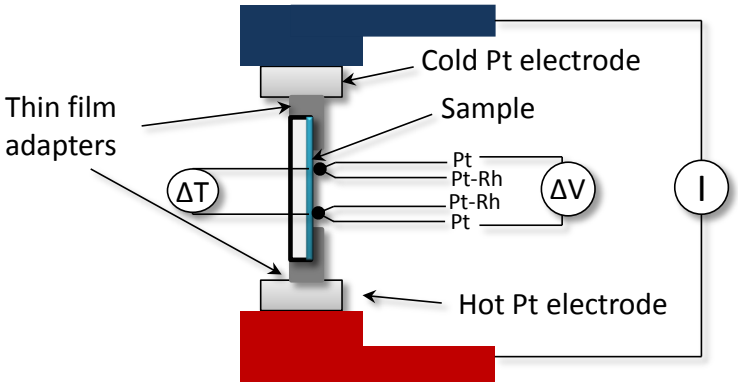

Figure 2.4. Seebeck coefficient and electrical conductivity measurement setup.

In the case of the electrical conductivity measurement, which is the inverse of the electrical resistivity, ρ, a four-probe method is used to avoid the contact resistance during the measurement. A constant current is applied between the two platinum blocks where the sample is placed so that a voltage drop is measured between the platinum wires of the thermocouples. Ohm´s law provides the electrical resistance, *R*, from the current, *I*, and the potential difference, *V*.

$$V = I \cdot R \tag{2.9}$$

Once the resistance is obtained, the electrical resistivity can be assessed by knowing the dimensions of the sample,

$$R = \rho \frac{L}{W \cdot d} \tag{2.10}$$

where *L* is the thermocouples separation, *W* and *d* are the width and the thickness of the sample, respectively.

This system is periodically calibrated in order to ensure the accuracy of the measurements. A constantan standard sample supplied by the company is used to check both the electrical resistivity and the Seebeck coefficient in the whole range of temperature, from room temperature to 800 ºC, as shown in Figure 2.5. Moreover, $CoSb_3$ bulk samples fabricated in our group are typically measured by this equipment and by another similar setup located at Fraunhofer Institut, Freiburg, Germany, giving the same results within the error intervals.

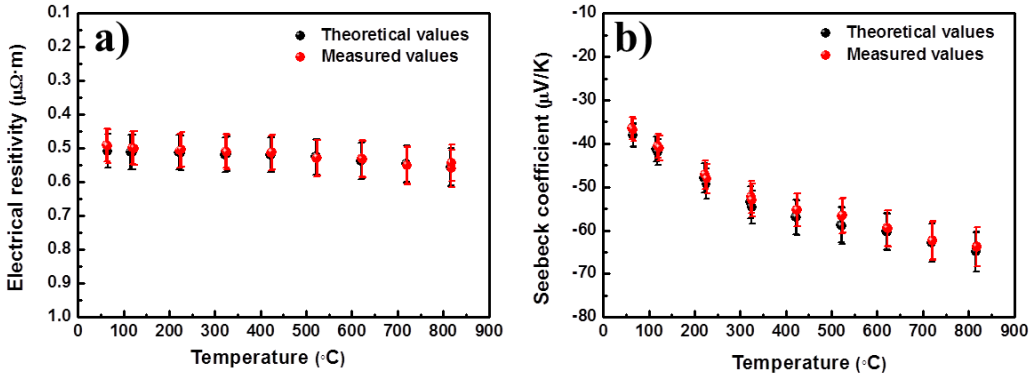

Figure 2.5. Example of one of the periodic checking of (a) electrical resistivity and (b) Seebeck coefficient values of the constantan standard sample.

This system is available in our group at Instituto de Microelectrónica de Madrid (IMM-CNM), CSIC.

2.2.10 Thermal conductivity

2.2.10.1 Photoacoustic technique

This technique is the core of this dissertation and will be explained in detail in chapter 3. It is based on the periodic heating of the surface of a sample by means of an incident modulated radiation. The surface of the sample periodically is heated and cooled down so that the air in contact with the sample expands and contracts like a thermal piston. These movements are translated into acoustic waves which are sensed by a microphone. The signal detected by the microphone is compared to the incident modulated signal from the laser so that, the thermal properties can be obtained from the phase shift between them. Figure 2.6 shows the measurement configurations that have been used: (a) front configuration, where the sample is illuminated in the same side as the acoustic waves are detected, and (b) rear configuration where the illumination and the acoustic waves are produced in opposite sides.

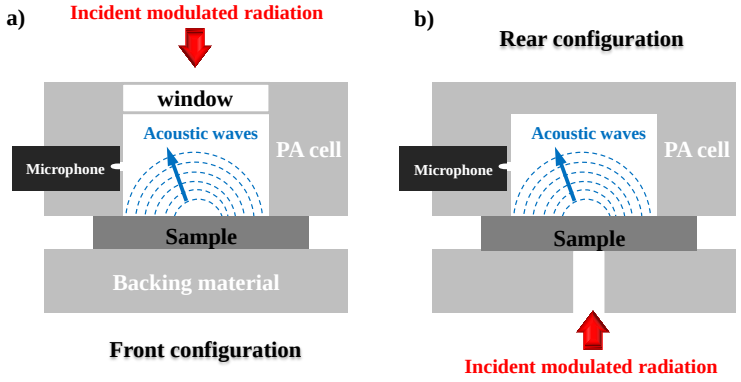

Figure 2.6. Photoacoustic setup in (a) front and (b) rear configurations.

The calculation of the thermal diffusivity or conductivity depends on the type of material to be analyzed. In the case of multilayered materials, such as the tellurium, bismuth telluride, PCDTBT and SiGe films, a multilayered model is used. This model was developed by Hu et. al [21] where the sample measurement is performed in the front configuration mode, and it is compared to a reference sample in order to avoid the influence of the PA cell.

On the other hand, the measurements of bulk samples are performed by measuring in both, front and rear configuration, so that normalization of the phase shift is obtained [22, 23].

It is worthy to note that both procedures use the phase instead of the amplitude of the signal since it is less sensitive to the reflectivity of the sample.

The extraction of the thermal conductivity requires the knowledge of other properties of the sample in both cases. In the case of bulk samples, the thermal conductivity is extracted from the thermal diffusivity, α, value which is the measured quantity, calculated by using the thickness of the

sample. By knowing the density, ρ, and specific heat, C_P, of the sample the thermal conductivity is calculated from the following relation:

$$k = \alpha \rho C_P \tag{2.11}$$

In the case of samples measured as multilayered materials, the properties that are necessary to account for each layer are: density, specific heat, thermal conductivity, thickness, optical absorption coefficient and thermal resistance between one layer and the subsequent one. Further details will be given in Chapter 4 for bulk measurements and Chapter 5 for films, porous structures and nanowire arrays measurements.

Density and specific heat are normally measured by the Archimedes' method and Differential Scanning Calorimetry, respectively, or taken from the literature. The thickness is always measured by SEM, profilometer or a micrometer, depending on the type of sample,. The optical absorption coefficient is not a critical magnitude since it is only important in the case of the first layer, i.e., the titanium layer that always covers all the samples. Finally, the thermal resistances are normally unknown and remain as unknown parameters during the fitting. However, there are some studies which allow us to predict their values depending on the sample .

In order to ensure the reliability of the measurements, a double-check was carried out with another photoacoustic system set in Mechanical Engineering Building in Purdue University (West Lafayette, Indiana) during a stay in that Lab. Other double-checks of the system were performed with two different setups described below, Time-Domain Thermoreflectance method and the Scanning Thermal Microscopy.

This experimental technique, which has been developed by the PhD candidate during this PhD work, is currently fully functional and available in our laboratory at Instituto de Microelectrónica de Madrid.

2.2.10.2 Time-Domain Thermoreflectance method (TDTR)

The Time-Domain thermoreflectance method was explained in Section 1.4.1.1. In our measurements, the samples were metallized with 70 nm aluminum layer to ensure the sensibility of the thermoreflectance coefficient to the employed laser wavelength which is a Ti: sapphire laser which creates short pulsed laser beams with 12.5 repetition rate [24]. This laser beam is split into pump and probe beam. The pump beam, modulated at a frequency of 0.8-10 MHz, is used to heat the surface of the sample since it is more powerful than the probe beam, which senses the change in the reflectivity of the aluminum layer. The signal is detected by a Si-photodetector connected to a RF lock in amplifier. The signal is fitted by using a 3D thermal diffusion model based on thermal quadrupoles[25], where the thermal boundary resistance between the aluminum layer and the sample is included.

The thermal conductivity measurements by TDTR were performed by Dr. Yee Rui Koh at Birck Nanotechnology Building in Purdue University (West Lafayette, Indiana) during the stay of the PhD candidate in that center.

2.2.10.3 Scanning Thermal Microscopy

The 3ω-SThM (Scanning Thermal Microscopy) was used to measure the thermal conductivity of some samples and check the reliability of the photoacoustic measurements. The 3ω-SThM [26] makes use of the Joule heating generated through a thermo-resistive probe when an electric current is passed across it. When the probe is approached to the surface of a sample, a heat flux exchange takes place between both elements. Therefore, the temperature of the probe is altered and its electrical resistance changes. The thermal conductivity of the sample is related to the third harmonic, 3ω, of the electrical response of the probe.

The thermal conductivity measurements by the 3ω-SThM technique were performed by the PhD students Miguel Muñoz Rojo and Adam A. Wilson.

2.2.10.4 Laser flash

The laser flash (deeply described in Section 1.4.1.2) is a transient technique based on a short pulse (< 1 ms) used to heat the front surface of the sample. The temperature rise in the rear face of the sample is detected by a thermocouple or an infrared camera so that the thermal diffusivity of the material is obtained.

Two different laser flash systems were used during this PhD work. The $CoSb_3$ sample used as a calibration sample for the photoacoustic experimental setup was measured by a Microflash Netzsch LFA 457 at Institut Fraunhofer, Freiburg, by Dr. Alexandre Jacquot. Conversely, a polyaniline blended with graphene (PANI/GNP) pellet was measured during a stay of the PhD candidate in the National Institute for Materials Science (NIMS), Tsukuba (Japan), with a system TC-7000; ULVAC-Riko, Japan, during a stay of the PhD candidate in that research center.

2.2.10.5 Low thermal conductivity measurements setup

This experimental setup was also developed during this PhD work. It is completely explained in Section 4.4.4.1. This technique is based on the steady state method to directly extract the thermal conductivity of bulk materials. This setup consists of two copper blocks which act as a heat source and heat sink when a sample is placed between them (see Figure 2.7 (a) and (c)). A thermocouple is located in each of the copper blocks very near to the surface in contact with the sample in order to sense the temperature when heating the top block (heat source). Several power heatings are applied

during the measurement and the temperature difference between both faces is recorded as seen in Figure 2.7 (b).

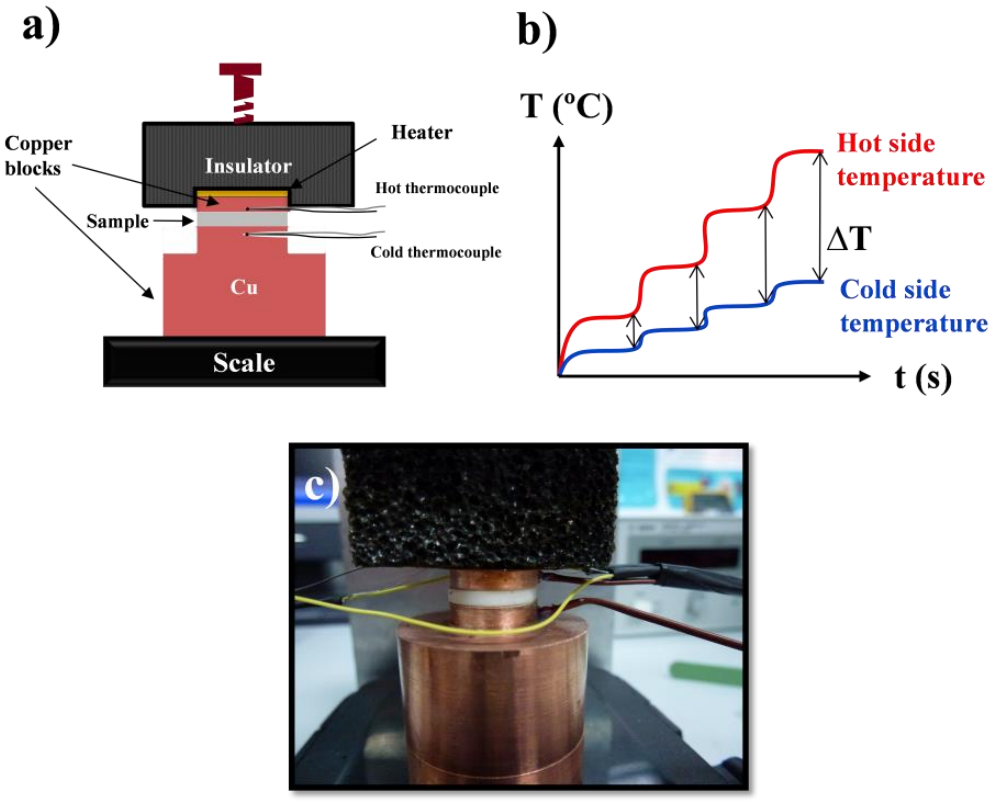

Figure 2.7. (a) Thermal conductivity experimental setup developed during this PhD thesis, used to measure polymer bulk samples, (b) temperature as a function of the time during a typical measurement of a sample and (c) picture of the experimental setup.

In order to avoid thermal losses coming from convection or radiation, a comparative method is conducted. For that purpose, a reference sample is also measured. The heating power through the standard is the same as the power through the sample. The following expression is used to extract the thermal conductivity,

$$\Delta T_R = \frac{(A/L)_S}{(A/L)_R}\frac{\Delta T_S}{\kappa_R}\kappa_S \tag{2.12}$$

where the subscripts R and S correspond to the reference and the sample, respectively. A and L are the section and the thickness of the sample and ΔT is the temperature difference created across the sample. By plotting the temperature gradient of the reference sample against $\frac{(A/L)_S}{(A/L)_R}\frac{\Delta T_S}{\kappa_R}$, the thermal conductivity of the sample is directly obtained.

2.3 References

1. Martín, J.; Manzano, C. V.; Martín-González, M., In-depth study of self-ordered porous alumina in the 140–400 nm pore diameter range. *Microporous and Mesoporous Materials* **2012,** *151*, 311-316.
2. Martín, J.; Manzano, C. V.; Caballero-Calero, O.; Martín-González, M., High-Aspect-Ratio and Highly Ordered 15-nm Porous Alumina Templates. *ACS Applied Materials & Interfaces* **2012,** *5*, 72-79.
3. Manzano, C. V.; Martín, J.; Martín-González, M. S., Ultra-narrow 12 nm pore diameter self-ordered anodic alumina templates. *Microporous and Mesoporous Materials* **2014,** *184*, 177-183.
4. Sun, C.; Luo, J.; Wu, L.; Zhang, J., Self-ordered anodic alumina with continuously tunable pore intervals from 410 to 530 nm. *ACS Applied Materials and Interfaces* **2010,** *2*, 1299-1302.
5. Masuda, H.; Fukuda, K., Ordered Metal Nanohole Arrays Made by a Two-Step Replication of Honeycomb Structures of Anodic Alumina. *Science* **1995,** *268*, 1466-1468.
6. Martín, J.; Martín-González, M.; Francisco Fernández, J.; Caballero-Calero, O., Ordered three-dimensional interconnected nanoarchitectures in anodic porous alumina. *Nat Commun* **2014,** *5*.
7. Lee, W.; Schwirn, K.; Steinhart, M.; Pippel, E.; Scholz, R.; Gosele, U., Structural engineering of nanoporous anodic aluminium oxide by pulse anodization of aluminium. *Nat Nano* **2008,** *3*, 234-239.
8. Lee, W.; Scholz, R.; GoÌˆsele, U., A Continuous Process for Structurally Well-Defined Al_2O_3 Nanotubes Based on Pulse Anodization of Aluminum. *Nano Letters* **2008,** *8*, 2155-2160.
9. Sulka, G. D.; Brzózka, A.; Liu, L., Fabrication of diameter-modulated and ultrathin porous nanowires in anodic aluminum oxide templates. *Electrochimica Acta* **2011,** *56*, 4972-4979.
10. Wasa, K., *Handbook of Sputter Deposition Technology: Fundamentals and Applications for Functional Thin Films, Nano-materials and MEMS*. William Andrew: 2012.
11. Rubio-Marcos, F.; Calvino-Casilda, V.; Bañares, M. A.; Fernandez, J. F., Novel hierarchical Co3O4/ZnO mixtures by dry nanodispersion and their catalytic application in the carbonylation of glycerol. *Journal of Catalysis* **2010,** *275*, 288-293.
12. Rubio-Marcos, F.; Manzano, C. V.; Reinosa, J. J.; Lorite, I.; Romero, J.; Fernández, J. F.; Martín-González, M. S., Modification of optical properties in ZnO particles by surface deposition and anchoring of NiO nanoparticles. *Journal of Alloys and Compounds* **2011,** *509*, 2891-2896.
13. Munir, Z. A.; Anselmi-Tamburini, U.; Ohyanagi, M., The effect of electric field and pressure on the synthesis and consolidation of materials: A review of the spark plasma sintering method. *J Mater Sci* **2006,** *41*, 763-777.
14. Su, L.; Gan, Y. X., *Advances in thermoelectric energy conversion nanocomposites*. INTECH Open Access Publisher: 2011.
15. Marinescu, I. D.; Uhlmann, E.; Doi, T., *Handbook of lapping and polishing*. CrC Press: 2006.
16. Abad, B.; Rull-Bravo, M.; Hodson, S. L.; Xu, X.; Martin-Gonzalez, M., Thermoelectric properties of electrodeposited tellurium films and the sodium lignosulfonate effect. *Electrochimica Acta* **2015,** *169*, 37-45.
17. Caballero-Calero, O.; Díaz-Chao, P.; Abad, B.; Manzano, C. V.; Ynsa, M. D.; Romero, J. J.; Rojo, M. M.; Martín-González, M. S., Improvement of Bismuth Telluride electrodeposited films by the addition of Sodium Lignosulfonate. *Electrochimica Acta* **2014,** *123*, 117-126.
18. Lewis, I. R.; Edwards, H., *Handbook of Raman spectroscopy: from the research laboratory to the process line*. CRC Press: 2001.
19. Brunauer, S.; Emmett, P. H.; Teller, E., Adsorption of Gases in Multimolecular Layers. *Journal of the American Chemical Society* **1938,** *60*, 309-319.
20. Barrett, E. P.; Joyner, L. G.; Halenda, P. P., The Determination of Pore Volume and Area Distributions in Porous Substances. I. Computations from Nitrogen Isotherms. *Journal of the American Chemical Society* **1951,** *73*, 373-380.
21. Hu, H.; Wang, X.; Xu, X., Generalized theory of the photoacoustic effect in a multilayer material. *Journal of Applied Physics* **1999,** *86*, 3953-3958.

22. Balderas-Lopez, J. A., Photoacoustic signal normalization method and its application to the measurement of the thermal diffusivity for optically opaque materials. *Review of Scientific Instruments* **2006,** *77*, 064902-4.
23. Balderas-López, J. A.; Mandelis, A., Self-normalized photothermal technique for accurate thermal diffusivity measurements in thin metal layers. *Review of Scientific Instruments* **2003,** *74*, 5219-5225.
24. Vermeersch, B.; Pernot, G.; Koh, Y.; Abumov, P.; Shakouri, A. In *Ballistic heat transport and associated frequency dependence of thermal conductivity in semiconductor alloys*, Thermal and Thermomechanical Phenomena in Electronic Systems (ITherm), 2012 13th IEEE Intersociety Conference on, May 30 2012-June 1 2012, 2012; 2012; pp 428-434.
25. Cassels, L. E.; Buehl, T. E.; Burke, P. G.; Palmstrøm, C. J.; Gossard, A. C.; Pernot, G.; Shakouri, A.; Haughn, C. R.; Doty, M. F.; Zide, J. M. O., Growth and characterization of TbAs:GaAs nanocomposites. *Journal of Vacuum Science & Technology B* **2011,** *29*, 03C114.
26. Muñoz Rojo, M.; Grauby, S.; Rampnoux, J. M.; Caballero-Calero, O.; Martin-Gonzalez, M.; Dilhaire, S., Fabrication of Bi_2Te_3 nanowire arrays and thermal conductivity measurement by 3ω-scanning thermal microscopy. *Journal of Applied Physics* **2013,** *113*.

Chapter 3:

Photoacoustic experimental setup

In this chapter the experimental setup and measurement design of the photoacoustic technique developed in this thesis are explained. Firstly, the experimental setup optimization, which involves the photoacoustic cell, microphone, laser, instrumentation, sources of noise, stability, and reproducibility, is described. Secondly, the theory and the measurement procedure was established for both bulk and multilayered samples. Finally, the sensitivity, uncertainty, fitting procedure, the selected metal transducer, calibration and detection limits are also discussed.

3.1 Introduction

Optical heating methods are being widely investigated as a powerful tool to measure thermal properties of materials. The main advantage of these techniques lies in the lack of contact resistances when heating the sample as explained in the introduction chapter of this thesis. In particular, in the photoacoustic (PA) technique, the thermal contact resistance is avoided not only in the heating procedure but also in the detection scheme. Moreover, both the experimental setup and measurements are considerably simpler than other techniques such as Time-Domain Thermoreflectance. In addition, this technique will allow for the study of thermal transport of all type of structures which is one of the main limitations of other techniques.

The photoacoustic effect is based on the acoustic waves created when an incident modulated radiation is absorbed by the surface of a solid and converted into heat by non-radiative de-excitation processes in the material. The air in contact with the sample expands and contracts as a thermal piston due to the periodic surface heating thus creating acoustic waves which are detected by a microphone. The signal is finally collected by a lock-in amplifier.

In order to obtain high quality measurements, it is necessary to design both, the experimental setup and the measurement procedure.

3.2 Experimental setup

As it can be seen in Figure 3.1, the experimental setup comprises several elements. The photoacoustic cell consists of a body with a cavity where the acoustic waves are generated. A microphone is placed inside the body of the cell and connected to the acoustic cavity by a small hole. The cavity is closed at its ends, by the sample and a window, in order to ensure that the acoustic waves are not perturbed by the atmospheric disturbances. A fiber laser is chopped with a selected frequency and impinges on the sample. The modulated radiation leads to a periodic heating and cooling of the sample. Consequently, the gas (air in our case) near the sample surface is heated and cooled, giving rise to acoustic waves that can be detected by the microphone. The microphone is connected to a pre-amplifier, which increases the photoacoustic (PA) signal. Afterwards, the PA signal is directed to a signal conditioning, which both powers the pre-amplifier and clean the acoustic signal after the pre-amplifier. The treated signal is finally connected to a lock-in amplifier, which compares it with a reference signal. This reference signal is used to modulate the laser beam so that it has the same frequency as the acoustic waves. From the phase shift between both signals, the thermal properties of the sample can be derived by a proper mathematical model.

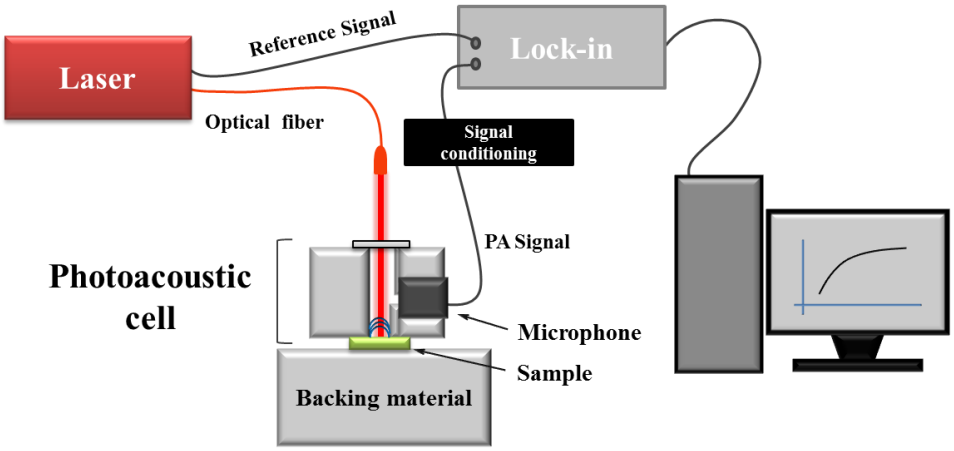

Figure 3.1. Photoacoustic experimental setup.

3.2.1 Photoacoustic cell design optimization

The PA cell has been designed in order to measure all types of structures: bulk materials, thin and thick films, and nanowires embedded into a matrix or porous structures.

The photoacoustic cell is comprised of the cell body with a cavity where the acoustic waves are generated and propagated until reaching the microphone. There are resonant and no resonant PA cells. A resonant cell takes advantages of a great improvement of the photoacoustic signal given by the resonances. Resonant cells are typically used in photoacoustic spectroscopy experiments (PAS), which analyze the sample response as a function of the incident wavelength[1]. Conversely, our experiment is performed by varying the frequency with a fixed wavelength so that a resonant-free cell is required. Otherwise, the signal would be greatly influenced by slight changes in the cell volume during the sample mounting. Finally, our PA cell is attached to a stage in order to assess the stability of the system. The requirements that must satisfy the PA cell are described below.

3.2.1.1 Material

The PA cell must be made of a very low reflective material, so the scattered light can leave the cell without creating any parasitic signals.

The material employed for the PA cell is the thermoplastic polymer poly(methyl methacrylate) (PMMA), also known as acrylic or acrylic glass. It is a synthetic polymer which is regarded as a type of glass. This material has a very high transmittance so that it is approximately transparent for wavelengths higher than 800 nm [2, 3]. As the laser wavelengths of the experiment are 980 nm and 1060 nm, polished PMMA results suitable as a material for the PA cell.

Absorption experiments were carried out in order to extract the optical absorption coefficient of the PMMA. Beer-Lambert law is used for that purpose and is given by,

$$I = I_0 exp(-\beta d) \tag{3.1}$$

where I and I_0 are the output and input light intensities, d is the thickness of the sample and β is the optical absorption coefficient. By taking several different thicknesses and measuring the optical intensity before and after going through the material, an optical absorption coefficient of around 0.01 cm^{-3} is obtained for wavelengths of 980 nm and 1070 nm. This value is low enough to ensure small reflections inside the PA cell and to guarantee a high transmittance of scattered light.

3.2.1.2 Cavity design

The PA cavity was designed with a cylindrical geometry so that its resonances can be longitudinal, azimuthal, radial and their combinations. Acoustic resonances are produced at those frequencies where standing waves are present in the cavity in such a way that the amplitude of the acoustic signal is sharply increased. In the case of carrying out photoacoustic spectrometry, acoustic resonances are desirable to increase the signal to noise ratio. In our case, we have always studied the PA signal as a function of the frequency so that acoustic resonances would disturb the measurement. In order to optimize the signal during the measurement, the cavity of the PA cell is designed so that acoustic resonances are avoided.

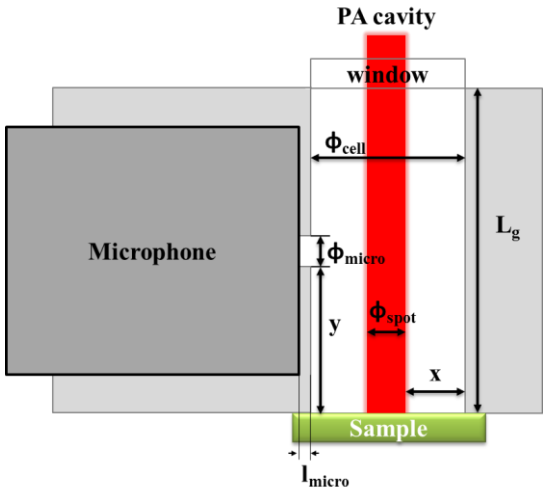

Figure 3.2. Photoacoustic cavity and the characteristic lengths. The red shadow depicts the incident laser beam impinging on the surface of the sample.

The important dimensions of a PA cavity are shown in Figure 3.2:

a) ***Gas column length, L_g.*** When the longitudinal dimension of a cylindrical cavity is larger than the diameter, the lowest resonance frequency occurs when the sound propagates in the axial direction. Resonances can disturb the PA signal provided that the gas length is a multiple of $\Lambda_s/2$, where Λ_s is the wavelength of the acoustic wave. In those cases, a stationary wave,

whose nodes correspond with the ends of the cavity, is produced. Therefore, in order to avoid these effects, it is necessary to ensure this condition,

$$\frac{\Lambda_s}{2} \gg L_g \tag{3.2}$$

The wavelength of the acoustic wave depends on both, the wave frequency, f, and the speed of sound in the media, v, as,

$$\Lambda_s = \frac{v}{f} \tag{3.3}$$

In our case, the experiments were performed in air at room temperature so that v = 346 m·s^{-1} (T = 25 ºC) [4]. Figure 3.3 shows the variation of the half acoustic wavelength as a function of the frequency. By taking into account the microphone detection limit (between 4 Hz as 20 kHz), an air column length of 8.4 mm will avoid axial resonances in our working frequency range, since the lowest resonance frequency is 20.6 kHz, which is high enough to be avoided. Moreover, this length will be also able to contain the microphone, whose diameter is 7 mm.

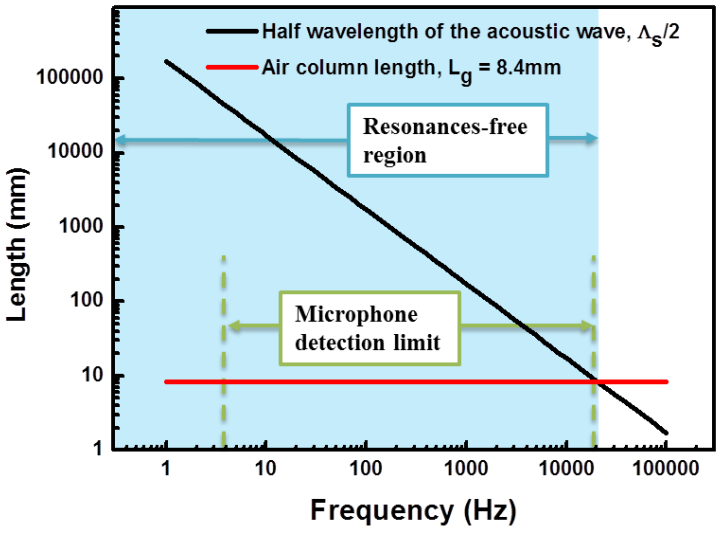

Figure 3.3. Comparison between the half wavelength of the acoustic wave generated by the modulated radiation and the 8.4 mm air column length as a function of the frequency.

The dimensions of the gas column length could be increased by using a gas with higher speed of sound, like helium (970 m·s^{-1} at 0 ºC). However, it would introduce an additional complexity in the experimental setup related to possible gas leakages. As the working frequency range is completely usable when employing air and the designed length is mechanical achievable, the PA cavity dimensions were calculated for air conditions.

A more complex analysis of the resonance frequencies in a cylindrical cavity closed on both sides includes all three dimensions, i.e., resonances can be longitudinal, azimuthal, radial and their combinations. This analysis can be performed by solving the wave equation with cylindrical boundary conditions giving the following resonance frequencies [5],

$$f_{m,n,q} = \frac{v}{2}\sqrt{\left(\frac{\beta_{mn}}{\phi_{cell}}\right)^2 + \left(\frac{q}{L_g}\right)^2} \tag{3.4}$$

where v is the speed of sound, β_{mn} is the transversal eigenvalue, q is the longitudinal eigenvalue, ϕ_{cell} is the cavity diameter and L_g is the gas column length.

The resonance frequencies are calculated for different dimensions of the gas column length and cell diameter and finally they were established as 8.4 mm and 4 mm, respectively. Table 3.I shows the different resonance frequencies associated with both axial and tangential waves. It is interesting to note that the resonance frequency given by Eq. 3.4 for $\beta_{mn} = 0$ is the same as calculated previously for the axial sound propagation. None of the other frequencies are lower than that one and therefore the selected dimensions are suitable for our photoacoustic experiment.

Table 3.I. Resonance frequencies in a cylindrical cavity with 4 mm in diameter and a gas column length of 8.4 mm.

m	n	β_{mn}	q	f_{mnq} (Hz)
0	0	0	0	0
0	0	0	1	**20595**
0	0	0	2	41190
0	1	1.2197	0	105504
0	1	1.2197	1	107495
0	1	1.2197	2	113260
0	2	2.2331	0	193163
0	2	2.2331	1	194258
0	2	2.2331	2	197506
1	0	0.5861	0	50698
1	0	0.5861	1	54721
1	0	0.5861	2	65322
1	1	1.697	0	146791
1	1	1.697	1	148228
1	1	1.697	2	152460
1	2	2.714	0	234761
1	2	2.714	1	235663
1	2	2.714	2	238347
2	0	0.9722	0	84095
2	0	0.9722	1	86581

2	0	0.9722	2	93641
2	1	2.1346	0	184643
2	1	2.1346	1	185788
2	1	2.1346	2	189182
2	2	3.1734	0	274499
2	2	3.1734	1	275271
2	2	3.1734	2	277572

b) ***Cavity diameter, ϕ_{cell}***. Quimby *et al.*[6] predicted that a one dimensional model of the heat transfer in a photoacoustic cell can be applied provided that the cavity radius is higher than the thermal diffusion length of the air at the working frequency. The PA cavity diameter was calculated so that the temperature oscillation damps down when reaching the cell walls and hence, there are no 3D effects or lateral heat flow. For the calculation, we compared the thermal diffusion length, μ, with the characteristic length given by,

$$x = \frac{\phi_{cell} - \phi_{spot}}{2} \tag{3.5}$$

where ϕ_{cell} and ϕ_{spot} are the PA cavity and beam spot diameters, respectively, as shown in Figure 3.4 (a). The thermal diffusion length is given by:

$$\mu = \sqrt{\frac{\alpha}{\pi f}} \tag{3.6}$$

where α is the thermal diffusivity and f is the frequency. The air thermal diffusivity is $2.1 \cdot 10^{-5}$ $m^2 \cdot s^{-1}$ [7]. Figure 3.4 (b) proved the validity of the one dimensional treatment of the heat flow for a cavity diameter of 4 mm. However, it will be necessary to be careful and sensible when carrying out the data analysis of experiments performed at very low frequencies (4 -10 Hz).

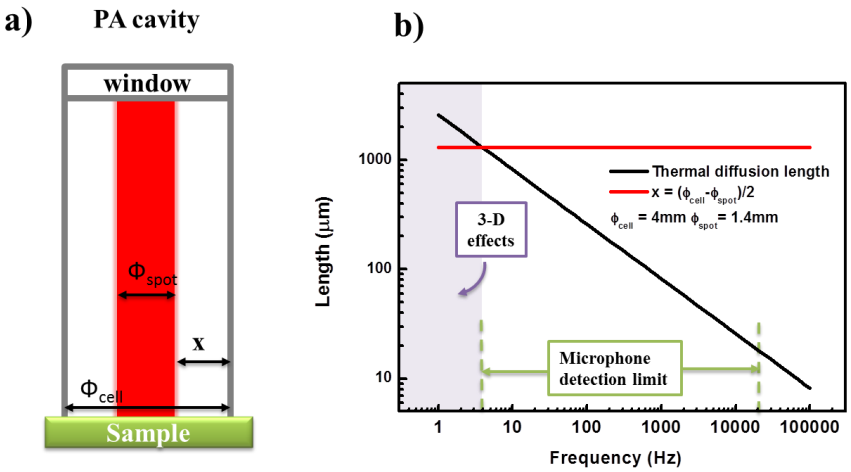

Figure 3.4. (a) PA cavity where the laser beam is depicted as the red shadow and (b) thermal diffusion length of the air as a function of the frequency compared with the characteristic length x.

c) ***Sample-microphone distance*, y**. This length is conditioned by the microphone size along with the sound attenuation distance. On the one hand, the minimum distance from the sample to the center of the microphone is the microphone radius, 3.5 mm. Moreover, there should be a piece of wall between the sample and the hole where the microphone is placed for mechanical stability. On the other hand, it is necessary to take also into account the sound attenuation given by Stokes´ law,

$$A(d) = A_0\, exp(-ad) \tag{3.7}$$

where $A(d)$ is the amplitude of the acoustic wave at a distance d from the sound source, i.e., the sample. A_0 is the initial amplitude and a is the attenuation coefficient which represents how far a sound wave can travel before its amplitude declines in a factor of *1/e*. Bass *et al.*[8, 9] studied the atmospheric absorption of sound for different conditions of relative humidity, pressure and frequency, showing how the attenuation increases when increasing the acoustic waves frequency. A significant attenuation was found for high frequencies at 100 m from the acoustic source. In our case, the distance from the acoustic source (sample) and the detection point (the microphone) is in the order of millimeters, so that the attenuation is negligible at this scale length. A simple calculation can be performed to check this claim. If the maximum attenuation obtained in reference [9] is taken, 10 dB/(100m·atm) at 20 kHz, we can calculate the attenuation for our selected length, 4.2 mm.

$$A(4mm) = exp - \left(\frac{10dB \cdot 0.0042m}{100m}\right) A_0 = 0.9996A_0 \tag{3.8}$$

This means that the signal at 4.2 mm is barely attenuated.

Therefore, the distance between the sample and the microphone is entirely conditioned by the mechanical stability of the PA cell so that it can be fixed as 4.2 mm.

d) ***Diameter and length of the microphone duct, ϕ_{duct} and l_{duct}.*** The cylindrical PA cavity, along with the duct space and the microphone cavity can behave as a Helmholtz resonator which is, precisely, a cavity connected to a duct that finishes in a hole (see Figure 3.5 (a)). As the microphone cavity volume ($6 \cdot 10^{-}4$ cm^{-3})[10] is much lower than the PA cavity volume (0.1 cm^{-3}), the associated Helmholtz resonance given by :

$$f_{Helmholtz} = \frac{v}{2\pi}\sqrt{\frac{A}{V \cdot L}} \tag{3.9}$$

where v is the sound velocity, A, and L are the section and the length of the duct and V is the total volume of the cavity, as shown in Figure 3.5 (a).

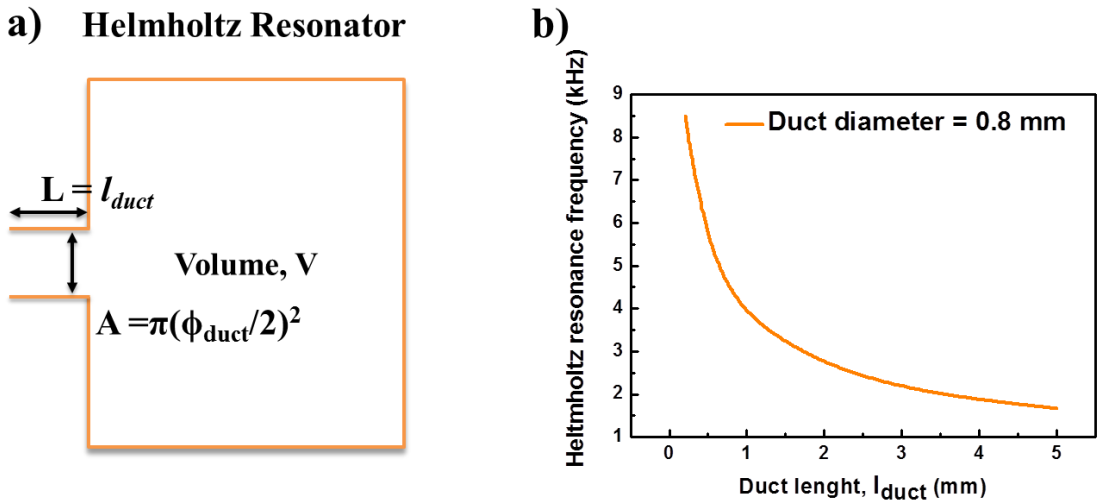

Figure 3.5. (a) Helmholtz resonator scheme and (b) Helmholtz resonance frequency as a function of the duct length.

In our case, the area of the duct is given by $\pi(\phi_{duct}/2)^2$ and the length by l_{duct} as depicted in Figure 3.5 (a). In order to select those dimensions corresponding to a satisfying Helmholtz resonance frequency, we fixed the duct diameter to 0.8 mm since it is the physical hole of the microphone. Therefore, we studied the resonance frequencies for different values of the duct length. Figure 3.5 (b) shows how the frequency increases when reducing this dimension. As the working frequency will be comprised in the microphone frequency range (4 Hz - 20 kHz), it is clearly seen that the Helmholtz resonance frequency is unavoidable since in order to make it lower than 4 Hz or higher than 20 kHz, the duct length should be around 1000 m or 0.035 mm, respectively, which does not make sense in any case. We finally fixed the duct length as 0.2 mm since it is mechanically feasible and the Helmholtz resonance frequency is 8497 Hz, which is higher than the typically frequency measurement range. Despite this fact, care must be taken when measuring thin films, since this frequency range is typically needed.

The final values of the characteristic dimensions are shown in Table 3.II.

Table 3.II. PA cell dimensions.

L_g(mm)	ϕ_{cell}(mm)	y (mm)	ϕ_{duct}(mm)	l_{duct}(mm)
8.4	4.0	4.2	0.8	0.2

3.2.1.3 Design

Once the dimensions were calculated, we designed the whole body of the PA cell. As seen in Figure 3.6 (a) and (b), it is comprised of a PMMA parallelepiped, where the PA cavity is contained. The microphone cavity is drilled and connected perpendicularly to the PA cavity by means of the duct hole. In the top part of the cell there is a hollow where the window, also made of polished PMMA

(Figure 3.6 (c)), is placed to close the PA cavity. On the other hand, the bottom part of the cell is designed in such a way that the cell can be attached to a stage where the sample will be placed.

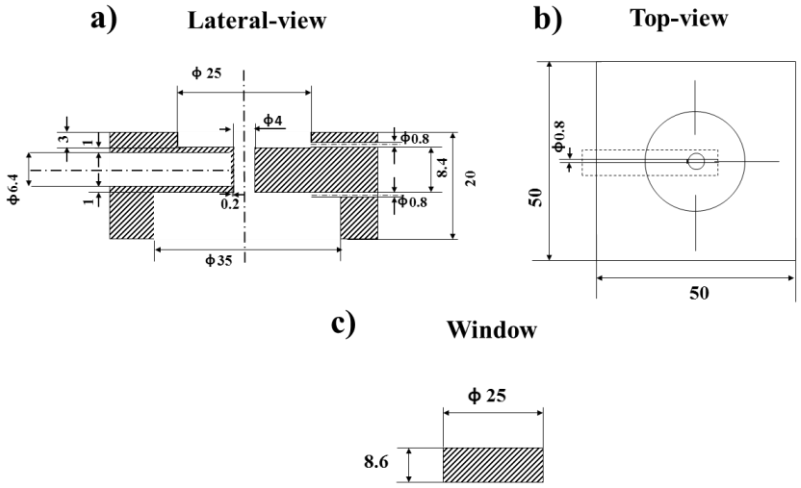

Figure 3.6. PA cell design with the selected dimensions and without the screws, (a) lateral-view, (b) top-view and (c) lateral view of the window. Dimensions are in mm.

The sketch of the lateral and top view of this backing material or stage is shown in Figure 3.7 (a) and (b), respectively. This piece must be thermally thick in terms of the experiment, i.e., its thickness should be higher than the thermal diffusion length. For that purpose, an aluminum block of 15 mm thick was selected which is thermally thick even for the lowest frequency. Aluminum is machined with little effort and provides the system with mechanical stability. The projection of this piece is used to place the sample and attach the PA cell. A hermetically seal is achieved by means of four screws which go through the PA cell and reach the stage where they are screwed. In order to attain a good and soft seal, a 6 mm in diameter O-ring is placed in the projection of the stage where the sample is placed. This O-ring will be especially useful when measuring brittle samples.

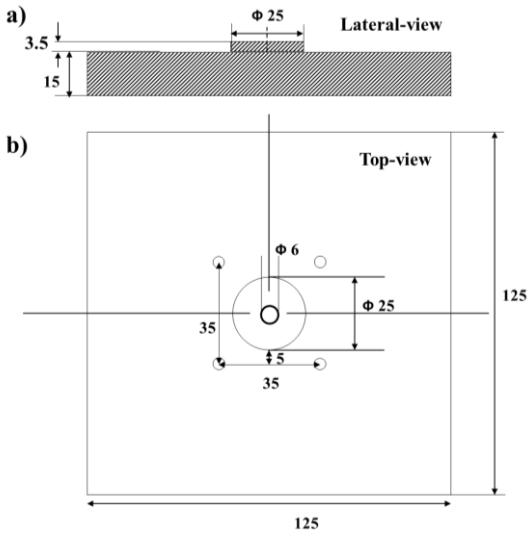

Figure 3.7. (a) Lateral-view and (b) top-view of the aluminum stage. Dimensions are in mm.

Figure 3.8 (a) and (b) show a 3D sketch of the stage or backing material and the PA cell, respectively. Figure 3.8 (c) and (d) show a schematic and a real image of the PA cell attached to the stage, respectively.

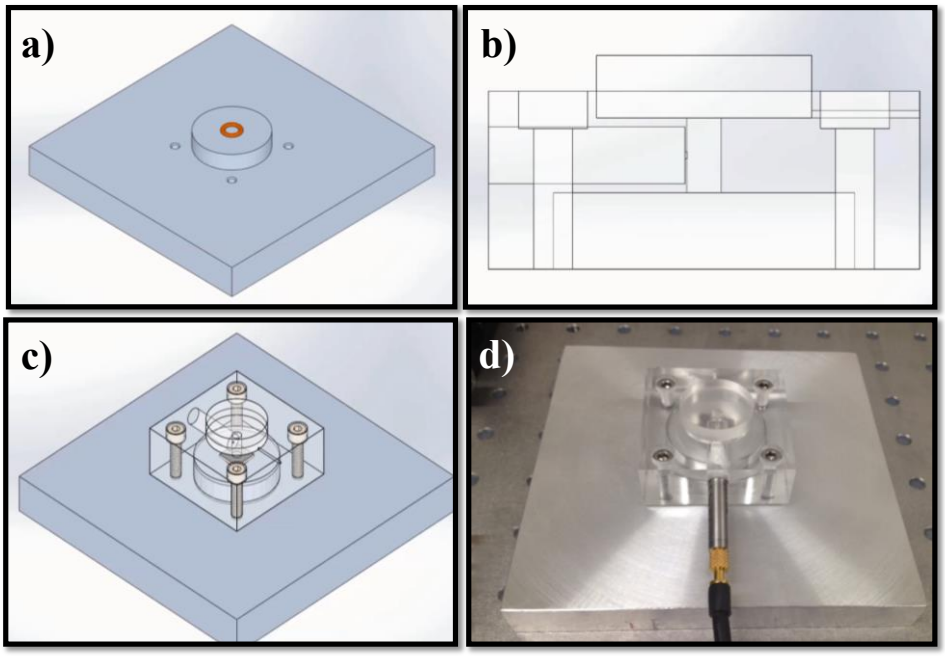

Figure 3.8. Schematic images of (a) stage, (b) PA cell and (c) PA cell attached to the stage and (d) a real image of the PA cell attached to the stage.

3.2.2 Microphone

A microphone is a device that converts sound into an electric signal. There are two microphone classifications depending on the transducer principle or the directionality.

Regarding the transducer principle, there are two types of microphones: dynamic and condenser microphones.

a) ***Dynamic microphones****:* the acoustic waves hit a thin plastic diaphragm and make it to vibrate. A coil of wire fixed to the back of the diaphragm vibrates along with it. When the coil moves back and forth, it passes across a magnetic field generated by a magnet, which produces an electrical signal that corresponds to the sound waves. This microphone is mostly used for loud sounds and it is not appropriate for high frequencies. Moreover, due to the magnet presence, it is difficult to make a very small dynamic microphone, which limits the mounting possibilities. Figure 3.9 (a) shows a schematic view of this type of microphone.
b) ***Condenser microphones****:* sound waves also strike a diaphragm and make it to vibrate. The diaphragm is fixed just in front of an electrically charged plate as shown in Figure 3.9 (b). As the diaphragm moves back and forth, the electric field between the diaphragm and the plate changes, which produces an electrical signal that corresponds to the acoustic waves. Since

there is no coil, the sound waves only have to move the diaphragm, which gives condenser microphones better performance at high frequencies.

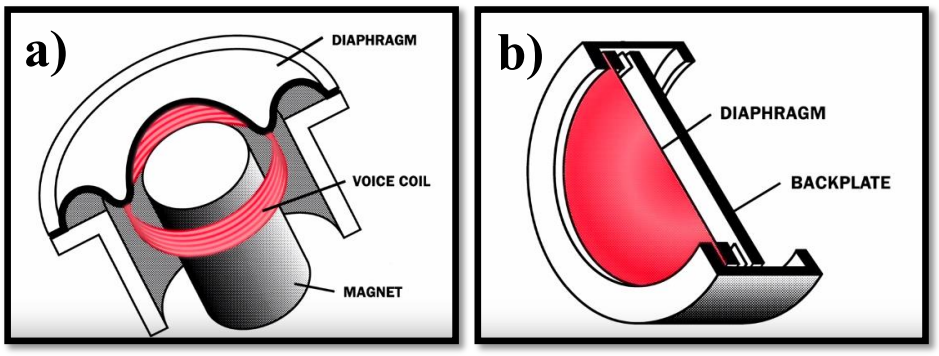

Figure 3.9. Classification of microphone as a function of the operating principle (a) Dynamic and (b) Condenser microphone. Image adapted from reference 11.

Depending on the directionality of the sound, there are three types of microphones as seen in Figure 3.10.

a) ***Free-Field****:* a free sound field is created when no objects perturb the acoustic waves. Free-fields can be achieved in anechoic rooms or outdoors far away from reflecting surfaces. The free-field microphone measures acoustic plane waves, which propagate in one direction. The best performance of free-field microphones is, then, achieved when the microphone is sufficiently far away from the acoustic source.

b) ***Pressure-Field:*** the sound pressure is measured just in front of the diaphragm which has the same phase and magnitude at any position within the field. It is frequently employed in cavities smaller than the wavelength of the acoustic wave in order to detect signals coming from a single source, which matches the PA experiment requirements.

c) ***Diffuse-Field:*** this type of microphone is also known as Random Incidence. It is omnidirectional so that it measures sound pressure coming from different sources, reflections and directions.

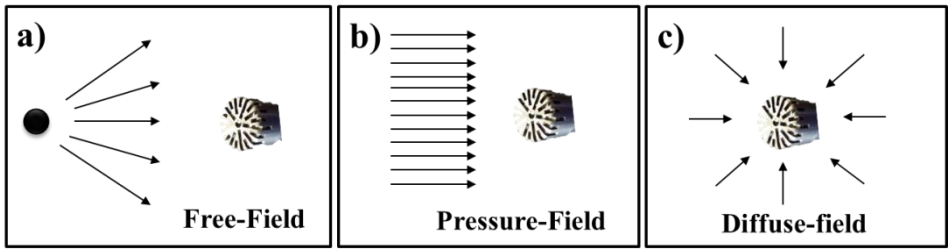

Figure 3.10. Different types of microphones depending on the directionality: (a) Free-field, (b) pressure-field and (c) Diffuse-field type.

Considering the characteristics of the different types of microphones, a *condenser pressure-field microphone* was selected. G.R.A.S Sound & Vibration 46BL ¼'' CCP pressure Microphone Set, composed of a ¼'' microphone Type 40BL and a ¼'' Preamplifier Type 26CB, which is shown in

Figure 3.11 (a) and (b), was chosen since it meets all the criteria imposed to the PA experiment, as explained below.

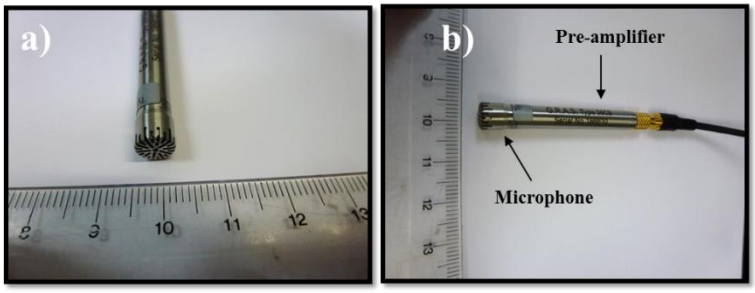

Figure 3.11. G.R.A.S. 46 BL ¼'' CCP Pressure microphone set employed in the PA setup (a) front view and (b) lateral view.

The microphone is depicted in Figure 3.12. A metal case covers a greatly tensioned diaphragm which is fixed parallel to an electrical insulator with a back-plate. These are the plates of the capacitor which generates the output voltage when the diaphragm is perturbed by the sound. The typical distance between the diaphragm and the back-plate is in the vicinity of 20 ± 0.8 μm, whereas the thickness of the diaphragm ranges from 1.5 to 8 μm depending on the microphone.

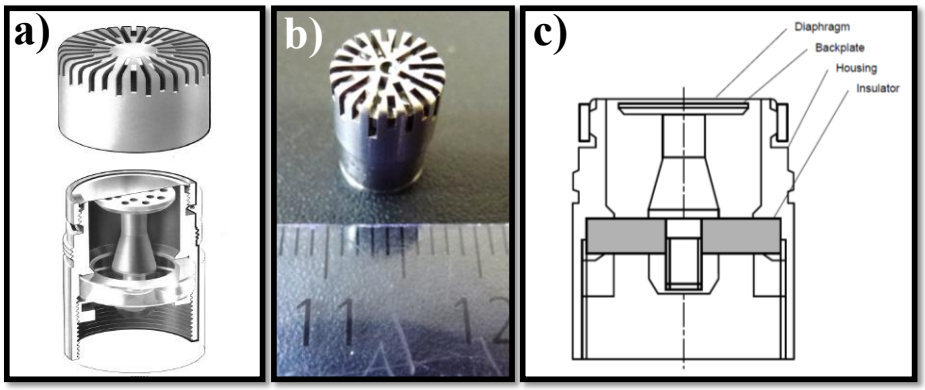

Figure 3.12. (a) Design (b) real image and (b) cross-section view of the condenser microphone.

For a good selection of the microphone and the preamplifier, the characteristics of both elements combined must be appropriated for a specific sound measurement so that one needs to make a compromise between the microphone size, sensitivity, frequency range, etc., which are normally entangled. The main characteristics when selecting the microphone are:

- **Dynamic range**: is the sound pressure level (SPL) range that the device is able to measure. The sound pressure level at a point indicates the instantaneous pressure, P, relative to a reference pressure of 20 μPa, P_{ref}.

$$L_P = 20log\frac{P}{P_{ref}} \tag{3.9}$$

The maximum limit of the dynamic range is given by the 3% distortion level caused by a displacement of the diaphragm. The minimum limit is related to the equivalent inherent noise level produced by the thermal agitation of the diaphragm.

- **Sensitivity**: SPL that the microphone is able to detect, which is expressed in millivolts per Pascal ($mV \cdot Pa^{-1}$). The higher the sensitivity is, the lower the SPL that can be detected.

- **Frequency response**: it is a measurement of the generated electrical signal produced by a sound in comparison to the signal at a reference frequency. A flat frequency response is desirable. However, it is limited at high and low frequencies depending on the microphone characteristics.

- **Temperature range**: temperatures at which the device is able to measure without signal distortion. High temperatures increase the inherent electronic noise which affects the lower limit of detection.

A preamplifier is still needed because the generated electrical signal is transferred to the lock-in amplifier and may not withstand along the cable if it is not amplified. A G.R.A.S constant current power (CCP) 26CB preamplifier connected to a CCP supply was used.

The specifications of the microphone combined with the preamplifier can be seen in Table 3.III. The microphone was selected due to its technical specifications. As the PA signal is expected to have a very low sound level, a high sensitivity and a wide dynamic range will ensure its detection.

Table 3.III. Microphone specifications.

Nominal sensitivity at 250Hz	18.0 $mV \cdot Pa^{-1}$
Frequency response: ±1dB	10 Hz – 10 kHz
Frequency response: ±2dB	4 Hz – 20 kHz
Dynamic Range	From: 25 dBA re. 20 μPa To: 150 dB re. 20 μPa
Temperature range	-30ºC to +60ºC

Moreover, the frequency response shown in Figure 3.13 is wide enough to measure many types of samples, from bulk materials to thin films while conserving the sensitivity. Finally, the temperature range allows the microphone to work at room temperature.

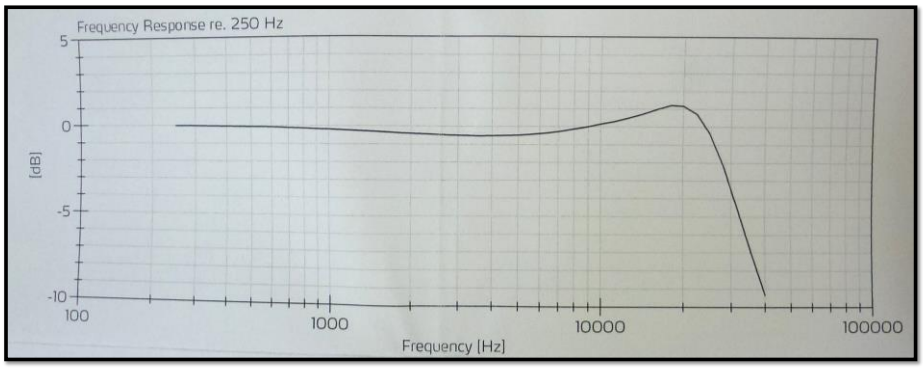

Figure 3.13. Calibration chart provided by G.R.A.S Sound & Vibration. Frequency response of the microphone and preamplifier combination. The frequency response is recorded by electrostatic actuator and is measured relative to the response at 250 Hz.

3.2.3 Laser

The modulated laser beam induces the thermal response of the surface sample in such a way that the acoustic waves are created. In this setup two different lasers were used for measuring at low and high frequencies.

- Low frequency regime: from 1 Hz to 4 kHz. The laser was a Fiber-Coupled laser diode with driver and TEC controller, model LDF-10 Series with a wavelength of 977 ± 5 nm.

- High frequency regime: from 4 kHz to 50 kHz. An Ytterbium fiber laser from IPG photonics was used with a wavelength of 1070 ± 5 nm.

Both devices own a built-in frequency generator which is modulated by the lock-in amplifier. Experiments are carrying out with a laser power of around 260 mW which is high enough to heat the samples.

3.2.3.1 Beam spot characterization

The radius of the beam is an important parameter in the heat transfer model, so its characterization becomes an essential step. In order to characterize the spot size, the knife-edge profiling technique was employed [12]. This method is depicted in Figure 3.14 (a). A laser beam is directed to a detector. A razor blade is mounted into a translational stage with a resolution of 500 μm which advances through the beam path and covers part of the beam. The power detected by the detector is related with the total power by the following expression,

$$P(x) = \frac{P_0}{2}\left(1 + erf\left(\frac{x\sqrt{2}}{\omega(z)}\right)\right) \tag{3.10}$$

where *erf(x)* is the error function, x is the razor blade position, $\omega(z)$ is the spot radius where the intensity has decayed by a factor e^2 and P_0 is the total power. From its derivative the Gaussian beam distribution can be obtained. The fiber-coupled laser diode has an approximately Gaussian intensity profile which follows,

$$I(r) = \frac{2A_0}{\pi\omega_0^2} exp\left(-\frac{2r^2}{\omega_0^2}\right) \tag{3.11}$$

where A_0 is the total power of the laser beam and ω_0 is $1/e^2$ beam radius. The $1/e^2$ beam radius is found to be 0.68 mm by fitting the experimental profile with these expressions (see Figure 3.14 (b) and (c)).

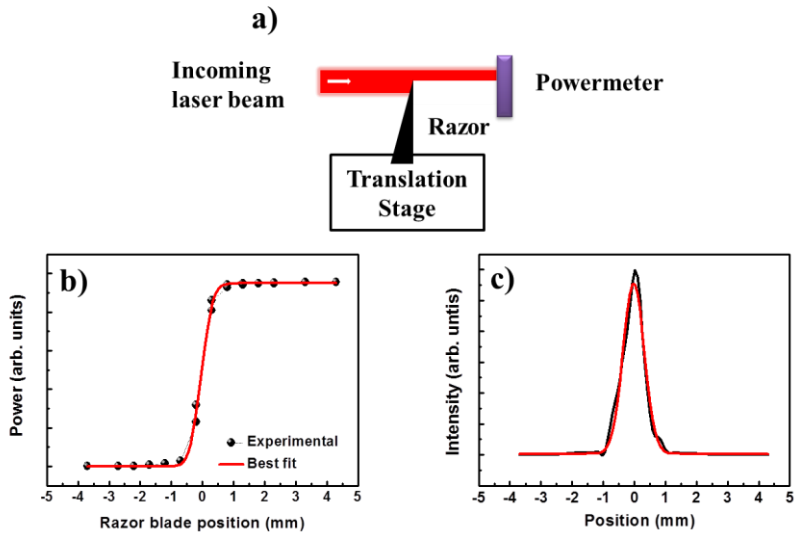

Figure 3.14. (a) Knife-edge measurement setup. Experimental data and best fit of (b) power detected and (c) derivative of error function. The spot $1/e^2$ radius is 0.68 mm.

It is worth noting that this method is a 1D measurement, so it does not take into account shape beam deviations. Diode lasers typically have elliptical beam shape. However, this effect can be neglected since the beam diameter variation between x and y directions is slight in comparison with the spot diameter and cell dimensions.

The same approach was carried out to analyze the spot size of the Ytterbium fiber laser.

3.2.4 Instrumentation

Apart from the microphone and the laser, there are other essential elements to carry out a good measurement. The electronics play an important role in the noise reduction. The electronic components used in this setup are: a signal conditioning and a lock-in amplifier.

3.2.4.1 Signal conditioning

The preamplifier increases the signal detected by the microphone. However, this signal can be still weak and is frequently affected by noise. In order to improve the quality of the acoustic signal before reaching the lock-in amplifier, a signal conditioning is introduced in the experimental setup. It enhances the operation and reliability of the measurement system with diverse functions from filtering to signal amplification. Moreover, this device is used as the power supply of the preamplifier.

In our experimental setup, a power module Type 12AQ from G.R.A.S Sound & Vibration was employed (see Figure 3.15) whose specifications can be seen in Table 3.IV.. It supplies a constant current supply (4mA) at 28 V DC to the preamplifier.

Table 3.IV. Specifications of the signal conditioning

Frequency response: ±0.1dB (gain from -20dB to 50dB)	10 Hz – 100 kHz
Frequency response: ±0.2dB (gain from -20dB to 50dB)	2 Hz – 200 kHz
Frequency response: ±0.1dB (gain from 60dB and 70dB)	10 Hz – 20 kHz
Lin filter	For linear response with a high-pass filter of 0.2 Hz
HP filter	For linear response with a high-pass filter of 20 Hz
AW filter	For an A-weighted response

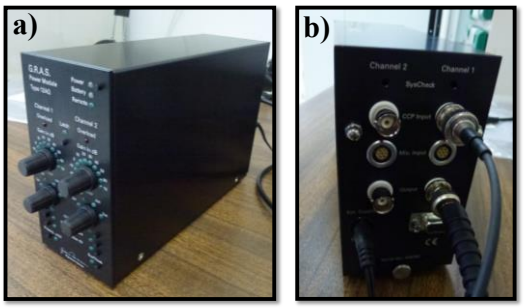

Figure 3.15. Power module Type 12AQ from G.R.A.S Sound & Vibration (a) Front panel and (b) rear panel.

3.2.4.2 Lock-in amplifier

Once the signal is amplified, it goes to the lock-in amplifier. Differentiating between the low PA signal and the background noise is one of the most challenging parts of the PA experiment. For that purpose, the lock-in amplifier is the perfect technique since it detects and measures very small AC signals. Moreover, these devices make use of the Phase-Sensitive-Detection (PSD) to isolate the signal component at a certain reference frequency from the background. Therefore, the lock-in amplifier is able to measure signals within a very narrow bandwidth.

The lock-in amplifier used in this work is a Signal Recovery model 7270. Specifications and operation modes of this device can be found in the user manual.

In order to achieve a measurement as stable as possible, lock-in amplifier parameters must be set carefully. The time constant of the output filters, which represents the time needed by the system to reach a value of (*1- 1/e)* factor (~ 63%) of its final value, is wisely selected depending on the working frequency. The time constant determines the Q-value of the lock-in amplifier which is given by $f_0/\Delta f$, where Δf is the bandwidth and f the working frequency. The Q-value is increased by increasing the time constant, which makes the output signal to be steadier and easier to measure. The experiments were performed with a time constant at least 25 times the inverse of the frequency, which ensures a good quality Q-value. Moreover, the low-pass filter is selected to be 24 dB/octave in order to achieve lower time constants for assuring stability.

3.2.5 Sources of noise

The PA experiment is affected by several sources of noise that should be taken into account and minimized as much as possible in order to have a good signal to noise ratio (SNR) [13]:

a) **Electrical noise***:* any random noise which has no phase relation with the modulation of the laser. Electrical noise includes the inherent noise of the microphone due to the thermal agitation of the diaphragm and limits the measurement to 25 dB. The input noise of the lock-in amplifier is 5 nV/$\sqrt{Hz}$. However, electrical noise normally has a wide frequency spectrum and can be filtered out by the phase sensitive detection (PSD) of the lock-in amplifier. In our case, the bandwidth depends on the time constant of the lock-in amplifier which is always selected to ensure an extremely narrow bandwidth. As explained above, the time constant is high enough to reduce the noise (at least 25 times the inverse of the reference frequency).

b) **Coherent acoustic background noise:** any noise contribution, not related to the light beam, which has exactly the same frequency as the reference. It can be avoided by increasing the laser intensity.

c) **Coherent photoacoustic background noise:** this contribution is related to the laser absorption by the window and the laser beam scattering produced by the cell walls and window. These two phenomena can create acoustic waves within the PA cavity that could disturb the PA signal. This noise contribution is greatly reduced by selecting the proper material as window (PMMA).

d) **1/f noise or "pink noise":** this contribution arises in many physical systems whose frequency spectrum is inversely related to the frequency and it is important at frequencies lower than 1 kHz [13, 14].

These error sources were minimized in order to have a high signal to noise ratio, which ensures the good quality of the measurements. SNR measurements were performed by measuring with and without laser radiation as a function of the frequency as shown in Figure 3.16 for both frequency regimes. The SNR value is obtained by,

$$SNR(dB) = 20log\frac{S}{N} \tag{3.12}$$

where S is the photoacoustic signal obtained when there is laser radiation and N the signal with the laser locked, i.e., the noise.

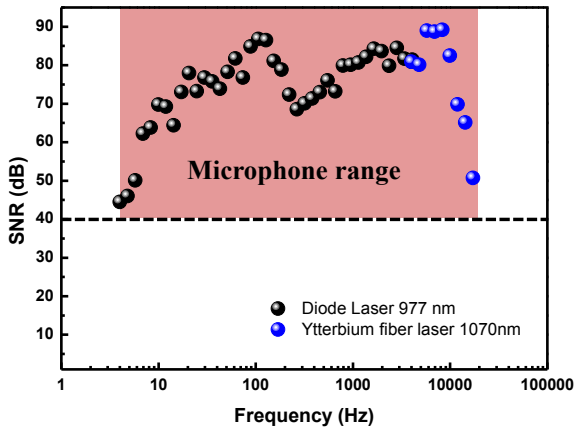

Figure 3.16. SNR as a function of the frequency for both lasers.

When all the above noise contributions were optimized, a SNR higher than 40 dB was obtained. Signal above this level can be considered as excellent. A frequency dependence can be found at frequencies lower than 1 kHz, due to the *1/f* noise of the electronic components [13]. At higher frequencies the SNR is optimum with a finally decay at very high frequencies due to the performance of the microphone. Even though, the performance of the experimental setup is excellent in the whole range of frequencies.

3.2.6 Temperature measurements

The acoustic signal is created by a periodically temperature increment of the sample surface due to the laser radiation. Temperature measurements were carried out in order to know the order of magnitude of this temperature rise. A T-type (copper-constantan) thermocouple made of wires with a diameter of 0.127 mm was positioned in contact with the surface of the sample very near to the laser beam to record the temperature. Figure 3.17 shows its variation as a function of the frequency for a laser power of 260 mW. The temperature increment created by the radiation is reduced when increasing the frequency. The temperature rise depends on the thermal conductivity of the sample,

thickness and laser frequency. This measurement was performed on bulk sample whose thermal conductivity is low, 1.4 $W \cdot m^{-1} \cdot K^{-1}$. For more (less) conductive samples, the temperature rise will be lower (higher).

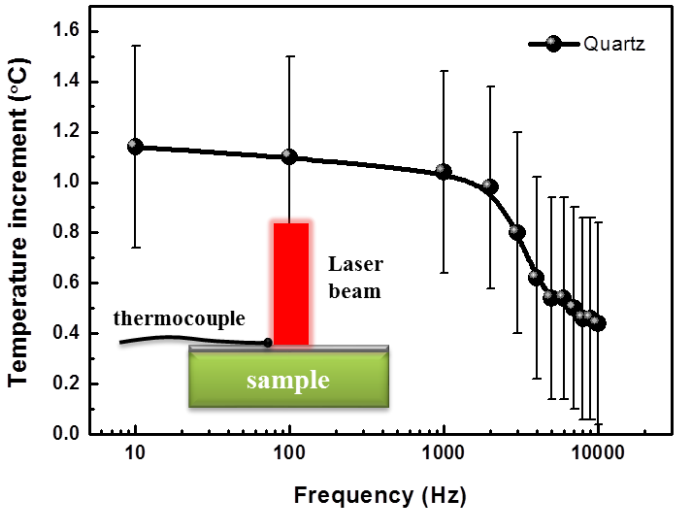

Figure 3.17. Temperature increment as a function of the laser frequency. The inset shows how the measurement is performed.

3.2.7 Stability and reproducibility

Once the experimental setup was developed, a deep study of the signal stability signal and reproducibility was carried out. A measurement is carrying out by sweeping a frequency range. The system must be found the steady state at each frequency after a certain time. This time depends on the time constant. Each measurement is thought so that the lock-in amplifier records the signal until 10 seconds after reaching the steady state. The mean average of the data store during this time is used to fit the theoretical model.

The stability of a measurement can be quantified as the relative variation of the amplitude and variation of the phase shift during the steady stage of each frequency. The amplitude variation is expressed as a percentage and is given by,

$$\Delta A(\%) = 100 \cdot \frac{(A_i - \bar{A})}{\bar{A}} \tag{3.13}$$

where A_i is every single point at a frequency and $\bar{A}$ is the mean amplitude for a frequency. Amplitude relative variations lower than 0.5 % are considered as stable measurement [15].

The phase variation is measured in degrees:

$$\Delta\varphi(deg) = \varphi_i - \bar{\varphi} \tag{3.14}$$

In this case, phase variations lower than 0.2 deg. are required for a high quality measurement [15].

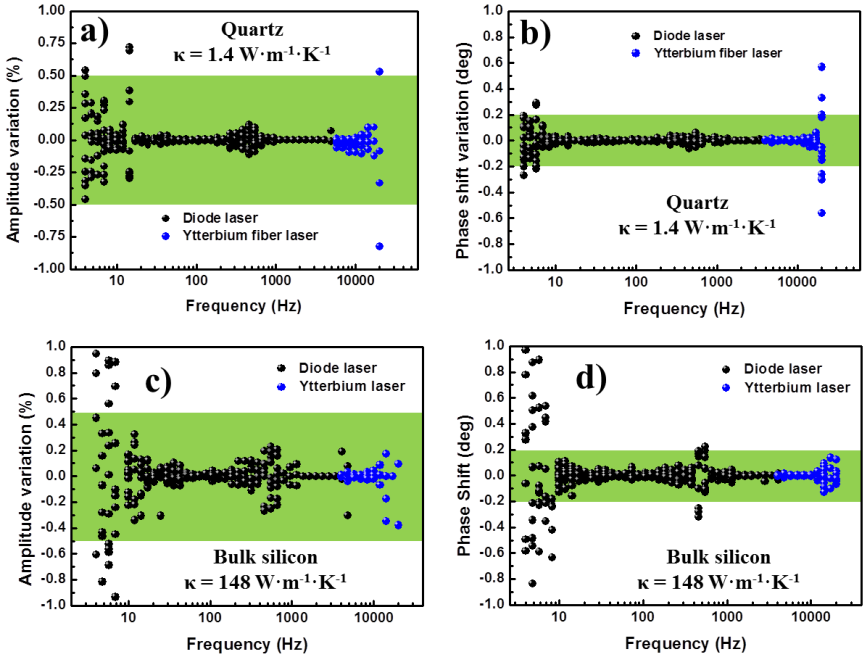

Figure 3.18. (a), (c) Amplitude and (b),(d) phase variations as a function of the frequency during the measurement of bulk quartz and silicon for both lasers.

As seen in Figure 3.18, amplitude and phase are found to be among the requirements for almost the whole frequency range. The green shadow depicts the allowed range for a good measurement. However, there are some wider variations in the extremes of the range, and therefore, caution must be taken when measuring at both frequency ranges. At very high frequencies (around 20 kHz), the microphone performance starts to decay while at low frequencies (around 4-10 Hz), 3D effects start to appear. Moreover, slight higher variations in the range from 100 to -1000 kHz can be also seen probably due to the *1/f* noise..

The reproducibility can be analyzed by the standard deviation between different measurements.

$$\sigma = \sqrt{\frac{1}{N-1}\sum_{i=1}^{N} (X_i - \bar{X})^2} \qquad (3.15)$$

In the case of the amplitude, it is necessary to calculate it as a percentage, so that the standard deviation is divided by the mean value at each frequency, which is known as coefficient of variation. A high quality measurement is established when the standard deviation is lower than 1 deg. and 5 % for the phase and the amplitude, respectively.

Figure 3.19 shows the amplitude and the phase coefficient of variation and standard deviation, respectively, of a low (quartz) and high conductive (silicon) sample as a function of the frequency. The quartz thermal diffusivity and conductivity are 7.9 10^{-7} $m^2 \cdot s^{-1}$ and 1.4 $W \cdot m^{-1} \cdot K^{-1}$, respectively. Silicon thermal diffusivity and conductivity are 8.9 10^{-5} $m^2 \cdot s^{-1}$ and 148 $W \cdot m^{-1} \cdot K^{-1}$, respectively. In the case of quartz, its amplitude standard deviation (Figure 3.19 (a)) is lower than 5% for the whole frequency range. Moreover, the phase shift standard deviation is lower than 1 deg. almost for the whole frequency range. For frequencies higher than 17 kHz, this value increases due to the rise in the instability during each measurement. In the case of silicon, the amplitude coefficient of variation remains lower than 5 % for almost all the frequency range (see Figure 3.19 (c)). In the case of frequencies higher than 10 kHz, this limit is overtaken probably due to the low heating level, as the amplitude signal decrease as f^{-1}. This behavior also occurs in the case of the phase shift standard deviation (see Figure 3.19 (d)).

It is worthy to note that highly conductive samples will have higher uncertainties than low conductive specimens.

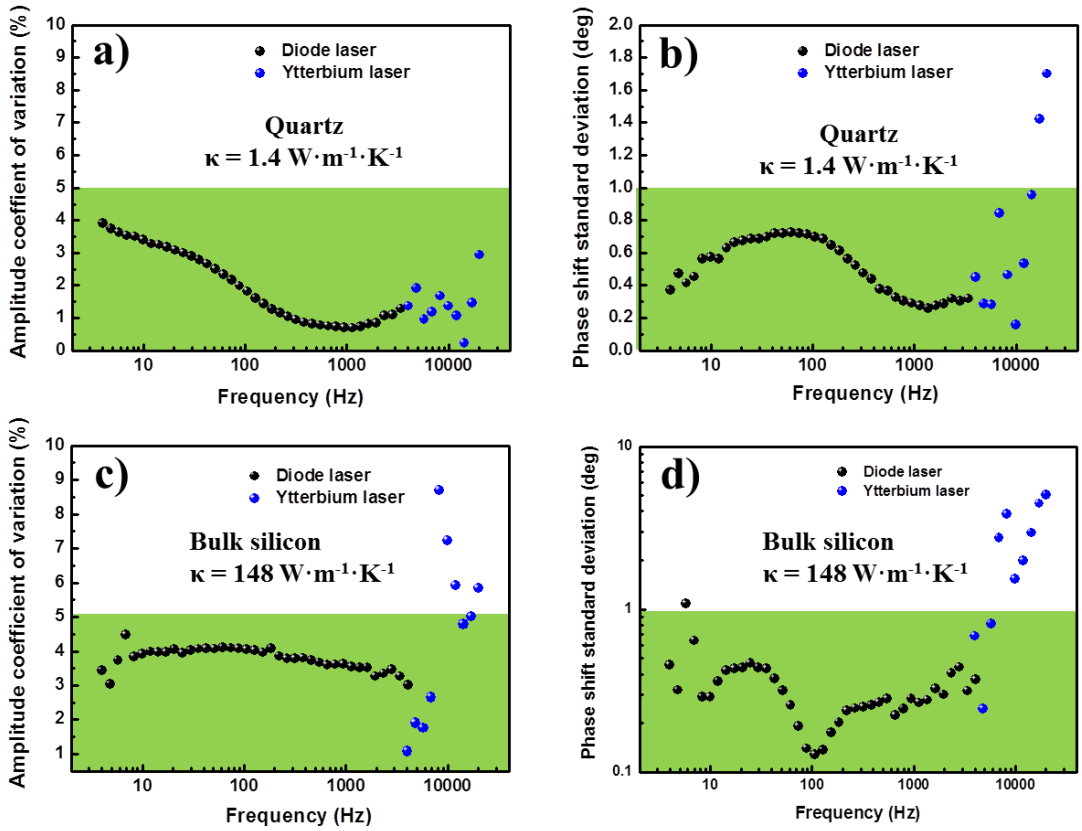

Figure 3.19. (a) and (c) Amplitude and (b) and (d) phase standard deviation as a function of the frequency for 4 different measurements for both lasers of two different bulk standard samples, quartz and silicon.

3.3 Theory and measurement procedure

There are different measurement procedures depending on the characteristics of the sample, as explained in the introduction part. The main difference lies in the number of layers of the sample, so that we distinguish between bulk samples and multilayered specimens.

In both cases, the magnitude to be analyzed is the phase shift between the reference radiation and the generated acoustic waves since the amplitude is affected by the reflectivity of the sample surface. Different normalization processes are carried out in order to remove the additional phase shift introduced by the delay associated with the electronics and the time that the acoustic waves take to reach the microphone (transfer function).

3.3.1 Bulk material

A variety of structures can be considered as a bulk material for this type of measurement: bulk materials themselves, nanowire arrays embedded in porous membranes or even the non-filled porous membranes.

The key idea of this measurement lies in the normalization process. In this case, two configurations are used: in front and rear configuration explained in chapter 2 and shown in Figure 3.20.

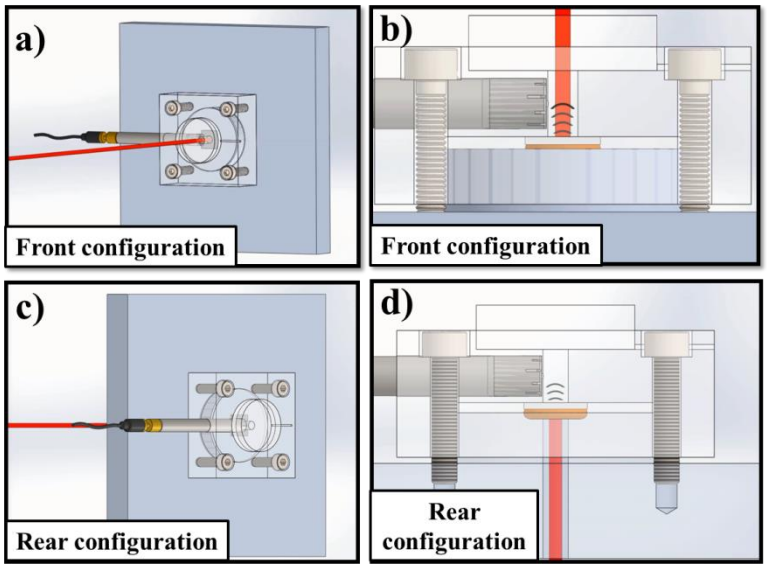

Figure 3.20. (a) Laser illumination and (b) acoustic waves generation in the front-configuration and (c) laser illumination and (d) acoustic waves generation in the rear-configuration.

3.3.1.1 Bulk theoretical model

The thermal diffusivity, α, of bulk materials can be determined by the well-known phase lag photoacoustic method. Considering a 1D heat diffusion model for a single layer, with a modulated heating and surface absorption, Balderas-López[16] described the normalized phase shift as,

$$tan(\Phi) = -tanh\left(\sqrt{\frac{\pi f}{\alpha}}l\right)tan\left(\sqrt{\frac{\pi f}{\alpha}}l\right) \tag{3.16}$$

where f is the modulation frequency and l is the thickness of the sample. Three different methodologies to extract the thermal diffusivity of solids can be derived from Eq. 3.16 depending on the range of the modulation frequency, i.e. the thermal regime established [17]. In order to establish the frequency range that comprises each thermal regime, it is necessary to estimate the critical frequency, f_c, (limit between thermally thick and thin regimes). It can be calculated by equalizing the thickness and the thermal diffusion length (Eq. 3.6) of a sample so that,

$$f_c = \frac{\alpha l^2}{\pi} \tag{3.17}$$

3.3.1.1.1 Low modulation frequency range ($f < f_c$)

The low modulation frequency range or the thermally thin regime is based on the series expansion of the functions hyperbolic tangent and tangent functions from Eq. (3.16). A linear behavior of the $tan(\Phi)$ as a function of the frequency is obtained, where Φ is the difference between the rear and front PA configurations phase shifts[17].

$$tan\left(\phi_{rear} - \phi_{front}\right) = tan(\Phi) \approx -x^2 = -\left(\frac{\pi}{\alpha}l^2\right)f \tag{3.18}$$

From the slope of the linear fitting of $tan(\Phi)$ vs. modulation frequency, the thermal diffusivity can be extracted.

3.3.1.1.2 High modulation frequency range ($f > f_c$)

In the high modulation range or thermally thick regime, the thermal diffusivity can be determined by the slope of the linear regression of the normalized phase shift on the root square of the frequency as,

$$\phi_{rear} - \phi_{front} = \Phi \approx -x = -\left(\sqrt{\frac{\pi}{\alpha}}l\right)\sqrt{f} \tag{3.19}$$

This expression is derived from Eq. 3.16 when $\sqrt{\frac{\pi f}{\alpha}}l \gg 1$ and it predicts that the normalized phase shift must be zero radians, when there is no laser modulation (*f = 0 Hz*). The proper modulation frequency can be found by taking this condition into account.

3.3.1.1.3 Tangent function discontinuities

As every tangent function has discontinuities, $tan(\Phi)$ in Eq. 3.16 also presents some discontinuities when,

$$\sqrt{\frac{\pi f}{\alpha}}l = \frac{\pi}{2}(2n+1) \tag{3.20}$$

where *n* is an integer number which can take values such as *n=0,1,2,3…* Therefore, $tan(\Phi)$ discontinuities will be found for,

$$\alpha_n = \frac{4fl^2}{\pi(2n+1)^2} \tag{3.21}$$

It is typically difficult to find experimentally more than one discontinuity, so the thermal diffusivity is normally extracted from the first discontinuity, *n = 0*, as:

$$\alpha = \frac{4f_1 l^2}{\pi} \tag{3.22}$$

where f_1 is the frequency which the first discontinuity appears at. The thermal diffusivity is derived from Eq. 3.22 by finding this frequency value.

We selected the high modulation frequency regime since it can be used to measure a wider range of samples since it allows the measurement of thicker samples than in the case of the low modulation frequency regime In order to ensure that we are measuring in the thermally thick regime, at least three times the critical frequency will be taken for the measurement [18]. Moreover, this regime also allows detecting the tangent discontinuity which serves as a doble-check procedure.

3.3.2 Multilayered structures measurement

Multilayered structures can be measured by normalizing with a bulk reference sample. Both samples are measured in front configuration as shown in Figure 3.20 (a). Figure 3.20 (b) shows a sketch of the generated acoustic waves when illuminating the surface of the sample.

The reference sample is a bulk sample (typically a piece of quartz) thick enough so that it is thermally thick for the whole range of frequencies that the setup is able to use. As Wang *et al* [15] explained, bulk materials have a frequency independent phase shift equal to -90 deg. Once both, the

reference and problem sample, are measured, the actual phase shift of the sample, ϕ_{sample}, is obtained as,

$$\phi_{sample} = \phi_{measured} - \phi_{reference} - 90 \tag{3.23}$$

where $\phi_{measured}$ and $\phi_{reference}$ are the measured phase shifts of the sample and the reference, respectively.

The model used to fit the data, which was developed by Hu *et al*,[19] considers a sinusoidal modulated monochromatic laser beam as a heat source. The light impinges directly onto the sample through the non-absorbing gas layer in contact with the sample surface. The sample consists in *N* layers whose indices extend from *1* to *N*. The air layer corresponds to *N+1* and the backing material is *0* and both of them are considered as thermally thick layers (see Figure 3.21).

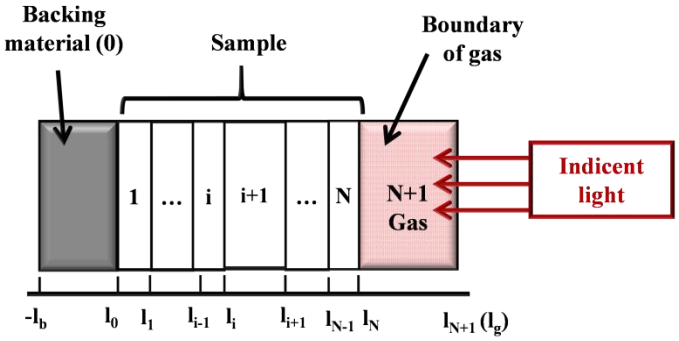

Figure 3. 21. Scheme of an N-layer sample.

The photoacoustic signal for this type of structures is derived by assuming a one dimensional model for the heat conduction, which is suitable provided that the thermal diffusion length in the air and in the sample is much smaller than the radius of the photoacoustic cell.[6] By solving the heat transfer equations applied to a multilayer sample, the transient temperature field could be derived:

$$\theta_{N+1} = (1-R)B_{N+1}e^{-\sigma_{N+1}x}e^{j\omega t} \tag{3.24}$$

where *R* is the reflectivity of the sample surface. The other terms are given by:

$$B_{N+1} = -\frac{[0 \quad 1]\cdot\sum_{m=0}^{N}\left(\prod_{i=0}^{m-1}U_i\right)\cdot V_m\cdot\begin{bmatrix}E_m\\E_{m+1}\end{bmatrix}}{[0 \quad 1]\cdot\left(\prod_{i=0}^{N}U_i\right)\cdot\begin{bmatrix}0\\1\end{bmatrix}} \tag{3.25}$$

$$U_i = \frac{1}{2}\begin{bmatrix}u_{11,i} & u_{12,i}\\ u_{21,i} & u_{22,i}\end{bmatrix};\ V_i = \frac{1}{2}\begin{bmatrix}v_{11,i} & v_{12,i}\\ v_{21,i} & v_{22,i}\end{bmatrix} \tag{3.26}$$

$$u_{1n,i} = \left(1 \pm \frac{\kappa_{i+1}\sigma_{i+1}}{\kappa_i\sigma_i} \mp \kappa_{i+1}\sigma_{i+1}R_{i,i+1}\right)\cdot exp(\mp\sigma_{i+1}l_{i+1}), n = 1,2; \tag{3.27}$$

$$u_{2n,i} = \left(1 \mp \frac{\kappa_{i+1}\sigma_{i+1}}{\kappa_i\sigma_i} \mp \kappa_{i+1}\sigma_{i+1}R_{i,i+1}\right) \cdot exp(\mp\sigma_{i+1}l_{i+1}), n = 1,2; \quad (3.28)$$

$$v_{n1,i} = 1 \pm \frac{\beta_i}{\sigma_i}, \quad n = 1,2; \quad (3.29)$$

$$v_{n2,i} = \left(-1 \mp \frac{\kappa_{i+1}\beta_{i+1}}{\kappa_i\sigma_i} + \kappa_{i+1}\beta_{i+1}R_{i,i+1}\right) \cdot exp(\beta_{i+1}l_{i+1}), \quad (3.30)$$

$$E_m = \frac{G_m}{\beta_m^2 - \sigma_m^2}; \quad (3.31)$$

$$G_m = \frac{\beta_m I_0}{2\kappa_m} e^{-\sum_{i=m+1}^{N}\beta_i l_i} \quad for\ m < N, \quad (3.32)$$

$$G_m = \frac{\beta_m I_0}{2\kappa_m} \quad for\ m = N, \quad G_m = 0 \quad for\ m = N+1 \quad (3.33)$$

where β_i is optical absorption coefficient, κ_i is the thermal conductivity, $R_{i,i+1}$ is the thermal contact resistance between the layer *i* and *i+1*, $a_i = \sqrt{\pi f/\alpha}$, is the thermal diffusion coefficient, $\sigma_i = (1 + j)a_j$ with $j = \sqrt{-1}$, α_i is the thermal diffusivity, f is the frequency modulation of the radiation, and I_0 is the incident monochromatic light flux. In the model, $l_{N+1} = 0$ and $\prod_{k=m}^{m-1} U_k$ is the unit matrix of size 2x2 and *m = 0,...,N+1*. According to *Hu et al*[19] and their generalized theory of the photoacoustic effect in a multilayer sample, both phase shift and amplitude of the photoacoustic signal are related with the temperature of the gas layer in contact with the surface of the sample so that the phase shift of the PA signal is given by the following equation:

$$Phase\ Shift = Arg(B_{N+1}) - \frac{\pi}{4} \quad (3.34)$$

Details of the complete calculation are given elsewhere.[19]

By fitting the measured ϕ_{sample} as a function of the frequency to the theoretical phase shift given by Eq. 3.34, the thermal conductivity of the unknown layer can be obtained. It is important to note that both thermal conductivity and diffusivity are included in the equations so that it is necessary to know both the density and specific heat in order to finally extract the thermal conductivity from the fitting.

3.3.2.1 Frequency simulations

The theoretical model above-mentioned will be useful provided that the frequency is low enough to make the heat go through all layers included.

By taking into account the thickness and properties of each layer, an optimum working frequency can be found, in which the phase shift measurement is more sensible. For that purpose, simulations of the phase shift given by Eq. 3.34 of a specific sample, as a function of a large frequency range are normally performed.

It is worthy to note, that the phase shift simulations are an approximation where all the properties have been taken as known. Therefore, variations from these calculations can occur in the experimental measurement.

3.4 Data analysis

3.4.1 Sensitivity

The sensitivity of a technique is the capability of measuring a specific parameter [18]. In this case the phase shift sensitivity is given by,

$$S_p = \frac{\partial \phi}{\partial p} p \tag{3.35}$$

where ϕ is the phase shift and p is the analyzed property. Here, the phase shift is calculated when the property is numerically varied by 1% and then normalized by the property in order to compare different properties. The sensitivity is used to choose the proper frequency range to perform an experiment.

3.4.2 Uncertainty analysis

Both density and specific heat are needed in order to finally extract the thermal conductivity of the analyzed sample for both measurement procedures, bulk and multilayered. Both magnitudes have measurement uncertainty which is calculated as the random error, E_r, within and 95% confidence interval for each sample since the random error was higher than other error sources:

$$E_{ran} = t_{n-1} \frac{\sigma}{\sqrt{n}} \tag{3.36}$$

where t_{n-1} is the Student-t distribution, n is the number of measurements, and σ is the standard deviation.

3.4.2.1 Bulk materials model

In the case of the high modulation frequency regime or thermally thick regime, the thermal diffusivity is extracted from the linear regression of the normalized phase shift as a function of the root

square frequency as given by Eq. 3.19. The thermal diffusivity uncertainty is thus calculated by the propagation of uncertainties from the expression,

$$\alpha = \frac{\pi}{m^2} l^2 \tag{3.37}$$

where α is the thermal diffusivity, m is the slope of the linear regression and l is the thickness of the sample. Therefore, the thermal diffusivity uncertainty is given by,

$$\Delta\alpha = \sqrt{\left(\frac{2l\pi}{m^2}\Delta l\right)^2 + \left(-\frac{2\pi l^2}{m^3}\Delta m\right)^2} \tag{3.38}$$

where Δl and Δm are the thickness and slope uncertainties, respectively. Several measurements are normally performed in order to improve the accuracy of the results, so a weighted average is finally carried out. The systematic error is included in uncertainty of the slope since the linear regression is performed by taking into account the instrumental errors. The uncertainty of the slope considers the uncertainty of the normalized phase shift, which in turn takes into account the phase shift uncertainty of both separately rear and front configuration measurements as,

$$\Delta\left(\phi_{rear} - \phi_{front}\right) = \sqrt{(\Delta\phi_{rear})^2 + \left(\Delta\phi_{front}\right)^2} \tag{3.39}$$

In the above expression, $\Delta\phi_{rear}$ and $\Delta\phi_{front}$ are the uncertainty values of the phase shift obtained during the rear and front measurements, respectively. $\Delta\phi_{rear} = \Delta\phi_{front} = 1$ deg so the uncertainty value associated with the phase shift difference is 1.4 deg

In the case of the tangent function discontinuity procedure, the uncertainty is given by the propagation of error of Eq. 3.22 as,

$$\Delta\alpha = \sqrt{\left(\frac{4l^2}{\pi}\Delta f_1\right)^2 + \left(\frac{8f_1 l}{\pi}\Delta l\right)^2} \tag{3.40}$$

where Δf_1depends on the frequency step selected for each measurement.

From the thermal diffusivity, the thermal conductivity is obtained by means of the density and specific heat so it is also necessary to take their associated uncertainties into account. The thermal conductivity is expressed by,

$$\kappa = \alpha\rho C_p \tag{3.41}$$

The uncertainty of the thermal conductivity is also obtained by calculating the error propagation.

$$\Delta\kappa = \sqrt{\left(\rho C_p \cdot \Delta\alpha\right)^2 + \left(\alpha C_p \cdot \Delta\rho\right)^2 + \left(\alpha\rho \cdot \Delta C_p\right)^2} \tag{3.42}$$

where $\Delta\rho$ and ΔC_p are the density and specific heat uncertainties.

It is worthy to note that the values of density and specific heat from the literature are frequently taken. Their uncertainty is taken as zero for those cases.

3.4.2.2 Multilayer model

The thermal conductivity measurement includes the random error, E_{ran}, the systematic error, E_{sist}, and those which arise from the density, specific heat and thickness of the samples are taken into account. The general expression used to quantify it is the following:

$$\Delta k = \sqrt{(E_{ran})^2 + (E_{sist})^2 + \left(k\frac{\Delta\rho}{\rho}\right)^2 + \left(k\frac{\Delta C_p}{C_p}\right)^2 + \left(k\frac{\Delta l}{l}\right)^2} \tag{3.43}$$

where E_{sist} is calculated by varying the experimental phase shift by ±1 deg and fitting again so that slightly different thermal conductivity values are derived. The difference between these values and the actual value obtained from the real experimental data is E_{sist}.

3.4.3 Post processing

3.4.3.1 Bulk material model

In the case of the high modulation frequency regime, from the relation between the normalized phase shift calculated from the front and rear measurements and the frequency, the thermal diffusivity is calculated by a simple linear regression. Since the intercept is equal to zero, it is necessary to check it experimentally otherwise that would be indicating a bad adhesion of the sample to the PA cell.

For the tangent function discontinuity, the procedure consists on finding the frequency of that discontinuity and applying Eq. 3.22.

3.4.3.2 Multilayer model

This phase shift described in section 3.3.2 depends on the properties of each layer and the interface resistances between them. As explained by Wang and colleagues [18], the fitting can be performed for several unknown properties. Nevertheless, the accuracy will be lower as the number of unknown properties is increased. We normally leave the thermal conductivity of the layer of interest along with the thermal contact resistance between this layer and the adjacent layers as unknown parameters.

The multiple parameter estimation from the model is carried out by means of the Levenberg-Marquardt (LM) nonlinear minimization algorithm which offers suitable accuracy and efficiency [18, 20]. The final values are greatly influenced by the initial guess values and the number of unknown parameters. Wang *et al.*[18] proved that the accuracy of the fitted values improves when the number of unknowns is lower than four.

The experimental data must be loaded as input files. Afterwards, the properties of the sample and reference are needed to get the solution of the equations. The properties of interest can be left as free parameters in the properties sample file and the initial guess values should be properly selected. The frequency range in which the phase shift is analyzed can be also selected. It is necessary to fix the number of layers of the sample to be fitted.

The software will provide different solutions along with the corresponding uncertainty per each parameter. The election of the most suitable solution depends on the sensitivity of that property in the selected frequency range and the physical sense.

3.5 Metal transducer

A transducer layer is deposited onto the surface of the samples in order to absorb the laser energy. Moreover, the metal transducer allows the sample and the reference to absorb the same amount of laser energy.[18] A good transducer must absorb as much energy as possible. For that purpose it must be optically opaque, i.e., the optical penetration length should be lower than the actual thickness of the layer. Different metal transducers were examined onto a silicon reference sample: aluminum, titanium and nickel. A thickness of 80nm was used in all the cases since it is higher than the optical penetration length. As seen in Figure 3.22, the PA signal when using titanium as a metal transducer is around 20 % and 40 % higher than that of the nickel and aluminum, respectively. A higher signal means a higher signal to noise ratio. For that reason, titanium was selected as the metal transducer. This metal has already been used in previous works [21].

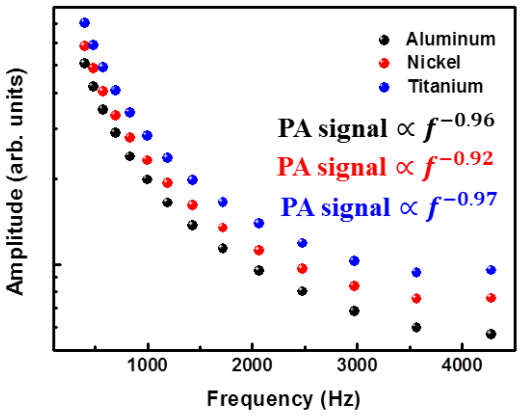

Figure 3.22. Amplitude comparison between aluminum, nickel and titanium as a metal transducer measured over a bulk silicon.

Regarding the values showed in Table 3.V, each of the three metal transducers deposited onto a bulk silicon match the case *optically opaque thermally thin solid* ($\mu_s \gg l; \mu_s \gg \mu_\beta$, where μ_s, l and μ_β are the thermal diffusion length, the thickness and the optical penetration length, respectively) proposed by Rosenwaig and Gersho [22].

Table 3.V. Optical penetration depth, reflectance and thermal diffusion length of three different metal transducers.

Metal transducer	**Optical penetration depth μ_β (nm) ~980nm**	**Reflectance (%) ~980nm**	**Thermal diffusion length μ_s (μm) f~ 400 Hz**
Titanium	26	59 [23]	86
Nickel	16	70	135
Aluminum	8	90 [23]	313

In this case, the PA signal is independent of the optical absorption coefficient and only depends on the thermal properties of the bulk material located under the metal transducer. Moreover, the PA signal theoretically varies as f^{-1} and the titanium measurements confirmed this tendency better than the other transducers, as can be seen in Figure 3.22. The PA signal is proportional to *(1-R)* being *R* the reflectivity of the material [15]. Therefore, the suitability of the titanium layer lies on its low reflectivity at our laser wavelengths (977 nm and 1070 nm) in comparison with the reflectivity of nickel and aluminum [23].

A SiO_2 thin film was also measured with aluminum and titanium as transducer layers and different results were obtained. Figure 3.23 (a) shows the amplitude of the acoustic signal as a function of the frequency and it can also be observed that aluminum transducers layer yields lower PA signal. Figure 3.23 (b) shows the normalized phase shift of SiO_2 as a function of the frequency for both

transducer layers and it is clearly seen how the trend is completely different and coherent results are obtained when using titanium due to its low reflectivity.

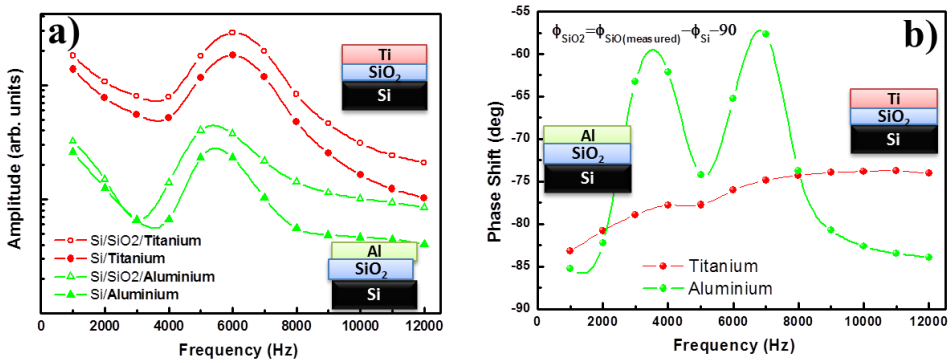

Figure 3.23. (a) Amplitude and (b) phase shift of a well-known 200 nm film sample (SiO_2) and a bulk reference sample (Si) metallized with 80 nm of two different metal transducers, titanium and aluminum.

The 80 nm titanium layer deposited on the sample surface was employed in order to absorb the radiation and convert it into heat by de-excitation processes in all types of samples, from transparent to opaque. The time needed by the heat waves to reach the bulk material under the titanium layer is given by,

$$\tau = \frac{l^2}{\alpha} \tag{3.44}$$

The thermal diffusivity of titanium is 9.3 $\cdot 10^{-6}$ $m^2 \cdot s^{-1}$, so $\tau = 0.7$ ns, which can be regarded as an instantaneous process, since the frequency range used to perform the experiments is much slower

3.6 Calibration

As a measurement technique, this setup must be checked periodically with standard samples in order to ensure the reproducibility and accuracy of the results. Moreover, it is necessary to ensure the proper operation of the PA system at various frequencies ranges. For that purpose, the samples shown in Table 3.VI are taken as calibration samples. From insulator, as a glass substrate, to highly conductive samples, like aluminum, and both bulk and multilayer samples were properly measured and used as reference samples. The standard deviation of the thermal diffusivity (bulk model) and the thermal conductivity (multilayered model) among different measurements in different periods of time was found to be low enough to ensure the precision of the system in all the cases. Further details about the measurements and the accuracy are given in Chapter 4 and Chapter 5 for bulk and multilayered samples, respectively.

Table 3.VI. Statistical summary of several measurements of different samples during different times

Sample	Model	Frequency range (Hz)	Mean value α ($m^2 \cdot s^{-1}$) κ ($W \cdot m^{-1} \cdot K^{-1}$)	Standard deviation
Smart membranes®	Bulk	60 - 250	$\alpha = (5.14 \pm 0.24)\ 10^{-7}$	$0.16 \cdot 10^{-7}$
Glass	Bulk	10 - 50	$\alpha = (4.48 \pm 0.24)\ 10^{-7}$	$0.22 \cdot 10^{-7}$
$CoSb_3$	Bulk	4 - 13	$\alpha = (1.92 \pm 0.10)\ 10^{-6}$	$0.18 \cdot 10^{-6}$
Sapphire	Bulk	15 - 100	$\alpha = (1.28 \pm 0.06)\ 10^{-5}$	$0.17 \cdot 10^{-5}$
Silicon	Bulk	200 - 400	$A = (8.28 \pm 0.46)\ 10^{-5}$	$0.42 \cdot 10^{-5}$
Aluminum	Bulk	100 - 500	$\alpha = (9.56 \pm 0.53)\ 10^{-5}$	$0.14 \cdot 10^{-5}$
Bi_2Te_3 film	Multilayered	400 – 4 k	$\kappa = 2.3 \pm 0.2$	0.12
298 nm SiO_2	Multilayered	1 k – 20 k	$\kappa = 1.46 \pm 0.15$	0.14
Smart membranes	Multilayered	10 - 100	$\kappa = 1.18 \pm 0.11$	0.02
PCDTBT	Multilayered	100 - 1000	$\kappa = 0.20 \pm 0.02$	0.02

The experimental setup was designed in order to make the measurements as reproducible as possible. However, there are some other factors that affect the measurement, apart from the sources of noise above discussed. The fixing of the sample in to the PA cell, the sealing of the PA cell to the sample, slightly changes in the relative position between the PA cell and the laser beam, among others, stand for the main error sources during the experiment which can explain measurement deviations.

For that reason, it is critically important to periodically check the reproducibility of the system in order to guarantee a high quality thermal properties result.

3.7 Detection limits

3.7.1 Bulk model

The main limitation of the PA technique is given by the thermal penetration of the heat waves. Since this method relies on not only the measurement in front-configuration but also in rear-configuration, there is a clear limitation regarding the thickness of the sample. Excessively thick samples will not be possible to measure since the heat waves could not propagate through the sample. No detectable acoustic waves are generated in the rear face when the thickness of the sample is larger than 3μ (being μ the thermal diffusion length, which depends on the frequency) [18]. As estimation, the measurable range can be calculated by taking into account that the lowest detectable frequency is 4 Hz. In order to be cautious we performed the limit calculations with a higher frequency, 10 Hz, so that 3D effects can be avoided. The maximum sample thickness is then given by:

$$l_{max} = 3\mu = 3\sqrt{\frac{\alpha}{10\pi}} \tag{3.45}$$

Figure 3.24 shows the measurement limits as a function of the thermal diffusivity and the thickness of the bulk sample. For instance, a sample with a thermal diffusivity value of 10^{-5} $m^2 \cdot s^{-1}$ must be lower than 1.7 mm. However, in order to measure low conductive samples the thickness must be much lower, in the range of hundreds of microns. The thickness is thus a critical parameter that should be rigorously measured.

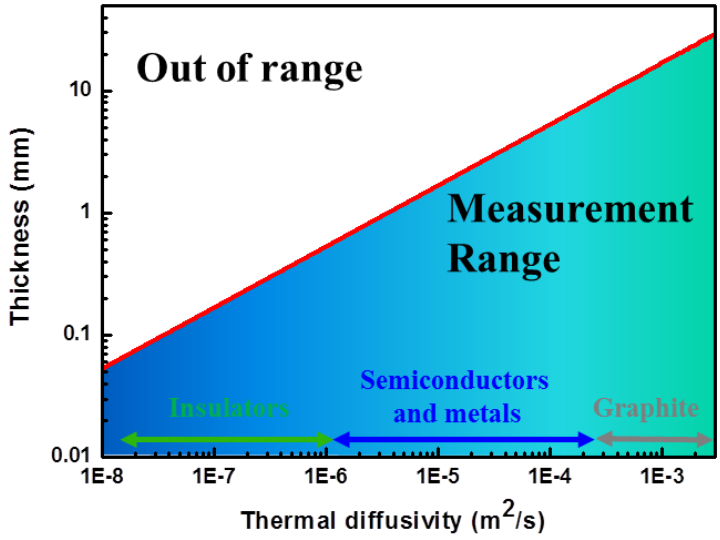

Figure 3.24. Measurement range in terms of thickness and thermal diffusivity for bulk samples by taking into account the microphone limit.

3.7.2 Multilayer model

There are different factors that can affect the photoacoustic experiment in the case of the multilayer model.

a) Film thickness

This method is limited when too thick or thin layers are investigated. Wang *et al.*[15] found a relation between the thickness, *l*, the thermal diffusion length, μ, and the associated thermal conductivity uncertainty for a phase shift uncertainty of ± 0.2 deg:

i) $\mu \sim 10\, l \rightarrow \Delta\kappa = \pm 5\%$ (see Figure 3.26 (a))

ii) $\mu \sim 100\, l \rightarrow \Delta\kappa = \pm 15\%$

iii) $\mu \sim 0.15\, l \rightarrow$ the bulk regime is reached. (see Figure 3.25 (c)). Heat waves only go through the layer under investigation so that it could be treated as a bulk material. Therefore, the phase shift does not contain information about the thermal properties and since it is equal to -90 deg.

However, the most accurate measurements are achieved when the thickness of the layer is in the order of the thermal diffusion length [15] (See Figure 3.25 (b)). For thicknesses much lower than the thermal diffusion length, the accuracy will be reduced. Therefore, there will be a limitation for thin and conductive samples. The limitation of the thickness is given by a reduction in the heating level when heating the sample.

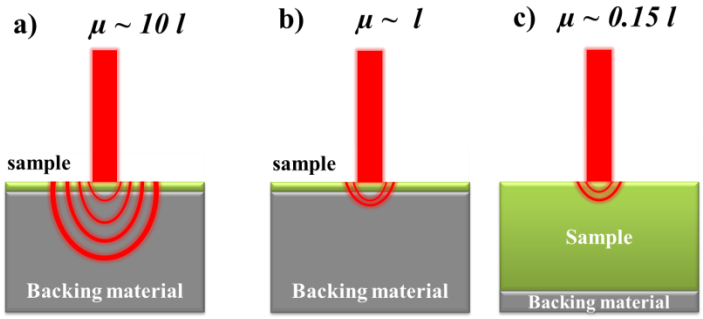

Figure 3.25. Thickness and thermal diffusion length relations which allows the estimation of the PA technique limits. (a) μ ~ 10 l (b) μ ~ l and (c) Bulk limit μ ~ 0.15.The red lines and curves depict the laser beam impinging on the surface of the sample and the heat waves, respectively.

In theory, extremely thin films could be measured if the modulated laser and the microphone could work at frequencies in the order of MHz, so that the thermal diffusion length would not be exceedingly larger than the thickness. In our case, the maximum operation frequency is 20 kHz so that we should established the limit for our experimental setup.

Table 3.VII. shows the thicknesses and thermal diffusivities of several samples used to establish the thickness limitation. The frequencies needed to accomplish the requirement established by Wang *et al.*[15] are calculated. Both, 200 nm SiO_2 and 500 nm $Si_{0.8}Ge_{0.2}$ films were found to be in the measurable frequency range and they were measured, indeed. Conversely, the frequency calculated to measure the gold layer resulted far away from our operation frequencies so that the measurement was unfeasible to be carried out.

Table 3.VII. Samples used to check the measurement limits.

Sample	Thickness (nm)	Thermal diffusivity ($m^2 \cdot s^{-1}$)	Frequency ($\mu = 10l$) (kHz)	Frequency ($\mu = 100l$) (kHz)	Measured
SiO_2	300	$8.3\ 10^{-7}$	29.5	0.3	✓
$Si_{0.8}Ge_{0.2}$	500	$7.3\ 10^{-7}$	9.3	0.09	✓
Au	150	$6.1\ 10^{-5}$ [24]*	8589	85.9	×

*A thermal conductivity reduction takes place in gold thin films. The values used to calculate that are $\kappa = 150\ W \cdot m^{-1} \cdot K^{-1}$, $\rho = 19300\ kg \cdot m^{-3}$ and $C_p = 128\ J \cdot kg^{-1} \cdot K^{-1}$.

As a general limitation condition, the minimum measurable thickness is given by:

$$l_{min} = \frac{1}{100}\sqrt{\frac{\alpha}{20000\pi}} \tag{3.46}$$

where the condition of $\mu \sim 100\ l$ and the limitation of the microphone to frequencies lower than 20 kHz was imposed.

On the other hand, the maximum thickness which can be detected and measured by using the multilayered model is related to the relation $\mu \sim 0.15\ l$ and the minimum frequency of the microphone, taken 10 Hz as in the previous case.

$$l_{max} = \frac{1}{0.15}\sqrt{\frac{\alpha}{10\pi}} \tag{3.47}$$

Figure 3.26 shows the relation between the thermal diffusivity and the minimum and maximum thickness that PA technique is able to analyze. The dark blue line depicts the minimum thickness given by Eq. 3.46 which has an uncertainty of ± 15% in the thermal conductivity determination. The grey line represents the minimum thickness which allows obtaining a thermal conductivity value with a lower uncertainty, ± 5%. Finally, the light blue line depicts the maximum thickness possible to be measured, given by Eq. 3.47. For instance, the minimum thickness required to measure a gold thin film (α = 6.1 10^{-5} $m^2 \cdot s^{-1}$ [24]) is 307 nm and 3070 nm for an uncertainty of ±15% or ±5%, respectively. Conversely, the maximum thickness would be found to be 9630 µm.

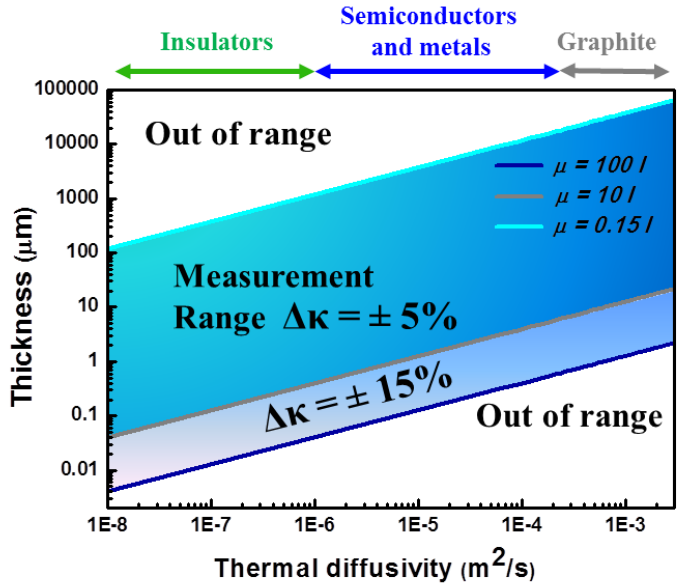

Figure 3.26. Measurement range in terms of thickness and thermal diffusivity by taking into account the microphone limit (10 Hz < f < 20 kHz) and the limitation conditions.

b) Substrate

As shown above, films can be measured if they are thin enough to allow the heat waves to reach the substrate. Thin films are normally deposited onto substrates that are properly selected to

achieve a good quality film deposition. However, there is a limitation when measuring the thermal properties of these structures by the PA technique.

When the film and backing material thermal diffusivity values are similar and the thermal contact resistance between both of them is low enough, the technique is not able to differentiate between the film and the substrate so that the thermal response behavior is the same as that of a bulk sample, and hence, no information is obtained from the phase shift analysis, which is ideally -90 deg.

Table 3.VIII. shows the thermal properties of different materials that can act as layer and substrate so that we can select the combinations that accomplish the limitation condition and check it.

Table 3.VIII. Density, specific heat, thermal conductivity and thermal diffusivity of different materials.

Material	**Density ($kg \cdot m^{-3}$)**	**Specific heat C_p ($J \cdot kg^{-1} \cdot K^{-1}$)**	**Thermal conductivity ($W \cdot m^{-1} \cdot K^{-1}$)**	**Thermal diffusivity($m^2 \cdot s^{-1}$)**
Glass	2520	500	1.1	$5.0\ 10^{-7}$
Sapphire	3970	750	42	$1.4\ 10^{-5}$
Chromium	7190	460	93.9	$2.8\ 10^{-5}$
$Si_{0.8}Ge_{0.2}$	3000	546	1.2	$7.3\ 10^{-7}$
Niobium	8570	265	53.7	$2.4\ 10^{-7}$
Ag_2Se	8216	278	~1.1	$\sim 5.0\ 10^{-7}$

We studied the influence of a 300 nm chromium layer over a glass, a sapphire and a niobium substrate by assuming a low thermal contact resistance between the film and the substrate (10^{-4} $mm^2 \cdot W \cdot K^{-1}$). The thermal diffusivity of chromium, niobium, sapphire and glass can be seen in Table 3.VIII. The thermal diffusivity differences between chromium and the different substrates are 14 %, 50 % and 97 %, respectively. Figure 3.27 shows a nearly constant phase shift of -90 deg when niobium and sapphire are used as substrates. However, the phase shift given by the chromium layer over the glass substrate shows a different behavior. In this case, the contrast between the thermal diffusivity values is high enough to obtain a thermal response different than that of a bulk sample.

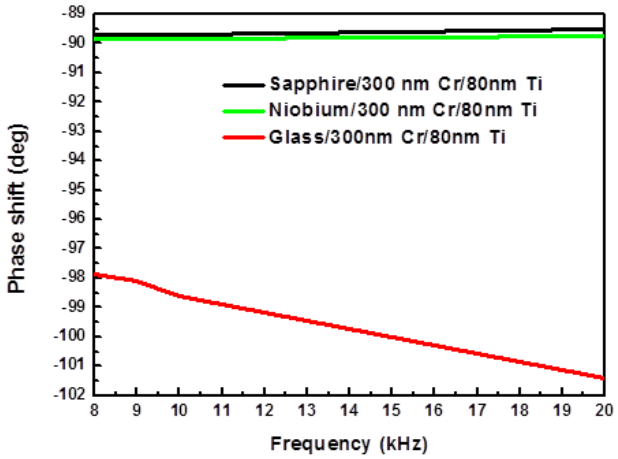

Figure 3.27. Phase shift as a function of the frequency modulation of (a) 300 nm Cr/nickel and (b) 300 nm Cr/sapphire. The theoretical phase shift of a bulk material is -90 deg.

Secondly, this phenomenon was experimentally studied. Sputtering was employed to study the influence of the thermal properties of the film and substrate. The thermal contact resistance between the film and the substrate can be also considered as negligible. In this case, two different semiconductor samples were studied over glass substrates.

500 nm $Si_{0.8}Ge_{0.2}$/glass

The thermal diffusivity of $Si_{0.8}Ge_{0.2}$ and glass are 7.3 10^{-7} $m^2 \cdot s^{-1}$ and 5.0 10^{-7} $m^2 \cdot s^{-1}$, respectively. The difference between them is around 46 %. Figure 1.28 (a) shows how the phase shift has a constant value in the vicinity of -90 deg when increasing the modulation frequency, which is the typical behavior of a bulk layer.

383.5 nm Ag_2Se/glass

The thermal diffusivity of glass is 5.0 10^{-7} $m^2 \cdot s^{-1}$ and the thermal diffusivity of the Ag_2Se film is unknown. Figure 3.29 (b) shows a bulk behavior, which is not possible even at high frequencies since it is an extremely thin layer. The explanation of such a bulk behavior can be found again in the similitude between the thermal diffusivity of the layer and the substrate. If we assume that approximation, we can estimate the thermal diffusivity of the layer to be the same as the glass substrate, i.e., 5.0 10^{-7} $m^2 \cdot s^{-1}$. From this value, an estimated thermal conductivity of the Ag_2Se film of 1.1 $W \cdot m^{-1} \cdot K^{-1}$ can be extracted by using the density and specific heat values of Table 3.VIII. This value is only estimation since it has at least an uncertainty of 50%, which is deduced from the case of $Si_{0.8}Ge_{0.2}$.

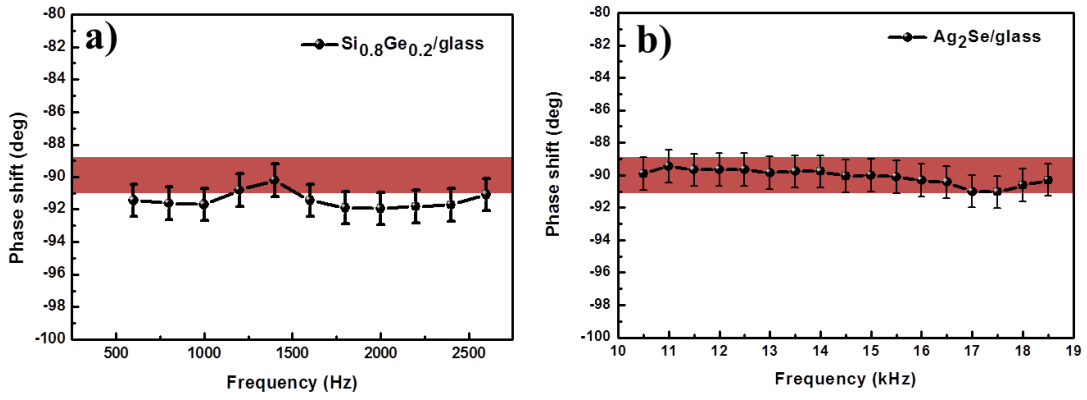

Figure 3.28. Phase shift as a function of the frequency modulation of (a) Si0.8Ge0.2 onto a glass substrate and (b) Ag_2Se onto a glass substrate. The theoretical phase shift of a bulk material is -90 deg. The red shadow depicts an uncertainty of ±1 deg for this value.

As a conclusion, the highest resolution is achieved when the thermal diffusivity of both, the film and the substrate, is as different as possible (at least higher than 50 %).

c) Thermal contact resistance

Hu *et al.*[19] found that the thermal conductivity and thermal contact resistances can be fitted at the same time since both of them influence separately the computational calculation. Conversely, there is a clear limitation of the PA technique when measuring the thermal conductivity of a layer located under a high thermal contact resistance with the upper layer. The sensitivity of the thermal properties of the analyzed layer is really low when this thermal contact resistance is considerably high (>10 $mm^2 \cdot K \cdot W^{-1}$). In our measurements, the layer of interest is typically located under the titanium layer. The thermal contact resistance between the layer under study and the titanium is normally low enough (< 0.01 $mm^2 \cdot K \cdot W^{-1}$)[15] to ensure a good sensitivity ince the deposition method (electron beam evaporation) ensures a good adhesion of the titanium to the sample.

3.8 Summary

In the first part of the chapter the experimental design of the photoacoustic experimental setup was discussed. The PA cavity dimensions were calculated by taking into account different phenomena that can influence the experiment, such as acoustic resonances, acoustic attenuation, 3D effects in the heat conduction or mechanical feasibility. A value of 1.4 mm was optimized for the beam spot diameter by the knife-edge profiling technique which allows 3D effects to be avoided in a PA cavity with a 4 mm radius. The election of the microphone was also discussed as well as the lock-in amplifier and lock-in operating conditions.

Error sources were discussed and minimized as much as possible. Moreover, stability and reproducibility studies were performed in order to show a reliable performance of the system which is able to take measurements with a standard deviation lower than 0.2 deg and 1% for the phase shift and the amplitude, respectively. The measurement procedure was also discussed for both bulk and multilayer models. Uncertainties associated with both procedures were calculated, takings into account both instrumental and random errors.

In addition, different metal transducers were studied. Titanium was demonstrated to be the most suitable transducer since its reflectivity is lower than that of other metals and hence, the PA signal is improved.

The detection limits were established for both methods and summarized in Figure 3.30. They depend on both, the thermal diffusivity and the thickness of the analyzed sample. In the case of the bulk model, as the thermal diffusivity is decreased, the sample must be thinner than more conductive samples. Conversely, for multilayered materials, a minimum and maximum thickness can be found which also depends on the thermal diffusivity of the sample.

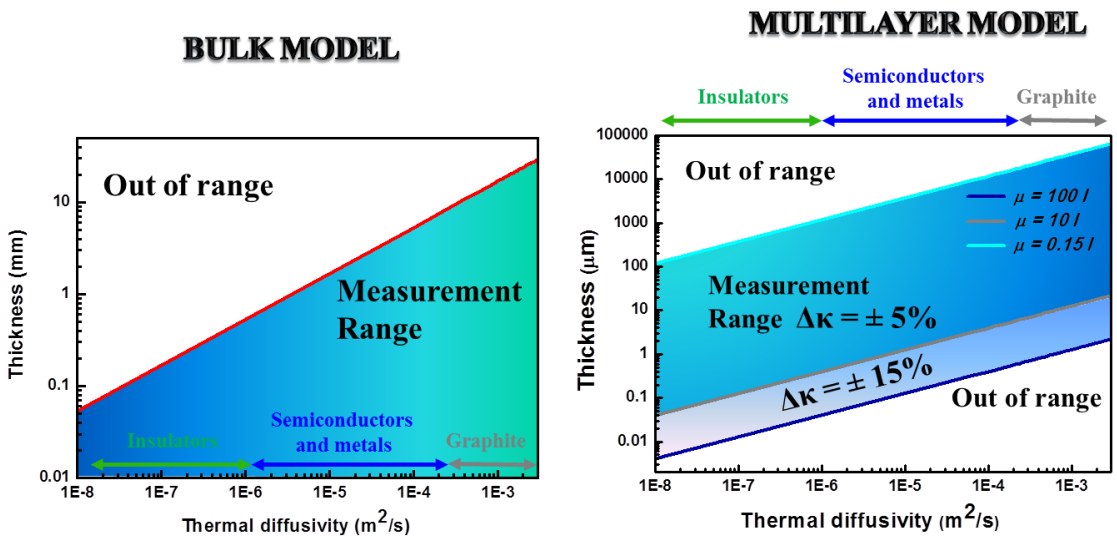

A substrate limitation has been also pointed out in the case of film measurements with a low thermal contact resistance between them. The values of the thermal diffusivity of the substrate and the thin film should differ by at least 50 %. Otherwise, the system would behave as a bulk material and a constant dependency of the phase shift with the frequency would be found, i.e., no thermal information would be obtained.

3.9 References

1. Rosencwaig, A., Photoacoustic spectroscopy of solids. *Physics Today* **1975,** *28*, 23-30.
2. Zidan, H. M.; Abu-Elnader, M., Structural and optical properties of pure PMMA and metal chloride-doped PMMA films. *Physica B: Condensed Matter* **2005,** *355*, 308-317.
3. Cirino, G.; Arruda, A.; Mansano, R.; Verdonck, P.; Neto, L. In *Fabrication of PMMA microlenses using a micromachined silicon mould*, Proceedings—Electrochemical Society, 2002; 2002; pp 188-195.
4. Lide, D. R., CRC Handbook of Chemistry and Physics. In Press, C., Ed. Boca Raton, 2005.
5. Morse, P. M., Vibration and sound. In McGraw-Hill Book Company, Inc: New York, Toronto, London, 1948.
6. Quimby, R. S.; Yen, W. M., On the adequacy of one dimensional treatments of the photoacoustic effect. *Journal of Applied Physics* **1980,** *51*, 1252-1253.
7. Shen, J.; Mandelis, A., Thermal-wave resonator cavity. *Review of Scientific Instruments* **1995,** *66*, 4999-5005.
8. Bass, H. E.; Sutherland, L. C.; Zuckerwar, A. J., Atmospheric absorption of sound: Update. *The Journal of the Acoustical Society of America* **1990,** *88*, 2019-2021.
9. Bass, H. E.; Sutherland, L. C.; Zuckerwar, A. J.; Blackstock, D. T.; Hester, D. M., Atmospheric absorption of sound: Further developments. *The Journal of the Acoustical Society of America* **1995,** *97*, 680-683.
10. Benedetto, G.; Maringelli, M.; Spagnolo, R., Method for the absolute calibration of photoacoustic cells. *Review of Scientific Instruments* **1987,** *58*, 975-978.
11. http://lions-wing.net/YHS/sound-tech.html
12. Ok, G.; Choi, S.-W.; Park, K. H.; Chun, H. S., Foreign object detection by sub-terahertz quasi-Bessel beam imaging. *Sensors* **2012,** *13*, 71-85.
13. Dumitras, D. C.; Dutu, D. C.; Matei, C.; Magureanu, A. M.; Petrus, M.; Popa, C., Laser photoacoustic spectroscopy: Principles, instrumentation, and characterization. *Journal of Optoelectronics and Advanced Materials* **2007,** *9*, 3655-3701.
14. Bak, P.; Tang, C.; Wiesenfeld, K., Self-organized criticality: An explanation of the 1/f noise. *Physical Review Letters* **1987,** *59*, 381-384.
15. Wang, X.; Hu, H.; Xu, X., Photo-Acoustic Measurement of Thermal Conductivity of Thin Films and Bulk Materials. *Journal of Heat Transfer* **2000,** *123*, 138-144.
16. Balderas-López, J. A.; Mandelis, A., Self-normalized photothermal technique for accurate thermal diffusivity measurements in thin metal layers. *Review of Scientific Instruments* **2003,** *74*, 5219-5225.
17. Balderas-López, J. A., Self-normalized photoacoustic techniques for thermal diffusivity measurements in metals. *Revista mexicana de física* **2004,** *50*, 120-126.
18. Wang, X.; Cola, B. A.; Bougher, T. L.; Hodson, S. L.; Fisher, T. S.; Xu, X., Photoacoustic technique for thermal conductivity and thermal interface measurements. *Annual Review of Heat Transfer* **2013,** *16*.
19. Hu, H.; Wang, X.; Xu, X., Generalized theory of the photoacoustic effect in a multilayer material. *Journal of Applied Physics* **1999,** *86*, 3953-3958.
20. Press, W. H.; Teukolsky, S. A.; Vetterling, W. T.; Flannery, B. P., *Numerical Recipes 3rd Edition: The Art of Scientific Computing*. Cambridge University Press: 2007; p 1256.
21. Cola, B. A.; Xu, J.; Cheng, C.; Xu, X.; Fisher, T. S.; Hu, H., Photoacoustic characterization of carbon nanotube array thermal interfaces. *Journal of Applied Physics* **2007,** *101*, 054313-9.
22. Rosencwaig, A.; Gersho, A., Theory of the photoacoustic effect with solids. *Journal of Applied Physics* **1976,** *47*, 64-69.
23. Bates, S. C., Low mass, low power, low cost space furnace. *SBIR Phase I Final Report-NASA Marshall Space Flight Center-Contract NAS8-99040* **1999**.
24. Wilson, A. A.; Munoz Rojo, M.; Abad, B.; Perez, J. A.; Maiz, J.; Schomacker, J.; Martin-Gonzalez, M.; Borca-Tasciuc, D.-A.; Borca-Tasciuc, T., Thermal conductivity measurements of high and low thermal conductivity films using a scanning hot probe method in the 3ω mode and novel calibration strategies. *Nanoscale* **2015,** *7*, 15404-15412.

Chapter 4:

Thermal diffusivity measurements of bulk materials

In this chapter, the experimental setup for measuring bulk materials is proved. For that purpose, six different samples with a wide range of thermal diffusivity values are measured by two different procedures. From those measurements, a study of the uncertainty and deviation is performed. Once the system is found to work properly, the thermal properties as well as the power factor of an inorganic material, zinc oxide doped with nickel oxide, and an organic material, polyaniline blended with graphene nanoplatelets are studied.

4.1 Reference samples

In order to ensure a reliable performance of the experimental setup and the good agreement with the theory explained in Chapter 3, six reference bulk samples with a wide range of thermal diffusivity values were measured. The characterization of their thermal diffusivity was carried out by two different procedures: i) exploring the normalized phase shift as a function of the root square frequency explained in Section 3.3.1.1.2 and ii) inspecting the frequency at which discontinuities of the tangent of the normalized phase shift are found which serves to calculate the thermal diffusivity as shown in Section 3.3.1.1.3. These analyses were performed when measuring in both front and rear configurations. The low modulation frequency range is not used since there is a harder restriction in the thickness of the sample when measuring low thermally conductive samples..

Figure 4.1 shows an example of the normalized phase shift data as a function of the square root of the frequency along with the best fitting for the six references. In order to ensure that the data considered is in the proper frequency range, a criterion for data selection, , is to select only the data points which yield a linear trend with an intercept of ~0.[1] The data fitting is carried out in the thermally thick regime, in all cases, as predicted by Balderas-López *et al.* [1]. The R^2 values show a good linear fitting for the six reference samples. Moreover, the intercept values are found to be near zero, in most cases, which indicates a good agreement between the frequency ranges selected and the theory used to extract the thermal diffusivity values.

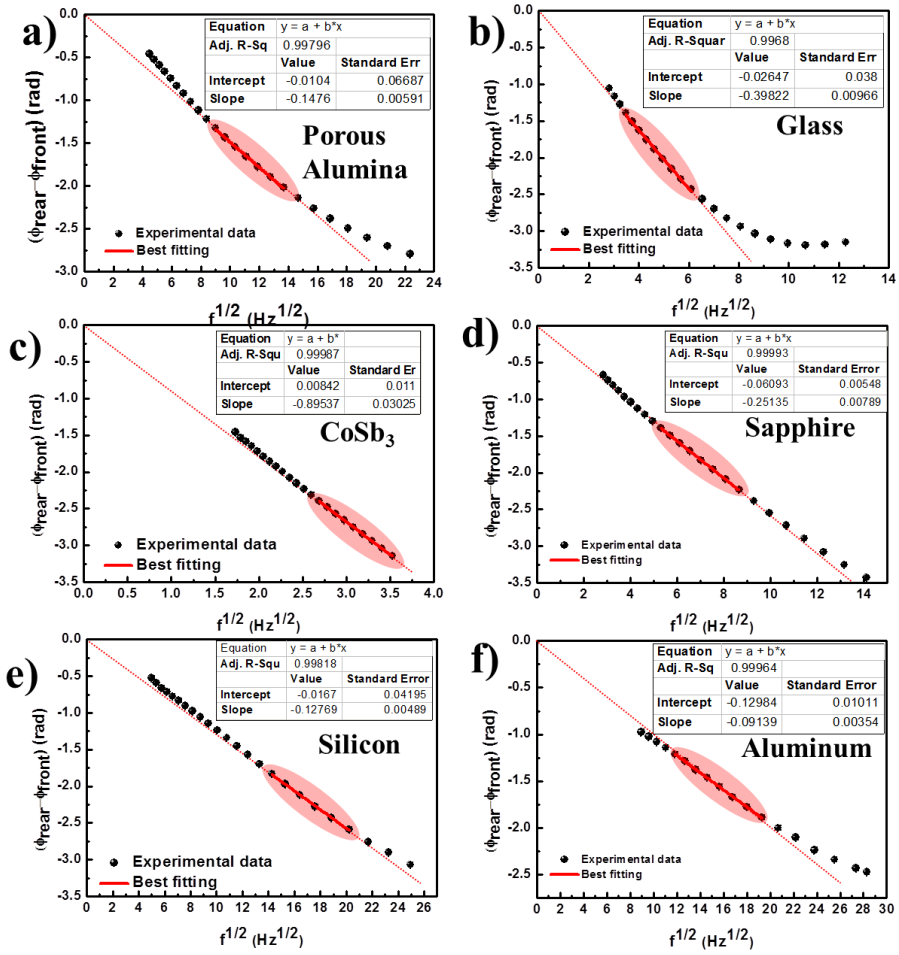

Figure 4.1. Normalized phase shift difference as a function of the frequency along with the best fitting for different reference samples (a) porous alumina, (b) glass, (c) $CoSb_3$, (d) sapphire, (e) silicon and (d) aluminum.

Table 4.I shows the thermal diffusivity values obtained for each reference sample. These values come from several independent measurements and the subsequent weighted average between them, as described in Chapter 3. The thermal diffusivity uncertainty value is calculated with the standard error of the slope given by the linear fit along with the thickness uncertainty (see Chapter 3). It is interesting to note that the deviation from the expected values are found to be lower than 10% in all the cases, which is considerably low regarding the difficulties of the thermal measurements. Moreover, the experimental uncertainty values are around 5%. Therefore, this method is highly accurate and precise.

Table 4.I. Thickness, thermal diffusivity values of the six reference samples obtained by the phase lag difference method and its deviation from the expected thermal diffusivity values.

Sample	Thickness (μm)	Expected thermal diffusivity ($m^2 \cdot s^{-1}$)	Thermal diffusivity (phase lag) ($m^2 \cdot s^{-1}$)	Dev. (%)
Smart membranes	60 ± 1	(5.40±0.53)·10^{-7}*	(5.14±0.24) 10^{-7}	5.0
Glass	150 ± 5	5.00·10^{-7} [2]	(4.48±0.24) 10^{-7}	10.4
$CoSb_3$	683 ± 10	(2.00±0.20) 10^{-6}*	(1.92±0.10) 10^{-6}	4.0
Sapphire	500 ± 10	1.17·10^{-5} [3]	(1.28±0.06) 10^{-5}	9.4
Silicon	646 ± 10	8.90·10^{-5} [4]	(8.28±0.46) 10^{-5}	7.0
Aluminum	500 ± 10	9.79·10^{-5} [4]	(9.56±0.53) 10^{-5}	2.3

*The thermal diffusivity of these samples was measured by other techniques. The porous alumina from Smart Membranes was measured by the photoacoustic technique using the multilayered model and the $CoSb_3$ sample measurement was carried out by the laser flash technique.

Figure 4.2 shows the behavior of the normalized phase shift tangent as a function of the frequency (Eq. 3.16) of three of the references, porous alumina, $CoSb_3$ and silicon whose thicknesses are 60 μm 683 μm and 646 μm, respectively. As predicted, a discontinuity in the tangent of the difference of the phase shift occurs at a given frequency. Those frequencies are found to be 116 Hz, 3.4 Hz and 170 Hz in the case of porous alumina, $CoSb_3$ and silicon, respectively, using Eq. 3.21.

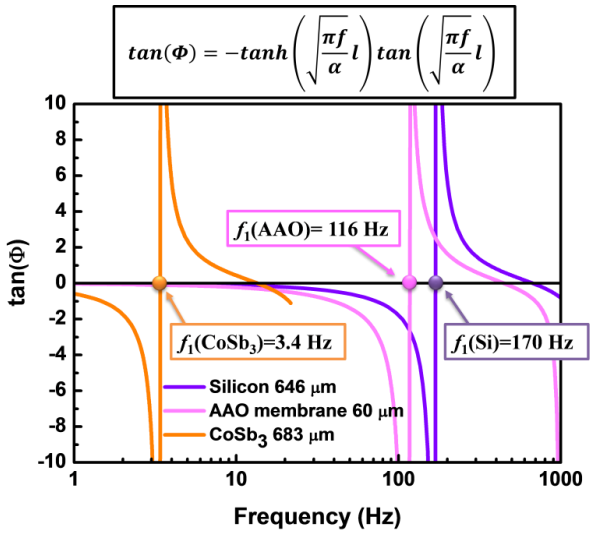

Figure 4.2. Theoretical analysis of the tangent of the phase shift as a function of the frequency for a porous alumina template (AAO), a CoSb3 pellet and a silicon wafer.

If some calculations are performed, it is easy to find a relation between the discontinuity frequency and the critical frequency given by:

$$f_1 = \frac{\pi^2}{4} f_c \tag{4.1}$$

From the above expression, it is straightforward to realize that the experiments must be carried out in the thermally thick regime, i.e., at frequencies higher than the critical frequency. This regime was

already explored when analyzing the phase shift difference as a function of the frequency root square. The frequency at which the discontinuity occurs depends on both the thermal diffusivity and the thickness of the samples. A limitation on the method can be established by taking into account the microphone frequency response (4Hz - 20 kHz) so,

$$4Hz < f_1 < 20\,kHz \tag{4.2}$$

Therefore, the limitations for the relation between the thermal diffusivity and the thickness of the sample are established. From Eq. 4.2 the minimum and maximum critic frequencies that can be measured are 1.6 Hz and 8106 Hz, respectively. However, the main limiting factor is the minimum critical frequency since it is difficult to find a bulk material with a critical frequency higher than 8106 Hz. For example, for a highly conductive material as gold, the thickness should be lower than 71 μm to reach that frequency. On the other hand, the minimum critical frequency is easily accessible for low conductive samples, although care must be taken in order to perform a good quality measurement.

We performed the same analysis as in Figure 4.2 from the experimental data obtained by measuring in rear and front configurations. Figure 4.3 shows an example of the experimental tangent of the normalized phase shift difference as a function of the frequency for the six reference samples. The discontinuity frequencies are shown for each sample and summarized in Table 4.II. The experimental uncertainty associated with the discontinuity frequency is found to be around 10%.

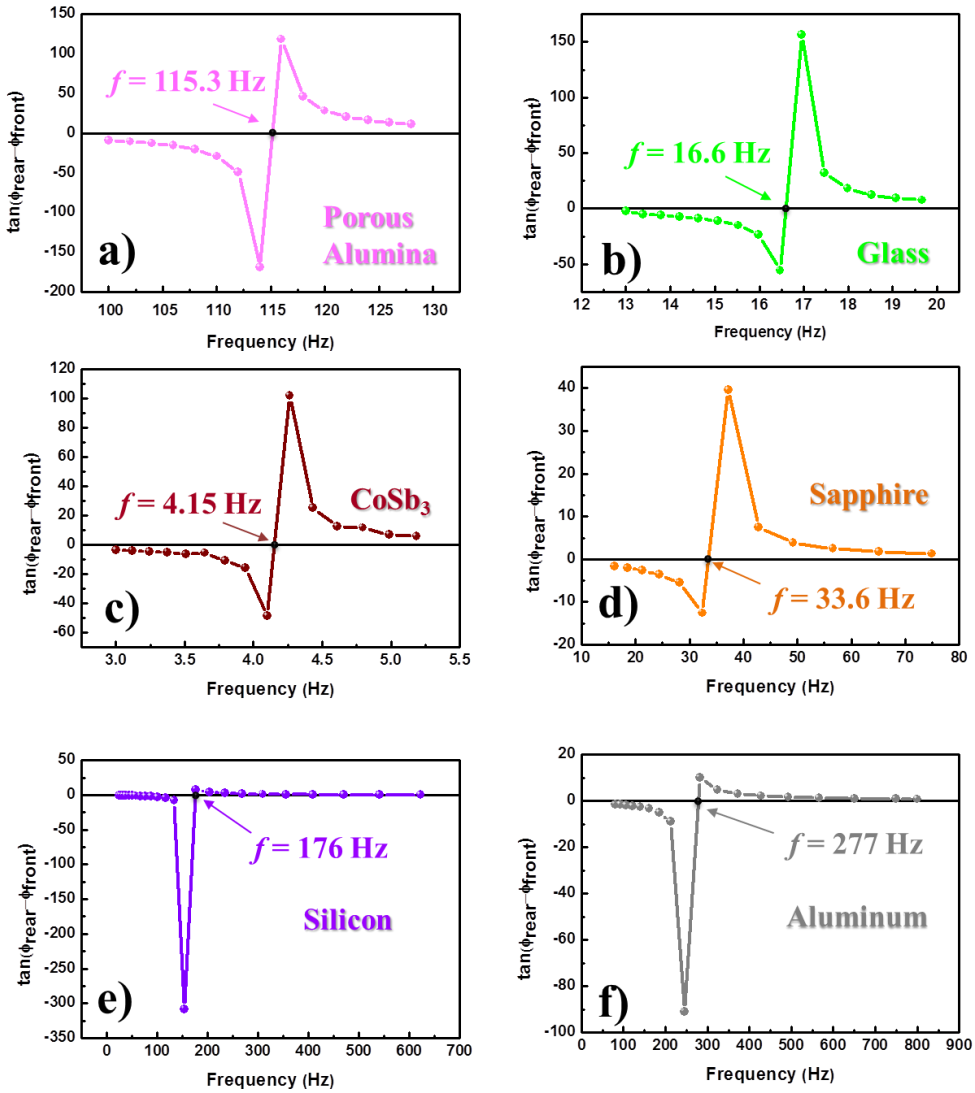

Figure 4.3. Experimental data of the tangent of the phase shift difference as a function of the frequency for different reference samples (a) porous alumina, (b) glass, (c) CoSb3, (d) sapphire, (e) silicon and (d) aluminum.

Both thickness and discontinuity frequency are used to extract the experimental thermal diffusivity (Table 4.II). The thermal diffusivity uncertainty is calculated from the propagation of uncertainties of Eq. 3.21 which involves both thickness and discontinuity frequency uncertainties. As in the previous method, several measurements were carried out in order to minimize the experimental uncertainty and the weighted average was performed in all cases. The thermal diffusivity uncertainty values are found to be in the vicinity of 5-7 %, which indicates that this method is rather precise. The deviation from the expected values is always lower than 12 %, which signifies that it is also reasonably accurate. It is interesting to note that the $CoSb_3$ pellet critic frequency is lower than the minimum frequency that the system is able to measure. This could explain that its experimental deviation, 12%, is higher than in the other cases, since the frequency range used to perform the experiment was below the microphone frequency response where the good quality of its performance starts to decay.

Table 4.II Thickness, critical frequency, thermal diffusivity values of the six reference samples obtained by the discontinuity of the tangent method and its deviation from the expected thermal diffusivity values.

Sample	Thickness (μm)	Critic frequency (Hz)	Expected thermal diffusivity (m^2/s)	Thermal diffusivity (m^2/s)	Dev. (%)
Smart membranes	60 ± 1	46.3	$(5.40\pm0.52)10^{-7}$*	$(5.29\pm0.28)\ 10^{-7}$	2.0
Glass	150 ± 5	6.7	$5.00\cdot10^{-7}$ [2]	$(4.71\pm0.28)\ 10^{-7}$	0.2
$CoSb_3$	683 ± 10	1.4	$(2.00 \pm 0.20)10^{-6}$*	$(2.25\pm0.12)\ 10^{-6}$	12.0
Sapphire	500 ± 10	18.0	$1.17\cdot10^{-5}$ [3]	$(1.08\pm0.08)\ 10^{-5}$	7.7
Silicon	646 ± 10	67.9	$8.90\cdot10^{-5}$ [4]	$(8.64\pm0.48)\ 10^{-5}$	3.0
Aluminum	500 ± 10	124.7	$9.79\cdot10^{-5}$ [4]	$(8.70\pm0.66)\ 10^{-5}$	11.1

*The thermal diffusivity of these samples was measured by other techniques. The porous alumina from Smart Membranes was measured by the photoacoustic technique working on the multilayer model and the $CoSb_3$ sample measurement was carried out by the laser flash technique.

For both methods, the experimental deviation or percent difference between the experimental and expected values is given by:

$$\%\ deviation = 100 \cdot \frac{|Expected\ value - Experimental\ value|}{Expected\ value} \tag{4.3}$$

The experimental uncertainty associated to the thickness is given by the experimental technique used to measure it. In the case of the alumina templates, the thickness was measured by Scanning Electron Microscopy, so the error is typically under 0.5 μm for this type of samples. The thickness of the glass slide was measured by an optical microscope with an uncertainty of 5 μm. Finally, the thicknesses of the rest of the bulk samples were measured with a micrometer, whose resolution is 1 μm. Despite of this low instrumental uncertainty, several measurements were taken from each sample so the random uncertainty was found to be 10 μm and hence, dominates the overall error.

Finally, Figure 4.4 shows the behavior of the measured thermal diffusivity as a function of the expected values. Both measurement methods are highly accurate since the slope values of the straight lines are close to 1, 0.996 and 0.973 for the phase lag difference and discontinuity tangent, respectively. These results mean that the overall experimental deviation is lower than 10 % for both methods.

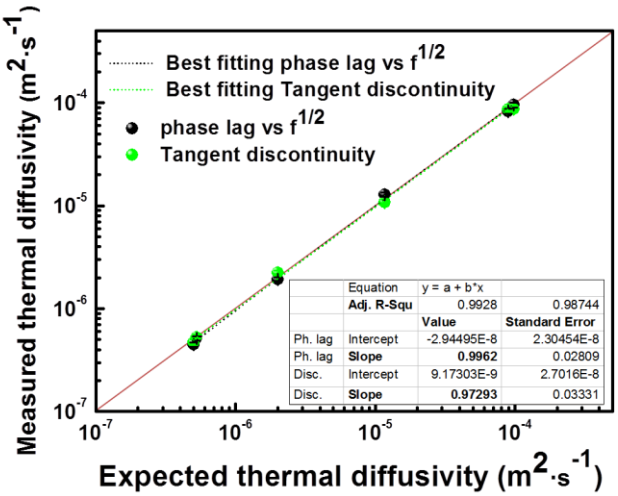

Figure 4.4. Measured thermal diffusivity as a function of the expected thermal diffusivity values for both methods along with the best fittings.

4.2 Zinc oxide pellets

Zinc oxide (ZnO) has been intensively studied during the last years due to its variety of properties and hence, the wide range of applications. Among the most interesting ZnO properties, one can find its hexagonal crystal structure, wide and direct band gap (3.44 eV)[5], transparency in the whole visible range and a large exciton binding energy (60 meV)[5].

Ceramic oxides stand for one of the most promising materials in terms of thermoelectricity which can operate at high temperatures mainly due to their thermal stability at temperatures higher than 1073 K. ZnO is one of the most promising oxides used for this purpose, especially when doped with different elements such as aluminum. ZnO has reached figure of merit values of 0.3 at 1273 K and 0.65 at 1247 K when doped with aluminum[6] and with gallium and aluminum[7], respectively. Therefore, this material becomes an interesting approach to improve the performance of thermoelectric modules at high temperatures.

Apart from the proper selection of the thermoelectric materials, there are other tactics to increase the thermoelectric efficiency such as nanostructuration or even the fabrication of hybrid materials. For instance, a figure of merit of 0.44 at 1000 K was obtained by Al-doped nanocomposites[8] and 0.54 at 1173 K for a hybrid material consisting on $Zn_{1-x}Ni_xO$/polyparaphenylene[9].

Previous studies of Ni-doped ZnO as a thermoelectric material were performed, synthesized by solid-state reaction[10] and by a liquid route[11]. In this work, a study of the nanostructuration during the fabrication of ZnO pellets by ball milling and the following spark plasma sintering is carried out. Moreover, the effect of the grain size in the thermoelectric properties is investigated. Finally, nickel

oxide (NiO) nanoparticles were used as a nickel dopant in order to improve the thermoelectric properties of the material.

4.2.1 Fabrication

Two types of ZnO particles were studied: ZnO microparticles with a particlee of 0.5 µm, named thereafter Regular ZnO, and ZnO-nanoparticles with a particles size of 70 nm, named thereafter ZnO nano. As doping materials, NiO-nanoparticles having a primary particles size of 20 nm are used to modify the ZnO materials by wt. % addition of 0.01, 0.1, 1 and 3 in excess of NiO. Mixed powders were obtained by ball milling and sintered by using a Spark Plasma Furnace (SPS) by in situ heat treatment of the pellets. The details of the ball milling and SPS procedures are given in Section 2.1.5 and 2.1.6, respectively.

4.2.2 Structural and morphological characterization

ZnO pure materials conventionally sintered shown large grains having polyhedral morphology and porosity, as seen in Figure 4.5. The grain size are in the range of 30-50 µm for regular ZnO (see Figure 4.5 (a)) and in the range of 15-25 µm for nano ZnO (see Figure 4.5 (b)). In both cases the appearance of straight grain boundaries, presence of triple point having 120 degrees and grain boundary or triple point porosity indicates a final stage of the sintering. It is worth to mention that lower starting particle in the case of nano ZnO produces also a large grain growth. A remarkable core structure is observed in several grains for the nano ZnO conventionally sintered sample. This core structure is characterized by the appearance of well faceted domains having parallel arrangement and widths <400 nm. This unusual domain structure resembles a limitation in the ordering of the wurtzite structure during grain the diffusion at the intermediate stage of sintering.

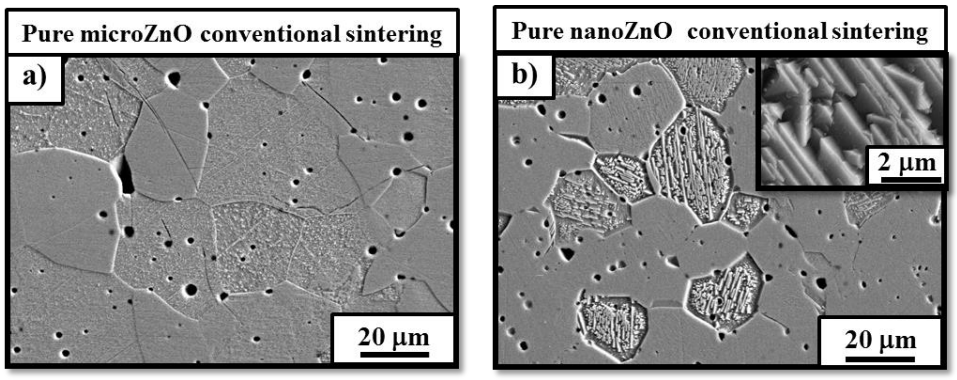

Figure 4.5. FE-SEM images of the surface of conventional sintering pure (a) micro ZnO and (b) nano ZnO.

Samples sintered by SPS at 850 ºC, showed in Figure 4.6 (f) and Figure 4.7 (a), present grain size lower than 2 µm thus indicating a limiting grain growth process assisted by high sintering rate and the SPS. The addition of the NiO produce a slight refinement of the microstructure and the grain size is also slightly lower but in the same range. By using a high temperature in the SPS sintering, 1100ºC,

the grain growth up to sizes in the range of 5-10 μm with straight grain boundaries and absence of enclosed porosity. Homogeneous grain size distribution is observed for the 1100 ºC SPS sintered regular ZnO where the effect of NiO addition is the grain refinement, as seen in Figure 4.6.

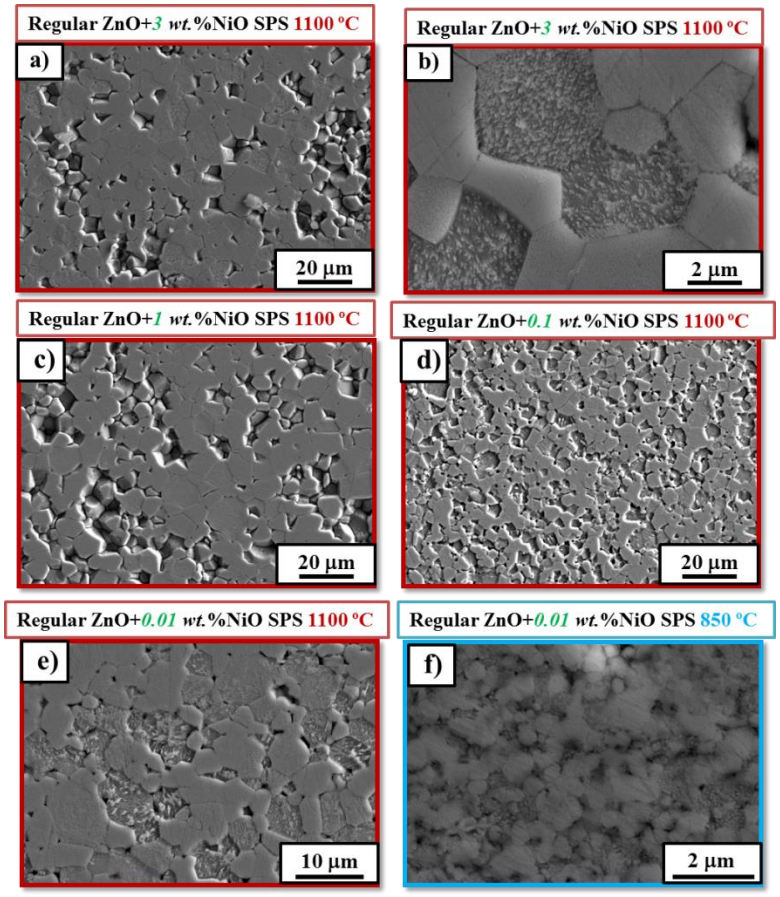

Figure 4.6. FE-SEM images examples of the surface of the Regular ZnO sintered at 1100 ºC with NiO concentration of (a) and (b) 3 wt. %, (c) 1 wt. %, (d) 0.1 wt. %, (e) 0.01 wt. % and (d) ZnO regular sintered at 850 ºC with 0.01 wt. % NiO.

The nano ZnO samples sintered at 1100 ºC by SPS shown only a smaller grain size than the regular ZnO ones (see Figure 4.7). However, the most remarkable feature is the nanostructuration shown by several grains in which the grain possesses a finer nanostructure inside the grain having sub-grains with size range <400 nm. In the case of regular ZnO + NiO SPS sintered at 1100 ºC, the presence of subgrains it is not clear at it is stated in nano ZnO based samples.

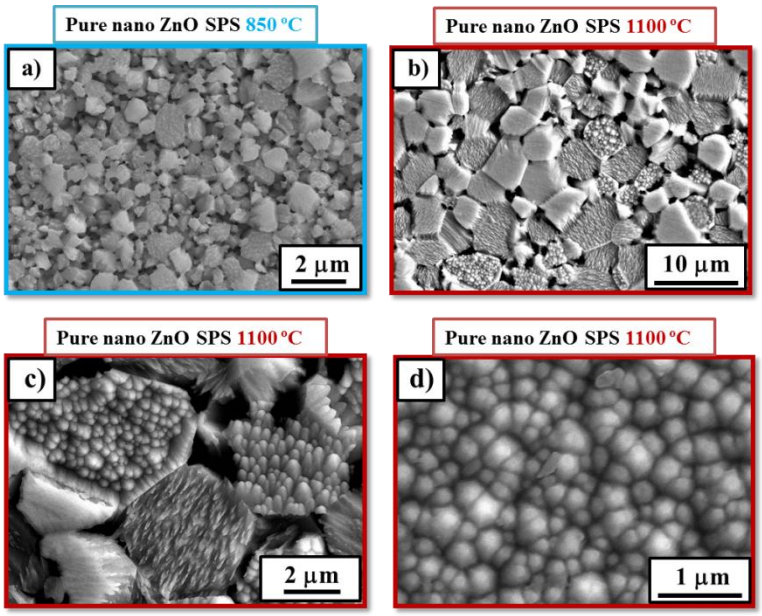

Figure 4.7. FE-SEM images examples of the surface of the pure nano ZnO sintered at (a) 850 ºC and (b), (c) and (d) 1100 ºC.

4.2.3 Electrical conductivity and Seebeck coefficient measurement

Figure 4.8 shows the electrical resistivity of the ZnO samples SPS sintered from (a) regular ZnO and (b) nano ZnO for two different sintering temperatures.

Regarding regular ZnO samples, meanwhile the 850 ºC sintered samples shown a decreasing of the resistivity with the increasing of the measurement temperature that indicates a semiconductor behavior, the samples sintered at 1100 ºC shown a metallic behavior (see Figure 4.8 (a)). The resistivity change could be attributed to the sintering atmosphere in which the presence of the graphite in the argon atmosphere produced a reduction atmosphere.

Moreover, the electrical resistivity is nearly the same when preparing the samples at 850 ºC and 1100 ºC, but there is a clear difference of the values when adding NiO nanoparticles. In the samples prepared at 1100 ºC, a progressive diminution of the electrical resistivity occurs up to 1 wt. % NiO reaching values as low as 0.11 Ω·cm at 66 ºC, and a following increase is observed when the NiO concentration is augmented up to 3 wt. %. Conversely, adding 0.1 wt. % of NiO nanoparticles to samples sintered at 850 ºC increase the electrical resistivity. The samples sintered at 850 ºC shown densities in the range of 5.4 - 5.5 $g \cdot cm^{-3}$ that is less than 90 % of the theoretical density. The local increasing of density in specimens from the sample could account for such differences.

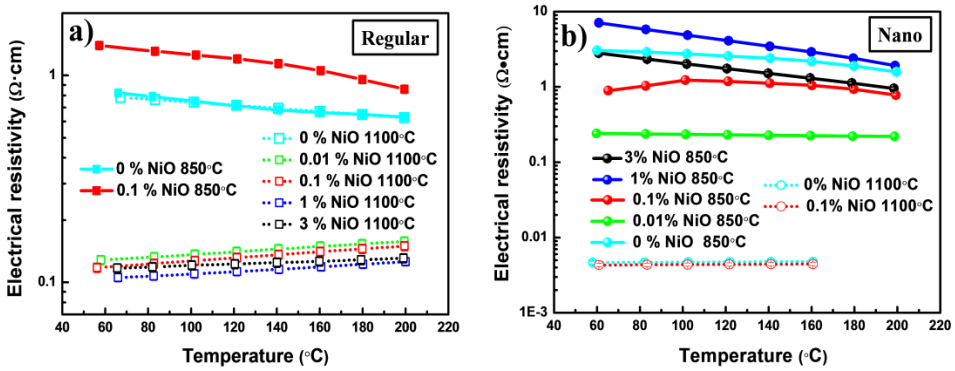

Figure 4.8. Electrical resistivity as a function of the temperature for samples prepared from (a) regular grain size and (b) nano grain size powders.

Samples prepared from nano ZnO powders sintered at 1100 ºC show an electrical resistivity three orders of magnitude lower than those prepared at 850 ºC. The addition of a 0.1 wt. % NiO nanoparticles yields the lowest value, 0.0043 Ω·cm at 60 ºC for samples prepared at 1100 ºC. Moreover, the addition of NiO nanoparticles in the samples sintered at 850 ºC reduces the electrical resistivity when using a 0.01 wt. % NiO and then increases again up to values even higher than the pure ZnO. The lowest value was found to be 0.25 Ω·cm at 60 ºC for the optimum NiO concentration, i.e., 0.01 % NiO at 850ºC.

From these results, it is clearly seen that there is a threshold in the NiO concentration for samples prepared from both ZnO raw materials and temperatures. This threshold yields the lowest electrical resistivity values and it always increases when this value is overtaken. This behavior was also observed by Colder *et al* [11] who explained the increase of the electrical conductivity by an appearance of an impurity level in the bandgap due to a change in the ZnO band structure when a substitution of Ni for Zn in the crystal structure takes places. The reduction in the electrical conductivity when further increasing the NiO concentration is explained by the formation of a secondary phase as observed in Figure 4.9, in which a contribution of NiO produce a new broad Raman band located between 520 and 600 cm^{-1}. This Raman broad band seems to do not affect the ZnO Raman peaks but shown a characteristic signature at Raman shift higher than 1100 cm^{-1} that indicates a correlation of the NiO presence with electronic carriers [12]. Figure 4.10 shows how the incorporation of NiO is promoting the appearance of such Raman band in both the nano and the regular ZnO material.

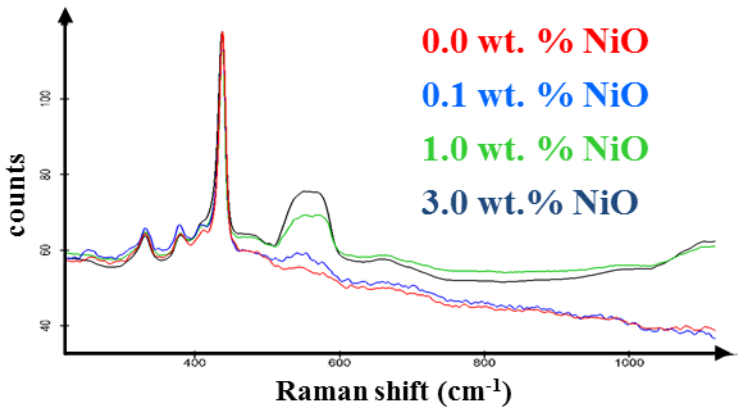

Figure 4.9. Raman Shift spectra of ZnO nano sintered at 850 ºC

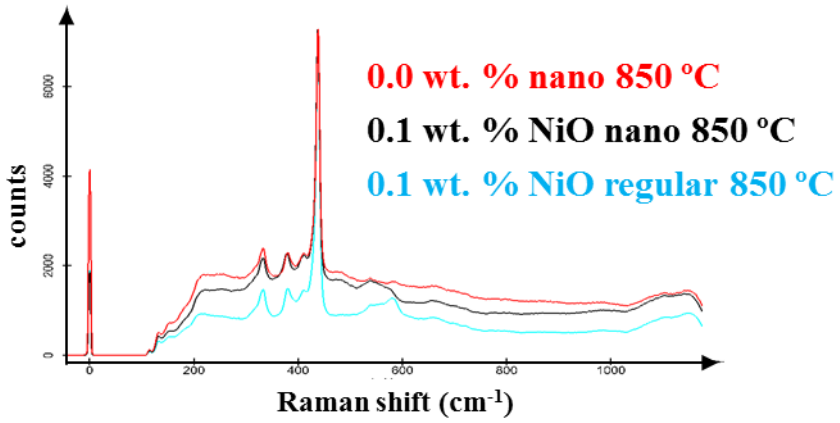

Figure 4.10. Raman Shift spectra of ZnO nano and regular sintered at 850 ºC

The reduction atmosphere promotes by the SPS sintering and the NiO content seems to be the responsible for the electrical change from semiconductor to metallic. In ZnO-doped materials this effect has been previously reported and it is consistent with a free-carrier density approaching exhaustion, and an electron mobility controlled mainly by lattice (both optical and acoustical) scattering that produced a PTC (Positive Temperature Coefficient) [13].

The Seebeck coefficient temperature dependence can be observed in Figure 4.11 for samples prepared from both (a) regular and (b) nano grain sizes powders. All the samples exhibit negative Seebeck coefficient which indicates n-type conduction.

Regarding samples from regular grain size powders (Figure 4.11 (a)), the lower sintered temperature (850 ºC) yields the highest Seebeck coefficient reaching values as high as -803 $\mu V \cdot K^{-1}$ at 200 ºC for pure ZnO. When adding NiO nanoparticles to samples sintered at 1100ºC, the Seebeck coefficient also increases until reaching a threshold with a constant Seebeck coefficient of approximately -845 $\mu V \cdot K^{-1}$, 0.1 wt. % NiO in this case, from which the Seebeck coefficient starts to

decrease. If the same quantity is added to samples prepared at 850 ºC then an enormous Seebeck coefficient is obtained with a maximum value of -1115 $\mu V \cdot K^{-1}$ at 56 ºC.

In the case of samples prepared from nano grain size powders (Figure 4.11 (b)), the lowest sintered temperature, 850 ºC, yields a huge constant Seebeck coefficient, -1270 $\mu V \cdot K^{-1}$, in comparison with sample sintered at 1100 ºC, -130 $\mu V \cdot K^{-1}$, when compared pure ZnO. The addition of NiO deteriorates the Seebeck coefficient in both cases.

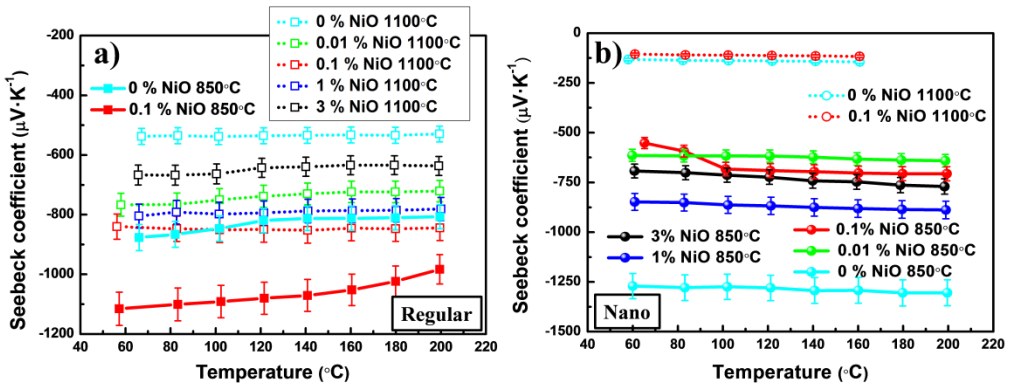

Figure 4.11. Seebeck coefficient as a function of the temperature for samples prepared from (a) regular grain size and (b) nano grain size powders.

The power factor combines the above-mentioned properties. Figure 4.12 shows the power factor for samples prepared from both grain size powders at the two different temperatures.

In the case of regular ZnO (Figure 4.12 (a)) with NiO addition, the power factor considerably improves when a sintering temperature of 1100 ºC is used, reaching values of approximately 620 $\mu W \cdot K^{-1} \cdot m^{-2}$ at 65 ºC for concentrations of 0.1 wt. % and 1 wt. % NiO. The addition of NiO for samples sintered at 850 ºC does not show any improvement in the power factor.

Equally, samples fabricated with nano grain size powders (Figure 4.12 (b)) exhibit the highest maximum power factors also for samples sintered at 1100 ºC. In particular, the maximum value was found to be 379 $\mu W \cdot K^{-1} \cdot m^{-2}$ at 56 ºC for pure ZnO shows. In the case of the samples sintered at 850 ºC, the maximum power factor is obtained for a NiO concentration of 0.01 wt. % due to its low electrical resistivity, 159 $\mu W \cdot K^{-1} \cdot m^{-2}$ at 60 ºC.

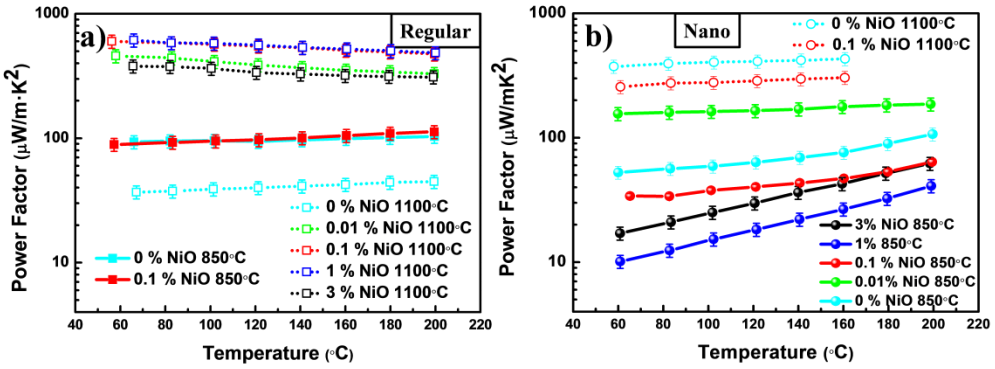

Figure 4.12. Power factor as a function of the temperature for samples prepared from (a) regular grain size and (b) nano grain size powders.

If we compared these values with the values found in the literature then it is worthy to note that a great improvement has been achieved in the studied temperature range. Colder *et al* [11] found a power factor of 120 $\mu W \cdot K^{-1} \cdot m^{-2}$ at the same temperature for a NiO addition of 0.03 wt. %, which is almost a factor 5 lower than the samples prepared from regular powders at 1100 ºC and concentrations of 0.1 wt. % and 1 wt. % NiO (620 $\mu W \cdot K^{-1} \cdot m^{-2}$ at 65 ºC) and a factor 3 lower than the pure ZnO prepared from nano powders at 1100 ºC (379 $\mu W \cdot K^{-1} \cdot m^{-2}$ at 56 ºC). Park *et al* [10] obtained a maximum power factor value of 180 $\mu W \cdot K^{-1} \cdot m^{-2}$ at 800 ºC also for a nickel atomic fraction of 0.03. Wu *et al* [9] found values comparable to our findings for $Zn_{1-x}Ni_xO$/polyparaphenylene, where concentrations of the polymer of 5 % and 9 % were found to yield the highest power factor values.

4.2.4 Thermal conductivity measurements

The thermal conductivity values were calculated from the thermal diffusivity measurements, the density and the specific heat which are summarized in Table 4.III. The thermal diffusivity was determined from the slope of Eq. 4.4 when measuring the different between the rear and front phase shift versus the root square of the frequency. Density values were determined by the Archimedes ‘method whereas specific heat was taken as a constant value from reference [14].

Table 4.III. Density, specific heat, thermal diffusivity and thermal conductivity values of the different samples.

Sample	[NiO] (wt. %)	Density ($kg \cdot m^{-3}$)	Specific heat ($J \cdot kg^{-1} \cdot K^{-1}$)[14]	Thermal diffusivity ($m^2 \cdot s^{-1}$)	Thermal conductivity ($W \cdot m^{-1} \cdot K^{-1}$)
Regular 850ºC	0	5170	500	$1.12 \cdot 10^{-5}$	28.9
Regular 850ºC	0.1	5452	500	$1.03 \cdot 10^{-5}$	28.8
Regular 1100ºC	0	5596	500	$1.29 \cdot 10^{-5}$	36.4
Regular 1100 ºC	0.01	5529	500	$1.24 \cdot 10^{-5}$	34.3
Regular 1100ºC	0.1	5467	500	$1.32 \cdot 10^{-5}$	36.1
Regular 1100ºC	1	5444	500	$8.81 \cdot 10^{-6}$	24.0
Regular 1100ºC	3	5606	500	$9.43 \cdot 10^{-6}$	26.4
Nano 850 ºC	0	5559	500	$1.06 \cdot 10^{-5}$	29.5
Nano 850 ºC	0.01	5465	500	$6.30 \cdot 10^{-6}$	17.2
Nano 850 ºC	0.1	-	500	-	-
Nano 850 ºC	1	5351	500	$5.95 \cdot 10^{-6}$	15.9
Nano 850 ºC	3	5348	500	$5.82 \cdot 10^{-6}$	15.6
Nano 1100 ºC	0	5505	500	$1.36 \cdot 10^{-5}$	37.7
Nano 1100 ºC	0.1	5486	500	$8.95 \cdot 10^{-6}$	19.2

The wurtzite zinc oxide presents a high intrinsic thermal conductivity, reaching values of 100 $W \cdot m^{-1}K^{-1}$ in the single crystal form[15]. Figure 4.13 (a) shows a room temperature thermal conductivity of pure ZnO of 28.9 $W \cdot m^{-1}K^{-1}$ and 36.4 $W \cdot m^{-1}K^{-1}$and for regular grain size samples sintered at 850 ºC and 1100 ºC, respectively. In the case prepared with nano grain sizes values of 29.5 $W \cdot m^{-1}K^{-1}$ and 37.7 $W \cdot m^{-1}K^{-1}$ were obtained at 850 ºC and 1100 ºC, respectively (See Figure 4.13 (b)). These values match the typical thermal conductivity ZnO values obtain at room temperature [11, 16]. It is clearly seen that samples sintered at 850 ºC present lower thermal conductivity values.

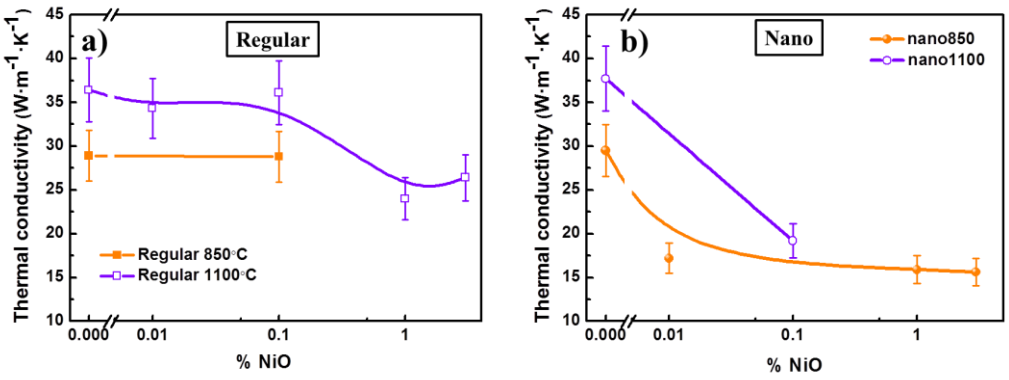

Figure 4.13. Thermal conductivity at room temperature as a function of the NiO concentration for samples prepared from (a) regular grain size and (b) nano grain size powders.

The addition of NiO reduces the thermal conductivity in both cases, reaching a threshold value from which the thermal conductivity remains constant. This value is different for regular grain size (0.01-0.1 wt. % NiO) than nano grain size (0.01 wt. % NiO), which match the threshold values found for both the electrical resistivity and Seebeck coefficient values. This effect was also observed by Colder *et al* [11] who observed a value of 17 $W \cdot m^{-1}K^{-1}$ for atomic fraction of nickel higher than 0.03. In our case, the constant values are approximately 25 $W \cdot m^{-1}K^{-1}$ and 15 $W \cdot m^{-1}K^{-1}$ for regular and nano

grain sizes, respectively. The difference between both values could be found in the grain size and in particular in the sub-grain structure of the SPS sintered nano ZnO, since sub-grains could cause the phonon scattering thus reducing the thermal conductivity.

4.2.5 Figure of merit

The figure of merit of these pellets can be estimated by assuming an isotropic character for the three measured magnitudes. Figure 4.14 shows the figure of merit as a function of the NiO concentration. The highest sintering temperature yields the highest figure of merit values for both types of samples. Moreover, the highest values are obtained for samples prepared from regular ZnO and a NiO content of 1 wt. % with a value of 0.0073 (see Figure 4.14 (a)) due to its low electrical resistivity combined with a high Seebeck coefficient which compensate the high thermal conductivity (29.5 $W \cdot m^{-1}K^{-1}$).

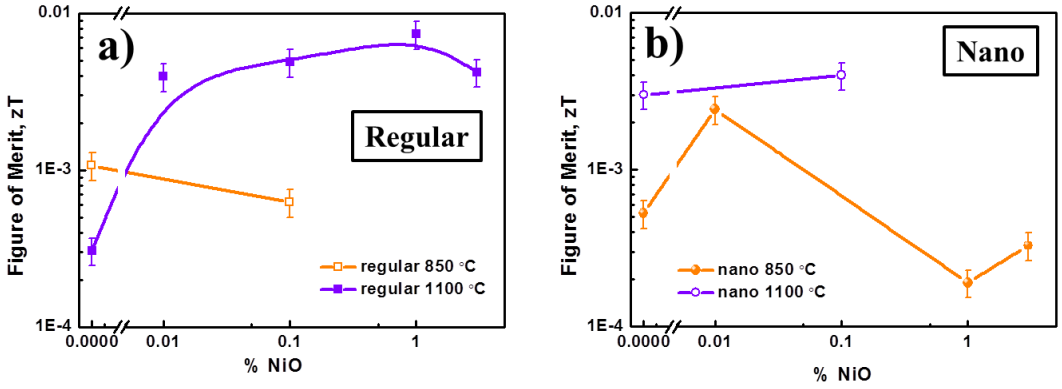

Figure 4.14. Figure of merit at room temperature as a function of the NiO concentration for samples prepared from (a) regular grain size and (b) nano grain size powders.

If our results are compared with the literature values, one can find that our figure of merit is lower than the highest values reported. However, those values are measured at temperatures much higher than our measurements, i.e., around 800 ºC. If we do the comparison at room temperature, our values are higher than the figure of merit achieved by Colder *et al* [11], lower than 0.004. Therefore, this preliminary study proves the good quality of the ZnO doped with nickel as a thermoelectric material. Further studies at higher temperatures are required since the best thermoelectric properties are expected to be found near 800 ºC.

4.3 Nanocomposites Polyaniline/Graphene nanoplatelets

Organic materials, are being recently studied as a promising thermoelectric materials due to their rising figure of merit [17-20], their commonly low thermal conductivity ($\kappa \approx 0.1\text{-}0.5\ W \cdot m^{-1} \cdot K^{-1}$ [21, 22]), flexibility, environmentally friendly, straightforwardly doping and de-doping, environmental stability, potential processing advantages and uncomplicated preparation in comparison with inorganic semiconductors. The enhancement in the power factor of these materials, is being accomplished by two different mechanisms: doping the polymers [23-25] or mixing them with diverse types of filling materials, such as graphene nanosheets (GN) [26, 27], carbon nanotubes (CNT)[28, 29], or graphene nanoplatelets (GNP) [30].

The commercial Nano Graphene Platelets or Graphene NanoPlatelets (GNPs) are made of exfoliated graphite nanoplatelets fabricated from graphene stacked layers of around 20 nm bonded by van der Waals forces with a length in the vicinity of 14 μm from the datasheet. This material is advantageous to synthesized nanocomposites due to their appropriate properties such as: respectable tensile strength, elevated corrosion resistance and high electrical and thermal conductivity [31, 32] Despite their high thermal conductivity, they can offer a simple way to enhance the thermoelectric properties when preparing nanocomposite with polymers like Polyaniline (PANI). PANI was selected due to its thermoelectric properties [33, 34]. PANI is a conductive polymer whose electrical conductivity value is found to be between 10^{-7} – $3 \cdot 10^{2}$ $S \cdot cm^{-1}$ depending on its oxidation states[24]. Conversely, PANI typically presents p-type conduction as most of Intrinsically Conductive Polymers. Furthermore, it is possible to achieve a negative Seebeck coefficient by doping[33, 35, 36]. The structure and morphology of these nanocomposites and their influence on the Seebeck coefficient, electrical conductivity and thermal conductivity when varying the volume fraction of GNP are studied and discussed.

4.3.1 Fabrication

The synthesis procedure of the nanoscomposites consists of two main stages: the synthesis of the polyaniline and the blend of the synthesized PANI with GNPs. A final cold pressing process was carried out in order to obtain the pellets. Details of the fabrication procedure are given in Section 2.17 and 2.1.8.

4.3.2 Structural and morphological characterization

FTIR spectra were carried out to elucidate the interactions between the polymeric matrix and the GNPs. Figure 4.15 (a) shows the characteristic FTIR spectra of PANI and PANI/GNPs nanocomposites. For the pure PANI, the absorption peaks situated at 1564 and 1471 cm^{-1} are assigned to the presence of quinoid ring and benzenoid rings vibrations in the emeraldine salt state, respectively [37].

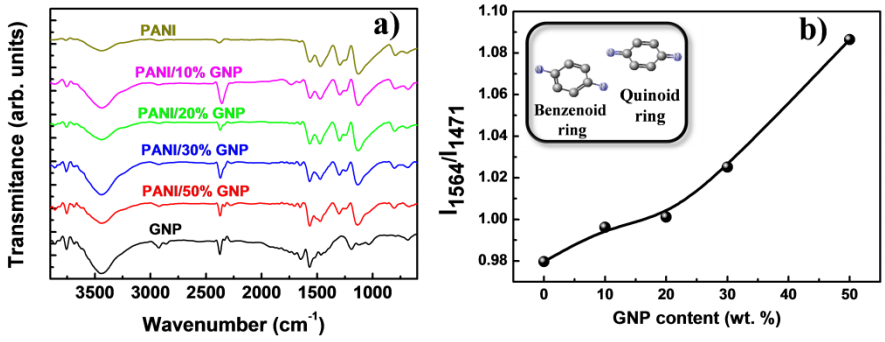

Figure 4.15. (a) FTIR spectra of PANI and PANI/GNP nanocomposites and (b) intensity ratio, I1564/I1471, of the pellets as a function of the GNPs content. The inset shows the chemical structure of the benzenoid and quinoid rings.

The peaks at 1296 cm^{-1} and 1240 cm^{-1} have been allocated to the C-N stretching vibration of the aromatic amine and the absorption peak at 1130 cm^{-1} has been assigned to the aromatic C-H in plane bending. The latter, is defined as "electronic-like band" typical of conductive PANI and show the extend of electron delocalization [37]. The absorption peak 796 cm^{-1} has been assigned to the out of plane bending vibration of C-H in the aromatic ring. The effective synthesis of PANI in its emeraldine hydrochloride salt form displayed in Figure 4.16 is confirmed by these peaks.

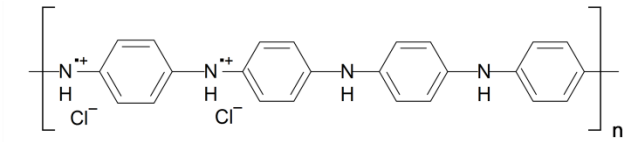

Figure 4.16. Chemical structure of polyaniline emeraldine hydrochloride salt state.

Zengin *et al* [38] and Yu *et al* [39] reported the interaction between PANI and GNPs by studying the variation in the peak intensity ratio between quinoid (≈1600 cm^{-1}) and benzenoid (≈1500 cm^{-1}) ring stretching. It is worthy to note that the intensity of the quinoid ring (I_{1564}) peak is lower than the benzenoid ring one (I_{1471}) in pure PANI. The ratio between the peaks, I_{1564}/I_{1471} increases when increasing the GNPs content as shown in Figure 4.15 (b). This analysis indicates a PANI abounding with quinoid rings in the PANI/GNPs composites than in the neat PANI. This increase of quinoid rings could elucidate the interaction of the π-bonded surface of GNP with the conjugated quinoid ring structure of PANI in such a way that the conjugation length is longer in the composites than on neat PANI[38] and the charge transport is promoted. This supposition is in good agreement with the electrical conductivity measurements, which indicate a rise of the electrical conductivity of the pure PANI when increasing the GNP content. Therefore, the increase in electrical conductivity can be owing to the addition of GNPs itself, but also to the GNP-PANI interactions.

Figures 4.17 show the morphology of the cross view of the PANI/GNP nanocomposites with different amounts of GNPs. The micrographs disclose a large aspect ratio (width-thickness ratio) of the

GNPs since the thickness is in the vicinity of 10 nm and the width is larger than 1 μm. GNPs clusters can also be distinguished when GNPs content is increased. Concerning the orientation of the GNPs embedded in the polymer matrix, most of the GNPs surfaces seem to be parallel to the sample surfaces. Furthermore, GNPs clusters show bent forms, possibly as a result of the elevated pressure during the cold pressing.

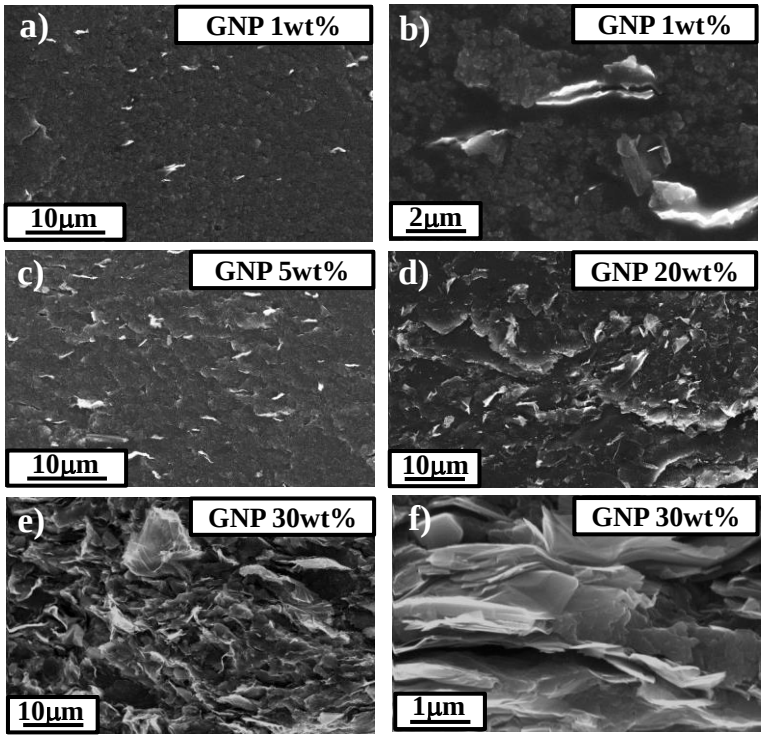

Figure 4.17. FE-SEM images of the rupture perpendicular to the pressure direction of the PANI/GNPs pellets of (a) and (b) GNP 1 wt.%, (c) GNP 5 wt.%, (d) GNP 20 wt.%, (e) and (f) GNP 30 wt.%.

The thermal stability of the nanocomposites has been demonstrated elsewhere[30]. Xiang *et al* discovered that the nanocomposites of PANI with content of GNP higher than 33 wt.% show decomposition in air atmosphere from 350 °C, which is 50 °C higher than the pure PANI.[30] Nonetheless, the temperature range of operation of these materials will not be higher than 100 °C.

4.3.3 Electrical conductivity and Seebeck coefficient

The electrical conductivity and the Seebeck coefficient have been systematically characterized at room temperature as a function of the GNPs volume fraction. Nevertheless, the composites were fabricated by calculating the weight of their constituents so the weight fraction was achieved. In order to determine the volume fraction of the samples, the density of the neat PANI and pure GNPs were measured and the following equation was used to calculate the volume fraction.

$$vol.\,\% = \frac{wt.\,\% \cdot \rho_{PANI}}{wt.\,\% \cdot \rho_{PANI} + (100 - wt.\,\%) \cdot \rho_{GNP}} \cdot 100 \qquad (4.4)$$

where *wt. %* and *vol. %* are the GNPs weight fraction and volume fraction, respectively, and ρ_{PANI} and ρ_{GNP} are the density of pure PANI, 1.37 $g \cdot cm^{-3}$, and the density of pure GNPs. The density measurement of the pure GNPs pellet, 1.89 $g \cdot cm^{-3}$, is slightly different than the datasheet value, 2.20 $g \cdot cm^{-3}$. This inconsistency could be owing to slight air gaps between the GNPs sheets that could be decreasing the effective density value of the pellet.

As seen in Figure 4.18 (a), the electrical conductivity rises up to three orders of magnitude when increasing the GNPs content from 0.48 $S \cdot cm^{-1}$ for pure PANI to 123 $S \cdot cm^{-1}$ for a 50 wt.% GNPs content. Moreover, the electrical conductivity of pristine GNP pellet was found to be 442 $S \cdot cm^{-1}$. The same measurements were performed after five months showing similar results, which indicate a good stability of the nanocomposite during this interval of time. The Seebeck coefficient (Figure 4.18 (b)) exhibits negative (n-type conduction) and positive (p-type conduction) values when the GNP content is lower and higher than 1 wt.%, respectively. A conversion from n-type polyaniline to p-type is accomplished with GNPs addition. The Seebeck coefficient is increased as the GNPs content increases from -2.6 $\mu V \cdot K^{-1}$ for neat PANI to +33.8 $\mu V \cdot K^{-1}$ for a 50 wt.% GNPs content and it is finally reduced up to +17.3 $\mu V \cdot K^{-1}$ for pure GNP sample. The positive value of the GNPs pure pellet elucidates the transition from n to p conduction in the composites when increasing the GNPs content. The power factor also as a function of the GNPs content undergoes a significant increase of several orders of magnitude achieving a value of 14 $\mu W \cdot m^{-1} \cdot K^{-2}$ for the maximum GNPs concentration, as seen in Figure 4.18 (c).

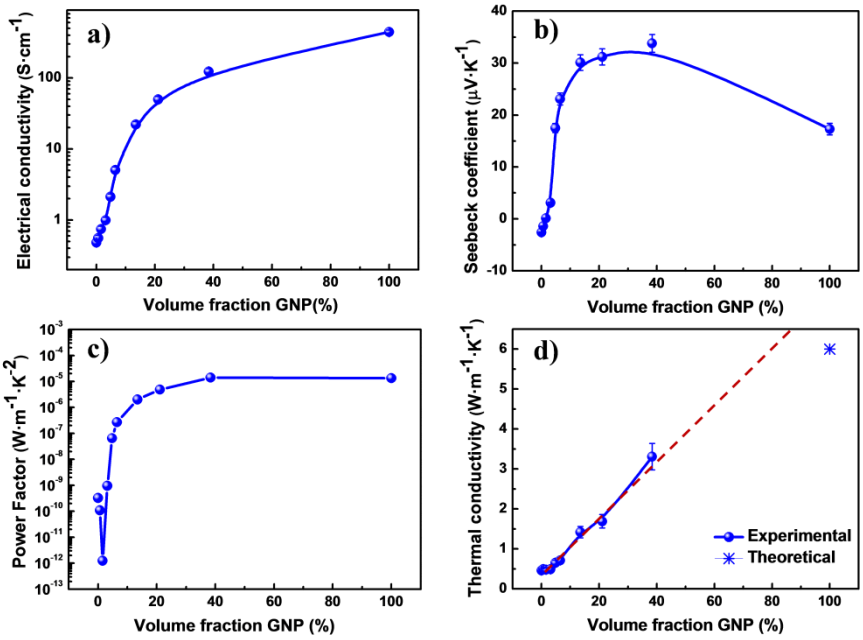

Figure 4.18. (a) Electrical conductivity, (b) Seebeck coefficient, (c) Power Factor and (d) thermal conductivity as a function of the GNPs volume fraction at room temperature (300K). The dash line of the graph (d) corresponds with the eye-guide for the thermal parallel resistor model and the asterisk-shape point is the datasheet value of the GNPs thermal conductivity.

Percolation law in composites can be described the improvement of the electrical conductivity, which predicts the electrical conductivity escalation when a critical volume fraction of filling material is attained [40, 41]. This phenomenon occurs provided that there is a considerable difference between both the electrical conductivity of the matrix and the filling material. In our case, the electrical conductivity values of neat PANI and pure GNPs are σ = 0.48 S·cm^{-1} and 442 S·cm^{-1}, respectively. The percolation law is described by the next power relation:

$$\sigma = \sigma_{GNP}|V - V^*|^p, \tag{4.5}$$

where V and V^* are the GNPs volume fraction and the critical volume fraction related to the threshold percolation, respectively, σ_{GNP} is the GNPs electrical conductivity and p is a critical exponent associated with the dimensionality of the established network. This expression is valid provided that $V>V^*$ and $(V-V^*)$ is slight. Despite the fact that the investigation has been performed with a very high dispersion of volume fraction values, a fitting of Eq. 4.5 has been evaluated with the assistance of LAB fit Curve fitting software. From the electrical conductivity measurements, the critical exponent was found to be $p \approx 1.31$. This exponent clarifies the sample dimensionality. A value of p = 4/3 is related to a two dimensions network, whereas p = 2 is the characteristic value of three dimensions network [42]. The fitting value p ≈ 1.31 (p ≈ 4/3) implies a charge transport in 2D, i.e., in the GNPs plane. This kind of electrical conduction could be linked to the fluctuation-induced tunneling model where hopping between GNPs through PANI barriers takes place [43, 44]. Moreover, the electrical conductivity of the GNP, σ_{GNP}, can be also extracted from the data fitting, 457 S·cm^{-1}, which results within the experimental uncertainty of our measurements of the pure GNPs pellet, 442 ± 44 S·cm^{-1}. Additionally, the percolation threshold was found to be 2.4 vol. %, or 1.5 wt. %, which indeed matches the n to p conduction type transition that is seen in the sign of the Seebeck coefficient. The threshold data are also related to the dispersion of the particles in the polymer matrix. Significantly low percolation threshold values suggest a uniform dispersion [43].

As it is feasible that PANI chains coat GNPs, electrical conductivity could be influenced by tunneling transport between GNPs, which are the main conductive constituents of the composite, across potential barriers generated by the PANI chains. In order to verify if the transport mechanism is related to the tunneling transport, a model based on fluctuation induced tunneling is employed[45]. This model allows the study of the tunneling through potential barriers with changeable heights as a result of local temperature oscillations. The electrical conductivity is described by this expression:

$$\sigma = \sigma_0 exp\left(-\frac{T_1}{T + T_0}\right), \tag{4.6}$$

$$T_1 = \frac{wA\varepsilon^2}{8\pi k}, \tag{4.7}$$

$$T_0 = \frac{2T_1}{\pi w \chi}, \tag{4.8}$$

where σ_0 is a constant, T is the temperature, w is the potential barrier width, A is the area of capacitance formed at the junction, k is the Boltzmann's constant, $\varepsilon = 4V_0/ew$, $\chi = (2mV_0/h^2)^{1/2}$, m and e are the electron mass and the charge respectively, V_0 is the potential height, and h is the Planck´s constant. At constant temperature the electrical conductivity is proportional to the potential barrier width, $Ln\sigma\ \alpha - w$. Therefore, a linear relation between the electrical conductivity and the GNP volume fraction, $Ln\sigma\ \alpha - V^{-1/3}$ when $V>V^*$, can be found by taking into consideration some spatial factors[42]. In Figure 4.19 the electrical conductivity is plotted versus $V^{1/3}$. The expected linear dependence for volume fractions higher than the percolation critical volume fraction is corroborated and thus the tunneling mechanism is confirmed. Lower GNPs contents do not show the linear dependence possibly attributable to a hopping transport between PANI chains. The linear trend is found for volume fractions larger than 3 vol.%, which is a little higher than the percolation threshold, 2.4 vol.%.

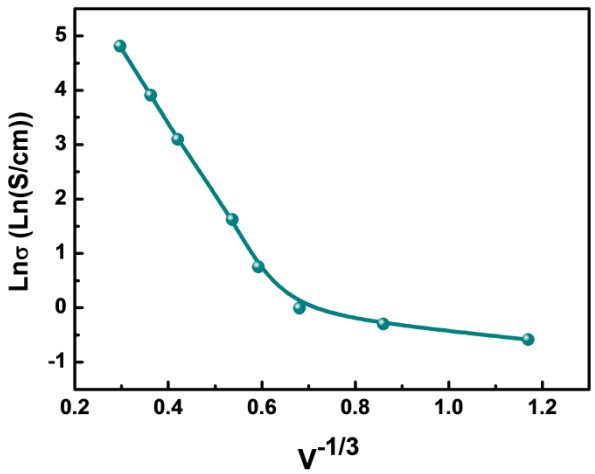

Figure 4.19. Plot of Lnσ vs. V-1/3. The linear dependence discloses the tunneling transport of the charge carriers.

The increase of the Seebeck coefficient is very astonishing since both neat PANI and pure GNPs present a lower Seebeck coefficient, -2.6 $\mu V \cdot K^{-1}$ and +17.3 $\mu V \cdot K^{-1}$ respectively. This improvement of the Seebeck coefficient could be justified in terms of the energy filtering of carrier by taking into consideration the grain boundaries that are generated by blending both materials during the nanocomposite fabrication. Previous works have proved that a rise in the Seebeck coefficient caused by grain boundaries takes place as low energy electrons are more powerfully scattered than the high energy ones [46-51]. This improvement of the Seebeck coefficient has already been remarked in previous investigations, such as carbon nanotubes blended with PANI composites[52] and in other very different structures, like Pt-Sb_2Te_3 nanocomposites [48], InGaAs/InGaAlAs superlattices or PbTe with Pb

precipitates [50]. Nevertheless, some theoretical study should be performed in order to understand this behavior more profoundly.

4.3.4 Thermal conductivity measurements

The thermal conductivity measurements were carried by three different techniques in order to ensure the reliability of the results. Apart from the photoacoustic technique, another experimental setup to measure directly the thermal conductivity of polymers was developed during this PhD work. This system is able to measure samples with a thickness of around 1 mm whose thermal conductivity is lower than 2 $W \cdot m^{-1} \cdot K^{-1}$. Therefore, samples with a thermal conductivity higher than this value were measured by the photoacoustic technique and the laser flash technique in the National Institute for Materials Science (NIMS), in Tsukuba (Japan), during a stay of this PhD candidate.

4.4.4.1 Low thermal conductivity measurement apparatus (κ system)

The experimental setup developed during this PhD work is based on the steady-state method which was chosen because it is considerably simpler than the transient method. This experimental setup allows the study of the heat flux going through a sample by conduction. Since the fundamental modes of heat transfer can be classified in conduction, convection and radiation, this experimental system was designed in order to minimize heat radiation and convection losses.

Figure 4.20 (a) shows the experimental setup which consists of two copper blocks which act as the heat source and the heat sink. The sample is placed between the blocks. The heat flux can be studied by measuring hot and cold temperatures via two thermocouples placed inside the blocks. They are located very near the contact surface to ensure that these temperatures fit with the surface temperature of the sample thanks to the high thermal conductivity of the copper. In order to prevent the influence of the convection in the sample the block located on the top acts as the heat source by means of a heater placed just in contact with it. Moreover, an insulator bulk material was located just in contact with this element, in order to reduce convection effects. The lower block acts as a heat sink whose size is considerably larger than the heating block in order to efficiently dissipate the heat. Figure 4.20 (b) shows the characteristic response of the hot and cold thermocouples as a function of time during a measurement. A typical measurement consists of studying the temperature of both hot and cold surfaces of the sample by establishing different heating powers and allowing the system to reach the steady state at each step.

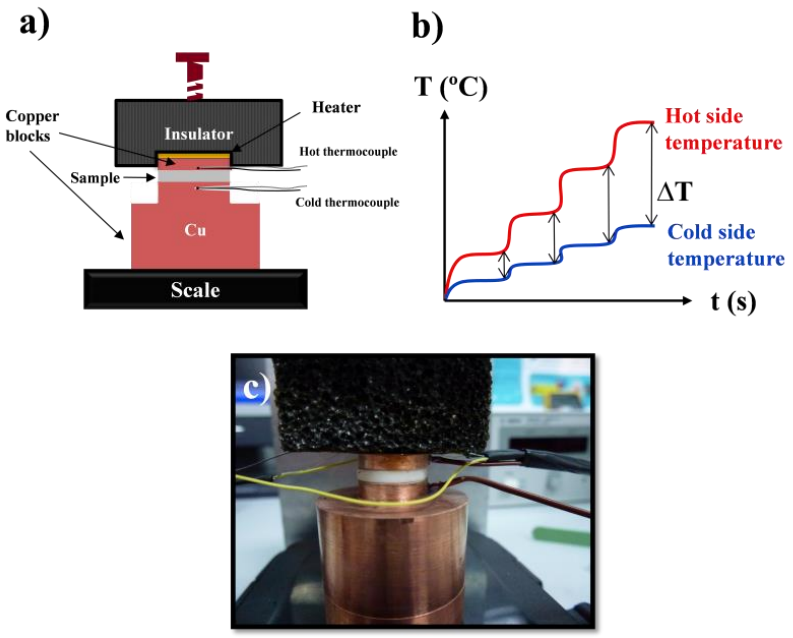

Figure 4.20. (a) Thermal conductivity experimental setup developed during this PhD thesis, used to measure polymer bulk samples, (b) temperature as a function of the time during a typical measurement of a sample and (c) picture of the experimental setup.

One of the most important hindrances to overcome is the thermal contact resistance, since the contacting area between the copper blocks and the sample is usually rough and irregular in such a way that the real contact is considerably lower than the real nominal contact surface area. In this way, micro-holes full of air are created limiting the heat transfer through the interface between the two surfaces, thus increasing the thermal contact resistance[53]. The thermal contact resistance was reduced by employing a layer of thermal paste as a thermal interface material. This material is able to decrease the thermal contact resistance by filling the air micro-holes and making the contact surface continuous. Moreover, this thermal paste is composed of silver nanoparticles, which makes the effective thermal conductivity sufficiently large (10 $W \cdot m^{-1} \cdot K^{-1}$) so the heat transfer by conduction is favored and thermal resistance is fairly reduced.

Nevertheless, this kind of systems has an enormous handicap in relation to the heat transfer control. Since the measurement is based on the heat transfer through the sample by conduction, heat losses due to both heat transfer mechanisms, radiation and convection, must be minimized [54]. In order to reduce their contributions a comparative method is carried out by comparing the sample to be measured with a reference sample whose thermal conductivity is well-known.

The physics behind the experiment is based on the study of the heat flux across the sample described by the Fourier´s Law, which means that the heat flux in the steady state is proportional to the cross section and the thermal conductivity as,

$$\dot{Q} = \frac{\Delta T}{R} = \kappa \cdot A \cdot \frac{\Delta T}{L}, \tag{4.9}$$

where $\dot{Q}$ is the heat flux, R is the thermal resistance, A is the cross section, κ is the thermal conductivity, ΔT is the temperature gradient created in the material and L is the thickness of the sample. The heating power through the standard is equal to the power through the sample so the following relation can be established:

$$\Delta T_R = \frac{(A/L)_S}{(A/L)_R}\frac{\Delta T_S}{\kappa_R}\kappa_S, \tag{4.10}$$

where the subscripts R and S corresponds with the reference and the sample, respectively. A and L are the section and the thickness of the sample and ΔT is the temperature difference created across the sample By plotting the temperature gradient against$\frac{(A/L)_S}{(A/L)_R}\frac{\Delta T_S}{\kappa_R}$, the thermal conductivity of the sample is directly obtained.

The limits of the techniques are given by the thermal resistance of the sample, R_S,. These limits can be derived by relating the sample thermal resistance with the loss thermal resistance, R_{loss}, and thermal contact resistance, R_c, as:

$$R_{loss} \gg R_S \gg R_c \tag{4.11}$$

By analyzing different reference samples with different thicknesses such as Teflon (κ = 0.4 $W \cdot m^{-1} \cdot K^{-1}$), PEDOT:PSS (κ=0.36 $W \cdot m^{-1} \cdot K^{-1}$), pyrex (κ = 1 $W \cdot m^{-1} \cdot K^{-1}$), macor (κ = 1.46 $W \cdot m^{-1} \cdot K^{-1}$), AISI 304 (κ = 16.2 $W \cdot m^{-1} \cdot K^{-1}$) the limits of the technique were found. For insulator and conductive samples, the sample thermal resistance should be lower than 35 $K \cdot W^{-1}$ and higher than 4 $K \cdot W^{-1}$, respectively. Therefore, there is a limitation in both thermal conductivity and thickness. Assuming a fixed diameter of 13 mm, the maximum and minimum thermal conductivity as a function of the thickness can be seen in Figure 4.21. These thermal conductivities were calculated by considering a maximum and minimum sample thermal resistance of 4 $K \cdot W^{-1}$ and 35 $K \cdot W^{-1}$, respectively.

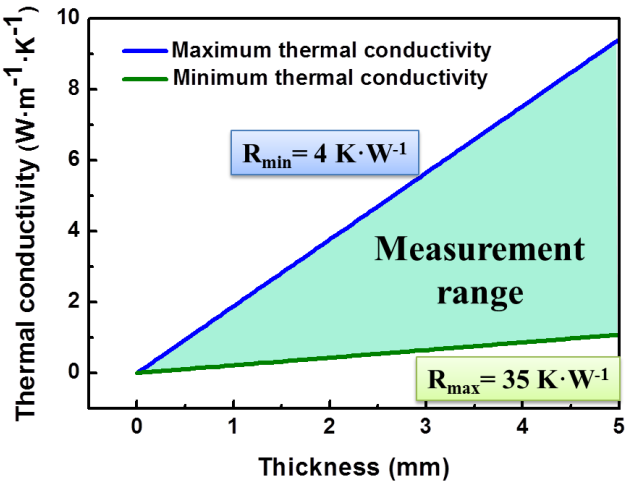

Figure 4.21. Thermal conductivity values that can be measured by this technique as a function of the sample thickness.

The PANI/GNP pellets have a thickness of around 1 mm so samples with a thermal conductivity higher than 2 $W \cdot m^{-1} \cdot K^{-1}$ need to be measured by a different technique.

4.3.4.1 Thermal conductivity values

PA technique and laser flash are used to measure the thermal diffusivity of materials. Therefore, density and specific heat measurements are needed in order to calculate the thermal conductivity values. The density was measured by Archimedes' method and the specific heat was estimated from the specific heat data found in the literature. The specific heat value corresponded to PANI fabricated in the same conditions is 1020 $J \cdot kg^{-1} \cdot K^{-1}$ [55]. The specific heat of the GNPs at room temperature can be approximated to 700 $J \cdot kg^{-1} \cdot K^{-1}$, which is the graphite specific heat [56]. The specific heat of the composite is thus calculated by taking the GNP volume fraction into consideration by the following expression:

$$(C_p)_{com} = \frac{(\%\ vol. \cdot \rho C_p)_{PANI} + (\%\ vol. \cdot \rho C_p)_{GNP}}{\rho_{com}}, \qquad (4.12)$$

where ρ_{com} is the composite density and $\%\ vol. \cdot \rho C_p$ is the multiplication of the volume fraction, the density and the specific heat of each component, PANI and GNP. Table 4.IV shows the composite values of the density and the specific heat as well as the thermal conductivity values obtained from the three different techniques. It is clearly seen that both the PA technique and the system developed to measure low thermal conductivity samples properly work. All the measurements are found to be within the interval of uncertainty.

Table 4.IV. Thermal conductivity of two different samples measured by three different techniques.

PANI/GNP	Density ($kg \cdot m^3$)	Specific heat ($J \cdot kg^{-1} \cdot K^{-1}$)	κ system ($W \cdot m^{-1} \cdot K^{-1}$)	PA technique ($W \cdot m^{-1} \cdot K^{-1}$)	Laser flash ($W \cdot m^{-1} \cdot K^{-1}$)
2.5 wt.%	1385	1020	0.48 ± 0.05	0.44 ± 0.03	-
50 wt.%	1605	860	-	3.7± 0.3	3.3 ± 0.3

Once the systems were checked, the rest of the nanocomposites were measured by means of the so-called κ system since it is able to directly measure the thermal conductivity and no specific heat and density extra measurements are needed. Figure 4.18 (d) shows the thermal conductivity as a function of the volume fraction of filling content. Neat PANI measurement results in a thermal conductivity of 0.46 $W \cdot m^{-1} \cdot K^{-1}$, in good agreement with previous values stated in literature[52]. The thermal conductivity rises as the GNPs content is increased up to one order of magnitude when compared to PANI.

The nanocomposite can be illustrated as a parallel thermal resistor[57] whose thermal conductivity is given by the expression:

$$\kappa = \frac{V_{GNP}\kappa_{GNP} + V_{PANI}\kappa_{PANI}}{V_{TOTAL}}, \tag{4.13}$$

where κ is the effective thermal conductivity measured, V_{GNP} is the GNPs volume fraction, κ_{GNP} is the GNPs thermal conductivity, V_{PANI} is the volume fraction of neat PANI, κ_{PANI} is the pure PANI thermal conductivity and V_{TOTAL} is the total volume of the pellet. Figure 4.22 shows a linear fitting from which the thermal conductivity of neat PANI and pristine GNP could be extracted by employing Eq. 4.13. Although a good linear fit is achieved, the neat PANI thermal conductivity was found to be 0.30 $W \cdot m^{-1} \cdot K^{-1}$ which is significantly different from the experimental obtained value, 0.46 $W \cdot m^{-1} \cdot K^{-1}$ possibly owing Eq. 4.13 is only valid for an ideal parallel thermal resistor. The two first data points of Figure 4.22, corresponding to pure PANI and the 1 wt. % GNPs content pellets, do not fit the equation since their content is lower than the percolation threshold so these points have not been taken into consideration. This fitting is used to verify that the nanocomposite could approximately work as a parallel thermal resistor like the represented sketch of the inset of Figure 4.22. Moreover, from the fitting the GNPs thermal conductivity value was found to be near to 7 $W \cdot m^{-1} \cdot K^{-1}$. The intrinsic thermal conductivity of the GNPs is different depending on the direction. GNPs have a much higher value in the direction parallel to the surface, κ >1000 $W \cdot m^{-1} \cdot K^{-1}$, than in the direction perpendicular to the surface, κ <10 $W \cdot m^{-1} \cdot K^{-1}$ [58]. The extracted results sustain that most GNPs are positioned parallel to the surface of the pellets and, hence, the heat flux across them takes place in the low thermal conductivity path as seen in the inset of Figure 4.22.

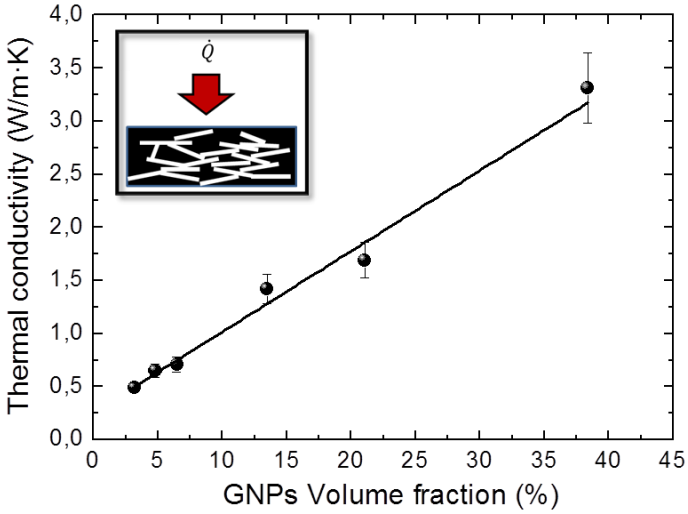

Figure 4.22. Linear fit of the thermal conductivity as a function of the volume fraction. The inset shows a scheme of the nanocomposite as a parallel thermal resistor.

These results could be used to deduce the positioning of the GNPs in the pellet so a notable anisotropy is clearly proved. This conclusion is also revealed thanks to the SEM images. In Figure

4.17 a cluster of GNPs with their surfaces parallel to the surface of the pellet can be distinguished. Due to this anisotropy, it is not possible to estimate the figure of merit. Both the electrical conductivity and the Seebeck coefficient measurements were carried out in the in plane direction, whereas the thermal conductivity measurements were performed in the out-of-plane direction. The power factor in the in plane direction of these nanocomposites (Figure 4.18 (c)) could be utilized as a scale to evaluate the quality of these results in comparison with previous works. The power factor achieved in this study, 14 $\mu W \cdot m^{-1} \cdot K^{-2}$ is higher than other investigations based on polyaniline such us the system PANI/GNPs composite thin film, 6 $\mu W \cdot m^{-1} \cdot K^{-2}$ [30]; PANI/GNs composite pellets, 5.6 $\mu W \cdot m^{-1} \cdot K^{-2}$ [27]; PANI/GNs composite pellets, 3 $\mu W \cdot m^{-1} \cdot K^{-2}$ [26]; PANI/CNTs composite pellets, 5 $\mu W/m \cdot K^{2}$ [52]; or PANI/Graphite, 4 $\mu W \cdot m^{-1} \cdot K^{-2}$ [59].

A summary of the state-of-the-art results is shown on Table 4.V. Since the samples are probably anisotropic, it is not feasible to estimate the figure of merit unless all the measurements are carried out in the same direction of the specimen.

Table 4.V. Summary of thermoelectric properties of the best composites of organic and inorganic materials. The symbols ⊥ and ‖ designate the direction of the measurement, perpendicular or parallel to the surface to the sample, respectively. In case the measurements are performed in different direction, zT is not estimated because the sample might be anisotropic.

Polymer	Additive	Nanofiller	Preparation method	Electrical conductivity ($S \cdot cm^{-1}$)	Seebeck coefficient ($\mu V \cdot K^{-1}$)	PF ($\mu W \cdot m^{-1} \cdot K^{-2}$)	Thermal Conductivity ($W \cdot m^{-1} \cdot K^{-1}$)	zT (T)	Year [Ref.]
P3HT	-	SW-CNT (81 wt.%)	Thin film	180 ‖	32 ‖	18 ‖	0.13 (bulk)⊥	-	2013 [29]
P3HT	$FeCl_3$	SW-CNT (42-81 wt.%)	Thin film	1100 ‖	29 ‖	95 ‖	-	-	2013 [29]
P3HT	$FeCl_3$	MW-CNT (10-40 wt.%)	Thin film	80 ‖	29 ‖	6 ‖	-	-	2013 [29]
P3HT	-	MW-CNT (50 wt.%)	Thin film	10 ‖	12 ‖	0.2 ‖	0.16 (bulk)⊥	-	2013 [29]
PANI	-	PbTe NP core-shell	Interfacial polymerization	0.02 ‖	626 ‖	0.8 ‖	-	-	2011 [60]
PANI	-	SW-CNT (40wt%)	*In situ* polymerization	125 ‖	40 ‖	20 ‖	1.5⊥	-	2010 [61]
PANI	**HCl**	**GNP (50 wt.%)**	**Mechanical grinding + cold pressing**	**123** ‖	**34** ‖	**14** ‖	**0.46-3** ⊥	-	**This work**
PANI	HCl	MW-CNT (40wt.%)	*In situ* polymerization and electro-spinning	17.1 ‖	10 ‖	0.17 ‖	-	-	2012 [62]
PANI	-	GN (50 wt%)	Thin film	59 ‖	31 ‖	5.6 ‖	-	-	2012 [27]
PANI	-	CNT (15.8wt%)	Two-step	61 ‖	29 ⊥		0.4-0.5 ⊥	-	2010 [52]
PANI	-	GN (30wt%)	Chemical polymerization	10-50 ‖	10-40 ‖	3 ‖	0.2-0.7⊥	-	2013 [26]
PANI	$HClO_4$	Graphite (50wt%)	Mechanical ball milling + cold pressing	120 (393K) ‖	19 (393 K) ‖	4 (393K) ‖	1.20 (393K)⊥	-	2011 [59]
PCDTBT	$FeCl_3$	-	Polymerization Procedure	160 ‖	34 ‖	19 ‖	-	-	2009 [17]
PEDOT	PSS	Te nanorods (85%)	Mixing	19 ‖	163 ‖	51 ‖	0.22-0.30⊥	-	2010 [63]
PEDOT	ToS	-	spin coating + partial electrochemical reduction	923 ‖	117 ‖	1270 ‖	-	-	2013 [19]
PEDOT	-	Graphene (2wt%)	Thin films	32 ‖	59 ‖	11 ‖	0.14 ⊥	-	2012 [64]
PEDOT	PSS, DMSO	SWCNT (35%)	-	400 ‖	25 ‖	25 ‖	0.2-0.4⊥	-	2009 [65]
PEDOT	PSS DMSO	-	Thin films by casting	300 ‖	14 ‖	6 ‖	-	-	2011 [66]
PEDOT	ToS	-	spin coating + partial chemical reduction	300 -10^{-4} ‖	40 -780 ‖	324 ‖	0.37 ‖	0.25 (RT)	2011 [18]
PVAc	-	CNT (20wt%)	-	48 ⊥	40 ⊥	7 ⊥	0.34	0.006 ⊥	2008 [28]
PANI	-	Graphene	Solution-assistant dispersion method	856 ‖	15 ‖	19 ‖	-	-	2014
P(NDIOD-T2)	N-DMBI	-	Doped in solution and spin cast	0.008 ‖	-850 ‖	0.6 ‖	-	-	2014 [67]
PEDOT	BTFMSI	-	Electrochemical deposition	1060 ‖	37 ‖	147 ‖	0.19 ⊥	0.22	2014 [68]
PEDOT	PSS, 5 % DMSO and 0.3% PEO	-		1061 ‖	38.4 ‖	157.35 ‖	-	-	2015 [69]
PANI	CSA	Graphene (48 wt. %)	In situ polymerization + dropping	814 ‖	26 ‖	55 ‖	-	-	2015 [70]
PCDTBT	$FeCl_3$	-	Drop casting	60 ‖	37 ‖	8 ‖	1 ⊥	0.0026	2015 [71]
PEDOT	PSS	F-C60	Solution+Spin-coting	720 ‖	34 ‖	83.2 ‖	0.25⊥	0.1	2015 [72]

4.5 Summary

In the first part of the chapter, the validity of the experimental setup to carry out bulk thermal diffusivity was proved. Six different samples were measured by two different procedures: the phase lag and the discontinuity of the tangent as a function of the frequency. A deviation from the expected thermal diffusivity values lower than 10 % was generally obtained for both methods. Moreover, the experimental uncertainty which involves both, instrumental and random uncertainties was found to be in the vicinity of 5 %, which is considerably low for a thermal diffusivity measurement technique.

Secondly, the thermoelectric properties of zinc oxide doped with different amounts of nickel oxide sintered by SPS were studied. The effect of varying the grain size of the raw material and the sintering temperature were examined. A threshold in the NiO concentration for both types of ZnO powders, regular and nano, and temperatures was found. This threshold produces the lowest electrical resistivity values, which is related with the appearance of an impurity level in the bandgap. On the other hand, if the NiO concentration is further increased, the electrical resistivity increases due to a secondary phase formation, observed by Raman spectroscopy. Regarding the Seebeck coefficient, huge values were found. Regular ZnO sintered at 1100ºC exhibits a Seebeck coefficient of around-845 $\mu V \cdot K^{-1}$ for a concentration of 0.1 wt. % NiO which yields a power factor of approximately 620 $\mu W \cdot K^{-1} \cdot m^{-2}$ at 65 ºC. Nano ZnO samples show the highest maximum power factor, 379 $\mu W \cdot K^{-1} \cdot m^{-2}$ at 56 ºC, for pure ZnO samples sintered at 1100 ºC. The thermal diffusivity of the pellets was measured by the phase lag method. Thermal conductivity values were calculated from the density and specific heat, showing values of pure ZnO of the same order of magnitude as the values previously reported. In particular, samples fabricated at 850 ºC exhibit the lower thermal conductivity values. The addition of NiO decreases the thermal conductivity until reaching a threshold value from which the thermal conductivity remains constant, 25 $W \cdot m^{-1}K^{-1}$ and 15 $W \cdot m^{-1}K^{-1}$, for regular and nano grain sizes, respectively. Finally, the figure of merit was calculated, showing the highest value for regular ZnO and 1 wt. % NiO sintered at 1100 ºC, with a value of 0.0073 at room temperature, which is higher than previously reported values for this material at this temperature range.

Finally, the thermoelectric properties of a composite made of polyaniline blended with graphene nanoplatelets (GNP) were studied. The power factor and the thermal conductivity were measured as a function of the GNP content. A power factor of 14 $\mu W \cdot m^{-1} \cdot K^{-2}$ for a GNP content of 50 wt. % was found, which was the highest reported until that moment in the literature. Moreover, the thermal conductivity was also determined. For that purpose, three different techniques were used to accurately measure it. An experimental setup based on the steady-state method was specially designed for polymer measurements. The photoacoustic technique and the laser flash were also used to corroborate the results. From those measurements, a parallel thermal conductor model could be established which indicated that the GNP were oriented parallel to the surface of the samples. Due to

the anisotropy of the samples, the figure of merit could not be calculated since the power factor was measured in the in-plane direction whereas the thermal conductivity was determined in the out-of-plane direction.

4.6 References

1. Balderas-López, J. A.; Mandelis, A., Self-normalized photothermal technique for accurate thermal diffusivity measurements in thin metal layers. *Review of Scientific Instruments* **2003,** *74*, 5219-5225.
2. Bertolotti, M.; Li Voti, R.; Liakhou, G.; Sibilia, C., On the photodeflection method applied to low thermal diffusivity measurements. *Review of Scientific Instruments* **1993,** *64*, 1576-1583.
3. http://www.almazoptics.com/sapphire.htm Sapphire properties.
4. Lide, D. R., CRC Handbook of Chemistry and Physics. In Press, C., Ed. Boca Raton, 2005.
5. Janotti, A.; Van de Walle, C. G., Fundamentals of zinc oxide as a semiconductor. *Reports on Progress in Physics* **2009,** *72*, 126501.
6. Tsubota, T.; Ohtaki, M.; Eguchi, K.; Arai, H., Thermoelectric properties of Al-doped ZnO as a promising oxide material for high-temperature thermoelectric conversion. *Journal of Materials Chemistry* **1997,** *7*, 85-90.
7. Ohtaki, M.; Araki, K.; Yamamoto, K., High thermoelectric performance of dually doped ZnO ceramics. *Journal of Elec Materi* **2009,** *38*, 1234-1238.
8. Jood, P.; Mehta, R. J.; Zhang, Y.; Peleckis, G.; Wang, X.; Siegel, R. W.; Borca-Tasciuc, T.; Dou, S. X.; Ramanath, G., Al-Doped Zinc Oxide Nanocomposites with Enhanced Thermoelectric Properties. *Nano Letters* **2011,** *11*, 4337-4342.
9. Wu, Z.-H.; Xie, H.-Q.; Zhai, Y.-B., Enhanced thermoelectric figure of merit in nanostructured ZnO by nanojunction effect. *Applied Physics Letters* **2013,** *103*, 243901.
10. Park, K.; Seong, J.; Kim, G. H., NiO added Zn 1− x Ni x O (0≤ x≤ 0.05) for thermoelectric power generation. *Journal of Alloys and Compounds* **2009,** *473*, 423-427.
11. Colder, H.; Guilmeau, E.; Harnois, C.; Marinel, S.; Retoux, R.; Savary, E., Preparation of Ni-doped ZnO ceramics for thermoelectric applications. *Journal of the European Ceramic Society* **2011,** *31*, 2957-2963.
12. Rubio-Marcos, F.; Manzano, C. V.; Reinosa, J. J.; Lorite, I.; Romero, J.; Fernández, J. F.; Martín-González, M. S., Modification of optical properties in ZnO particles by surface deposition and anchoring of NiO nanoparticles. *Journal of Alloys and Compounds* **2011,** *509*, 2891-2896.
13. Fernández-Hevia, D.; de Frutos, J.; Caballero, A. C.; Fernández, J. F., Bulk-grain resistivity and positive temperature coefficient of ZnO-based varistors. *Applied Physics Letters* **2003,** *82*, 212-214.
14. Robie, R. A.; Haselton Jr, H. T.; Hemingway, B. S., Heat capacities and entropies at 298.15 K of MgTiO3 (geikielite), ZnO (zincite), and ZnCO3 (smithsonite). *The Journal of Chemical Thermodynamics* **1989,** *21*, 743-749.
15. Özgür, Ü.; Alivov, Y. I.; Liu, C.; Teke, A.; Reshchikov, M. A.; Doğan, S.; Avrutin, V.; Cho, S. J.; Morkoç, H., A comprehensive review of ZnO materials and devices. *Journal of Applied Physics* **2005,** *98*, 1-103.
16. Cheng, H.; Xu, X. J.; Hng, H. H.; Ma, J., Characterization of Al-doped ZnO thermoelectric materials prepared by RF plasma powder processing and hot press sintering. *Ceramics International* **2009,** *35*, 3067-3072.
17. Aïch, R. d. B.; Blouin, N.; Bouchard, A. l.; Leclerc, M., Electrical and Thermoelectric Properties of Poly(2,7-Carbazole) Derivatives. *Chemistry of Materials* **2009,** *21*, 751-757.
18. Bubnova, O.; Khan, Z. U.; Malti, A.; Braun, S.; Fahlman, M.; Berggren, M.; Crispin, X., Optimization of the thermoelectric figure of merit in the conducting polymer poly(3,4-ethylenedioxythiophene). *Nature Materials* **2011,** *10*, 429-433.
19. Park, T.; Park, C.; Kim, B.; Shin, H.; Kim, E., Flexible PEDOT electrodes with large thermoelectric power factors to generate electricity by the touch of fingertips. *Energy & Environmental Science* **2013,** *6*, 788-792.
20. Kim, G. H.; Shao, L.; Zhang, K.; Pipe, K. P., Engineered doping of organic semiconductors for enhanced thermoelectric efficiency. *Nature Materials* **2013**.
21. Choy, C. L., Thermal conductivity of polymers. *Polymer* **1977,** *18*, 984-1004.
22. Hu, M.; Yu, D.; Wei, J., Thermal conductivity determination of small polymer samples by differential scanning calorimetry. *Polymer Testing* **2007,** *26*, 333-337.

23. Kaneko, H.; Ishiguro, T.; Takahashi, A.; Tsukamoto, J., Magnetoresistance and thermoelectric power studies of metal-nonmetal transition in iodine-doped polyacetylene. *Synthetic Metals* **1993,** *57*, 4900-4905.
24. Holland, E. R.; Pomfret, S. J.; Adams, P. N.; Abell, L.; Monkman, A. P., Doping dependent transport properties of polyaniline-CSA films. *Synthetic Metals* **1997,** *84*, 777-778.
25. Li, J.; Tang, X.; Li, H.; Yan, Y.; Zhang, Q., Synthesis and thermoelectric properties of hydrochloric acid-doped polyaniline. *Synthetic Metals* **2010,** *160*, 1153-1158.
26. Lu, Y.; Song, Y.; Wang, F., Thermoelectric properties of graphene nanosheets-modified polyaniline hybrid nanocomposites by an in situ chemical polymerization. *Materials Chemistry and Physics* **2013,** *138*, 238-244.
27. Du, Y.; Shen, S. Z.; Yang, W.; Donelson, R.; Cai, K.; Casey, P. S., Simultaneous increase in conductivity and Seebeck coefficient in a polyaniline/graphene nanosheets thermoelectric nanocomposite. *Synthetic Metals* **2012,** *161*, 2688-2692.
28. Yu, C.; Kim, Y. S.; Kim, D.; Grunlan, J. C., Thermoelectric Behavior of Segregated-Network Polymer Nanocomposites. *Nano Letters* **2008,** *8*, 4428-4432.
29. Bounioux, C.; Diaz-Chao, P.; Campoy-Quiles, M.; Martin-Gonzalez, M. S.; Goni, A. R.; Yerushalmi-Rozen, R.; Muller, C., Thermoelectric composites of poly(3-hexylthiophene) and carbon nanotubes with a large power factor. *Energy & Environmental Science* **2013,** *6*, 918-925.
30. Xiang, J.; Drzal, L. T., Templated growth of polyaniline on exfoliated graphene nanoplatelets (GNP) and its thermoelectric properties. *Polymer* **2012,** *53*, 4202-4210.
31. Li, B.; Zhong, W.-H., Review on polymer/graphite nanoplatelet nanocomposites. *J Mater Sci* **2011,** *46*, 5595-5614.
32. Li, Y.; Zhu, J.; Wei, S.; Ryu, J.; Sun, L.; Guo, Z., Poly(propylene)/Graphene Nanoplatelet Nanocomposites: Melt Rheological Behavior and Thermal, Electrical, and Electronic Properties. *Macromolecular Chemistry and Physics* **2011,** *212*, 1951-1959.
33. Park, Y. W.; Lee, Y. S.; Park, C.; Shacklette, L. W.; Baughman, R. H., Thermopower and conductivity of metallic polyaniline. *Solid State Communications* **1987,** *63*, 1063-1066.
34. Ginder, J. M.; Epstein, A. J.; MacDiarmid, A. G., Electronic phenomena in polyaniline. *Synthetic Metals* **1989,** *29*, 395-400.
35. Dalas, E.; Sakkopoulos, S.; Vitoratos, E., Chemical preparation, direct-current conductivity and thermopower of polyaniline and polypyrrole composites. *J Mater Sci* **1994,** *29*, 4131-4133.
36. Y.W. Park, J. S. M., M.K. Bak, J.-I. Jin, Electrical properties of polyaniline and substituted polyaniline derivatives. *Synthetic Metals* **1989**, 389–394.
37. Quillard, S.; Louarn, G.; Lefrant, S.; Macdiarmid, A. G., Vibrational analysis of polyaniline: A comparative study of leucoemeraldine, emeraldine, and pernigraniline bases. *Physical Review B* **1994,** *50*, 12496-12508.
38. Zengin, H.; Zhou, W.; Jin, J.; Czerw, R.; Smith, D. W.; Echegoyen, L.; Carroll, D. L.; Foulger, S. H.; Ballato, J., Carbon Nanotube Doped Polyaniline. *Advanced Materials* **2002,** *14*, 1480-1483.
39. Yu, Y.; Che, B.; Si, Z.; Li, L.; Chen, W.; Xue, G., Carbon nanotube/polyaniline core-shell nanowires prepared by in situ inverse microemulsion. *Synthetic Metals* **2005,** *150*, 271-277.
40. Kirkpatrick, S., Percolation and Conduction. *Reviews of Modern Physics* **1973,** *45*, 574-588.
41. Sherman, R. D.; Middleman, L. M.; Jacobs, S. M., Electron transport processes in conductor-filled polymers. *Polymer Engineering & Science* **1983,** *23*, 36-46.
42. Kilbride, B. E.; Coleman, J. N.; Fraysse, J.; Fournet, P.; Cadek, M.; Drury, A.; Hutzler, S.; Roth, S.; Blau, W. J., Experimental observation of scaling laws for alternating current and direct current conductivity in polymer-carbon nanotube composite thin films. *Journal of Applied Physics* **2002,** *92*, 4024-4030.
43. Musumeci, A. W.; Silva, G. G.; Liu, J.-W.; Martens, W. N.; Waclawik, E. R., Structure and conductivity of multi-walled carbon nanotube/poly(3-hexylthiophene) composite films. *Polymer* **2007,** *48*, 1667-1678.
44. M, R.; Yoon, C. O.; Yang, C. Y.; Moses, D.; Smith, P.; Heeger, A. J.; Cao, Y., Transport in polyaniline networks near the percolation threshold. *Physical Review B* **1994,** *50*, 13931-13941.
45. Sheng, P.; Sichel, E. K.; Gittleman, J. I., Fluctuation-Induced Tunneling Conduction in Carbon-Polyvinylchloride Composites. *Physical Review Letters* **1978,** *40*, 1197-1200.

46. Medlin, D. L.; Snyder, G. J., Interfaces in bulk thermoelectric materials: A review for Current Opinion in Colloid and Interface Science. *Current Opinion in Colloid & Interface Science* **2009,** *14*, 226-235.
47. Minnich, A. J.; Dresselhaus, M. S.; Ren, Z. F.; Chen, G., Bulk nanostructured thermoelectric materials: current research and future prospects. *Energy & Environmental Science* **2009,** *2*, 466-479.
48. Ko, D.-K.; Kang, Y.; Murray, C. B., Enhanced Thermopower via Carrier Energy Filtering in Solution-Processable Pt–Sb2Te3 Nanocomposites. *Nano Letters* **2011,** *11*, 2841-2844.
49. Zebarjadi, M.; Esfarjani, K.; Dresselhaus, M. S.; Ren, Z. F.; Chen, G., Perspectives on thermoelectrics: from fundamentals to device applications. *Energy & Environmental Science* **2012,** *5*, 5147-5162.
50. Heremans, J. P.; Thrush, C. M.; Morelli, D. T., Thermopower enhancement in PbTe with Pb precipitates. *Journal of Applied Physics* **2005,** *98*, 063703-6.
51. He, M.; Ge, J.; Lin, Z.; Feng, X.; Wang, X.; Lu, H.; Yang, Y.; Qiu, F., Thermopower enhancement in conducting polymer nanocomposites via carrier energy scattering at the organic-inorganic semiconductor interface. *Energy & Environmental Science* **2012,** *5*, 8351-8358.
52. Meng, C.; Liu, C.; Fan, S., A Promising Approach to Enhanced Thermoelectric Properties Using Carbon Nanotube Networks. *Advanced Materials* **2010,** *22*, 535-539.
53. Grujicic, M.; Zhao, C. L.; Dusel, E. C., The effect of thermal contact resistance on heat management in the electronic packaging. *Applied Surface Science* **2005,** *246*, 290-302.
54. John H. Lienhard IV, J. H. L. V., A Heat Transfer Texbook. In 4th ed. ed.; Press, P., Ed. Phlogiston Press: Cambridge, Massachusetts, U.S.A., 2011.
55. Abad, B.; Díaz-Chao, P.; Almarza, A.; Amantia, D.; Vázquez-Campos, S.; Isoda, Y.; Shinohara, Y.; Briones, F.; Martín-González, M. S. In *Thermal diffusivity measurement system applied to polymers*, AIP Conference Proceedings, 2012; 2012; pp 354-357.
56. Pop, E.; Varshney, V.; Roy, A. K., Thermal properties of graphene: Fundamentals and applications. *MRS Bulletin* **2012,** *37*, 1273-1281.
57. Agari, Y.; Uno, T., Estimation on thermal conductivities of filled polymers. *Journal of Applied Polymer Science* **1986,** *32*, 5705-5712.
58. Graphene Nanoplatelets. In STREM Chemicals, INC.: 2012.
59. Wang, L.; Wang, D.; Zhu, G.; Li, J.; Pan, F., Thermoelectric properties of conducting polyaniline/graphite composites. *Materials Letters* **2011,** *65*, 1086-1088.
60. Wang, Y. Y.; Cai, K. F.; Yin, J. L.; An, B. J.; Du, Y.; Yao, X., In situ fabrication and thermoelectric properties of PbTe–polyaniline composite nanostructures. *J Nanopart Res* **2011,** *13*, 533-539.
61. Yao, Q.; Chen, L.; Zhang, W.; Liufu, S.; Chen, X., Enhanced Thermoelectric Performance of Single-Walled Carbon Nanotubes/Polyaniline Hybrid Nanocomposites. *ACS Nano* **2010,** *4*, 2445-2451.
62. Wang, Q.; Yao, Q.; Chang, J.; Chen, L., Enhanced thermoelectric properties of CNT/PANI composite nanofibers by highly orienting the arrangement of polymer chains. *Journal of Materials Chemistry* **2012,** *22*, 17612-17618.
63. See, K. C.; Feser, J. P.; Chen, C. E.; Majumdar, A.; Urban, J. J.; Segalman, R. A., Water-Processable Polymer−Nanocrystal Hybrids for Thermoelectrics. *Nano Letters* **2010,** *10*, 4664-4667.
64. Kim, G. H.; Hwang, D. H.; Woo, S. I., Thermoelectric properties of nanocomposite thin films prepared with poly(3,4-ethylenedioxythiophene) poly(styrenesulfonate) and graphene. *Physical Chemistry Chemical Physics* **2012,** *14*, 3530-3536.
65. Kim, D.; Kim, Y.; Choi, K.; Grunlan, J. C.; Yu, C., Improved Thermoelectric Behavior of Nanotube-Filled Polymer Composites with Poly(3,4-ethylenedioxythiophene) Poly(styrenesulfonate). *ACS Nano* **2009,** *4*, 513-523.
66. Liu, C.; Jiang, F.; Huang, M.; Yue, R.; Lu, B.; Xu, J.; Liu, G., Thermoelectric Performance of Poly(3,4-Ethylenedioxy-thiophene)/Poly(Styrenesulfonate) Pellets and Films. *Journal of Elec Materi* **2011,** *40*, 648-651.
67. Schlitz, R. A.; Brunetti, F. G.; Glaudell, A. M.; Miller, P. L.; Brady, M. A.; Takacs, C. J.; Hawker, C. J.; Chabinyc, M. L., Solubility-Limited Extrinsic n-Type Doping of a High Electron Mobility Polymer for Thermoelectric Applications. *Advanced Materials* **2014,** *26*, 2825-2830.

68. Culebras, M.; G?mez, C. M.; Cantarero, A., Enhanced thermoelectric performance of PEDOT with different counter-ions optimized by chemical reduction. *Journal of Materials Chemistry A* **2014,** *2*, 10109-10115.
69. Yi, C.; Wilhite, A.; Zhang, L.; Hu, R.; Chuang, S. S. C.; Zheng, J.; Gong, X., Enhanced Thermoelectric Properties of Poly(3,4-ethylenedioxythiophene):poly(styrenesulfonate) by Binary Secondary Dopants. *ACS Applied Materials & Interfaces* **2015,** *7*, 8984-8989.
70. Wang, L.; Yao, Q.; Bi, H.; Huang, F.; Wang, Q.; Chen, L., PANI/graphene nanocomposite films with high thermoelectric properties by enhanced molecular ordering. *Journal of Materials Chemistry A* **2015,** *3*, 7086-7092.
71. Maiz, J.; Muñoz Rojo, M.; Abad, B.; Wilson, A. A.; Nogales, A.; Borca-Tasciuc, D. A.; Borca-Tasciuc, T.; Martín-González, M., Enhancement of thermoelectric efficiency of doped PCDTBT polymer films. *RSC Advances* **2015,** *5*, 66687-66694.
72. Zhang, K.; Wang, S.; Zhang, X.; Zhang, Y.; Cui, Y.; Qiu, J., Thermoelectric performance of p-type nanohybrids filled polymer composites. *Nano Energy* **2015,** *13*, 327-335.

Chapter 5:

Multilayered model: films, porous structures and nanowires measurement

This chapter proves the validity of the photoacoustic technique for measuring samples composed of several layers by means of the multilayered model. For that purpose, measurements of reference samples are firstly shown. Once the system along with the model was demonstrated to be valid, several studies of different types of materials and structures such as thin and thick films, porous alumina membranes and nanowires embedded into alumina membranes are presented to show the validity of the technique to measure different morphology types.

5.1 Reference samples

In order to ensure both the reliable operation of the experimental setup and the good accord with the theory explained in Section 3.3.2, reference samples with different thermal conductivity values were examined. Multilayered structures are measured by normalizing with a bulk reference sample. The reference sample is a bulk piece of fused silica thick enough so that it is thermally thick for the whole range of frequencies that the setup is able to use (see its properties in Table 5.I). As explained by Wang *et al.* [1], bulk materials have a frequency independent phase shift equal to -90 deg. Once the reference and problem sample are measured, the actual phase shift of the sample,ϕ_{sample} is obtained as:

$$\phi_{sample} = \phi_{measured} - \phi_{reference} - 90 \tag{5.1}$$

where $\phi_{measured}$ and $\phi_{reference}$ are the measured phase shifts of the sample and the reference, respectively. By fitting the extracted ϕ_{sample} as a function of the frequency, the thermal conductivity of the unknown layer can be obtained.

Table 5.I. Reference samples properties used to normalize the phase shift of the sample under study.

Sample	Thickness (μm)	Density ($kg \cdot m^{-3}$)	Specific Heat ($J \cdot kg^{-1} \cdot K^{-1}$)	Thermal conductivity ($W \cdot m^{-1} \cdot K^{-1}$)
Fused silica	1000	2200 [2]	753 [2]	1.35 [2]

All the reference samples are formed by the investigated layer onto a substrate so that the model involves two layers (the layer under study and the absorbing material) along with the backing material (the substrate) and the air layer. Moreover, the thermal resistances between these layers also play an important role. It will be necessary to leave them as free parameters when performing the fittings. As a general procedure, a simulation of the phase shift is typically carried out in order to locate the most suitable frequency range where the phase shift is found to be more sensible, as explained in section 3.3.2.1. These simulations are only an approximation since the actual parameters could be different from the fixed values used to perform them. Then, measurements are carried out and a final election of the frequency range is made by evaluating the sensitivity of the thermal conductivity as a function of the frequency.

Figure 1 (a), (b) and (c) show the fitting of the reference samples at the most sensible frequency range found for each case. Details of the thermal conductivity extraction are given below for each sample.

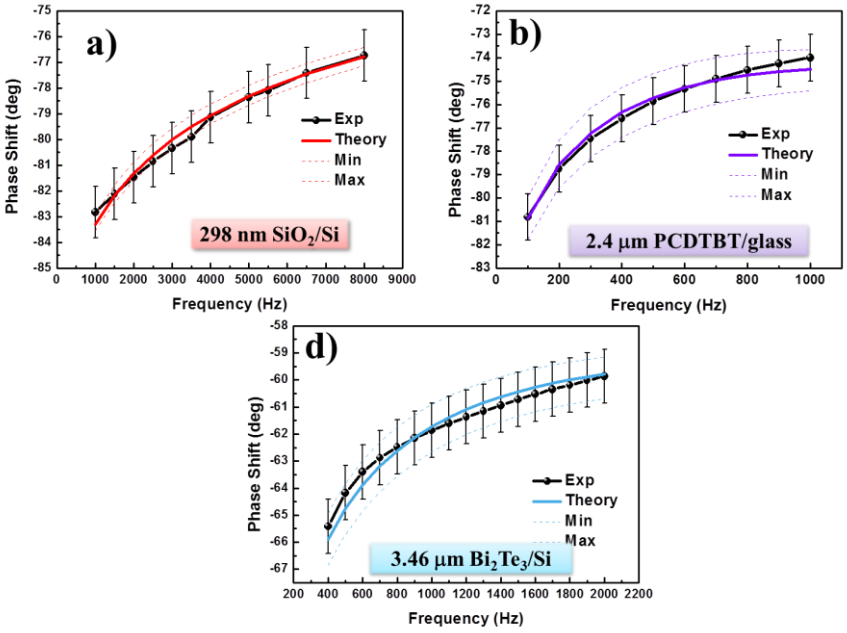

Figure 5.1. Examples of experimental phase shift as a function of the frequency along with the best fitting for (a) SiO_2 (b) PCDTBT and (c) As-grown Bi_2Te_3 films.

5.1.1 SiO_2 thin film

One of the most common samples used to characterize the thermal conductivity of a system is a thermally grown amorphous silica layer, SiO_2. In this work, a layer of 298 nm of SiO_2 was fabricated by thermal oxidation onto a silicon substrate in the Mechanical Engineering Building of Purdue University (Indiana, USA) by Dr. Stephen L. Hodson.

Amorphous silica is a well-known material, whose thermal properties can be found in the literature and are shown in Table 5.II. Moreover, this sample was also measured by the photoacoustic setup developed in Purdue University under the supervision of Professor Xianfan Xu. The experimental value obtained by this technique is in good agreement with the literature data, 1.35 $W \cdot m^{-1} \cdot K^{-1}$ [3].

Table 5.II. Properties of the each layer used to perform the fitting of the SiO_2 thin film thermal conductivity.

Sample	Thickness (µm)	Density ($kg \cdot m^{-3}$)	Specific Heat ($J \cdot kg^{-1} \cdot K^{-1}$)	Measured Thermal conductivity ($W \cdot m^{-1} \cdot K^{-1}$)	Expected thermal conductivity ($W \cdot m^{-1} \cdot K^{-1}$)	Desv. (%)
Si	500	2330 [3]	712 [3]	-	148 [3]	-
SiO_2 (vitreous)	0.298	2220 [3]	745 [3]	***1.46 ± 0.15***	1.35 [3]	8
Ti	0.08	4506 [3]	523 [3]	-	21.9	-
Air	0	1.176	1007	-	0.026	-

Figure 5.1 (a) shows an example of the experimental phase shift as a function of the frequency and the best fitting performed by the multilayered model for the SiO_2 sample. In order to ensure the suitability of the fitting, the sensitivity was also checked finding the highest sensitivity of the thermal conductivity of the investigated layer for the frequency range selected. The density and specific heat of the thermally grown amorphous silicon dioxide were taken from the literature [3] and the thermal conductivity was finally found to be 1.46 $W \cdot m^{-1} \cdot K^{-1}$. As shown in Table 5.II, this value differs from the literature value in an 8 %, which can be considered as satisfactory.

5.1.2 Organic materials: PDCTBT film

A polymer known as poly [N-9'-heptadecanyl-2,7-carbazole-alt-5,5-(4',7'-di-2-thienyl-2',1',3-benzothiadizole)] (PCDTBT) was also used to test the experimental setup. In this case, the thermal conductivity was measured by two different techniques, Photoacoustic technique and Scanning Thermal Microscopy (SThM) in order to check the ability of PA technique to measure polymer films.

The films of PCDTBT were fabricated *via* drop casting on glass substrates. As explained in Section 2.1.3, in order to produce a 50 $mg \cdot mL^{-1}$ solution, chloroform at room temperature was employed to dissolve PCDTBT supplied by Solaris Chem Inc. Then, the polymer solution was drop-casted on a glass substrate and the film was finally obtained after the total evaporation of the chloroform solvent, achieved at room temperature for 24 h. A film of PCDTBT was produced with a thickness of 2.4 μm and roughness of around 90 nm.

Table 5.III. Properties of the each layer used to perform the fitting of the PCDTBT film thermal conductivity.

Layer	**Thickness (μm)**	**Density ($kg \cdot m^{-3}$)**	**Specific heat ($J \cdot g^{-1} \cdot K^{-1}$)**	**Measured Thermal conductivity ($W \cdot m^{-1} \cdot K^{-1}$)**	**Expected thermal conductivity ($W \cdot m^{-1} \cdot K^{-1}$)**	**Desv. (%)**
Glass	1000	2520 [3]	875 [4]	-	1.1 [3]	-
PCDTBT	2.4	1160	810	***0.20 ± 0.02***	0.25 ± 0.04 (SThM) [5]	20
Ti	0.08	4506 [3]	523 [3]	-	21.9	-
Air	0	1.176	1007	-	0.026	-

The polymer films were detached from the glass slide by plunging them in distilled water. This procedure yields to a free-standing PCDTBT film whose density and specific heat could be measured without the influence of the substrate.

An example of the experimental phase shift as a function of the frequency range is shown in Figure 5.1 (b). The frequency range was selected by ensuring the highest sensitivity of the thermal conductivity of the polymer film. The PA technique yielded a value of 0.20 ± 0.02 $W \cdot m^{-1} \cdot K^{-1}$, which is within the error interval of the measurement carried out by the SThM of our group, 0.25 ± 0.04

$W \cdot m^{-1} \cdot K^{-1}$. No literature values of the thermal conductivity of PCDTBT can be found. However, its thermal conductivity is in the range of the common polymers [6, 7].

5.1.3 Bismuth telluride electrodeposited thick films

Electrodeposited bismuth telluride (Bi_2Te_3) films were examined by both, PA technique and Time Domain thermoreflectance (TDTR) during a stay in Purdue University (Indiana, USA), in order to study the performance of the PA technique on samples with high roughness.

Bismuth telluride based alloys stand for the main bulk thermoelectric material for applications working from room temperature to approximately 100 ˚C [8]. The crystal structure of Bi_2Te_3 is rhombohedral-hexagonal, whose unit cell parameters at room temperature are a = 3.8 Å and c = 30.5 Å. This material is a semiconductor with a band gap of 0.15 eV [9]. Its structure is composed of five layers along the *c-axis*: Te(1)-Bi-Te(2)-Bi-Te(1) as seen in Figure 1 (a). Te(1) and Te(2) are covalently bonded with Bi, whereas van der Waals bonds are established between adjacent Te(1) layers.

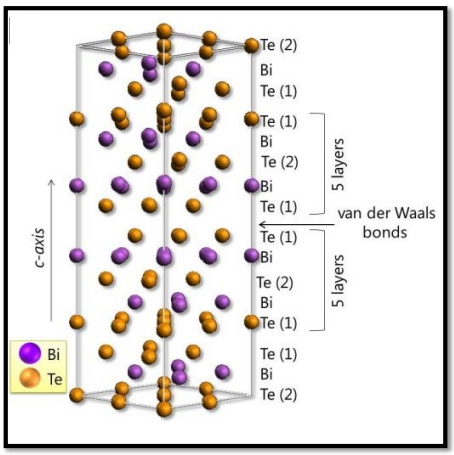

Figure 5.2. Bi_2Te_3 crystal structure. Figure taken from reference [10].

Because of the crystal structure of Bi_2Te_3, its electrical and thermal conductivities are highly anisotropic[11-13]. Nevertheless, the Seebeck coefficient is approximately isotropic [14]. The thermal conductivity of a Bi_2Te_3 single crystal measured in the perpendicular direction to the *c-axis* is $\kappa_{\perp c}$ = 2.2 $W \cdot m^{-1} \cdot K^{-1}$. Conversely, the value parallel to the *c-axis* is found to be $\kappa_{// c}$ =1 $W \cdot m^{-1} \cdot K^{-1}$at room temperature.[15] Therefore, there is a factor of 2.2 between the thermal conductivities in the direction perpendicular and parallel to the *c-axis*. Different works reported a ratio of 2 [13, 15, 16] or 3 [17] between both directions for Bi_2Te_3 single crystal materials.

5.1.3.1 Fabrication

The electrodeposition procedure was performed by using pulsed electrodeposition between a constant potential for 0.1 s and zero current density for 0.01 s. The applied potential was selected to

match the conditions performed in reference [18] which in this case corresponded to a value of + 0.05 V *vs.* Ag/AgCl.

5.1.3.2 Structural and morphological characterization

The crystal orientation was studied by X-ray diffraction. One peak that can be indexed to the Si substrate (JCPDS 27-1402) is observed in Figure 5.3. Peaks located at 2θ = 41.148 º and at 2θ = 89.278 º can be attributed to the (1 1 0) and (2 2 0) first and second diffraction orders of Bi_2Te_3 (JCPDS 015-0863), respectively, thus, revealing that the film is highly oriented along the direction perpendicular to the *c-axis*, i.e., the [1 1 0] direction.

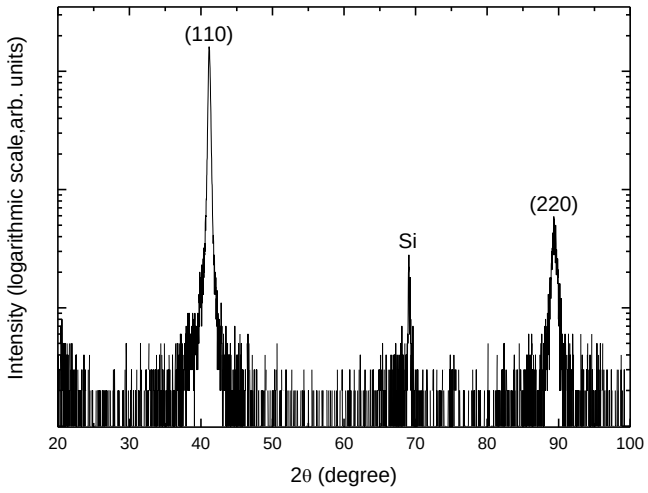

Figure 5.3. X-ray diffractogram of the bismuth telluride film. Figure taken from reference [10].

Figure 5.4 (a) and (b) shows the SEM images of the top-view and the cross-section of the electrodeposited film, respectively. From the top-view a particle size in the order of microns can be distinguished. Moreover, a columnar type of growth is observed from the lateral view with the *c-axis* parallel to the substrate. The thickness measured by the profilometer 4.5 µm ± 0.3 µm is confirmed by the measurement on the SEM cross-sectional view resulting in a value of approximately 4 µm. This measurement is especially important, since a variation in the thickness of the sample yields a variation in the final value of the thermal conductivity. The experimental error is given by the roughness of the film of approximately 300 nm, which is higher than the films previously measured.

Moreover, the chemical composition was studied by Energy Dispersive X-ray spectroscopy (EDX), showing atomic percent values of bismuth and tellurium of 40 ± 2 % and 60 ± 2 %, respectively, which is the composition predictable to yield the best thermoelectric performance for Bi_2Te_3. .

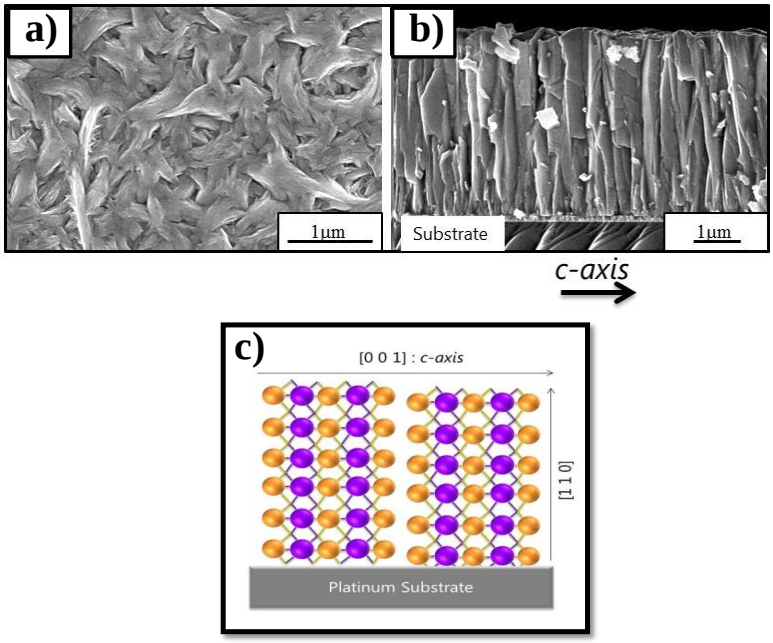

Figure 5.4. SEM images of (a) top view, (b) cross section of the electrodeposited Bi_2Te_3 film with the *c-axis* parallel to the platinum substrate and (c) sketch of the crystal structure of the Bi_2Te_3 with the *c-axis* parallel to the substrate. Figure taken from reference [10].

5.1.3.3 Thermal conductivity

The thermal conductivity of the Bi_2Te_3 film was calculated by assuming the chromium and gold layer previously deposited onto the silicon as a part of the thermal resistance between the silicon and the Bi_2Te_3 layer. This will be a common approach for films grown by electrodeposition, since both chromium and gold have a high thermal conductivity enough (93.9 $W \cdot m^{-1} \cdot K^{-1}$ and 318 $W \cdot m^{-1} \cdot K^{-1}$, respectively) and are thin enough (5 nm and 150 nm, respectively) so that their contribution to the thermal resistance is quite low. Table 5.IV shows the properties employed for the fitting of the sample thermal conductivity.

Thermal conductivity along [1 1 0] and [0 0 1] directions were measured. The thermal conductivity value in the out-of-plane direction, i.e., along the [1 1 0] direction (see Figure 5.4 (c)), was measured by PA technique and TDTR given values of 2.3 ± 0.2 $W \cdot m^{-1} \cdot K^{-1}$and 2.4 ± 0.2 $W \cdot m^{-1} \cdot K^{-1}$, respectively. Similar values can be found in the literature for the single crystals along the same crystal orientation[14, 17]. The TDTR measurement was performed in the Birck nanotechnology building (Purdue University) by Dr. Yee Rui Koh under the supervision of Professor Ali Shakouri.

Table 5.IV. Properties of the each layer used to perform the fitting of the Bi_2Te_3 film thermal conductivity.

Layer	Thickness (µm)	Density ($kg \cdot m^{-3}$)	Specific heat ($J \cdot kg^{-1} \cdot K^{-1}$)	Measured Thermal conductivity ($W \cdot m^{-1} \cdot K^{-1}$)	Expected thermal conductivity ($W \cdot m^{-1} \cdot K^{-1}$)	Desv. (%)
Si	500	2330 [3]	712 [3]	-	148 [3]	-
Bi_2Te_3	3.46	7740 [3]	194 [19]	2.3 ± 0.2	2.4 ± 0.2 (TDTR) [10]	0.04
Ti	0.08	4506 [3]	523 [3]	-	21.9 [3]	-
Air	0	1.176	1007	-	0.026	-

The phase shift data as a function of the frequency is shown in Figure 5.1 (c), which shows the best fitting obtained for the frequency range which gives the highest sensitivity of the thermal conductivity of the film. The PA measurement was performed on the as-grown sample with the sample deposited onto the platinum and silicon substrate whereas the TDTR substrate had to be transferred to glass substrate in order to achieve a highly reflective surface with a roughness in the vicinity of 20 nm. Table 5.IV shows the good accordance between both techniques with a deviation lower than 1% which proves that the PA technique is able to measure samples with surfaces as rough as 300 nm at this frequency range.

Finally, the thermal conductivity along the [0 0 1] direction was measured by fabricating a bismuth telluride film preferentially oriented along that direction. For this purpose, the time of the electrodeposition cycle with zero current density was changed. A value of 1.2 ± 0.2 $W \cdot m^{-1} \cdot K^{-1}$ was measured by the TDTR method. A factor in the vicinity of 2 was found for the thermal conductivity values measured in the direction perpendicular and parallel to the *c-axis* for electrodeposited films which agrees with the ratio calculated in previous works for single crystal bulk materials [16] [13].

These measurements corroborate the good performance of the PA technique for measuring structures by using the multilayered model.

5.2 Tellurium electrodeposited thick films

Tellurium is a p-type semiconductor with a narrow band-gap (0.34 eV). Figure 5.5 shows its crystal structure, which is highly anisotropic due to the presence of helical chains bounded by covalent unions between the atoms and bounded with other chains by van der Waals forces. These chains turn out to be a hexagonal lattice with the *c-axis* perpendicular to the hexagonal base or parallel to the helical chains [20].

Applications such as gas sensors[21], piezoelectrics [22], photoconductors [23], photonic crystals [24], submillimeter wave detectors [25], and thermoelectric devices [26] have been the spotlight of tellurium thin films investigations.

The thermoelectric properties of bulk tellurium have already been investigated. The Seebeck coefficient is found to be around +500 $\mu V \cdot K^{-1}$ along the *c-axis* direction [26], which reveals p-type conduction. Previous studies showed an electrical resistivity of 2900 and 5000 $\mu\Omega \cdot m$ in the direction parallel and perpendicular to the *c-axis* respectively at room temperature[27],[28]. Regarding the thermal conductivity, a value of approximately 3 $W \cdot m^{-1} \cdot K^{-1}$ for the bulk material is normally assumed. However, it depends on the crystal orientation so that thermal conductivities are 3.37 $W \cdot m^{-1} \cdot K^{-1}$ and 1.96 $W \cdot m^{-1} \cdot K^{-1}$ for the direction parallel and perpendicular to the *c-axis* at room temperature, respectively [29],[30]. Assuming the isotropy of the Seebeck coefficient and using the above-mentioned electrical resistivity and thermal conductivity values for each direction, a figure of merit of 0.008 for both directions at room temperature can be estimated.

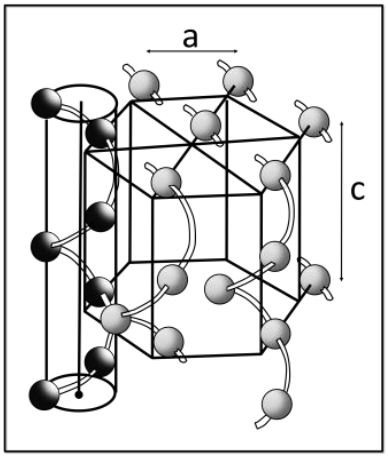

Figure 5.5. Tellurium crystal structure. Figure taken from reference [31].

The electronic properties are being investigated with diverse preparation methods and over different temperature ranges [27,32-36]. Goswami *et al.*[37] examined the semiconducting properties of films prepared by vacuum deposition and detected that the Seebeck coefficient revealed no temperature dependence near room temperature. The Seebeck coefficient of films grown by vacuum deposition was intensely investigated by Phahle [36] and afterward by Damodara *et al.*[38], which exhibited a value as elevated as 500 $\mu V \cdot K^{-1}$ and 400 $\mu V \cdot K^{-1}$, respectively, at room temperature; in consonance with the earlier measured value [37]. Lately, Bodiul *et al.* [26] researched the thermoelectric performance of both films and monocrystalline whiskers of tellurium prepared by a vacuum-condensation method. The power factor, $S^2\sigma$, of these thin films was found to be 100 $\mu W \cdot m^{-1} \cdot K^{-2}$ with a Seebeck coefficient in the vicinity of 350 $\mu V \cdot K^{-1}$ and an electrical conductivity value of 1100 $\mu\Omega \cdot m$. Nevertheless, scarce studies on tellurium films by electrodeposition were hitherto carried out. Jiang *et al.* [39] reported Seebeck coefficient measurements of tellurium films prepared by electrochemical deposition on polyaniline-coated macroporous phenolic foam with a maximum thermopower value of 342 $\mu V \cdot K^{-1}$ at 473K [39].

Another key idea to underline is that the electro-reduction of tellurium is the base of the electrodeposition mechanism of numerous telluride-based chalcogenides such as CdTe for solar cells [40], ZnTe for optoelectronics and non-linear optics [41], or PbTe [42, 43] and Bi_2Te_3 [44-46] for thermoelectric materials. The electrodeposition mechanism of those semiconductors and their ternary alloys arises from a stimulated codeposition mechanism once the electrochemical reduction of tellurium from the solution takes place. The tellurium is firstly nucleated by reduction at the cathode with any of the next reactions [44]:

$$HTeO_2^+(aq) + 3H+(aq) + 4e^- \rightarrow Te^0(s) + 2H_2O \qquad E^0 = +0.551 \text{ V vs NHE}$$

$$HTeO_2^+(aq) + 5H^+(aq) + 6e^- \rightarrow H_2Te\,(aq) + 2H_2O \qquad E^0 = +0.121 \text{ V vs NHE}$$

$$Te^0(s) + 2H^+ + 2e^- \rightarrow H_2Te\,(aq) \qquad E^0 = -0.739 \text{ V vs NHE}$$

$$2H_2Te(aq) + HTeO_2^+(aq) \rightarrow 3\,Te^0(s) + 2H_2O + H^+(aq) \quad \Delta G^0 = -498.118 \text{ kJ/mol}$$

and reacts with cadmium [47], zinc [47], lead [48] or bismuth [44] to yield the compound. For the above-mentioned explanations, adjustment of the quality of the electrodeposited tellurium could be attractive in order to understand the operation of these compounds.

A potential method to modify the growth mechanism and control the quality of the films can be achieved by adding surface active agents. Sodium lignosulfonate (SLS) is a surfactant that was previously found to change the quality of the films prepared by electrodeposition [49]. Nevertheless, the characteristic effect of SLS on tellurium deposition had not been investigated until now. Our main objective was to understand the influence of sodium lignosulfonate on the electrodeposition process and the thermoelectric properties of tellurium thick films.

5.2.1 Fabrication of the tellurium films

Tellurium thick films have been fabricated by electrodeposition in an aqueous solution of $1 \cdot 10^{-2}$ M $HTeO_2^+$ from Fluka Chemika® tellurium powder, 1M of Panreac® 65 % HNO_3 with and without 0.06 $g \cdot L^{-1}$ lignosulfonic acid sodium salt from Sigma Aldrich®. The solution preparation involves the dissolution of the $HTeO^{2+}$ in nitric acid and the subsequent addition of deionized water to achieve the required volume. The working electrode comprises a 150 nm platinum layer deposited via electron-beam evaporation onto a silicon wafer (1 0 0) with a 5 nm chromium layer between the silicon and the platinum.

Cyclic voltammetries (CVs) were carried out in order to investigate the diverse deposition mechanism and locate the optimal deposition potential The limits of the CV were selected to be between -0.5 V and 1.0 V *vs.* Ag/AgCl (3M) electrode with a scanning rate of 0.01 $V \cdot s^{-1}$.

Figure 5.6 displays the principal tellurium reduction peaks without and with SLS at -0.13 V and -0.20 V, respectively. The principal cathodic peak can be associated with the reduction of the $HTeO_2^+$ to Te, observed also by Martín-González *et al.* [44], who investigated the electrochemical performance of tellurium without additives. The potential shift between both solutions can be described by the adsorption of the surfactant onto the electrode, which delayed the reduction of tellurium by reducing the amount of reduction spots available at the electrode surface. The current plateau when adding SLS to the solution shows lower current density than in the case of no SLS. This implies that surfactant molecules could be adsorbed onto the platinum surface, thus reducing the current density, j_p. When the applied potential is more negative than -0.3 V, another noticeable cathodic wave appears in both solutions relating to the hydrogen evolution. Conversely, only one oxidation peak emerges in the oxidation region with an applied potential of around V = 0.6 V in both cases. It is notable that there is a significant difference between the oxidation area peaks. As the section of working electrode was the same in both experiments, this difference could be connected to the total charge going through the electrode and the total volume of tellurium deposited on the electrode surface. The total charge passing across the electrode is inferior in the case of the CV with SLS so that the quantity of tellurium deposited on the electrode is lower. That could be corroborated by estimating the charges of the anodic peak (Q_+) and cathodic zone (Q_-) analyzed without hydrogen evolution from both CV. The charges were found to be Q_-= -56.1 mC and Q_+= 40.7 mC for the case without SLS and Q_-= -44.3 mC and Q_+= 21.1 mC with SLS, respectively. This reveals the inhibitor nature of the surfactant on tellurium electrodeposition.

The films growth was conducted at three different potentials along the reduction peak, -0.13V, -0.10V, and -0.07V when no SLS is used and -0.18V, -0.19V, and -0.20V for the solution with SLS, as shown in inset on Figure 5.6. The films were fabricated by applying the driving force for one hour, which produce films with thicknesses in the range of several microns that totally cover the platinum electrode surface.

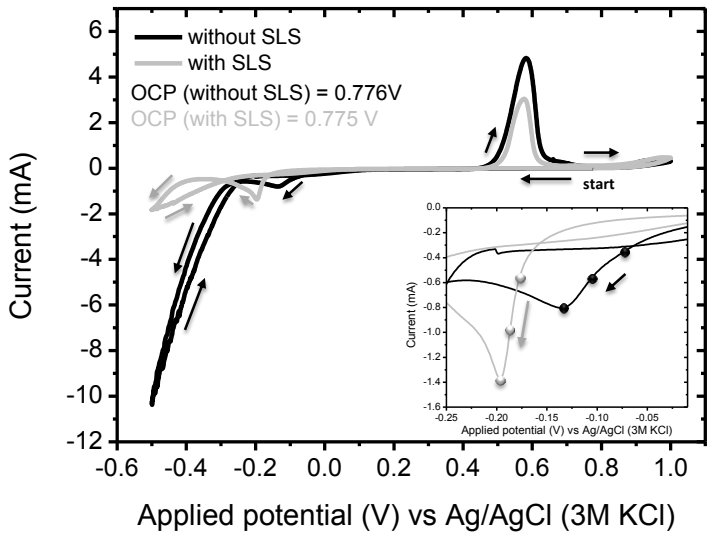

Figure 5.6. Cyclic Voltammogram of $HTeO_2^+$ 0.01 M in 1M HNO_3 with (gray) and without (black) 0.06 $g \cdot L^{-1}$ SLS with a scan rate of 0.01 $V \cdot s^{-1}$ at room temperature. The inset shows the principal reduction peak for both solutions and the three different locations where the electrodepositions were carried out. Arrows show the scan direction of the CV. Figure taken from reference [31].

5.2.2 Structural and morphological properties

Figure 5.7 displays the X-Ray diffractograms of the films fabricated at different potentials as well as the reference pattern of Te powder (JCPDS 36-1452) for both solutions. The XRD was measured after transferring the films from the substrate to a glass slide in such a way that no platinum and silicon peaks are found.

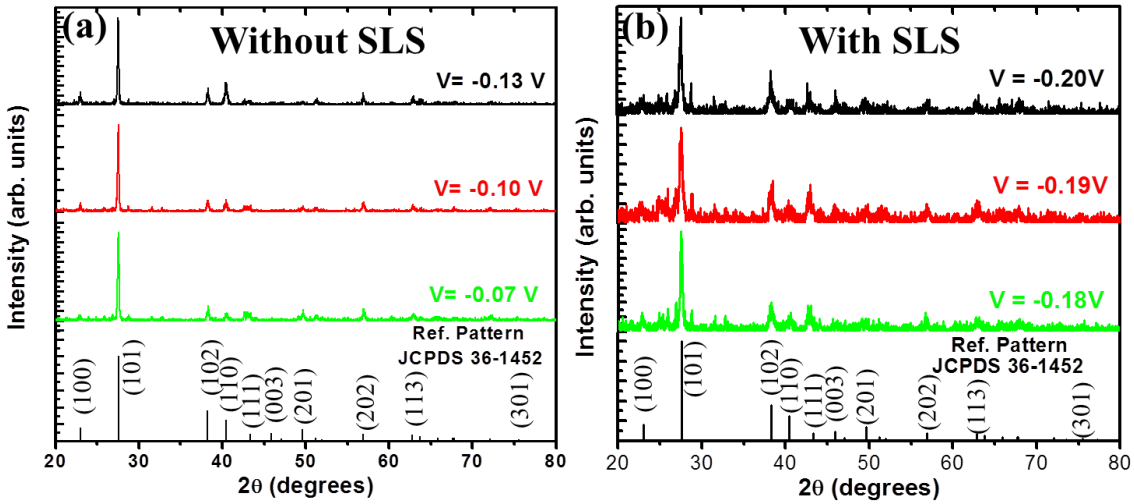

Figure 5.7. X-ray diffractograms for the films fabricated in three different potentials from both solutions (a) without and (b) with SLS. Figure taken from reference [31].

Several diffraction peaks can be seen in Figure 5.7 and are identified with the diffraction peaks of the hexagonal phase of tellurium reference pattern. In the case of no SLS (see Figure 5.7 (a)), the (1

0 1) diffraction peak found at 2θ = 27.563 ° becomes the strongest for the three deposited films as in the reference pattern. The second order diffraction peak, (2 0 2) located at 2θ = 56.878° is also observed in the diffractogram. Smaller diffraction maxima like (1 0 2) at 2θ = 38.261° and (1 1 0) at 2θ = 40.446° can be also found. The diffraction peaks for (1 0 1), (1 0 2) and (1 1 0) are the strongest in the standard pattern, so that the XRD diffractogram of films grown without SLS reveals a microstructure comparable to that of polycrystalline pattern. Nevertheless, when changing the applied potential, the relative intensity between these peaks is observed to vary. Furthermore, other less strong peaks are found, such as (1 0 0), (1 1 1), (2 0 1) and (1 1 3). The full width at half maximum (FWHM) of the (1 0 1) diffraction peak was determined to be 0.15 º, 0.16 º and 0.21 º for the -0.13 V, -0.10 V, and -0.07 V, respectively. The minor the FWHM, the larger the crystallite size is so that a more negative applied potential gave rise bigger grain sizes.

In the case of the solution with SLS, the (1 0 1) diffraction peak is the sharpest and the weaker (2 0 2) diffraction peak is also observed. Furthermore, a textured direction cannot be differentiated since other diffraction peaks can be found in these samples, such as (1 0 0), (1 0 2), (1 1 0), (1 1 1), and (0 0 3). The FWHM of the (1 0 1) diffraction peak has found to be 0.33 º, 0.36 º and 0.32 º for -0.20 V, -0.19 V and -0.18 V, respectively. The FWHM values are fairly similar for the three films, possibly owing to the small change in the applied voltage.

A crystalline character can be expected for both solutions due to the presence of sharp peaks. Furthermore, since no specific crystal orientation can be distinguished in any case, a polycrystalline character is assumed for both solutions. Nevertheless, the relative intensity between the highest diffraction peak (1 0 1) and (1 1 0) has been significantly altered with the addition of the surfactant. Essentially, the direction (1 1 0) looks to be faintly impeded by the presence of the SLS. Besides, the crystallite size of the films prepared without SLS is larger than in the case when SLS is employed.

Figures 5.8 displays the morphology of the tellurium films prepared at the three different without SLS. The most negative applied potential produces the largest particle size. Nevertheless, a reduction of the microstructure order when using more negative applied potential can be observed from the cross-section views. These figures also reveal a wad of structures with voids rising up directly from the substrate. This type of growth is feasible as a result of the greatly anisotropic crystal growth of Te [50, 51]. The crystals are arbitrarily positioned originally from a nucleation site so that the polycrystalline character of the films is distinguished in the XRD pattern. The thicknesses of the films were determined by the profilometer giving values of 4.6 µm, 3.4 µm, 3.0 µm, which are found to be in good agreement with the values obtained by the SEM images, 4.5 µm, 3.5 µm and 3.0 µm for V = -0.13V, V=-0.10V and V = -0.07V, respectively (see Figure 5.8).

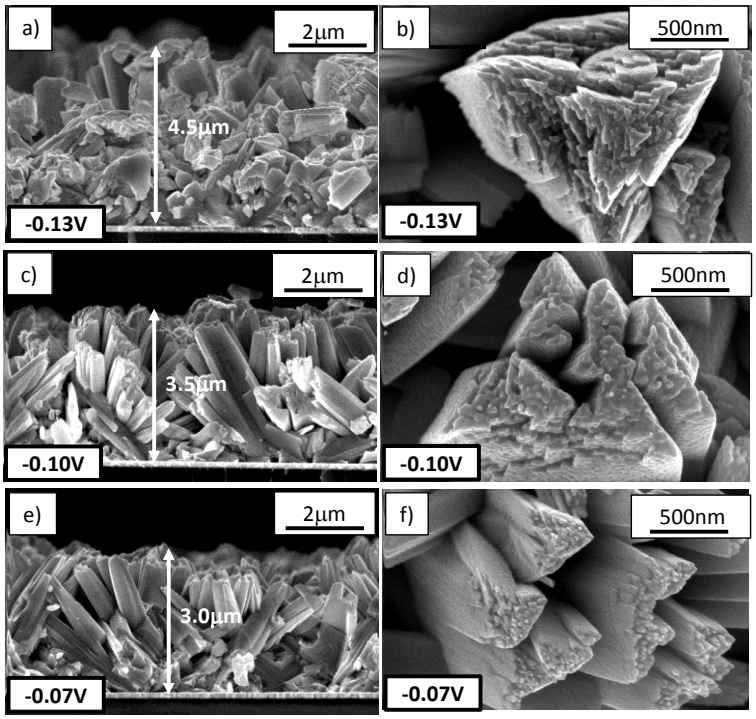

Figure 5.8. FE-SEM images of the as-grown electrodeposited films without SLS. (a) Cross section and (b) top-view of the film grown at -0.13 V, (c) cross-section and (d) and top-view of the film grown at -0.10 V, (e) cross-section and (f) top-view of the film grown at -0.07 V. The thicknesses of the films are indicated with an arrow. Figure taken from reference [31].

In the case of the solution with SLS, negligible differences can be identified between the films grown by different applied voltages, as seen in Figure 5.9. All of the films have a characteristic columnar type of growth confirmed by the cross-section images. Furthermore, the top images of the films display arrow-like morphology with a substantial number of crystals. The kind of growth is totally distinct than without SLS. The conventional tellurium growth mechanism is stopped by the surfactant which works as an anti-coagulation instrument, reducing the growth in the classic directions. SLS inhibits the growth of the tellurium particles, transforming the crystal growth behavior so that smoother and denser films are achieved as showed in the SEM images. The thicknesses were determined by the profilometer, 2.9 μm, 2.9 μm and 2.5 μm are in good agreement with those estimated from the SEM cross-views, 3.0 μm, 3.5 μm and 3.0 μm for V = -0.20 V, V=-0.19 V and V = -0.18 V, respectively, (see Figure 5.9).

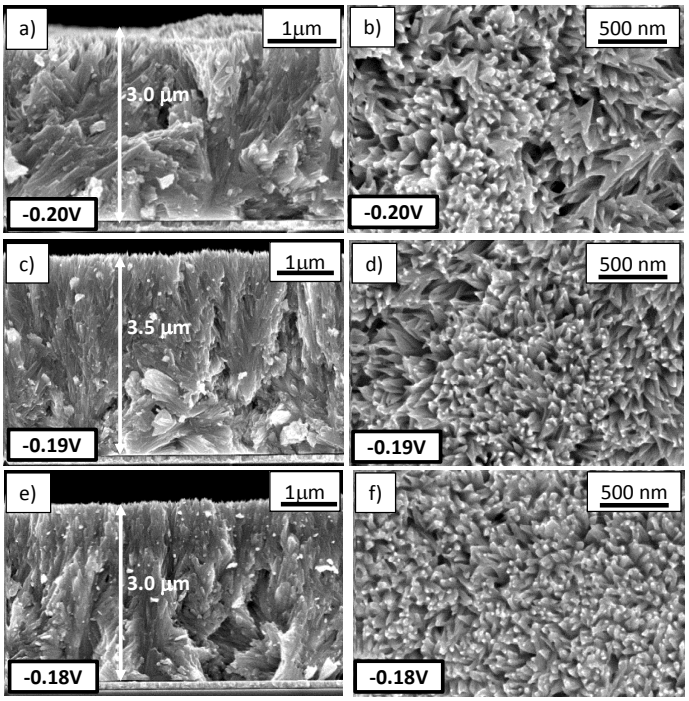

Figure 5.9. FE-SEM images of the as-grown electrodeposited films with SLS. (a) Cross section and (b) top-view of the film grown at -0.20 V, (c) cross-section and (d) top-view of the film grown at -0.19 V, (e) cross-section and (f) top-view of the film grown at -0.18 V. The thicknesses of the films are marked with arrows. Figure taken from reference [31].

5.2.3 Electrical resistivity and Seebeck coefficient

The in-plane power factor has been determined as a function of temperature for the films fabricated from both solutions. For that purpose, both electrical resistivity and Seebeck coefficient were measured.

Figure 5.10 shows the behavior of the electrical resistivity which decreases as the temperature increases revealing the characteristic behavior of a semiconductor. The minimum electrical resistivity values are found at 105 °C, with a value of 197 μΩ·m for the film fabricated without SLS at -0.07 V and a 509 μΩ·m for the film prepared at -0.20 V with SLS. Conversely, the near-to-room temperature values (35 °C) are 229 μΩ·m and 798 μΩ·m, without and with SLS, respectively. These values are an order of magnitude lower than those of observed by Bottom *et al.*[28] for a single crystal, 5600 μΩ·m and 2900 μΩ·m, obtained for the perpendicular and parallel direction to the *c-axis*, respectively. This dramatic diminution could be connected to structural defects in the material. In the case of tellurium films, structural defects such as adsorbed surface impurities, a potential barrier at the grain boundaries or surface states, among other, can be found. The surface states on the surface of tellurium films is the typical mechanism previously studied which can performance as electrically active defects [35]. The activation energy of these impurities in the band gap can be determined from the slope between the logarithm of the electrical resistivity, ρ, against $1/T$, where T is the absolute temperature, as the

electrical resistivity measurements are close to the temperature where the electrical activation of those impurities occurs [36].

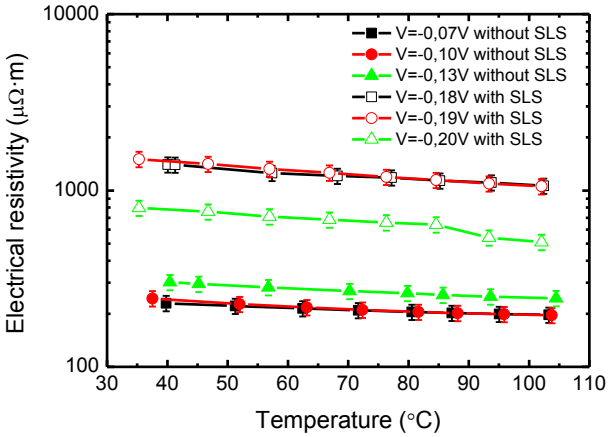

Figure 5.10. Electrical resistivity of the films fabricated at different applied voltages for both solutions, with (open symbols) and without (solid symbols) SLS. Figure taken from reference [31].

Figure 5.11 shows the activation energies together with the electrical resistivity at room temperature of the films, with values ranging from 50 meV to 68 meV (without SLS) and from 87 meV to 108 meV (with SLS). These values are in good accordance with previous studies. Phahle *et al.*[36] estimated an activation energy of 180 meV and an electrical resistivity about 500 μΩ·m at a comparable temperature range and Goswami *et al.*[37] calculated activation energy values from 178 meV to 58 meV, for samples fabricated by thermal evaporation. A comparable trend between the activation energy and the electrical resistivity can be observed for the films with and without SLS, which signifies that the electrical resistivity is intimately connected to the impurity level. Moreover, films from SLS solution have deeper levels, and hence, higher activation energy than in the case of the films fabricated without SLS. Consequently, the electrical resistivity is lower when no SLS is used.

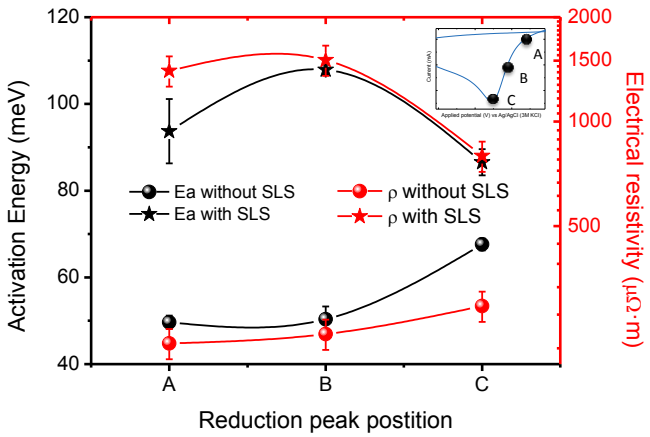

Figure 5.11. Comparison of the activation energy and electrical resistivity at room temperature for different applied voltages for solutions without SLS (-0.07 V, -0.10 V and -0.13 V) and with SLS (-0.18 V, -0.19 V and -0.20 V). Figure taken from reference [31].

For films deposited without SLS, the electrical resistivity increases when the applied potential is made more negative, which controverts the idea that the sample grown at the highest driving force, -0.13 V, has larger grain sizes. Nevertheless, poor ordering of the crystals is obvious when contrasted with -0.10 V and -0.07 V films which can thus explain the high electrical resistivity.

Concerning the samples fabricated with SLS, as the surfactant interrupts the typical growth of Te, the crystallite size is significantly smaller than that of films deposited without SLS. Therefore, more grain boundaries are present which justify the increase in the electrical resistivity. This observation is in good accordance with previous studies where an increase in the electrical resistivity was detected in Bi_2Te_3 films when adding SLS [49]. In the case of the films fabricated with SLS, as the driving force of the solution increases the electrical resistivity is reduced.

Regarding the Seebeck coefficient, Figure 5.12 reveals p-type conduction for all the films. Furthermore, the thermopower vaguely increases with temperature, which could be characteristic of an extrinsic behavior as there should be a temperature at which the tellurium becomes intrinsic and the Seebeck coefficient starts to decay as the temperature is augmented [52]. The highest values found for the film deposited at -0.07 V without SLS is in the vicinity of 285 $\mu V \cdot K^{-1}$, and for films with SLS at -0.20 V is around 284 $\mu V \cdot K^{-1}$, both close to 105 °C. These Seebeck coefficient values are larger than those found by Jiang *et al.*[39] for electrodeposited tellurium on polyaniline, 240 $\mu V \cdot K^{-1}$, at a similar temperature.

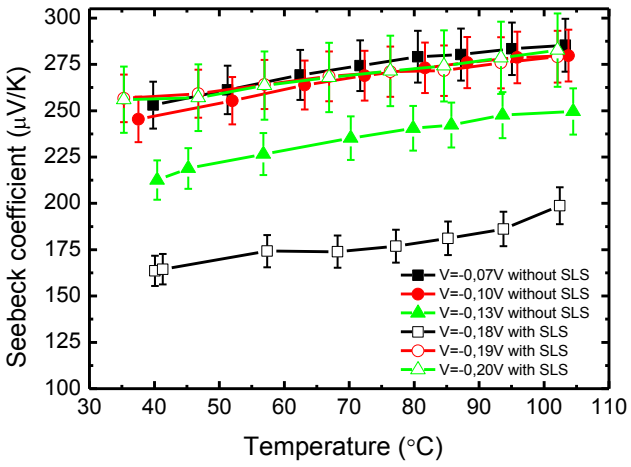

Figure 5.12. Seebeck coefficient of the films deposited at different applied potentials for both solutions, with (open symbols) and without (solid symbols) SLS. Figure taken from reference [31].

The power factor showed in Figure 5.13, which is a result of the both above-mentioned magnitudes, increases as the applied voltage is less negative when no SLS is used or more negative in the case of adding SLS. The highest calculated values are 415 $\mu W \cdot m^{-1} \cdot K^{-2}$ (without SLS) and 110 $\mu W \cdot m^{-1} \cdot K^{-2}$ (with SLS) for -0.07 V and -0.20 V at 105 °C, respectively. These quantities are of the

same order of magnitude of those of Bi_2Te_3 fabricated by electrodeposition [49] [45]. Furthermore, our power factor values close to room temperature, 280 $\mu W \cdot m^{-1} \cdot K^{-2}$ (without SLS) and 82 $\mu W \cdot m^{-1} \cdot K^{-2}$ (with SLS), are comparable to those achieved by Bodiul *et al.*[26], who obtained a value of 100 $\mu W \cdot m^{-1} \cdot K^{-2}$ at room temperature for tellurium films deposited by a vacuum condensation method. It is remarkable that in the case of the sample fabricated without SLS, an enhancement by a factor of more than two has been reached at room temperature.

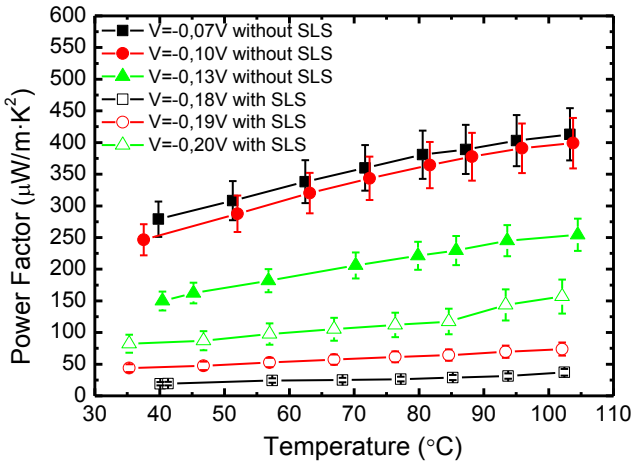

Figure 5.13. Power factor of the films deposited at different applied voltages for both solutions, with (open symbols) and without (solid symbols) SLS. Figure taken from reference [31].

5.2.4 Thermal conductivity

The thermal conductivity was measured by the photoacoustic technique in the out-of-plane direction. As in the case of the Bi_2Te_3 thermal conductivity calculation, the chromium and platinum (κ = 71.6 $W \cdot m^{-1} \cdot K^{-1}$) layer are considered as a part of the thermal resistance between the silicon and the Te layer. Table 5.V summarizes the layer properties used for the data reduction carried out to extract the thermal conductivity of the layer under study, i.e., the tellurium film.

Table 5.V. Properties of the each layer used to perform the fitting of the Te film thermal conductivity prepared without SLS at V = -0.07 V which yielded the highest figure of merit.

Layer	Thickness (μm)	Density ($kg \cdot m^{-3}$)	Specific heat ($J \cdot kg^{-1} \cdot K^{-1}$)	Thermal conductivity ($W \cdot m^{-1} \cdot K^{-1}$)
Si	500	2330 [3]	712 [3]	148 [3]
Te	3.0	6240 [3]	202 [3]	*1.0 ± 0.1*
Ti	0.08	4506 [3]	523 [3]	21.9 [3]
Air	0	1.176	1007	0.026

Figure 5.14 displays an example of the experimental phase shift together with the best fitting performed for the sample with the best thermoelectric properties which was prepared without SLS at V = -0.07 V.

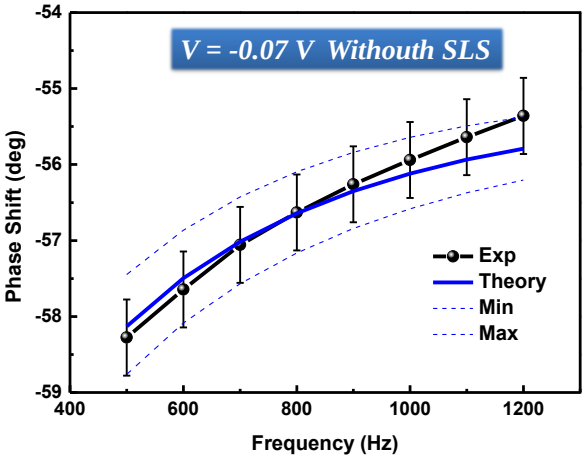

Figure 5.14. Experimental phase shift as a function of the frequency along with the best fitting for the sample with the highest figure of merit, i.e., the one grown at V = -0.07 V without SLS.

Table 5.VI goes over the thermal conductivity values of the tellurium films which result approximately a third of the bulk value for all the films (3 $W \cdot m^{-1} \cdot K^{-1}$)[30], which makes this material promising in terms of thermoelectricity. The thermal conductivity of the films with the highest power factors are 0.8 $W \cdot m^{-1} \cdot K^{-1}$ at V=-0.20 V (with SLS) and 1.0 $W \cdot m^{-1} \cdot K^{-1}$ at V=-0.07 V (without SLS).

As explained above, the grain size of the tellurium films deposited with SLS is smaller than that of grown without SLS so that it could influence the phonon transport along the structure. When the grain size is decreased, phonon boundary scattering could be governing and consequently, a decrease in the thermal conductivity would be accomplished [53]. Figure 5.15 shows the tendency of the thermal conductivity as a function of the applied voltage. When no SLS is used, the thermal conductivity falls when the applied potential is less negative since the grain size is decreased (see Table 5.VI, where the estimated crystallite sizes were determined by means of the Scherrer equation). Conversely, the thermal conductivity of films with SLS as a function of the applied voltage is not as affected, since all the films have around the same crystallite size.

Table 5.VI. Room temperature values of power factor in the in plane direction, thermal conductivity in the out of plane direction, the estimated figure of merit and the calculated crystallite size from the XRD analysis of the films grown with and without SLS using Scherrer formula. Figure of merit is calculated because the films are polycrystalline and not highly oriented.

Surfactant	Applied voltage	Crystallite size (nm)	PF ($\mu W \cdot m^{-1} \cdot K^{-2}$)	κ ($W \cdot m^{-1} \cdot K^{-1}$)	zT
No	-0.07	43 ± 4	280 ± 48	1.0±0.1	0.09±0.01
No	-0.10	52 ±5	246 ± 42	1.1±0.1	0.07±0.01
No	-0.13	60 ± 6	152 ± 26	1.3±0.1	0.035±0.007
SLS	-0.18	28 ± 3	19 ± 3	0.9±0.1	0.006±0.001
SLS	-0.19	25 ± 3	44 ± 7	0.9±0.1	0.015±0.003
SLS	-0.20	27 ± 3	82 ±14	0.8±0.1	0.031±0.006

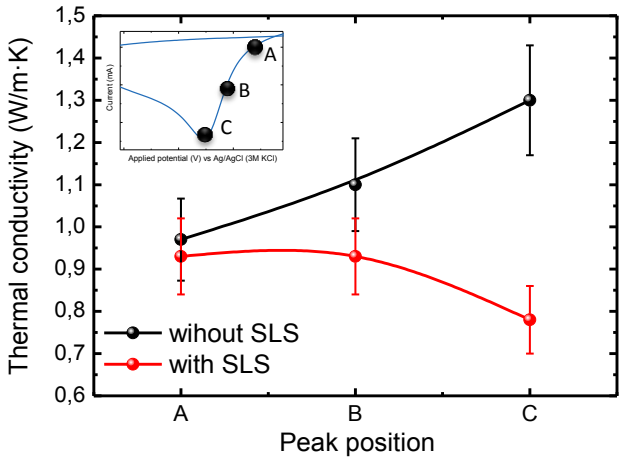

Figure 5.15. Thermal conductivity as a function of the applied voltage (peak position) for both solutions, with and without surfactant. Figure taken from reference [31].

The thermal conductivity values of these tellurium films is comparable to those of Bi_2Te_3-alloys previously achieved by electrodeposition, in the vicinity of 1 $W \cdot m^{-1} \cdot K^{-1}$ [54].

Finally, the figure of merit could be estimated since a polycrystalline structure is confirmed by the XRD data (see Figure 5.7). As seen Table 5.VI, the best figure of merit at room temperature, 0.09, is achieved when using the solution without SLS at -0.07 V as a result of its high power factor. In the case of the solution with SLS, the highest figure of merit is 0.03 at -0.20 V since its electrical resistivity is larger attributable to the smaller grain size. In both cases, these values are one order of magnitude higher in the estimated bulk figure of merit at room temperature, 0.008, essentially owing to the large reduction in the thermal conductivity achieved by electrochemical deposition.

5.3 Thermal conductivity of bismuth telluride films grown by electrodeposition with sodium lignosulfonate

The thermal conductivity of a bismuth telluride film grown with 0.09 $g \cdot L^{-1}$ of SLS by pulsed electrodeposition (1 s at -0.04 V and 2 s at zero current) was also studied in order to investigate the effect of the sodium lignosulfonate in the thermal transport of this material.

The thermal conductivity measurement was carried out in the same manner as for the bismuth telluride film without SLS (explained in Section 5.1.3). By measuring the sample in the same frequency range and taking the thickness of the sample (7 µm) into account a value of 1.8 ± 0.2 $W \cdot m^{-1} \cdot K^{-1}$ was obtained. The initial assessment could be that the thermal conductivity of the film has changed versus the values previously obtained for highly oriented Bi_2Te_3 films without SLS. In order to evaluate this value, the X-ray diffractogram of this sample is analyzed, which is shown in Figure 5.16.

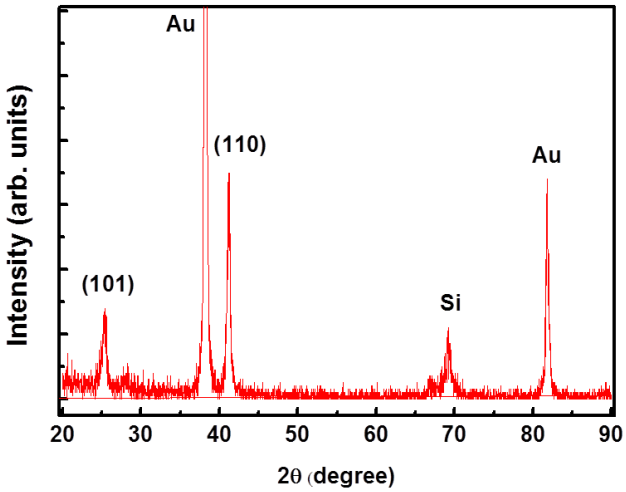

Figure 5.16. X-ray diffractograms for the Bi_2Te_3 film grown with SLS.

As the thermal conductivity is highly anisotropic, the preferred orientation of this film is studied by Harris texture analysis. The texture coefficients can be calculated by,

$$TC_{(hkl)} = \frac{\frac{I_{(hkl)}}{I^0_{(hkl)}}}{\frac{1}{N}\sum\frac{I_{(hkl)}}{I^0_{(hkl)}}} \qquad (5.2)$$

where $I_{(hkl)}$ and $I^0_{(hkl)}$ are the intensity of (h k l) peak observed in the experimental X-ray diffractogram and the theoretical value from the database (JCPDS= 15-0863), respectively. *N* is the number of

reflection considered in the analysis. In this case N = 2 since only (1 0 1) and (1 1 0) reflections are present.

Table 5.VII shows the texture coefficient for both reflections, being higher in the case if the (1 0 1) peak than in the (1 1 0). From the texture coefficients, it is straightforward to see that the film has a preferential oriented along the [1 0 1] direction. It can also be calculated that the film has a 73 % preferred oriented along the [1 0 1] direction and 27 % along the [1 1 0] direction.

Table 5.VII. Harris texture coefficient of Bi_2Te_3 films grown with SLS by pulsed electrodeposition.

Peak (hkl)	Intensity XRD	Intensity JCPDS	Texture coefficient ($TC_{(hkl)}$)
1 0 1	28	4	1.428
1 1 0	70	25	0.570

As the film is preferentially oriented along the [1 0 1] direction and the thermal conductivity along the *c-axis* and perpendicular to it has different values ($\kappa_{\perp c}$= 2.2 $W \cdot m^{-1} \cdot K^{-1}$ and $\kappa_{//c}$= 0.79 $W \cdot m^{-1} \cdot K^{-1}$)[17] ,then both contributions should be present in this orientation.

$$\kappa_{[1\,0\,1]} = 0.5 \cdot \kappa_{[1\,0\,0]} + 0.5 \cdot \kappa_{[0\,0\,1]} \tag{5.3}$$

Plus, we have to take into account that the samples is also partially oriented along the [1 1 0] direction, around 27 % of the sample. By making a simple calculation,

$$\kappa_{film} = 0.27 \cdot \kappa_{[1\,1\,0]} + 0.73 \cdot \kappa_{[1\,0\,1]} \tag{5.4}$$

Assuming these first approximations, an estimated thermal conductivity value of 1.7 $W \cdot m^{-1} \cdot K^{-1}$ is obtained for a film of this orientation. This value is in good agreement with the value obtained by the photoacoustic technique, 1.8 ± 0.2 $W \cdot m^{-1} \cdot K^{-1}$, thus, indicating that the sodium lignosulfonate does not affect the thermal transport in the case of Bi_2Te_3.

5.4 $Si_{1-x}Ge_x$ thin films

The thermal conductivity of $Si_{1-x}Ge_x$ thin films were measured by the PA technique. Silicon is a widely used semiconductor material due to its interesting properties as well as is abundancy, low-cost manufacturing and non-toxicity. Improvements of its transport properties can be achieved by combining it with germanium, forming $Si_{1-x}Ge_x$. $Si_{1-x}Ge_x$ is a commonly studied material with a band gap of approximately 1-2 eV at room temperature and high electrical conductivity and Seebeck coefficient but relatively low thermal conductivity [55]. When compared with silicon, $Si_{1-x}Ge_x$ has a much lower thermal conductivity and a similar electrical conductivity. Therefore, $Si_{1-x}Ge_x$ is being investigated as a promising thermoelectric material with high figures of merits at high operating

temperatures (800 - 1000 K)[55] apart from its applications as a photovoltaic[56] and metal-oxide-semiconductor field-effect transistors (MOSFETs) [56].

The $Si_{1-x}Ge_x$ presents an isotropic and cubic structure. From a thermoelectric point of view, the best stoichiometry of this material is found for x = 0.2, i.e., $Si_{0.8}Ge_{0.2}$, and [1 1 1] as crystalline orientation. These characteristics yield to the lowest thermal conductivity value found for this compound. Despite the electrical conductivity of $Si_{0.8}Ge_{0.2}$ is low, it can be improved by doping with boron or phosphorous which produces p- and n-type semiconductor, respectively. This procedure increases the electrical conductivity by preserving the low thermal conductivity values. In order to fabricate the doped $Si_{0.8}Ge_{0.2}$, high temperature or mixture of gases are needed for most of the techniques used for that purpose, such as chemical vapor deposition (CVD)[57] or molecular beam epitaxy (MBE)[58]. Therefore, a proper doping level turns into a difficult task when fabricating the required stoichiometry with the desired crystal orientation. Thermal conductivity values of around 5 $W \cdot m^{-1} \cdot K^{-1}$ have been reported for the n-type bulk $Si_{1-x}Ge_x$. Conversely, in the case of films, lower values around 3 $W \cdot m^{-1} \cdot K^{-1}$ were achieved [59]. Both values are greatly reduced when compare with bulk silicon thermal conductivity at room temperature, around 150 $W \cdot m^{-1} \cdot K^{-1}$ [60].

In this PhD work, a study of the influence in the thermal conductivity of the $Si_{0.8}Ge_{0.2}$ metal induced crystallization (MIC) fabrication conditions was conducted.

5.4.1 $Si_{1-x}Ge_x$ Fabrication

Two different $Si_{0.8}Ge_{0.2}$ boron doped thin films were fabricated via MIC by using sputtering technique. Aluminum nitride (AlN) covered with a 25 nm gold layer was used as a substrate to grow the $Si_{0.8}Ge_{0.2}$ layer. The metal induces the crystallization of the $Si_{0.8}Ge_{0.2}$ during a thermal treatment at which the gold is incorporated into the film, creating a eutectic point. This procedure allows for the crystallization of the material at much lower temperatures which prevents the loss of the dopants. Two different thermal treatments of the films were carried out in order to study the influence on the thermal conductivity: *i)* a direct growth on a heated substrate at 500 ºC inside the sputtering chamber was performed (*in situ* thermal treatment) and *ii)* post-deposition thermal treatment at 500 ºC in a controlled atmosphere by means of a rapid thermal annealing (RTA) (*ex situ* thermal treatment).

The fabrication of these films was carried out by the PhD student of our group, Jaime Andrés Pérez Taborda.

5.4.2 $Si_{1-x}Ge_x$ thermal conductivity measurements

The thermal conductivity of the thin films fabricated with both procedures were measured by the PA multilayered model. To this end, it is necessary to take the properties of the underneath layers as well as those of the film under study into account. Table 5.VIII shows the layers used for the fitting

model. The sample is composed of the substrate which in turns, is made of two layers, 500 µm sapphire and 5 µm AlN layer where the SiGe films were deposited. The properties of the layers of the substrate were taken from the datasheet. In the case of the SiGe layer, the specific heat capacity and the density were taken as C_p ($Si_{1-x}Ge_x$)= (19.6 + 2.9x) $J \cdot mol^{-1} \cdot K^{-1}$ [61], and ρ ($Si_{1-x}Ge_x$) = (2.329 + 3.493x – 0.499x^2) $g \cdot cm^{-3}$ [62], respectively, using x = 0.2 in our samples.

Table 5.VIII. Thickness, density, specific heat and thermal conductivity of each of the layers used in the PA model. The italic letters indicate that those are the thermal conductivity values extracted from the fitting.

Layer	Thickness (µm)	Density ($kg \cdot m^{-3}$)	Specific heat ($J \cdot kg^{-1} \cdot K^{-1}$)	Thermal conductivity ($W \cdot m^{-1} \cdot K^{-1}$)
Sapphire	500	3970	765	46
AlN	5	3260	920	285
SiGe (In-situ)	0.5	3000	546	*1.13 ± 0.13*
SiGe (Ex-situ)	0.5	3000	546	*1.23 ± 0.12*

Regarding the thermal resistances between the layers, both R_{th}(Sapphire/AlN), R_{th}(AlN/SiGe) and R_{th}(SiGe/Ti) were assumed to be negligible since the sputtering and e-beam evaporation technique yield a good quality thermal contact. Thus, these thermal resistances were fixed as 0.0001 $mm^2 \cdot W \cdot K^{-1}$. The free parameters for the fitting were R_{th}(Ti/air) and the thermal conductivity of the SiGe layer. Figure 5.17 show the fitting obtained under these conditions for the sample prepared with (a) in-situ and (b) ex-situ thermal treatments.

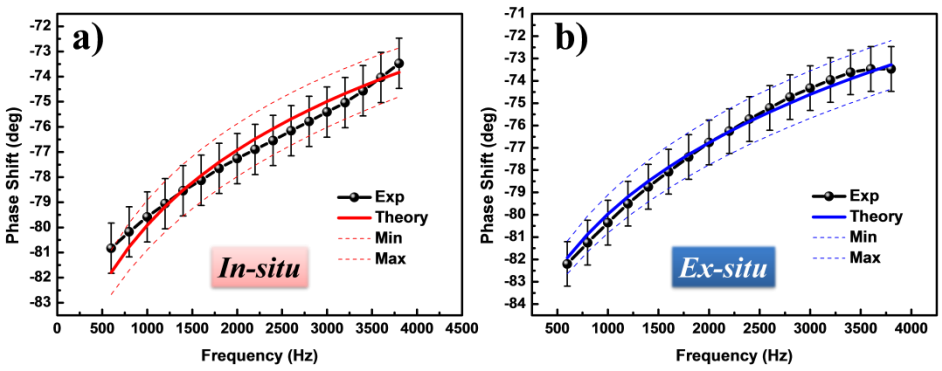

Figure 5.17. Experimental phase shift as a function of the frequency along with examples of the fitting for the samples prepared with (a) *in situ* and (b) *ex situ* thermal treatments.

The obtained results are much lower than the values reported in the literature (3 $W \cdot m^{-1} \cdot K^{-1}$) for similar thin films. [63, 64]. Nevertheless, a value of the thermal conductivity of 1.2 $W \cdot m^{-1} \cdot K^{-1}$ for SiGe nanowires has been reported. This reduction is explained in terms of the scattering of the high-frequency phonons by the Ge atoms which act as impurities as well as the size confinement of the nanowires which yields the low-frequency phonon boundary scattering. However, in our case, the reduction of the thermal conductivity can be explained by phonon scattering processes at the grain boundaries created by clusters formed during the crystallization across the film.

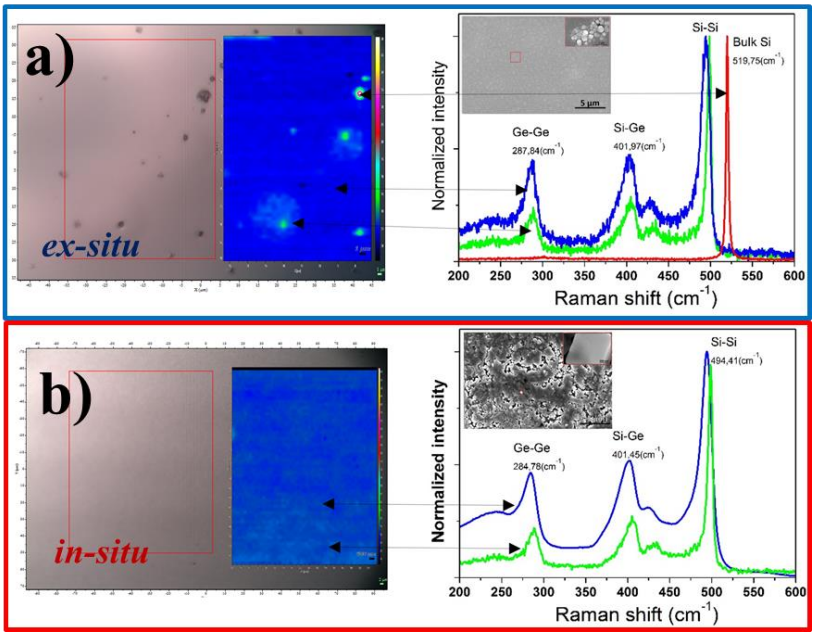

Figure 5.18. Optical image and Raman mapping of the Si-Ge films for (a) 500 °C ex-situ and (b) 500 °C in-situ samples. The mapping area covers 0.35 μm × 0.7 μm. The colors of the different spectra in the Raman mapping correspond to $Si_{0.8}Ge_{0.2}$ (blue), nano-$Si_{1-x}Ge_x$ (green), and pure Si (red). The inset displays a SEM image of the samples surfaces.

The structural characterization of these films allowed the clusters to be found, being pure Si for the *ex-situ* sample and silicon-rich/germanium cluster for the *in-situ* sample. The pure silicon clusters could be detected by Raman mapping as shown in Figure 5.18 (a). The silicon-rich/germanium clusters are also detected by Raman mapping (see Figure 5.18 (b)). The formation of these clusters can explain the reduction of the thermal conductivity.

5.5 Anodic aluminum oxide membranes

Anodic aluminum oxide membranes are composed of a hexagonally close packed (HCP) ordered structure.[65, 66] These structures, which are frequently prepared by a two-step anodization process,[67] can be fabricated with a wide range of pore diameters depending on the acid electrolyte employed during the anodization steps, ranging from about 8 nm to 530 nm.[68-71] Then, AAO membranes can be filled by different methods, for instance electrochemical deposition, pressure injection, vapor deposition or methods based on wetting phenomena, among others,[72, 73] thus producing nanowires within the membrane.

One-dimensional (1D) structures have been revealed to be an interesting method to decrease the thermal conductivity of materials, as the characteristic lengths can be similar to the phonon mean free path. Size effects are recognized to intensely change the thermal properties by phonon scattering processes at the interfaces, thereby reducing thermal conductivity.[46, 74, 75] Lately, this approach allowed a notable enhancement in thermoelectric efficiency. The thermal conductivity of the

nanowires (NWs) can be diminished in comparison with bulk values by boundary scattering, on condition that the nanowire characteristic length is minor than the phonon mean free path. Inside out, latest works have reported that thermal conductivity can be controllably enlarged by infiltrating polymers inside a matrix, as it is feasible to alter the thermal conductivity of the polymer nanowires by changing the crystal orientation, achieving values up to an order of magnitude higher than that of bulk polymers (around 0.2 $W \cdot m^{-1} \cdot K^{-1}$)[76].

The techniques employed to determine thermal conductivity can be split into two major classes: those capable of measure a single nanowire and those that measure the whole nanowire array, i.e., the nanowires embedded into the membrane. Microchip suspended structures[77] and Raman thermography[78] are found among the techniques capable to measure the thermal conductivity of a single nanowire. Other techniques, time-domain thermoreflectance (TDTR),[79] laser flash[80], Scanning Thermal Microscopy (SThM)[81] or Photoacoustic technique (PA) [82] have been utilized to determine the effective thermal conductivity of the whole composite. With the intention of obtaining the thermal conductivity of the single nanowire, the effective medium theory (EMT) must be applied as long as the heat goes across the matrix and the temperature in the in-plane direction can be considered isothermal.[79] Furthermore, this theory neglects the thermal resistances at the interfaces between the alumina and the nanowires [83]. With proper simplifications coming from these approximations, the EMT is given by this expression:

$$\kappa_{com} = x\kappa_{NW} + (1-x)\kappa_{AAO}, \tag{5.5}$$

where κ_{com} is the composite effective thermal conductivity, x is the real packing density or porosity, κ_{NW} is the thermal conductivity of a single nanowire and κ_{AAO} is the thermal conductivity of the AAO. It is evident that characterizing both the thermal conductivity of the AAO membrane and its porosity becomes an essential task in order to extract a correct value of the single nanowire thermal conductivity. Moreover, many techniques which are capable to measure κ_{com}, (TDTR, laser flash, or PA techniques) need information of the density and the specific heat of the composite. Therefore, it is also critical to determine the associated skeletal AAO membrane values (*i.e.* when there is nothing inside the matrix) in order to calculate the composite values from these two expressions:

$$\rho_{com} = x\rho_{NW} + (1-x)\rho_{AAO} \tag{5.6}$$

$$\left(C_p\rho\right)_{com} = x\left(C_p\rho\right)_{NW} + (1-x)\left(C_p\rho\right)_{AAO} \tag{5.7}$$

where the subscripts *com*, *NW*, and *AAO* stand for composite, nanowire and AAO membrane, respectively. Table 5.IX summarizes different values of both effective, κ_{com} and skeletal, $\kappa_{AAO,}$ thermal conductivity of the AAO membranes at room temperature reported in previous works. Stark *et al.*[84] reported a thermal conductivity value of 1.6 $W \cdot m^{-1} \cdot K^{-1}$ for a thin non-porous amorphous alumina film, measured by the bolometer strip technique. Commercial porous alumina membranes from

Whatman® have also been investigated, founding values of κ_{AAO} of 1.9 $W \cdot m^{-1} \cdot K^{-1}$ [85] and 1.31 $W \cdot m^{-1} \cdot K^{-1}$ [82] for membranes of round 20 nm and 200 nm in pore diameter, respectively. Lee *et al.*[86] determined the effective thermal conductivity of AAO membranes with different porosities, κ_{com}, fabricated by using different acid solutions as 1.31-1.62 $W \cdot m^{-1} \cdot K^{-1}$ for oxalic acid, 0.53-1.01 $W \cdot m^{-1} \cdot K^{-1}$ for sulfuric acid and 0.82-1.12 $W \cdot m^{-1} \cdot K^{-1}$ for mixed acid depending on the anodization temperature. Chen *et al.*[80] investigated a 120 nm pore diameter of unfilled AAO membrane by means of the laser flash technique, showing a κ_{com} value of 0.98 $W \cdot m^{-1} \cdot K^{-1}$ with a 25 % porosity. Furthermore, samples of 30 nm pore diameter fabricated in a sulfuric acid solution have been found to have values of κ_{com} of 1.4 $W \cdot m^{-1} \cdot K^{-1}$ and 30 % of porosity.[87] Finally, AAO membranes anodized in phosphoric acid with three different porosities were investigated and a value of κ_{aao} = 1.38 $W \cdot m^{-1} \cdot K^{-1}$ was obtained for all of them.[76] Thus, κ_{aao} values fluctuate significantly, oscillating from 1.9 to 0.8 $W \cdot m^{-1} \cdot K^{-1}$, as can be seen in Table 5.IX.

The difference between these values may result not only from the thermal conductivity measurement, but also from the assessment of the porosity, density and specific heat, as slight changes could lead to a significant inaccuracy in the calculation of the skeletal thermal conductivity. In order to enhance the metrology and found general values of the thermal conductivity and density, a methodical study of density, specific heat, porosity and thermal conductivity of different AAO membranes as a function of the pore diameter was performed.

Table 5.IX. Literature values of thermal conductivity at room temperature for different varieties of alumina. For porous samples, the skeletal thermal conductivity has been calculated by applying the effective medium theory whether it was not calculated in the original work.

Type of sample	Remarks	Thermal conductivity ($W \cdot m^{-1} \cdot K^{-1}$)	Method	Ref.
Al		237		3
α -Al_2O_3 corundum/sapphire	Purity dependent (80-99%)	15-40	--	88
		30	--	89
	Sintered	35 (273K) 26 (373 K)	--	3
amorphous - Al_2O_3	Thin film: anodic oxidation	1.6±0.2	Bolometer strip	84
amorphous-Al_2O_3	Thin film: RF sputtering on AlN	1.20	3ω	90
amorphous - Al_2O_3	Thin film: RF sputtering on MgO	1.15	3ω	25
amorphous - Al_2O_3	Thin film: RF sputtering on Si	1	3ω	25
amorphous - Al_2O_3	Thin film: DC sputtering on Si	1.6	3ω	90
amorphous - Al_2O_3	Minimum thermal conductivity theory	1.6	theory	90
AAO Whatman®	Pore diameter:20nm Porosity: 30%	κ_{com}=1.33 κ_{aao}=1.9±0.3	Photothermoelectric technique	85
AAO Whatman®	Pore diameter:200nm Porosity: 72%	κ_{com} = 0.38±0.02 κ_{aao} =1.31±0.10	PA	82
AAO Sulfuric acid	No data about pore diameter/ porosity	κ_{com} =0.65, 0.81, 0.85	Transient heat flow	91
AAO Oxalic acid	No data about pore diameter/ porosity	κ_{com}=0.63,0.79,0.86,1.30,1.33	Transient heat flow	91
AAO Oxalic acid	Pore diameter:35 nm Porosity: 13 %	κ_{com} =1.31→ κ_{aao} =1.62	Steady-State technique	86
	Pore diameter:26 nm Porosity: 4 %	κ_{com} =1.5 → κ_{aao} =1.6		
AAO Sulfuric acid	Pore diameter:16 nm Porosity: 34%	κ_{com} =0.53 → κ_{aao} =0.8	Steady-State technique	86
	Pore diameter:12nm Porosity: 1%	κ_{com} =1.01→ κ_{aao} =1.1		
AAO Phosphoric acid	Pore diameter:120nm Porosity: 25%	κ_{com} =0.98 → κ_{aao} =1.3	Laser flash	80
AAO Sulfuric acid	Pore diameter: 30 nm Porosity: 30%	κ_{com} =1.4±0.1 → κ_{aao}=1.9	Laser flash	87
AAO phosphoric acid	Pore diameter: 120nm Porosity: 8 %	κ_{com} = 1.27 → κ_{aao} =1.38	3ω technique	76
	Pore diameter: 220nm Porosity: 25%	κ_{com} =1.04 → κ_{aao} =1.38		
	Pore diameter: 350 nm Porosity: 55%	κ_{com} = 0.64→ κ_{aao} =1.38		

5.5.1 Morphology characterization

Figure 5.19 (a) to (i) shows field emission scanning electron microscopy (FE-SEM) images of the surface topography of the samples anodized in various acid electrolytes and different conditions accompanied by two commercial samples (see (j) and (k)). The anodization process produces a honeycomb-like arrangement of hexagonal cells with long-range order, with a pore in the centre of each cell, whose size depends on the fabrication conditions. A histogram was constructed from these images in order to establish the pore diameter distributions which are displayed alongside their respective image in Figure 5.19. The average pore diameter for each AAO membrane, D_p, was calculated by analyzing such images taken at several zones of each sample. In the lab-made AAOs, the pore diameters vary from 17 nm to 396 nm. AAO membranes directly fabricated from the anodization process, have pore diameters of 17 nm (see Figure 5.19 (a)), 28 nm (b), 39 nm (c), and 149 nm (e), from the electrolytes sulfuric acid (H_2SO_4) with ethylene glycol 50 wt.%, sulfuric acid, oxalic acid ($H_2C_2O_4$) and phosphoric acid (H_3PO_4), respectively. The additional AAO membranes were prepared by widening the pristine ones during different times, which produces a wide range of pore diameters: 67 nm (see Figure 5.19 (d)), 184 nm (f), 223 nm (g), 267 nm (h) and 396 (i). The inter-pore distance, D_{int}, is representative of the electrolyte used in each case and it is conserved during the widening process.

Commercial porous alumina samples, from Smart Membranes® and Whatman® (see Figure 5.19 (k) and (j), respectively), were also analyzed. The investigation of these samples is imperative as many groups utilize them for numerous types of studies. Figure 5.19 (k) shows an average pore diameter of approximately 40 nm for the Smart Membranes alumina. Conversely, an irregular pore shape can be distinguished in the SEM image of the Whatman alumina (Figure 5.19 (j)), whose diameter distribution ranges significantly (with a large quantity of pores oscillating between 100-400 nm) when rivaled to lab-made AAO membranes.

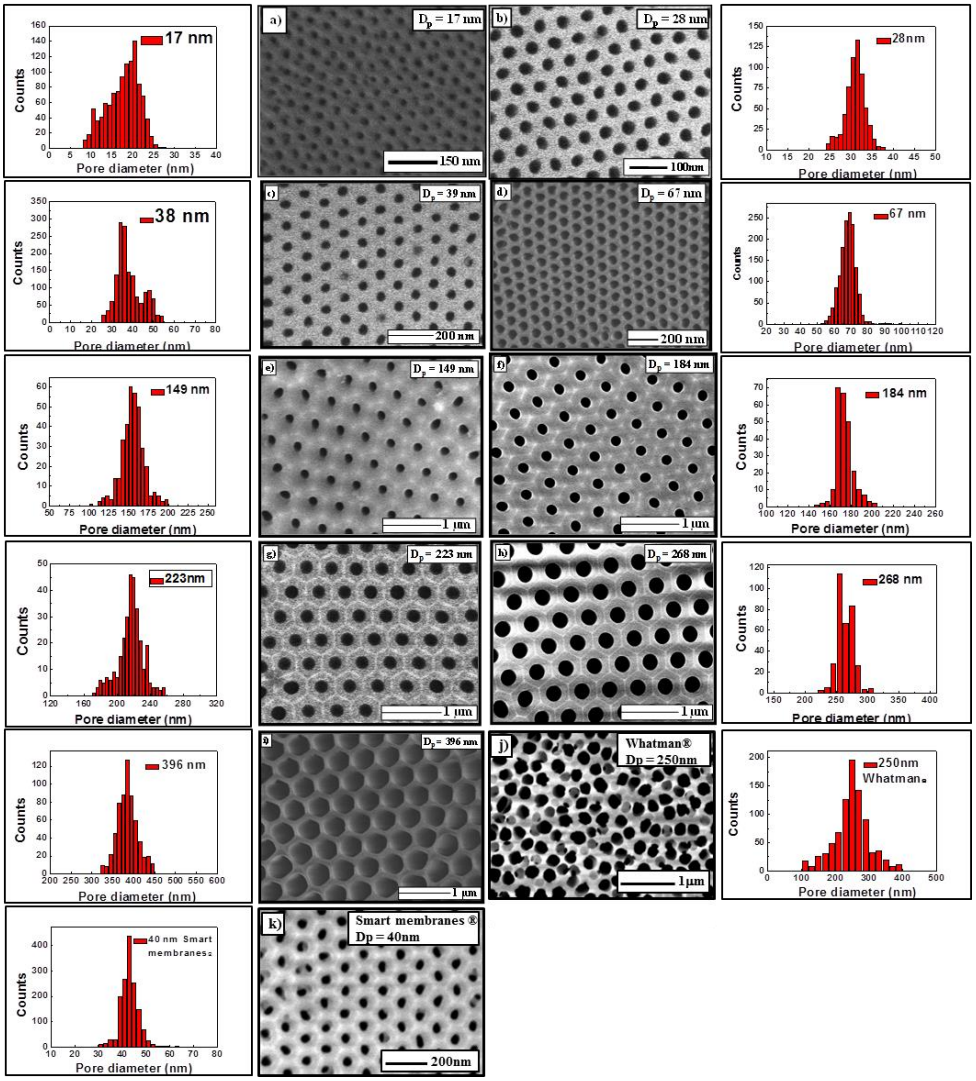

Figure 5.19. FE-SEM images of the top-surface of AAO membranes with different pore diameter along with the statistical distribution of the pore diameter for each sample for lab-made samples (from (a) to (i)) and commercial ones ((j) and (k)).

Figure 5.20 (a) shows the cross section of a commercial porous alumina from Whatman and (b) the cross section of a lab-made AAO. The channels of the lab-made AAO membrane are totally parallel with each other, which is characteristic of all the lab-made fabricated membranes, as well as the commercial sample from Smart Membranes.

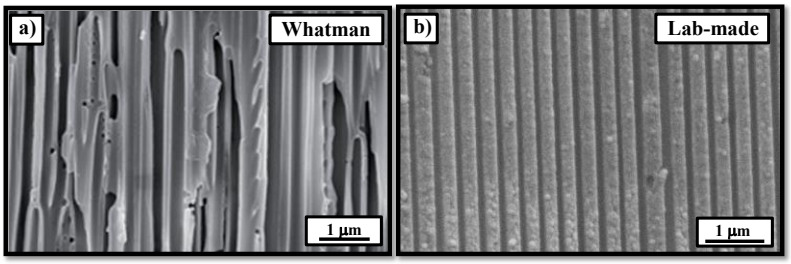

Figure 5.20. Cross section of (a) Whatman commercial of 200 nm pore diameter AAO membrane and (b) lab-made 200 nm AAO membranes.

Figure 5.21 shows a porosity increment as the pore diameter is made larger for samples fabricated with the identical electrolyte, as seen for the oxalic and phosphoric acid AAO membranes. This obeys the predictable tendency given that a reduction in the pore walls and the resulting pore widening takes place during the widening step while maintaining the inter-pore distance.

Pristine AAO membranes fabricated by anodizing in oxalic and phosphoric, of 39nm and 149nm, have low porosity of 15.6 % and 9 %, respectively. Conversely, it is well-known that anodization processes performed in sulfuric acid produces remarkable dissolving of the pore walls so that the porosity of the pristine AAO membranes from sulfuric acid is larger, 23.6 %, as reported in Table 5.X for #28nm.[69] This porosity value was confirmed by the BET technique which serves to verify both average pore diameter and porosity values determined by image analysis.

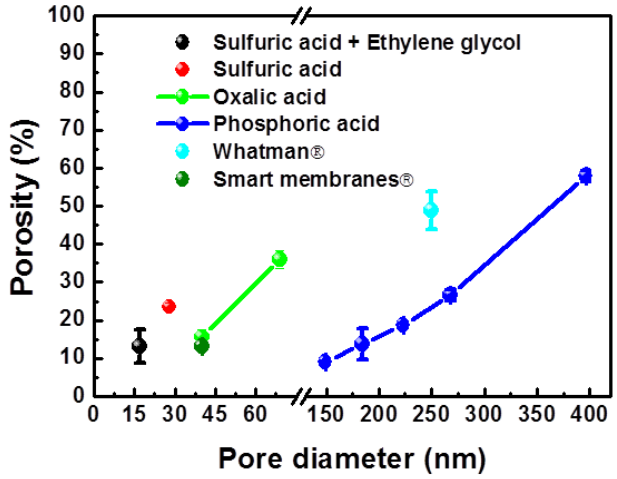

Figure 5.21. Porosity as a function of the diameter for both commercial and lab-made samples fabricated from different acid electrolytes. The samples that are joined by lines correspond to membranes that have been widened from the pristine one.

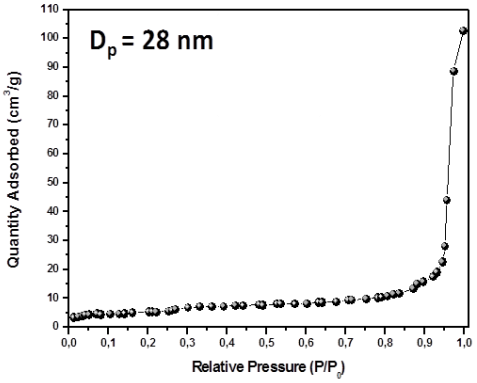

Figure 5.22. Nitrogen adsorption isotherm of AAO membrane of 28 nm in pore diameter AAO

BET via nitrogen adsorption was employed to prove that the reasonable values were obtained by measuring this sample. This technique is optimum for mesoporous samples (2-50 nm) and fails for samples with porous higher than 200 nm. The resulting isotherm reveals mesoporosity for the AAO membrane, as seen in Figure 5.22, with average pore diameter of 27.2 nm and specific surface area of 19 $m^2 \cdot g^{-1}$ for the 28 nm sample. This pore diameter results is in good agreement with the value obtained from the SEM image analysis.

The porosity is determined from the pore volume provided by the BET experiment, 0.16 $cm^3 \cdot g^{-1}$, as explained in Section 2.2.4. The porosity determined by SEM analysis is 23.6 ± 1.0 %, close to the value found by the BET technique, 26.4 ± 3.0 % as both values are within the experimental error intervals.

Once the porosity analysis was proved to be valid, the other AAO membranes were analysed by SEM image analysis. In the case of the sample of 17nm, also fabricated from a sulfuric acid electrolyte with 50 wt.% ethylene glycol, a porosity of 13.1 % was determined. The lower porosity might be ascribed to the ethylene glycol providing a shielding effect on the AAO membrane pore walls as suggested by Martín *et al.*[68, 69] The porosity of the Whatman AAO membrane sample is challenging to obtain as the image analysis is only usable on condition that the channels are parallel to each other. Nevertheless, as seen in Figure 5.20, the Whatman AAO channels are not parallel and they are even communicated so that the related porosity presents higher uncertainty as determined from a statistical analysis.

Table 5.X. Values of pore diameter, porosity, skeletal and composite density, composite specific heat capacity and skeletal and composite thermal conductivity of the AAO membranes.

Sample Name	Pore diameter D_p (nm)	Porosity P (%)	Skeletal density ρ_{AAO} ($g \cdot cm^{-3}$)	Composite Specific heat C_{pcom} ($J \cdot g^{-1} \cdot K^{-1}$)	Composite density ρ_{com} ($g \cdot cm^{-3}$)	Composite thermal conduct. κ_{com} ($W \cdot m^{-1} \cdot K^{-1}$)	Skeletal thermal conduct. k_{aao} ($W \cdot m^{-1} \cdot K^{-1}$)
#17nm	17	13.1	2.789	0.791	2.424	0.94	1.08
#28nm	28	23.6	2.773	0.782	2.119	0.82	1.06
#39nm	39	15.6	2.972	0.889	2.508	1.13	1.33
#67nm	68	35.9	2.928	0.889	1.877	0.83	1.28
#149nm	149	9.0	2.928	0.772	2.665	1.30	1.43
#184nm	184	13.8	2.996	0.772	2.583	1.16	1.34
#223nm	223	18.7	2.848	0.772	2.316	1.08	1.32
#268nm	268	26.7	2.868	0.772	2.103	0.92	1.25
#396nm	396	58.0	2.797	0.772	1.175	0.63	1.46
Smart membranes®	40	13.1	2.930	0.857	2.546	1.18	1.35
Whatman ®	250	48.9	2.840	0.877	1.452	0.68	1.31

5.5.2 Density

The density of the AAO membranes was determined by Archimedes' principle. Nevertheless, in order to calculate the effective density required for the thermal conductivity data reduction, the rule of mixtures given by Eq. 5.6 was used. Considering that the AAO membrane is filled of air with a density value of 1.275 $kg \cdot m^{-3}$ at room temperature (300 K) and using the porosity of each sample, the composite density values were determined as function of the pore diameter, as seen in Table 5.X and Figure 5.23 (b).

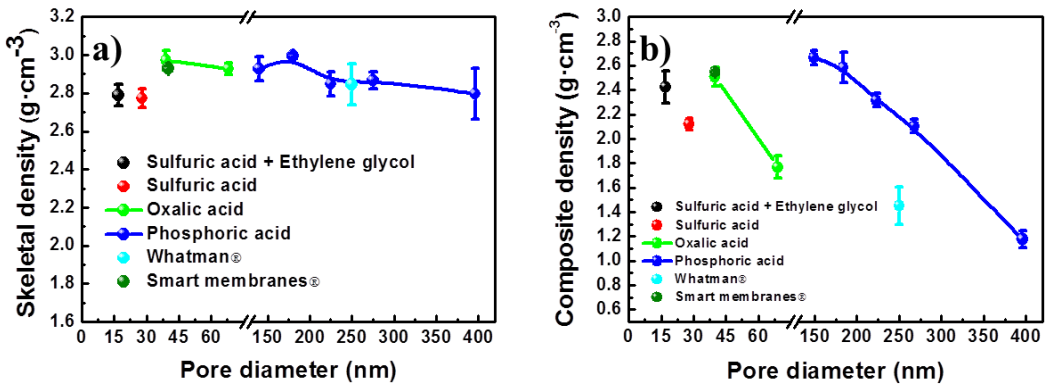

Figure 5.23. (a) Skeletal and (b) composite density at room temperature as a function of the pore diameter for both commercial and lab-made samples fabricated from different acid electrolytes. The samples that are joined by lines correspond to membranes that have been widened from the pristine one.

The skeletal density of the AAO templates varies from 2.770 g·cm^{-3} to 2.930 g·cm^{-3}, which is in accordance with previous investigations.[92] These values are lower than that of the crystalline alumina, 3.6 g·cm^{-3}. [90] The decrease in the density values can be understood by the contamination of the alumina with the anions of the electrolyte as anion-contaminated alumina has been found to have lower density than the anion-free pure alumina.[93] It is well-known that the density of the alumina membranes changes strongly with the anodization conditions.[92] The skeletal density values of the alumina samples prepared by anodizing in sulfuric acid are 2.773 g·cm^{-3} for #28nm, and 2.789 g·cm^{-3} for #17nm, which is in accordance with previous works on samples fabricated with sulfuric acid electrolytes, whose density ranged between 2.4 g·cm^{-3} and 3.2 g·cm^{-3}.[92] In the case of the AAO samples fabricated in the oxalic acid electrolyte, values of 2.972 g·cm^{-3} and 2.928 g·cm^{-3} were obtained for #39nm and #67nm, respectively, which matches with the value measured for the AAO from Smart Membranes, 2.930 g·cm^{-3}. Finally, the density of the AAO membranes fabricated using phosphoric acid electrolyte and the commercial Whatman alumina all yielded values in very good accordance with each other: 2.928 g·cm^{-3}, 2.996 g·cm^{-3}, 2.848 g·cm^{-3}, 2.868 g·cm^{-3} and 2.797 g·cm^{-3} for #149nm, #184nm, #223nm, #268nm, #396nm, respectively, for the AAO membranes prepared in-lab, and 2.840 g·cm^{-3} for the Whatman AAO, as seen in Figure 5.23 (a).

The composite density is lower than the skeletal density due to the air component (Eq. 5.6). If composite density is plotted against the porosity of the membranes, two linear trends can be observed for the samples depending on the electrolyte used to prepare them. Figure 5.24 displays two different groups of samples: those fabricated in phosphoric and oxalic acid and those fabricated in sulfuric acid.

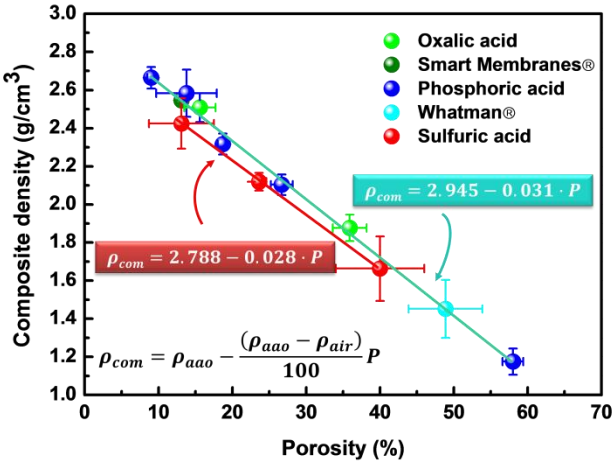

Figure 5.24. Composite density as a function of the porosity for both sets of samples.

If a linear fitting is carried out, two different values of the skeletal density are obtained depending on the electrolyte used. In the case of the phosphoric and oxalic acid a value of ρ_{aao} =2.945±0.013 g·cm^{-3} is obtained from the intercept, with an R^2 value 0.99591, indicating a good fitting. For samples fabricated by sulfuric acid, only two had been prepared for use as a membrane

with well-established pore diameter. In order to confirm the linear tendency in density, another membrane was fabricated in sulfuric acid with a posterior chemical etching, in order to incorporate another data for composite density with a higher porosity, 40%, whose skeletal density value is 2.770 ± 0.054 $g \cdot cm^{-3}$. Fitting this data produces an R^2 value of 0.99923, which reveals a high-quality linear fitting. From the intercept, the value of the skeletal density was found to be 2.788 ± 0.193 $g \cdot cm^{-3}$ where the uncertainty is around 6 % of the value. This uncertainty is tolerable, considering that the composite density values are influenced by the porosity and the small pore size increases its uncertainty when analysing the SEM images. Furthermore, this uncertainty is taken into consideration in the later thermal conductivity extraction.

These density results serve to unite all the values reported in the literature and can be employed to calculate the composite density by knowing the porosity of the membrane, depending on the acid solution used to fabricate the sample.

5.5.3 Specific Heat

Figure 5.25 shows the specific heat as a function of the pore diameter for all the membranes. The values of samples fabricated from the same electrolyte and the following widening process were obtained by weighted averages as all the values were very similar. As seen in Table 5.X, the values oscillate from 0.772 $J \cdot g^{-1} \cdot K^{-1}$ to 0.889 $J \cdot g^{-1} \cdot K^{-1}$. The C_p value of aluminium is in the vicinity 0.897 $J \cdot g^{-1} \cdot K^{-1}$ [3] and the non-porous aluminium oxide (Al_2O_3) is approximately 0.800 $J \cdot g^{-1} \cdot K^{-1}$.[94] Although AAO membranes have been recognized as amorphous[95], the specific heat of the AAO membranes does not vary significantly compared with that of the crystalline aluminium oxide specific heat. The AAO membranes fabricated from sulfuric acid solution have a specific heat values of 0.791 $J \cdot g^{-1} \cdot K^{-1}$, 0.782 $J \cdot g^{-1} \cdot K^{-1}$ for #17nm, #28nm, respectively. In the case of the oxalic acid solution, the specific heat was 0.889 $J \cdot g^{-1} \cdot K^{-1}$. For membranes prepared from phosphoric acid solution the specific heat is 0.772 $J \cdot g^{-1} \cdot K^{-1}$. Conversely, specific heat values of commercial membranes were found to be 0.857 $J \cdot g^{-1} \cdot K^{-1}$ and 0.877 $J \cdot g^{-1} \cdot K^{-1}$ for the Smart Membranes® and Whatman®, respectively.

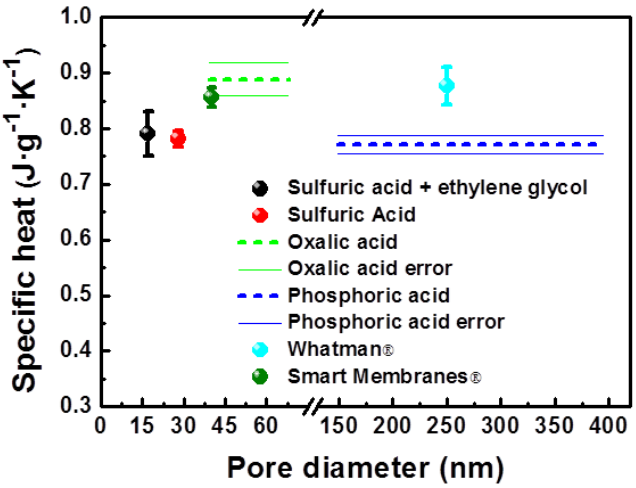

Figure 5.25. Specific heat at room temperature as a function of the pore diameter for both commercial and lab-made samples fabricated from different acid electrolytes. The samples that are joined by lines correspond to membranes that have been widened from the pristine one.

The specific heat measurements were carried out by DSC from -10ºC to 60ºC. Figure 5.26 shows the characteristic curve obtained in the case of the one of the AAO fabricated in the phosphoric acid electrolyte.

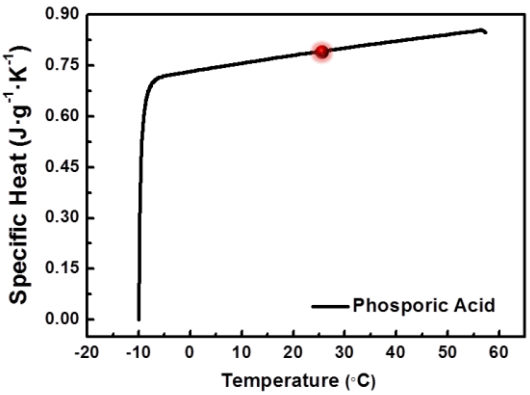

Figure 5.26. Typical curve obtained in the specific heat measurement. The red point depicts the value used for the thermal conductivity data reduction.

5.5.4 Thermal conductivity

The thermal model associated to AAO membranes, showed in Figure 5.27, is simplify by a 2 layer model (80 nm titanium layer and the AAO membrane) together with the air gas layer and the aluminium backing material where the sample is positioned during the measurement.

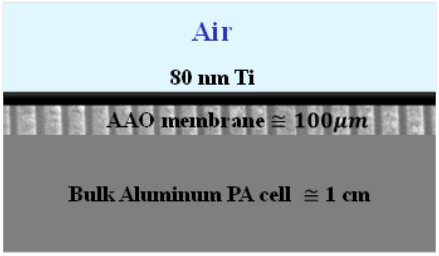

Figure 5.27. Scheme of the 2-layer model used for measuring the AAO membranes.

This model can be used as long as the frequency is low enough to make the heat go across the two layers, to finally reach the aluminium backing material. The thermal diffusion length ($\mu = \sqrt{\alpha/\pi f}$, α is the thermal diffusivity and f is the laser frequency) is utilized to estimate the thermal penetration length of the heat waves. Table 5.XI shows the thermal diffusion lengths for both layers accompanied by those associated to the air gas layer and aluminium backing material.

Table 5.XI. Thermal diffusion lengths of the materials which compose the model.

Frequency (Hz)	**Air (α=1.9·10^{-5} m^2·s^{-1}) (μm)**	**Titanium (α=0.93·10^{-5} m^2·s^{-1}) (μm)**	**AAO membrane (α=0.11·10^{-5} m^2·s^{-1}) [3] (μm)**	**Aluminum (α=12.3·10^{-5} m^2·s^{-1}) (μm)**
1	2459	1721	581	6257
10	778	544	184	1979
100	246	172	58	626
1000	78	54	18	198

By taking into consideration that the AAO membranes thickness is higher than 40 μm, the model is valid when the frequency modulation is lower than 100 Hz as seen Table 5.XI. Nevertheless, a particular study should be done for each membrane as it is necessary to use the thickness of each sample.

Besides, the 1D model can only be used on condition that the thermal diffusion length of the gas is lower than the PA cell radius even if the heat flow is actually 3D, as explained in Section 3.2.1.2.[96] Our PA cell has a diameter of 4 mm and the laser beam diameter is in the vicinity of 1.4 mm. The thermal diffusion length of the gas could be as high as 1.3 mm. As observed in table 5.XII, the thermal diffusion length is lower than 1.3 mm for frequencies higher than 4 Hz. Moreover, the fittings were usually carried out by removing the very low frequency values (4 Hz – 10 Hz) in order to avoid 3D effects.

Table 5.XII. Thermal diffusion length of the air as a function of the frequency.

Frequency (Hz)	**Air Thermal diffusion length (α=1.9·10-5 $m^2 \cdot s^{-1}$) (µm)**
4	1230
6	1004
8	870
10	778

In order to ensure an accurate measurement, it is necessary to define the frequency range where the phase shift measurement is more sensible. For this aim, simulations of the phase shift as a function of a large frequency range were carried out. The properties of the each layer were kept as constant, whereas the thickness of the AAO membrane was modified as the actual samples had different thicknesses.

Figure 5.28 displays the behavior of the phase shift as a function of the modulation frequency for three different thicknesses. For very low frequency modulation, around 1-5 Hz, the phase shift is dramatically reduced. Then, the phase shift increases again also abruptly for frequencies through 5-100 Hz. Both ranges could be a good range of performing the experiment to decrease the experimental uncertainty since the phase shift change is around 30 deg. and the lock-in amplifier uncertainty along with other possible experimental errors sources is approximately 1 deg. Nevertheless, it is necessary to take into consideration the operation frequency range of the microphone which, 4 Hz to 20 kHz. For this reason, in order to guarantee a good performing of the microphone, a frequency range from 5-100 Hz was chosen to conduct the measurements. If the frequency is further increased, a bulk regime is reached characterized by the no variation of the phase shift, being closed to -90 deg. which is the predictable value for bulk materials.[97] That means that the heat does not go across the AAO membrane to any further extent and it is considered as the backing material. It is worthwhile to note, that the phase shift simulations are an approximation with all the properties taken as known so that some differences of these calculations can find.

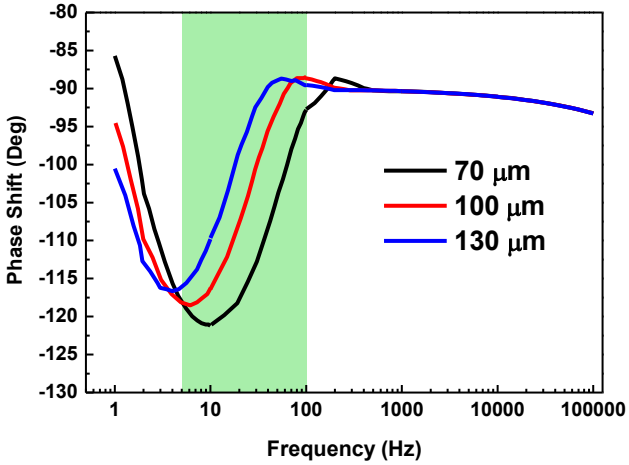

Figure 5.28. Simulated phase shift of the AAO membranes with different thicknesses onto the backing material as a function of the frequency.

Concerning the absorbing layer, as shown in Figure 5.29, the 80 nm titanium layer is continuous when AAO membranes with small pore diameters are employed (See Figure 5.29 (a)). Nevertheless, when using samples with larger pore diameter samples, the titanium layer is not continuous (See Figure 5.29 (b)). Even though the AAO membrane was not completely covered by the titanium layer, we achieved a very high quality fitting with high sensitivity to the thermal conductivity. Furthermore, the values resulted quite consistent regarding the literature values. The justification of the validity of the experiment can be found in the effective medium theory itself given by Eq. 5.5.

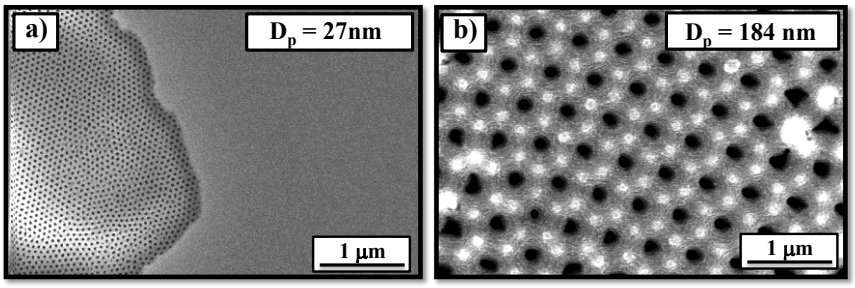

Figure 5.29. (a) #27nm and(b) #184nm AAO membranes covered by a 80nm titanium layer.

Since the thermal conductivity of the air is two orders of magnitude lower than that of the skeletal thermal conductivity of the alumina, EMT can be simplified as,

$$\kappa_{com} = (1 - P)\kappa_{AAO} \tag{5.8}$$

Most heat is primarily going throughout the solid alumina and consequently, the effect of the non-continuous layer is also insignificant because the solid alumina is completely covered in all the cases.

The thermal conductivity of the titanium layer value was 21.9 $W \cdot m^{-1} \cdot K^{-1}$ for all the fittings. In order to check the validity of this value in the data reduction process, we carried out the fittings with different values of the thermal conductivity of the titanium layer. We use values as low as 1 $W \cdot m^{-1} \cdot K^{-1}$ and the calculated thermal conductivity of the AAO membrane remained equal as the one initially extracted, so that we can ensure that the measurements are not influenced by this effect. Also, this technique has been already used by Smith *et al.*[98] who measured other kind of samples by using the same thickness and material as absorbing layer, i.e., 80 nm titanium layer, obtaining satisfactory results.

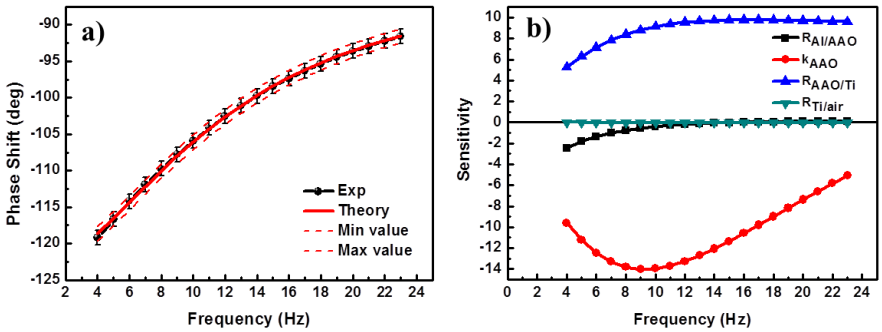

Figure 5.30. (a) Representative PA data fitting of the thermal conductivity measurement of AAO membrane with the experimental and theoretical values along with the maximum and minimum theoretical values when ±1 deg in the experimental phase shift is considered. (b) Representative sensitivity of the four unknown fitted parameters.

Figure 5.30 shows a typical fitting (a) and the sensitivity of the all fitted properties (b). The unknown properties are the AAO thermal conductivity, the thermal resistance between the titanium layer and the air, $R_{Ti/air}$, the thermal resistance between the AAO and the titanium layer, $R_{AAO/Ti}$, and the thermal resistance between the backing aluminium and the AAO, $R_{Al/AAO}$. As seen in Figure 5.30 (b), the AAO thermal conductivity sensitivity is the highest compared with that of the thermal resistances. Thus, the result is fairly accurate and hence, the fitting uncertainty of the measurement is minimized. Table 5.XIII shows the parameters employed in the fitting showed in Figure 5.30 (a).

Table 5.XIII. Parameters used for the PA data fitting.

Layers	**Density (kg m^3)**	**Thermal conductivity (W m^{-1} K^{-1})**	**Specific heat ($J \cdot kg^{-1} \cdot K^{-1}$)**	**Thickness (µm)**	**Optical absorption length (µm)**	**Heat resistance (mm^2 K W^{-1})**
Al	2700	237	897	9000	$8.093 \cdot 10^{-3}$	2727 ± 350
Air/AAO	2103	0.92 ± 0.02	771.7	120	0.001	7.26 ± 0.62
Ti	4500	21.9	522	0.080	$2.565 \cdot 10^{-2}$	1070 ± 165
Air	1.176	0.026	1007	0	0.001	0

Ti/Air resistance was left as a free parameter to be fitted in order to be more thorough. Nevertheless, if we maintain it as a constant with a value as low as 0.01 $mm^2K \cdot W^{-1}$, which is more physically probable, we found the same values with a 2 % of difference. The Al/AAO resistance is high since it arises from the mechanical contact between both materials which include air gaps apart from the pores themselves. Concerning the AAO/Ti resistance, it is more reliable to leave it as a free parameter, as the titanium layer of the highest pore diameter samples is not completely covering and it is more exact not to assume a constant value. Moreover, it is worthy to note that the sensitivity of these parameters is much lower than that of the thermal conductivity, so that a variation in one of the resistances does not greatly alter the finally thermal conductivity value.

In Table 5.X, the composite thermal conductivity, κ_{com}, is displayed together with the skeletal value, which is determined by the effective medium theory as Eq. 5.5 explains. The dispersion of these data can be understood by plotting the composite thermal conductivity values as a function of the porosity, which yields a straight line (see Figure 5.31 (a)). The effective thermal conductivity is reduced when increasing porosity, due to the air contribution within the pores, which has a very low thermal conductivity (0.026 $W \cdot m^{-1} \cdot K^{-1}$) in comparison with the solid amorphous alumina thermal conductivity (about 1-1.5 $W \cdot m^{-1} \cdot K^{-1}$). This reduction could be thought caused by boundary scattering. Nevertheless, this really can be ruled out since: i) the heat conduction when measuring the thermal conductivity occurs along the direction of the nanochannels so that the reduction in the wall thickness of the AAO membrane only affects the heat transport owing to the increase in percentage of air within the sample and ii) although the heat transfer were to take place in the in plane direction, the phonon mean free path of the amorphous alumina is in the order of the interatomic distance [84], which signifies that this diminution in the wall thickness would not influence the heat conduction in the solid alumina unless the wall thickness were condensed to the order of inter-atomic spacing of amorphous alumina, which is not physically possible. Consequently, the reduction of composite thermal conductivity is righter explained by the effective medium theory, which predicts a linear trend between the effective thermal conductivity and porosity as seen in Figure 5.31 (a), from which the skeletal thermal conductivity can be calculated.

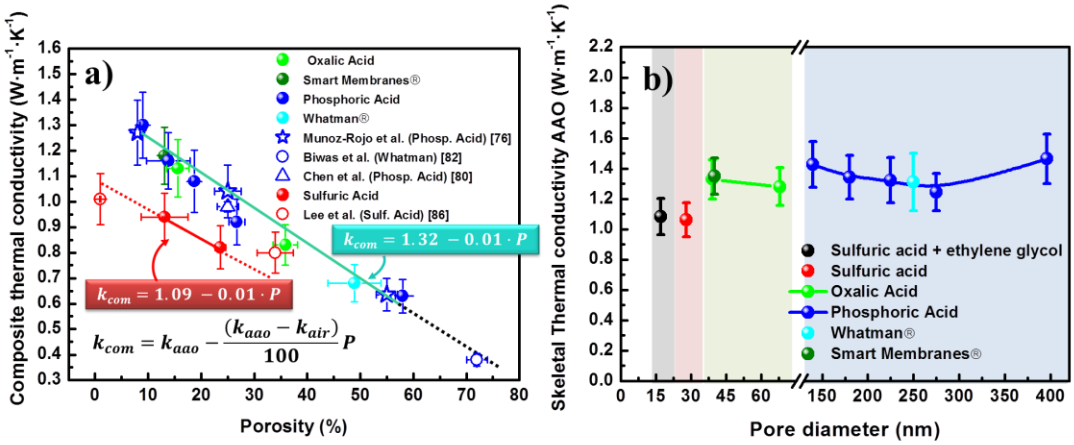

Figure 5.31. (a) Effective thermal conductivity versus the porosity. Rule for calculating any alumina template thermal conductivity values by calculating the porosity % and the relation of the fitting values with the effective medium theory is presented (b) skeletal thermal conductivity value for each sample by applying the EMT independently.

The effective thermal conductivity of AAO membranes fabricated in oxalic and phosphoric acid solutions along with lab-made aluminas measured by Chen *et al.*[80], by Muñoz-Rojo *et al.*[76] and a Whatman® alumina previously measured by Biwas *et al.*[82], show the same tendency. This insinuates that the skeletal thermal conductivity, κ_{aao}, is the same for all these samples. As in the case of the skeletal density, κ_{aao} can be extracted from the intercept of the line with porosity equal to zero. This value corresponds to κ_{aao} =1.32±0.04 W·m^{-1}·K^{-1}, for all the phosphoric and oxalic acid membranes. Furthermore, the uncertainty of these values is significantly reduced as a result of the data fitting. Although the uncertainty of the intercept could be considered to be the experimental uncertainty associated to the skeletal thermal conductivity, it is more rigorous to calculate its uncertainty by calculating the average value of the experimental uncertainties of all the measured samples and the result was 10.9% uncertainty in thermal conductivity, so that the final value is: κ_{aao} =1.32±0.14 W·m^{-1}·K^{-1}. The R^2 results 0.96153 which is still close to 1. The linear tendency is finally verified by the literature values which go along the same trend, showing an R^2 of 0.99235 when fitting them together with our values giving a value of κ_{aao} =1.31 W·m^{-1}·K^{-1}. Values obtained by Muñoz-Rojo *et al.*[76] and Chen *et al.*[80] are expected to have the same trend since the AAO membrane used in these works were highly ordered with parallel nanochannels, so that both porosity and thermal conductivity could be accurately determined. Regardless of the highly irregularities of the Whatman AAO membrane investigated by Biswas *et al.*[82], the thermal conductivity determined in this work also fit our linear tendency, possibly due to an exhaustive statistics of both porosity and thermal conductivity measurements of this sample were performed. Nevertheless, some data, presented in Table 5.IX, did not fit the expected trend. For the case of the oxalic acid solution, Lee *et al.* obtained values of κ_{aao} of around 1.6 W·m^{-1}·K^{-1}, which is far from our result. This can be attributable to a low quality of the samples as seen in the SEM images exposed in that work, where pores seem to be communicated. This

fact could produce inaccuracies in the determination of the porosity and the later extraction of thermal conductivity.[86]

In the case of AAO membranes prepared in the sulfuric acid electrolyte, two data points are not enough to carry out the fitting. The sample with a porosity of 40 % membrane has transversal nanochannels so that it is perfectly possible to apply the density rule of mixtures but the effective medium theory cannot be applied due to the directionality of heat transport across the template. The two data point fitting would provide a value of κ_{aao} = 1.09 $W \cdot m^{-1} \cdot K^{-1}$. Lee *et al.* obtained values that approximately fit our linear trend as shown in Figure 5.31 (a). Nevertheless, if a linear fitting is carried out a value of R^2 of 0.90418 is found. The value of the skeletal conductivity obtained from that fitting is 1.01 $W \cdot m^{-1} \cdot K^{-1}$ which is a little bit lower than that of extracted by fitting only the two points.

Finally, in order to be more thorough in the analysis, the skeletal thermal conductivity of both samples was estimated independently, using the EMT, and finally an average of both values was taken, yielding a value of skeletal thermal conductivity of 1.07 ± 0.11 $W \cdot m^{-1} \cdot K^{-1}$. Values of κ_{aao}, around 1.9 $W \cdot m^{-1} \cdot K^{-1}$, were located in the literature which disagrees considerably from our result, κ_{aao} =1.07 $W \cdot m^{-1} \cdot K^{-1}$.[85, 87] Borca-Tasciuc *et al.*[85] investigated a Whatman alumina of 20 nm with a porosity variation between 25 % and 36 %. 30% of porosity was employed in that work to perform the calculation of the skeletal thermal conductivity. This severe variation and the heat conduction along this irregular structure could be responsible for the deviation between this work and our finding. Cai *et al.* [87] also found a value of around 1.9 $W \cdot m^{-1} \cdot K^{-1}$ which could differ from our result due to the necessity of knowing density and specific heat of both the AAO membrane and the aluminum foil for the two-layer model developed in that work.

The calculated skeletal thermal conductivity values against the pore diameter are also shown in Figure 5.31 (b). For sulfuric acid solution, the thermal conductivity was found to be 1.08 $W \cdot m^{-1} \cdot K^{-1}$ and 1.06 $W \cdot m^{-1} \cdot K^{-1}$ for #17nm and #28nm, respectively. In the case of the oxalic acid solution, values of 1.33 $W \cdot m^{-1} \cdot K^{-1}$ and 1.28 $W \cdot m^{-1} \cdot K^{-1}$ were obtained for #38nm and #69nm, close to the value determined for the AAO from Smart Membranes®, 1.35 $W \cdot m^{-1} \cdot K^{-1}$, fabricated in similar conditions. In the case of the phosphoric acid, all the values were found to range from 1.3 to 1.5 $W \cdot m^{-1} \cdot K^{-1}$ which match the value of the commercial Whatman® AAO, 1.31 $W \cdot m^{-1} \cdot K^{-1}$, also grown with phosphoric acid. As explained above, samples prepared in the same acid electrolyte, give rise to the same values of skeletal thermal conductivity of AAO.

A strong reduction in the skeletal thermal conductivity of these amorphous alumina samples in comparison with the crystalline alumina whose thermal conductivity is in the range of 15-45 $W \cdot m^{-1} \cdot K^{-1}$ at room temperature is observed, as seen in Table 5.X [88, 99]. This is a usual phenomenon when a crystalline material turns into amorphous, such as SiO_2. Thermal conductivity of crystalline SiO_2 is found to be around 10 $W \cdot m^{-1} \cdot K^{-1}$ whereas its amorphous counterpart has 1 $W \cdot m^{-1} \cdot K^{-1}$ at room

temperature.[89] In amorphous materials, heat is carried through localized vibrations. These localized vibrations give rise to the minimum thermal conductivity of the material.[89] Moreover, the change in density between crystalline and amorphous phases could favour this thermal conductivity reduction.

Thermal diffusivity has also been calculated (See Table 5.XIV) from the thermal conductivity, density and specific heat. As in the case of the thermal conductivity, the AAO membranes fabricated in sulfuric acid conditions have the lowest thermal diffusivity.

Table 5.XIV. Skeletal density, specific heat, skeletal thermal conductivity and skeletal thermal diffusivity values for each solution together with the commercial membranes

Acid solution	**Skeletal density ρ_{aao} ($g \cdot cm^{-3}$)**	**Specific heat C_p ($J \cdot g^{-1} \cdot K^{-1}$)**	**Skeletal thermal conductivity κ_{aao} ($W \cdot m^{-1} \cdot K^{-1}$)**	**Skeletal Thermal diffusivity α_{aao} 10^{-7}($m^2 \cdot s^{-1}$)**
Sulfuric Acid	2.788 ± 0.193	0.787 ± 0.040	1.07 ± 0.11	4.85 ± 0.50
Oxalic Acid	2.945 ± 0.013	0.889 ± 0.030	1.32 ± 0.14	5.04 ± 0.15
Phosphoric Acid	2.945 ± 0.013	0.772 ± 0.016	1.32 ± 0.14	5.81 ± 0.18
40 nm Smart Membranes® (Oxalic Acid)	2.945 ± 0.013	0.857± 0.018	1.32 ± 0.14	5.23 ± 0.16
200 nm Whatman® membrane (Phosphoric Acid)	2.945 ± 0.013	0.878 ± 0.034	1.32 ± 0.14	5.11 ± 0.16

In order to understand the low values of the thermal conductivity for alumina membranes prepared in sulfuric acid, micro-Raman spectroscopy was carried out. As can be observed in Figure 5.32, the Raman spectrum of the AAO grown in sulfuric acid solution exhibits a different spectrum than what is found for oxalic and phosphoric acid templates measured under the same conditions. In the sulfuric acid spectrum, two clear bands found at the wavelengths 980 cm^{-1} and 1053 cm^{-1} are recognized. They can be associated with the ν_1 and ν_3 vibrations, respectively, of the SO_4 group in aluminium sulphate [69]. This shows an evident bonding of the SO_4 groups from the electrolyte with the aluminium from the template. In addition, the band located at 452 cm^{-1} has been previously assigned to alumina E_g (external) mode, and the band placed at 627 cm^{-1} was attributed to the infrared (IR) active modes, according to literature.[69] Conversely, for oxalic and phosphoric acid solutions, there are not evident bands by reason of their higher luminescence. This suggests a remarkable structural difference among the three types of alumina membranes, which clarifies why those AAO membranes prepared from the sulfuric acid solution are less thermally conductive with a slightly lower skeletal density and also explains the data dispersion found in the literature about the density of AAO membranes.[92, 93]

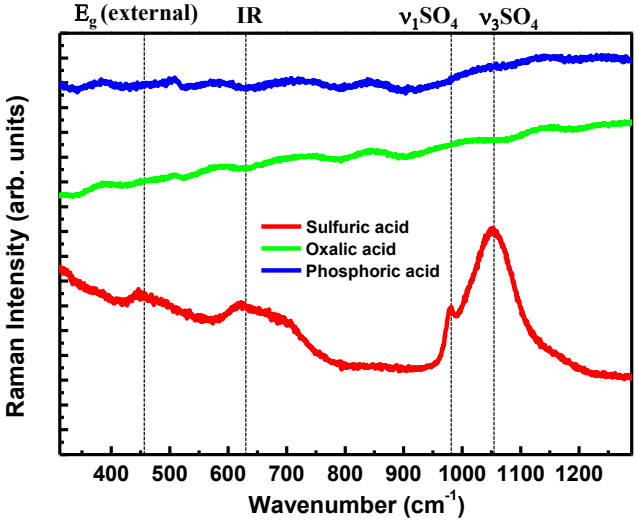

Figure 5.32. Raman spectra of the AAO anodized in sulfuric, oxalic and phosphoric acid measured under the same conditions.

In conclusion, we established *two rules* from where any AAO membrane effective thermal conductivity and density can be calculated, by knowing the electrolyte used to prepare the template and analysing the percentage of porosity of the sample. The general equations and the skeletal values are summarized in Table 5.XV.

Table 5.XV. Skeletal thermal conductivity and density as function of the porosity together with the overall values for each acid solution.

Acid solution	**AAO Density calculation rule** $\rho_{com} =$	**Skeletal density ρ_{aao} ($g \cdot cm^{-3}$)**	**AAO thermal conductivity rule** $k_{com} =$	**Skeletal thermal conductivity κ_{aao} ($W \cdot m^{-1} \cdot K^{-1}$)**
Oxalic and Phosphoric Acid	$2.945 - 0.031P$	2.945 ± 0.013	$1.32 - 0.04P$	1.32 ± 0.14
Sulfuric Acid	$2.788 - 0.028P$	2.788 ± 0.193	–	1.07 0.11

5.6 Three dimensional anodic aluminum oxide membranes

Three-dimensional anodic alumina membranes (3D-AAO) are an motivating new form of network[100], which are constituted of a geometric space-frame of intersected nanoholes that can be filled with different materials. The open space-frame structure of 3D-AAO templates gives them with some important properties. For instance, they can perform as a host of functional materials within the spaces of the framework and thus 3D membranes could be used to design materials with exceptional properties. 3D-AAO structure fabrication has been recently established which permits researchers to

study different physical phenomena when it is filled by different materials[100, 101]. These structures are formed by longitudinal pores as the regular AAO membranes with the integration of transversal pores interconnected so that a highly ordered 3D network is created with a hexagonal arrangement in both longitudinal and transversal directions. In addition, alumina presents a high mechanical, chemical and thermal stability which made this material appropriate for many kind of studies[92, 102, 103].

Up to now, optical phenomena have been investigated when these 3D structures are filled with materials like polymers or bismuth telluride, showing a photonic crystal behavior[100, 101]. Nevertheless, there is a scarcity of studies about the thermal properties of these structures. They can be used not only as building blocks for thermal engineering by hosting different filler materials into the framework but also to study the effect of the nano architecture in the heat transport of the filler material itself. In this direction, the study of the thermal conductivity in this structure is definitely attractive as the low dimension of the interconnected channels can produce a reduction in the thermal conductivity of the filler material by phonon scattering processes. As seen in the previous section, the thermal conductivity of the AAO membranes does not suffer any decrease when lowering the dimensions as anodic aluminum oxide is an amorphous material so that the phonon mean free path is in the order of the interatomic distance and hence, the heat conduction is not influenced by a diminution in the dimensions [104]. In order to determine the thermal conductivity of the filler materials it is indispensable not only to know the porosity and the skeletal thermal conductivity of the 3D membrane itself, but also to develop a thermal model which permits the determination of the thermal conductivity of the filler material. In the case of ordinary AAO membranes, the effective medium theory can be applied since the membrane can be approximated to two thermal resistors in parallel. In the case of the 3D alumina, this model is not valid since this sample can be seen as a thermal resistor which combines resistors both in series and in parallel.

For that purpose, the effective thermal conductivity of a non-filled 3D-AAO membrane was measured. The density, specific heat and the porosity need to perform the data reduction were also characterized. Furthermore, once the effective thermal conductivity was obtained, a thermal conduction model was developed in order to extract the thermal conductivity of the skeletal 3D alumina membrane whose value is required for future study of filler materials. This thermal model was utilized to study the effect of different filler materials and the length and number of transversal nanochannels of the membrane which can be controlled during the fabrication process. The effective thermal conductivity of the whole composite can be design by these parameters and thus, the heat flux across the structure can be controlled depending on the application while keeping lateral conduction across the transversal nanochannels.

5.6.1 Results and thermal model

The morphology of top and transversal views of the 3D nanostructure was analyzed by SEM as shown in Figure 5.33. The top view (Figure 5.33 (a)) displays a hexagonal close packed arrangement of the pores. The pore diameter of the longitudinal pores was analyzed by a histogram as shown in Figure 5.33 (b), exhibiting an average pore diameter of 40 nm as the pore size distribution reveals. Initially, pores of 25 nm were obtained from the sulfuric acid solution[104] but a larger final pore diameter was achieved as a result of the widening process during the etching step. Figure 5.33 (c) shows the cross-section view where the longitudinal pores interconnected with the transversal nanochannels in the horizontal direction of the image can be distinguished, thus proving the 3D nanochannel network creation as observed by Martin *et al.*[100] Besides, as described in the reference[100], the transversal nanochannels present also hexagonal symmetry. From Figure 5.33 (c) an average diameter of approximately 30 nm and an interchannel distance in the vicinity 230 nm were measured for the transversal nanochannels. The number of nanochannels, *N*, depends on the number of pulses selected in the software used for the second anodization process so that the experiment was designed in such a way that the 3D membrane with 120 nanochannels was obtained. Furthermore, both the top and bottom parts of the 3D alumina membrane present around 1.2 µm of alumina without any transversal nanochannels which offers mechanical stability to the whole sample. Finally, the length perpendicular to the 3D membrane surface was found to be 33.4 µm.

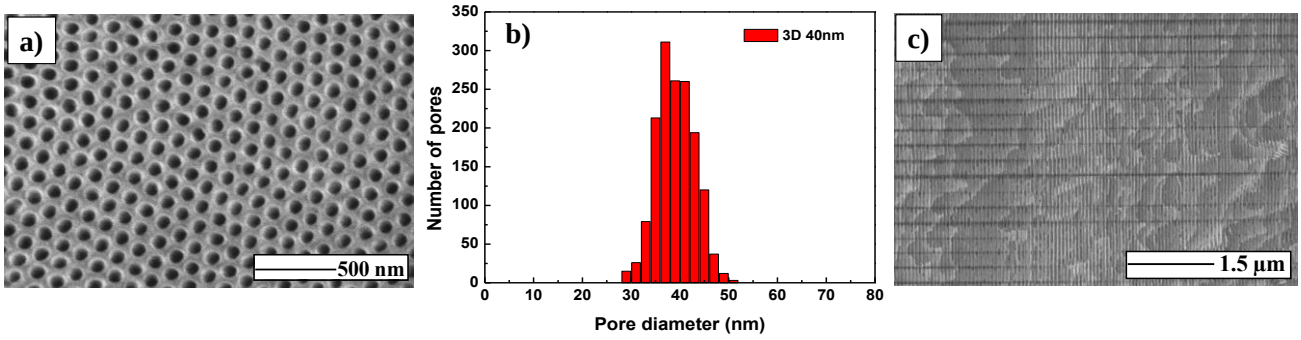

Figure 5.33. (a) Top-view (b) pore diameter histogram and (c) cross-section of the 3D-AAO membrane.

In order to determine the overall porosity of the 3D structure it is required to take into consideration both the longitudinal pores and the transversal nanochannels. The so-called top-porosity arises from the longitudinal pores and is calculated by the top SEM image analysis.

The overall porosity of the 3D AAO membrane is experimentally determined by BET via nitrogen sorption. The isotherm obtained reveals extensive mesoporosity for the 3D membrane with a mean pore size of 35 nm, specific surface area of 1.6 $m^2 \cdot g^{-1}$ and a pore volume of 0.014 $cm^3\ g^{-1}$. The average pore size is acceptable given that the pore diameter of the longitudinal pores is around 40 nm

and the transversal nanopores pore diameter is found to be in the vicinity of 30 nm. These BET experiments provided a value of porosity of 40 ± 6 % for this sample. This value is reasonable as it is higher than the porosity associated to the longitudinal channels calculated from the SEM images, 31.8%.

The skeletal density of the 3D AAO membrane, ρ_{AAO}, was found to be 2.770 ± 0.054 g·cm^{-3} which is in good agreement with previous studies of AAO samples prepared in sulfuric acid which obtained values of 2.4 g·cm^{-3} and 3.2 g·cm^{-3} [92]. Also, it is also in good accordance with our exhaustive study shown in section 5.6.2 where a value of 2.788 g·cm^{-3} for AAO membranes prepared under the sulfuric acid solution was demonstrated [104]. The composite density, ρ_{com}, of the non-filled 3D-AAO membrane can be calculated by the rule of mixtures given by Eq. 5.6, taking the air density as 1.275 · 10^{-3} g·cm^{-3} at room temperature (300 K). This rule yields to a composite density value of 1.662 ± 0.169 g·cm^{-3}.

Figure 5.34 displays the specific heat of the sample as a function of the temperature, showing an increment of the specific heat when increasing the temperature. The room temperature value of 0.885 J·g^{-1}·K^{-1} was used for the thermal conductivity data reduction for the 3D membrane.

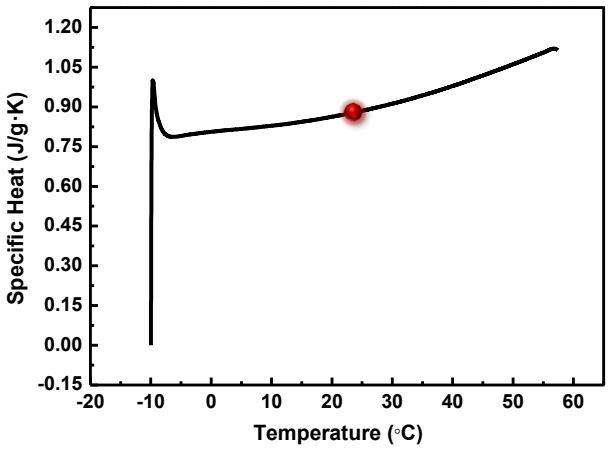

Figure 5.34. Specific heat as a function of the temperature. The red point depicts the specific value employed for the thermal conductivity data reduction.

With porosity, density and specific heat values summarized in Table 5.XVI, the effective thermal conductivity could be obtained, κ_{com} = 0.38 ± 0.06 W·m^{-1}·K^{-1}, which is a very low value compared with an ordinary AAO with longitudinal pores and much larger porosity, 58%, whose effective thermal conductivity resulted κ_{com} = 0.64 W·m^{-1}·K^{-1} (See Table 5.X) [104].

Table 5.XVI. Values of the porosity, skeletal and composite density, composite specific heat capacity and skeletal and composite thermal conductivity of the 3D-AAO membrane.

Porosity P (%)	**Skeletal density ρ_{AAO} ($g \cdot cm^{-3}$)**	**Composite Specific heat C_p ($J \cdot g^{-1} \cdot K^{-1}$)**	**Composite density ρ_{com} ($g \cdot cm^{-3}$)**	**Composite thermal conductivity k_{com} ($W \cdot m^{-1} \cdot K^{-1}$)**	**Calculated Skeletal thermal conductivity k_{aao} ($W \cdot m^{-1} \cdot K^{-1}$)**
40 ± 6	2.770 ± 0.054	0.885 ± 0.025	1.662± 0.169	0.38 ± 0.06	1.25 ± 0.25

The reason can be found in the thermal conduction model for each membrane. In the case of the ordinary sample described in section 5.6.4, the sample consists of a common AAO template with longitudinal pores. The heat conduction based on the Effective Medium Theory (EMT) can be thought as a thermal parallel resistor so that the heat flux can find a channel to go through the cross-plane direction. Conversely, in the case of 3D structure, the heat conduction model is more complex since the heat conduction takes place across a combination between parallel and series resistances. The EMT must be adapted in order to obtain the skeletal thermal conductivity. If EMT were used, an underestimated value of the skeletal thermal conductivity would be calculated. A value of 0.62 $W \cdot m^{-1} \cdot K^{-1}$ is obtained when the overall porosity (40%) is used, which is too low. Nevertheless, the 3D sample must be considered as a thermal resistor circuit as shown in Figure 5.35 (a). This circuit has three parallel components which are represented in Figure 5.35 (b): two of them are shared with the EMT, i.e., the solid alumina (R_{aao}) and the pores (R_{air}) contribution but there is a new term which results from the interconnected transversal nanochannels. This component is composed of some series resistances: the solid alumina on the top (R_{aao1}) and bottom (R_{aao2}) of the membrane before and after the transversal channels appear, and the resistances due to de solid alumina and air associated with the channels (R'_{aao} and R'_{air}), which must be multiplied by the number of nanochannels, N. This circuit is a simplified model which neglects the thermal contact resistances between longitudinal pores as the effective medium theory but also disregards the thermal contact resistances between the filler material (air in this case) and the alumina along channel 3 of Figure 5.35 (a) and (b) as a first approximation.

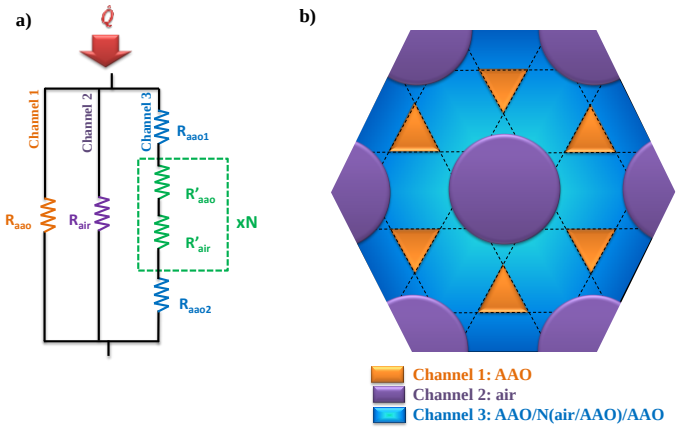

Figure 5.35. (a) 3D AAO sample thermal resistor model where $\dot{Q}$ is the heat going through the samples and (b) top-view of a section with the transversal channels (dashed lines) of the 3D ordered AAO membrane.

With these assumptions, the mathematical model is developed from this circuit so that the total thermal resistance is given by,

$$\frac{1}{R_T} = \frac{1}{R_{aao}} + \frac{1}{R_{air}} + \frac{1}{2 \cdot R_{aao1} + N \cdot (R'_{aao} + R'_{air})}, \tag{5.9}$$

where each of the components is defined as,

$$R_{aao} = \frac{L_T}{(1 - P_{\parallel} - \overline{P_{\perp}}) \cdot \kappa_{aao}}, \tag{5.10}$$

$$R_{air} = \frac{L_T}{P_{\parallel} \cdot \kappa_{air}}, \tag{5.11}$$

$$R_{aao1} = R_{aao2} = \frac{L_{aao-top}}{\overline{P_{\perp}} \cdot \kappa_{aao}}, \tag{5.12}$$

$$R'_{aao} = \frac{L_{interchan}}{\overline{P_{\perp}} \cdot \kappa_{aao}}, \tag{5.13}$$

$$R'_{air} = \frac{L_{channel}}{\overline{P_{\perp}} \cdot \kappa_{aao}}, \tag{5.14}$$

where R_T is the equivalent resistance of the whole circuit, L_T is the length the membrane, $P_{\parallel}$ is the top-porosity associated with the longitudinal channels, κ_{aao} is the skeletal thermal conductivity of the AAO membrane, κ_{air} is the air thermal conductivity, $L_{aao\text{-}top}$ is the length of the top porous alumina without transversal nanochannel, which is considered to be the same as that of the bottom part, $\overline{P_{\perp}}$ is the mean top-porosity corresponded to the transversal nanochannels, $L_{interchan}$ is the distance between two transversal nanochannels, and $L_{channel}$ is the average pore diameter of these nanochannels.

By substituting each magnitude in Eq. 5.9, the effective thermal conductivity can be expressed as,

$$\kappa_{com} = P_{\parallel} \cdot \kappa_{air} + (1 - P_{\parallel} - \overline{P_{\perp}}) \cdot \kappa_{aao} + \frac{1}{2 \cdot \left(\frac{L_{aaoTop}/L_T}{\overline{P_{\perp}} \cdot \kappa_{aao}}\right) + \frac{N}{\overline{P_{\perp}} L_T} \cdot \left(\frac{L_{channel}}{\kappa_{air}} + \frac{L_{interchan}}{\kappa_{aao}}\right)} \tag{5.15}$$

In order to calculate κ_{aao}, it is necessary to estimate $\overline{P_{\perp}}$. For that aim, the top-view porosity corresponding to the transversal nanochannels, $P_{\perp}$, must be determined. Figure 5.36 illustrates a top view of a hexagonal cell without (a) and with (b) transversal channels at full scale. An image analysis of both images was performed.

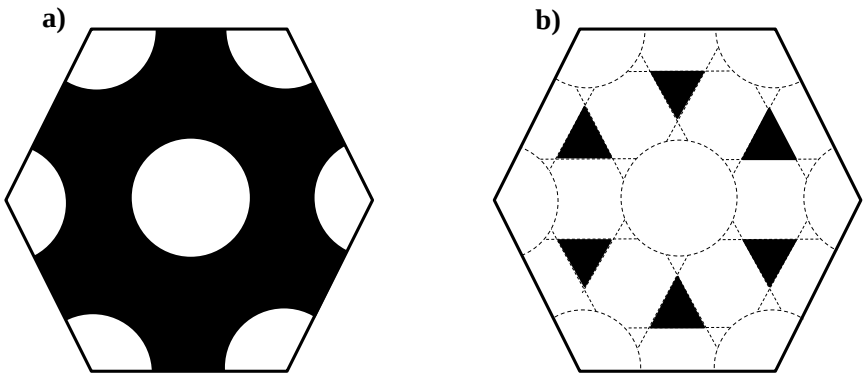

Figure 5.36. Cross-section of the 3D membrane of a region (a) without transversal channels and (b) with the transversal channels. The black part corresponds to solid alumina and the white one with air. Both sketches depict a hexagonal unit cell. All the dimensions have been taken from the SEM image: D_p = 40 nm; D_{int} = 66 nm; $L_{channel}$ = 30 nm, where D_p is the pore diameter, D_{int} is the interpore distance and $L_{channel}$ is the transversal channel size.

To confirm that this analysis is valid for our structure, the same analysis corresponded to Figure 5.36 (a) is performed in five top-view SEM images of the 3D structure (like Figure 5.33 (a)), which provided a value of 31.8 %. The analysis of the sketch of Figure 5.36 (a) gave a value of 33.8 %. The difference between these two values can be considered within the uncertainty interval. This proof allows us to estimate the porosity of a cross-section of the 3D AAO structures with transversal nanochannels given that it is not viable to determine it by SEM images analysis. A value of 90.3 % is obtained, which includes both, longitudinal and transversal nanochannels. The value of the transversal channel part is 90.3 % - 31.8 % = 58.5 %. That implies that in a cross-sectional view with transversal nanochannels, 58.5 % of the total area arises from transversal nanochannels. However, this value is related with the cross section of the pore where its area is maximized. Actually, there is a gradual porosity along the transversal channel, i.e., in the cross plane direction as seen in Figure 5.37 (a). In order to take this effect into consideration, it is required to calculate the mean transversal porosity, $\overline{P_\perp}$.

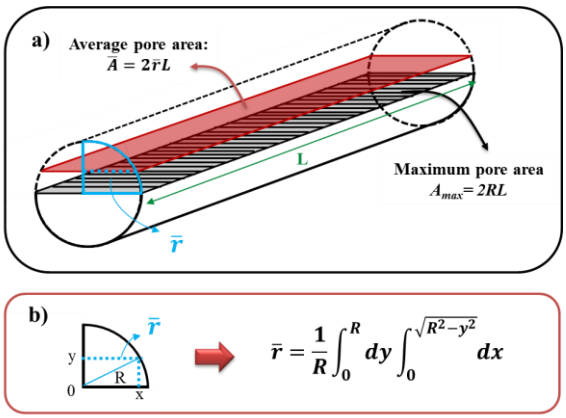

Figure 5.37. (a) Sketch of a transversal pores between longitudinal pores. The striped area corresponds to the porosity calculated from the SEM image analysis, $P_\perp$. The shadow area is the average area of the pore. (b) Calculation of the average radio used to estimate the average area of the pore.

The mean value of a continuous function is defined as:

$$\overline{f(x)} = \frac{1}{b-a}\int_a^b f(x). \tag{5.16}$$

In a 3D-AAO membrane, the function is given by the section of the transversal pores which are approximated as cylinders, $A = 2R{\cdot}L$, where R and L are the radius and length of the cylinder. The problem can be simplified to the calculation of the mean radius of the cylinder as Figure 5.37 (b) depicts. The limit of integration of the x variable is calculated by the Pythagorean Theorem so that the average pore area can be expressed as:

$$\bar{A} = 2\bar{r}L = \frac{2L}{R}\int_0^R r dr = \frac{2L}{R}\int_0^R dy \int_0^{\sqrt{R^2-y^2}} dx. \tag{5.17}$$

If the first integral is solved:

$$\bar{A} = \frac{2L}{R}\int_0^R \sqrt{R^2-y^2}\,dy. \tag{5.18}$$

By integrating the cross sectional area of the transversal pores:

$$\bar{A} = \frac{\pi}{2}RL = \frac{\pi}{4}A_{max}, \tag{5.19}$$

where A_{max} is the section area of the pore with radius $L_{channel}/2$, which is the distance between two longitudinal pores, i.e., the wall thickness. The porosity is proportional to the area in such a way that the same relation can be used for $P_{\perp}$:

$$\overline{P_{\perp}} = \frac{\pi}{4}P_{\perp}. \tag{5.20}$$

The top-view porosity corresponding to the transversal nanochannels was found to be 58.5 % so that, we finally obtain a value of $\overline{P_{\perp}} = 45.9\%$.

Additionally, this model allows the calculation of the overall porosity of the 3D AAO membrane by the relation:

$$P = P_{\parallel} + \left(\overline{P_{\perp}} \cdot \frac{(N \cdot L_{channel})}{L_T}\right). \tag{5.21}$$

If values of Table 5.XVII are used, the 3D AAO membrane porosity is found to be in the vicinity of 37 % from Eq. 5.21, which is within the uncertainty interval of the porosity determined by the BET technique, 40 ± 6%.

Table 5.XVII. Values used for the calculation of the skeletal thermal conductivity of the 3D membrane along with the information source.

$P_{\parallel}$ (%)	κ_{air} ($W \cdot m^{-1} \cdot K^{-1}$)	$\overline{P_{\perp}}$ (%)	L_{aaoTop} (μm)	$L_{channel}$ (nm)	$L_{interchan}$ (nm)	N	L_T (μm)
31.8	0.026	45.9	1.2	30	230	120	33.4
SEM	Tabulated	Calculated	SEM	SEM	SEM	Theoretical	SEM

5.6.2 Skeletal thermal conductivity calculation

The values utilized in this model together with their source of information are shown in Table 5.XVII. As explained above, the top-porosity ($P_{\parallel}$) was determined by SEM image analysis. The air thermal conductivity was considered as a constant. The size of the channels were measured from the SEM images along with a calculation by taking into account that the number of channels, *N*, is a fixed number that is imposed in the software for the anodization process. The total length of the membrane is measured from the SEM images. Finally, the average porosity associated to the transversal channels, $\overline{P_{\perp}}$, is calculated by averaging the gradual porosity along the radius of the transversal pore.

From the above model, a value of 1.25 ± 0.25 $W \cdot m^{-1} \cdot K^{-1}$ is found for the skeletal 3D AAO membrane which match the obtained values obtained for the AAO prepared in sulfuric acid solutions [104]. This result aids to prove the validity of the 3D thermal model.

5.6.3 Thermal conductivity engineering

Once the skeletal thermal conductivity of the 3D AAO template was calculate, a study of the influence of the number of nanochannels and the length of the membrane in the composite thermal conductivity was performed. For that purpose, the resistance term which arises from the top and bottom part of the AAO without transversal channels is neglected, as long as their length is lower than 25 % of the entire membrane, so that the total length of the alumina is given by:

$$L_T = N \cdot (L_{channel} + L_{interchannel}). \tag{5.22}$$

Besides, it is obligatory to impose a constraint condition given by the total length of the nanochannels cannot be equal or larger than the total length of the AAO membrane. In the case that both lengths were identical, the interchannel distance would be zero which does not make sense. Experimentally, the minimum interchannel distance that can be accomplished for $L_{channel}$ = 30 nm is approximately 30 nm so that, the constraint condition would be:

$$L_T > 0.06N. \tag{5.23}$$

The composite thermal conductivity can be written as a function of the $L_{channel}$, N and L_T as:

$$\kappa_{com} = P_{\parallel} \cdot \kappa_{mat} + (1 - P_{\parallel} - \overline{P_{\perp}}) \cdot \kappa_{aao} + \frac{1}{\frac{N \cdot L_{channel}}{\overline{P_{\perp}} \cdot L_T} \cdot \left(\frac{1}{\kappa_{mat}} - \frac{1}{\kappa_{aao}}\right) + \frac{1}{\overline{P_{\perp}} \cdot \kappa_{aao}}}, \qquad (5.24)$$

where, κ_{mat} is the thermal conductivity of the filler material. The previously calculated value of $\overline{P_{\perp}}$ will be used so that it takes $L_{channel}$ = 30 nm as a fixed quantity.

Figure 5.38 shows the behavior of the effective thermal conductivity as a function of the number of nanochannels of two AAO membranes with different lengths for air and five filler materials. It is easy to find out the effective medium theory when the number of nanochannels is $N = 0$ in Eq. 5.24. Conversely, there is a limit on the number of nanochannels given by the constraint condition in Eq. 5.23. In Figure 5.38 this limit is 556 and 1666 nanochannels for lengths of 33.4 µm and 100 µm, respectively. It is clearly seen that it is possible to control the effective thermal conductivity by managing the number of nanochannels and the length of the alumina membrane, which directly involves a control of the interchannel distance since three magnitudes are correlated by means of the Eq. 5.22.

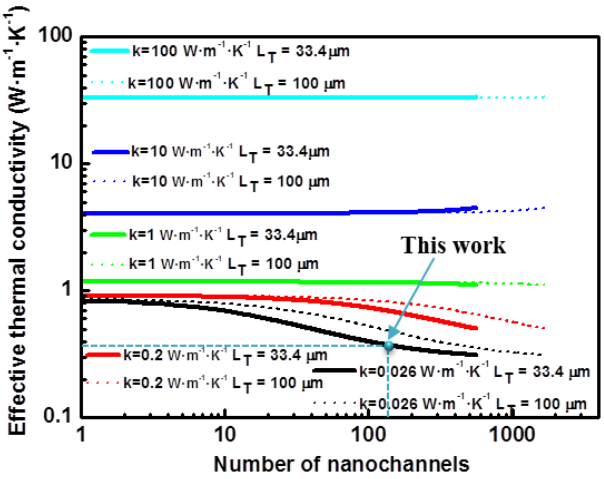

Figure 5.38. Effective thermal conductivity versus the number of the nanochannels which follows Eq. 5.24 for two different 3D-AAO membranes lengths and filler materials with different thermal conductivities, κ = 0.026 W·m^{-1}·K^{-1} (black line), κ = 0.2 W·m^{-1}·K^{-1} (red line), κ = 1 W·m^{-1}·K^{-1} (green line), κ = 10 W·m^{-1}·K^{-1} (dark blue line), κ = 100 W·m^{-1}·K^{-1} (light blue line).

However, it is also interesting to study the influence of varying both the number of transversal nanochannels and the length of the 3D structure at the same time. Figure 5.39 shows this variation for the non-filled alumina matrix (Figure 5.39 (a)) and five different filler materials with different thermal conductivities: a polymer with a thermal conductivity of 0.2 W·m^{-1}·K^{-1} (like PCDTBT[105]) (Figure 5.39 (b)) and materials whose thermal conductivities of 1 W·m^{-1}·K^{-1} (like bismuth telluride [10]) (Figure 5.39 (c)), 1.25 W·m^{-1}·K^{-1} (like 3D AAO membrane) (Figure 5.39 (d)), 10 W·m^{-1}·K^{-1} (ceramics), (Figure 5.39 (e)) and 100 W·m^{-1}·K^{-1} (metals) (Figure 5.39 (f)). Additionally, Figure 5.39 (d) shows to the

effective thermal conductivity values estimated when a filler material with the same thermal conductivity as the skeletal alumina template is introduced, 1.25 $W \cdot m^{-1} \cdot K^{-1}$. As expected, the composite thermal conductivity value is found to be the same as the skeletal AAO membrane value and it is not dependent on neither the number of nanochannels nor the thickness of the sample as it behaves as a bulk material and, thus, corroborating also the validity of Eq. 5.24.

Figure 5.39 (a), (b) and (c) show a reduction in the composite thermal conductivity if the filler material is less thermally conductive than the skeletal alumina when the number of nanochannels is increased, since increasing the number of nanochannels entails to increase the relative volume of filler material. An opposite tendency can be found when increasing the thickness of the sample for a fixed number of nanochannels; the effective thermal conductivity increases given that the interchannel distance increases in such a way that the relative quantity of alumina in comparison with the filler material is increased. If the length has a tendency to infinite, the effective thermal conductivity would reach the EMT value as it can be derived from Eq. 5.24.

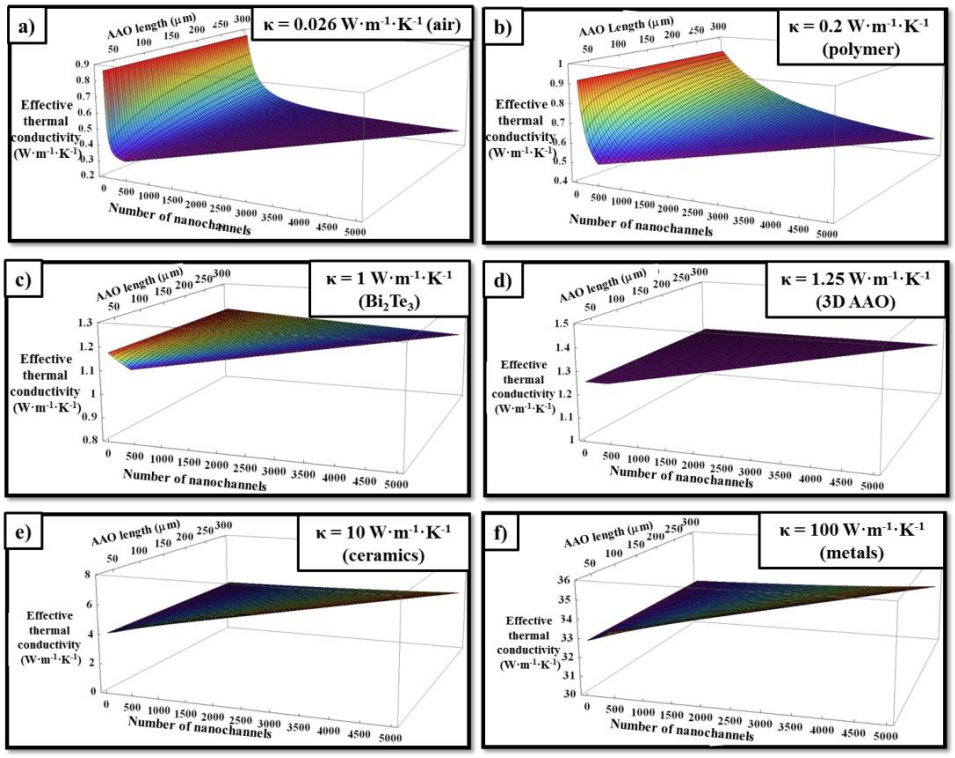

Figure 5.39. Effective thermal conductivity as a function of the number of nanochannels and the length of the 3D AAO membranes for different filler materials with thermal conductivities of (a) 0.026 $W \cdot m^{-1} \cdot K^{-1}$ (air) (b) 0.2 $W \cdot m^{-1} \cdot K^{-1}$ (polymer) (c) 1 $W \cdot m^{-1} \cdot K^{-1}$ (Bismuth telluride), (d) 1.25 $W \cdot m^{-1} \cdot K^{-1}$ (3D-AAO membrane), (e) 10 $W \cdot m^{-1} \cdot K^{-1}$ (ceramics) and (f) 100 $W \cdot m^{-1} \cdot K^{-1}$ (metals).

In the case of filler materials with higher thermal conductivity than that of the alumina, the effective thermal conductivity tends to the ordinary AAO membranes value, i.e., without transversal

nanochannels, as shown in Figure 5.39 (e) and (f) where a notable reduction of the effective thermal conductivity in comparison with the filler material itself is obtained, from 10 $W \cdot m^{-1} \cdot K^{-1}$ and 100 $W \cdot m^{-1} \cdot K^{-1}$ to 4 $W \cdot m^{-1} \cdot K^{-1}$ and 32 $W \cdot m^{-1} \cdot K^{-1}$, respectively. This value tends to be independent of the number of the nanochannels and the length because the thermal resistance of the filled transversal nanochannels is much lower than the longitudinal filled pores.

5.6.4 Experimental validation of the 3D AAO thermal model

In order to prove the validity of the thermal model developed for this structure, a reference material with a thermal conductivity of 0.2 $W \cdot m^{-1} K^{-1}$ was introduced into the 3D porous alumina membrane, as seen in Figure 5.40 (a). The reference material is provided under confidential agreement from the European project 240497.

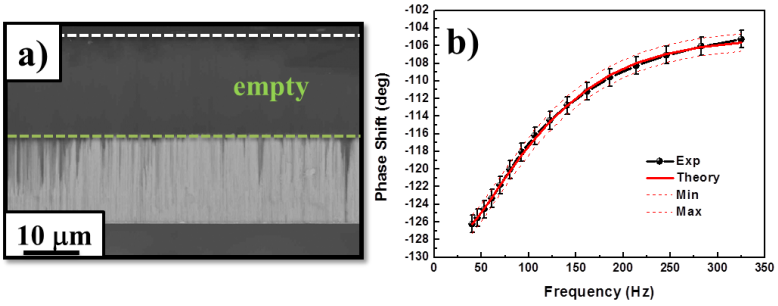

Figure 5.40. (a) Cross-section view of an 3D-AAO membrane filled with a material with a thermal conductivity of 0.2 $W \cdot m^{-1} K^{-1}$ and (b) Experimental phase shift as a function of the frequency along with the best fit.

The effective thermal conductivity was calculated by assuming two different layers: the region of the 3D alumina membrane filled with the material as well as the empty region. By taking into account their associated thicknesses and the required properties (density and specific heat) for the fitting, the effective thermal conductivity of the composite, 0.59 ± 0.06 $W \cdot m^{-1} K^{-1}$, was finally obtained (see Figure 5.40 (b)).

Once the composite value was extracted, the thermal model was used to calculate the thermal conductivity of the filler as reference material. Table 5.XVII shows the values used to calculate the thermal conductivity of the filler as reference material. These values were mainly obtained by SEM images together with a similar analysis to the one performed in Section 5.6.1.

Table 5.XVIII. Different values used to extract the thermal conductivity of the filler material.

$P_{\parallel}$ (%)	κ_{aao} ($W \cdot m^{-1} \cdot K^{-1}$)	$\overline{P_{\perp}}$ (%)	L_{aaoTop} (μm)	$L_{channel}$ (nm)	$L_{interchan}$ (nm)	N	L_T (μm)
56.4	1.25	19.8	1	20	260	120	35.6
SEM	Tabulated	Calculated	SEM	SEM	SEM	Theoretical	SEM

Finally, a thermal conductivity of the filler as reference material of 0.20 ± 0.07 $W \cdot m^{-1}K^{-1}$ is obtained, which is in accordance with the expected value 0.20 $W \cdot m^{-1}K^{-1}$, thus, indicating the good performance of the thermal model.

In conclusion, tuning the effective thermal conductivity by controlling the geometric parameters of the 3D-AAO membrane is possible by using this structure. When filling the structure with materials with low thermal conductivity, from air (0.026 $W \cdot m^{-1}K^{-1}$) to polymers (0.2 $W \cdot m^{-1}K^{-1}$), variations up to 60 % in the effective thermal conductivity can be reached just by adjusting the geometric parameters. Conversely, in the case of filler materials with thermal conductivities higher than that of alumina, a composite with a preferred thermal conductivity is possible to be designed by choosing the proper top porosity and the filler material. This structure is really valuable since the three dimensional framework allows the electrical conduction in the in-plane direction, while achieving a thermal conductivity lower than that of the filler material itself which could be from a thermoelectric point of view. Moreover, this model could be employed to identify nanosize effects given that any deviation of the values will be related to phonon boundary scattering as this model is designed without taking any size effect into account.

5.7 Bismuth telluride and antimony telluride nanowires (NWs)

As explained in Section 5.1.3, Bi_2Te_3 is the main candidate as an n-type thermoelectric material for applications near room temperature. Conversely, antimony telluride, Sb_2Te_3 is also a promising thermoelectric material with a p-type conduction. The crystal structure is also rhombohedral crystal very similar to the Bi_2Te_3 structure previously described [106].

The suitability of both compounds as thermoelectric materials along with the expected thermal conductivity reduction when reducing the dimensions, were the main motivations for studying the thermal transport of the nanowires as a function of the diameter, composition and crystal orientation.

5.7.1 Fabrication

The Bi_2Te_3 and Sb_2Te_3 NWs synthesis was carried out by template-assisted electrodeposition. The template-assisted electrodeposition method was used to grown the nanowires embedded into an AAO membrane. For that purpose, one of the surfaces of the AAO is metallized with 5 nm of Cr and 150 nm of Au in order to ensure the metallic contact needed by the electrodeposition process. Pulsed electrodeposition between a constant potential (on time) and a zero current density (off time) was used in order to obtain a uniform growth. The on and off times were optimized depending on the membrane used. The applied potential is always referred to the reference electrode, i.e., Ag/AgCl.

During the electrodeposition process, some of the samples were overgrown so that a polishing process had to be carried out in order to remove the surplus Bi_2Te_3 material deposited outside the membrane. This process, which was explained in Section 2.1.5, consists of using alumina powder of different particle size as a polishing agent for the surface of the membrane until the tip of the nanowires are at the same level than the alumina surface. Conversely, some other samples were not completely filled with Bi_2Te_3, so any polishing process was needed in these cases.

5.7.2 Structural and morphology characterization

In order to obtain the thermal conductivity of the individual nanowire, the effective medium theory is applied. To that end, the porosity of the membranes needs to be measured. SEM images of each of the samples were taken in order to analyze its porosity. Moreover, PA technique also requires an accurate estimation of the thicknesses of the samples. In the case of samples which are not completely filled to the top of the template, both the length of the nanowires and the non-filled AAO membrane thickness are measured by SEM since both data are needed for the thermal conductivity data reduction.

5.7.3 Nanowires thermal conductivity measurements

The thermal conductivity of the NWs embedded into the matrix could be measured by the PA technique. The thermal conductivity measurements of the nanowire embedded in the AAO matrix are performed by evaporating 80 nm titanium layer onto the surface where the gold was previously deposited. This procedure was established in order to measure all the samples by irradiating firstly the nanowire array for both the completely and partially filled. The gold layer was studied to not influence the measurement as it can be considered as a part of the thermal contact resistance between the titanium and the alumina membrane. The best operation frequency range is chosen by taking the thermal penetration depth of the heat waves into account and ensuring a high sensitivity of the thermal conductivity. In the case of the completely filled samples, the frequency range used is low enough to ensure the heat waves penetration through the whole membrane and reach the backing material, i.e., the aluminum where the sample is positioned so that a four layer model has to be used. Otherwise, if the heat waves do not reach this backing material, the system would behave as a bulk material and no information could be extracted from the phase shift measurement. In the case of partially filled membranes, the frequency is modulated in a frequency range that ensures the heat penetration through: AAO/Bi_2Te_3, AAO/air and even the backing material so that a five layer model should be used.

The properties of each layer should be known so that density and specific heat can be calculated by using Eqs. 5.17 and 5.18, respectively. The Bi_2Te_3 bulk density and specific heat values used for these calculations are the ones already employed in Section 5.1.3 (ρ=7740 kg·m^{-3} and C_p=194 J·kg^{-1}·K^{-1})[3, 19]. In the case of Sb_2Te_3, the density and specific values were ρ= 6500 kg·m^{-3} [3] and C_p=

206 $J \cdot kg^{-1} \cdot K^{-1}$ [107]. These values along with the AAO membrane density, specific heat and thermal conductivity values obtained in Section 5.5.2, 5.5.3 and 5.5.4, respectively, allow for the calculation of the properties of the layer AAO/Bi_2Te_3. The properties of the layer AAO/air are calculated by using also the AAO membrane values and the air properties shown in Table 5.X.

Experimental uncertainty is calculated by the propagation of errors. It is worthy to note that the NW thermal conductivity uncertainty is fairly high due to the addition of the uncertainties of the composite thermal conductivity, porosity and alumina thermal conductivity, being the last one was taken as the uncertainty obtained from the fitting in Figure 5.23 (a).

Several measurements on different days and fittings at different frequency ranges were performed for all the samples in order to reduce the uncertainty as much as possible and find an accurate thermal conductivity.

5.7.4 Thermal conductivity of Bi_2Te_3 nanowires: the n-type leg

In this study different parameters that may affect the thermal properties of the Bi_2Te_3 nanowires are studied as an initial approximation.

5.8.4.1 Bi_2Te_3 nanowires preferred oriented along [1 1 0] as a function of the diameter.

Nanowires with three different diameters, 30 nm, 45 nm and 52 nm, were prepared in order to evaluate its influence in the thermal conductivity. Its morphology was analyzed by SEM images showed in Figure 5.41. An example of the top-view of the nanowires at the same level as the alumina membrane for 30 nm and 45 nm is showed in Figure 5.41 (a) and (c), respectively. From these images, an estimation of the filling fraction is found to be higher than 95 %. Figure 5.41 (b), (d) and (f) show the cross-section of the whole membrane. Finally, Figure 5.41 (e) displays a magnification of the cross section of sample with a nanowire diameter of 52 nm.

The crystallinity of the three samples can be investigated by means of Figure 5.42, where the X-ray diffractograms of the three nanowire diameter samples are showed. The strongest diffraction peak is (1 1 0), which is located at 41.15 º. The (3 0 0) peak is also found at 75.10 º. The samples also show the (2 2 0) showing that the wires show a high preferential orientation along [1 1 0]. Therefore, the *c-axis* is perpendicular to the nanowire long direction in all the cases.

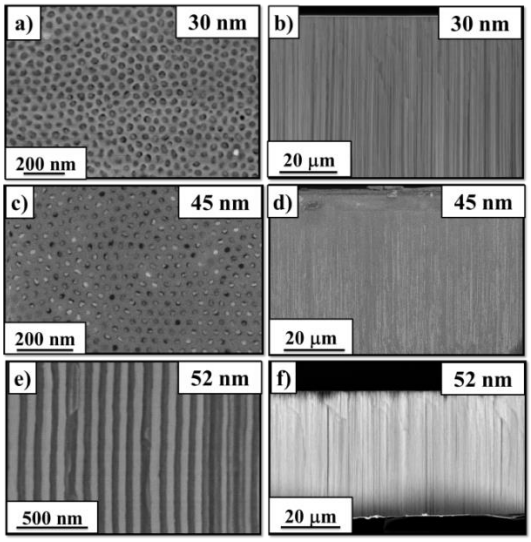

Figure 5.41. Example of (a) top-view and (b) cross-section of the sample with a nanowire diameter of 30 nm, (c) top-view and (d) cross-section of the sample with a nanowire diameter of 45 nm and (e) magnified cross-section and (f) overall cross-section of the sample of nanowire diameter of 52 nm.

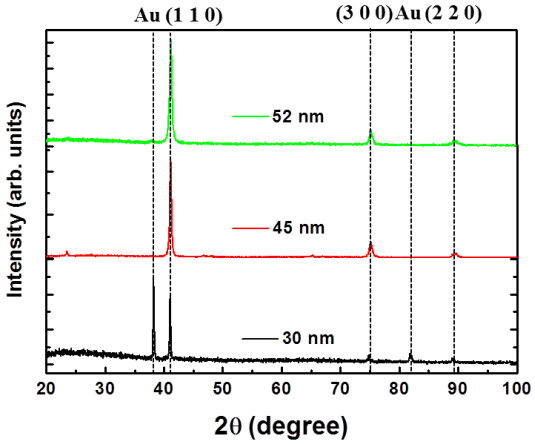

Figure 5.42. X-ray diffractograms of the bismuth telluride nanowire templates of 30 nm 45 nm and 52 nm in diameter. The c-axis of the Bi_2Te_3 structure is along the nanowire longest length.

Table 5.XIX shows growth conditions, the porosity calculated by image analysis as well as the mean pore diameter of each sample. Also, the composition of these samples is showed, which was studied by Energy Dispersive X-ray spectroscopy (EDX), and it is found to be Bi_2Te_3 in the three samples.

Table 5.XIX. Composition, growth conditions, thickness, pore diameter and porosity of the investigated samples.

Composition	**Growth conditions**	**D_p (nm)**	**P (%)**	**Composite thermal conductivity ($W \cdot m^{-1} \cdot K^{-1}$)**	**NW thermal conductivity ($W \cdot m^{-1} \cdot K^{-1}$)**
Bi_2Te_3	-0.009V 1s, 0A 0.1s 12h30'	52 ± 4	21.2±1.9	1.18 ± 0.08	***0.8 ± 0.2***
Bi_2Te_3	-0.0036 V 1 s, 0 A 0.1s, 7h	45 ± 3	17.0 ±1.5	1.20 ± 0.06	***0.7 ± 0.4***
Bi_2Te_3	-0.05V 1s, 0A 0.1s, 15h	30 ± 2	36.4± 3.6	0.91 ± 0.09	***0.6 ± 0.3***

As an example, the data fitting of the sample with 30 nm diameter can be seen in Figure 5.43. The experiments fits really well the theory expected phase shift obtained for the used data given a value of the composite thermal conductivity of 0.91 ± 0.09 $W \cdot m^{-1} \cdot K^{-1}$.

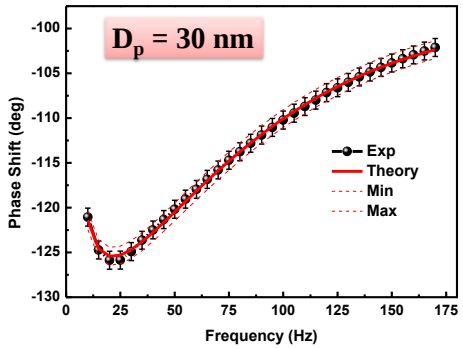

Figure 5.43. Typical fitting of the experimental data obtained by the PA technique for the 30 nm diameter template. The fitting was performed by taking the five layers whose properties values are given in Table 5.XV into consideration.

When comparing the values obtained, 0.8 ± 0.2 $W \cdot m^{-1} \cdot K^{-1}$ for 52 nm, 0.7 ± 0.4 $W \cdot m^{-1} \cdot K^{-1}$, for 45 nm and 0.6 ± 0.3 $W \cdot m^{-1} \cdot K^{-1}$ for 30 nm, a general reduction can be observed. By considering only these measurements we must be cautious since in all the cases the observed differences are within the experimental error of the measurement. However, if we take into account the tendency that the group is observing for higher diameters, where a reduction in the thermal conductivity from films with 2.2 $W \cdot m^{-1} \cdot K^{-1}$ to 300 nm nanowires of 1.87 $W \cdot m^{-1} \cdot K^{-1}$ and 75 nm nanowires of 1.00 $W \cdot m^{-1} \cdot K^{-1}$ have been observed[108]. We can conclude that reducing the nanowire diameter promote a further reduction in the thermal conductivity.

However, the thermal conductivity associated to three nanowire diameters exhibits a general reduction of a factor ~ 3.5, when compared with the thermal conductivity of the bulk single crystal calculated in the direction perpendicular to the *c-axis*, 2.2 $W \cdot m^{-1} \cdot K^{-1}$ [17].

It is worth to mention that the 30 nm nanowire diameter is among the lowest size measured until the date which is a substantial advance in the Bi_2Te_3 nanowires thermal conductivity measurements.

5.8.4.2 Thermal conductivity of Bi_2Te_3 nanowires as a function of Te content.

As explained in section 5.2.5, the electrodeposited tellurium presents lower thermal conductivity than that of the bulk. For that reason, the thermal conductivity of the bismuth telluride nanowires with a similar nanowire diameter, but with different tellurium content, were studied to understand if small variations on the stoichiometry have influenced in the thermal transport properties.

In this case, four different compositions were grown by pulsed electrodeposition (see growth conditions in Table 5.XX): $Bi_{1.4}Te_{3.6}$, $Bi_{1.8}Te_{3.2}$, $Bi_{1.9}Te_{2.9}$, and the stoichiometric Bi_2Te_3 with nanowires diameters ranging from 40 nm to 52 nm since have been already proved that thermal transport along these nanowire diameters is equivalent. Figure 5.44 displays an example of (a) a magnified view of the Bi-Te nanowires and (b) the whole membrane cross section which was used to calculate the thicknesses of the different layers for the photoacoustic model.

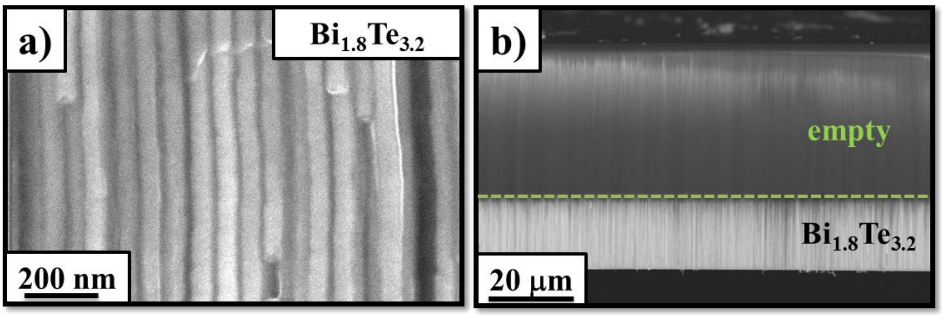

Figure 5.44. Example of (a) magnification of a cross section and (b) cross-section of the whole sample for the sample with a composition of $Bi_{1.8}Te_{3.2}$.

Figure 5.45 shows two examples of the experimental fitting for two samples, (a) $Bi_{1.9}Te_{3.1}$ and (b) $Bi_{1.4}Te_{3.6}$.

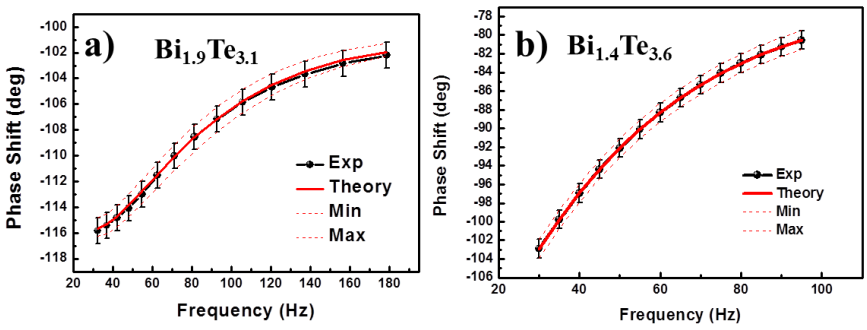

Figure 5.45. Experimental phase shift as a function of the frequency of (a) $Bi_{1.9}Te_{3.1}$ and (b) $Bi_{1.4}Te_{3.6}$.

Table 5.XX summarizes the growth conditions, pore diameter, porosity, composite thermal conductivity and the single nanowire thermal conductivity. Again, although the variations are small and so within the experimental error, it can be seen that for the different stoichiometries there is not a big variation on the thermal conductivity of the nanowires (comparing 2:3 with 1.9:3.1). However, when the samples are Te-rich, like in the $Bi_{1.4}Te_{3.6}$ case, the thermal conductivity is reduced. This can be explained by the formation of Te-clusters inside the nanowires, as observed by Rodriguez-Fernandez, *et al.* [109]. These Te-clusters are formed in Te-rich nanowires and they can actually act as additional scattering defects for the phonons. Additionally, as it was already shown in Section 5.2.4, the thermal conductivity of tellurium grown by electrodeposition shows lower thermal conductivity than Bi_2Te_3. So, the formation of tellurium clusters in Te-rich Bi_2Te_3 samples can definitively reduce the thermal conductivity of the nanowires.

Table 5.XX. Growth conditions, pore diameter, porosity, composite thermal conductivity and the single nanowire thermal conductivity for different stoichiometries.

Composition	**Growth conditions**	**D_p (nm)**	**P (%)**	**Composite thermal conductivity ($W \cdot m^{-1} \cdot K^{-1}$)**	**NW thermal conductivity ($W \cdot m^{-1} \cdot K^{-1}$)**
$Bi_{1.4}Te_{3.6}$	0.04 V a 1s, 0A a 0.1s 20h	40 ± 3	51	0.76 ± 0.08	***0.5 ± 0.2***
$Bi_{1.8}Te_{3.2}$	0 V a 1 s, 0 A 0.1s, 7h30'	45 ± 3	48	0.91 ± 0.10	***0.6 ± 0.2***
$Bi_{1.9}Te_{3.1}$	0.037 V a 1 s, 0 A 0.1s,12h30'	51 ± 4	21	1.18 ± 0.10	***0.7 ± 0.3***
Bi_2Te_3	-0.009V 1s, 0A 0.1s 12h30'	52 ± 4	21.2±1.9	1.18 ± 0.08	***0.7 ± 0.2***

5.8.4.3 Influence of the addition of a surfactant in the electrodeposition of Bi_2Te_3 nanowires

As it was already studied in the case of Te and Bi_2Te_3 films, the influence of the addition of sodium lignosulfonate during the nanowires electrodeposition has been also investigated. For that purpose, nanowires with a stoichiometry of $Bi_{1.8}Te_{3.2}$ with and without SLS were examined. The growth conditions can be seen in Table 5.XXI. Figure 5.44 shows an example of the cross section views of the $Bi_{1.8}Te_{3.2}$ without SLS.

Moreover, the structural properties were examined by XRD, which is showed in Figure 5.46. As seen, both samples are highly oriented along the [1 1 0].

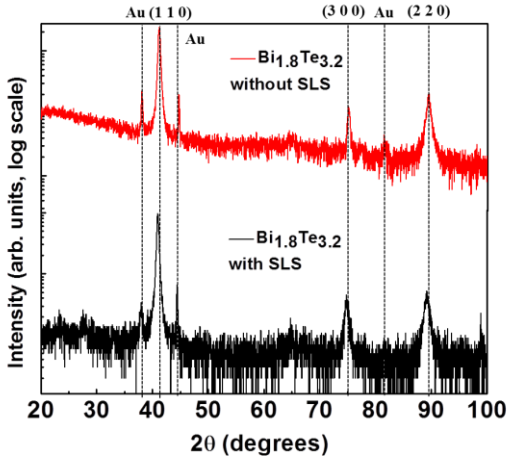

Figure 5.46. X-Ray diffractograms for samples prepared with and without SLS with different stoichiometries.

The thermal conductivity was also measured by the photoacoustic technique. The composite and nanowire thermal conductivity along with the porosity and pore diameter are summarized in Table 5.XXI.

Table 5.XXI. Stoichiometry, growth conditions, nanowire diameter, porosity, composite thermal conductivity and nanowire thermal conductivity of the samples prepared with and without SLS.

Composition	**Growth conditions**	**D_p (nm)**	**P (%)**	**Composite thermal conductivity ($W \cdot m^{-1} \cdot K^{-1}$)**	**NW thermal conductivity ($W \cdot m^{-1} \cdot K^{-1}$)**
$Bi_{1.8}Te_{3.2}$ (No SLS)	0 V at 1 s, 0 A 0.1s, 7h30'	45 ± 3	48	0.91 ± 0.10	***0.6 ± 0.2***
$Bi_{1.8}Te_{3.2}$ (SLS)	0.04 V a 1 s, 0 A 0.1s, 7h30'	40 ± 3	41	*0.91 ± 0.09*	***0.6 ± 0.3***

From these results, we can conclude that the thermal conductivity is not influenced by the addition of SLS, as in the case of Bi_2Te_3 films grown with and without SLS. Clearly, the thermal properties of the Bi_2Te_3 nanowires are then more affected by crystal orientation, composition, and diameter than by the addition of a surfactant like SLS.

5.8.4.4 Modulated Bi_2Te_3 nanowires

We have initiated the study of morphological modulated nanowires. In principle the modulation should affect the scattering of phonons.

For this study, we have been prepared by electrodeposition with the aid of the porous alumina whose walls shape is modulated during the anodization process. The diameter of the nanowires is modulated as explained in Figure 5.47 (a). The electrodeposition was carried out at -0.1 V during 1 s

and 0.1 s at zero current density during 4 hours in the presence of sodium lignosulfonate. From this process, diameter modulated nanowires are obtained, as seen in Figure 5.47 (b), where some zones of the nanowires are wider than the nanowire itself whose diameter is found to be around 45 nm.

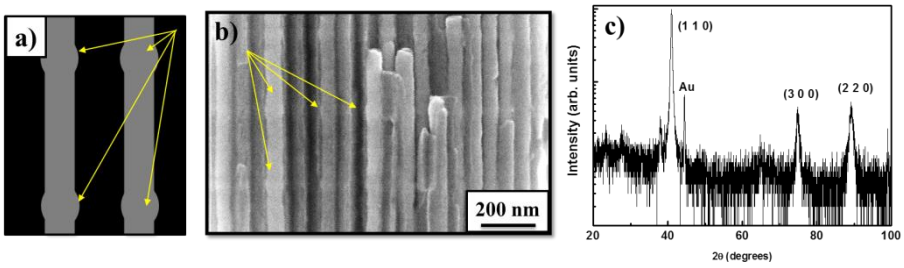

Figure 5.47. (a) Sketch and (b) SEM image of the modulated nanowires embedded into alumina matrix. The yellow arrows indicate the modulation regions and (c) XRD of the nanowires.

The stoichiometry was found to be $Bi_{1.8}Te_{3.2}$ and X-ray diffractogram showed in Figure 5.47 (c) suggests the nanowires are preferentially oriented along the [1 1 0] direction but also the [0 1 5] direction and the [1 0 0] directions are observed. So it can be concluded that the nanowires are similar in composition and orientation as the one on Section 5.7.4.3. The effective thermal conductivity was measured, obtaining a value of 0.91 ± 0.09 $W \cdot m^{-1} \cdot K^{-1}$. By using the effect medium theory together with a porosity of 42 % (calculated from SEM image analysis plus accounting for the modulation of the walls), a nanowire thermal conductivity of 0.7 ± 0.3 $W \cdot m^{-1} \cdot K^{-1}$, which matches the value previously obtained for the nanowires prepared from the solution with SLS.

From this result, the thermal conductivity of the modulated nanowires seems not to be affected by this diameter modulation and by this modulation distance. However, further studies with different diameter modulations, different distances between modulations, better composition and more pure crystal orientation must be carried out in a close future to really determine the effect of the modulation on the thermal properties of the nanowires.

In summary, for Bi_2Te_3 nanowires the effect of: diameter, crystal orientation, stoichiometry, the addition of SLS during the nanowires growth, and an initial study of the modulation have been studied. As explained above, Bi_2Te_3 is an n-type material. However, since a thermoelectric device is comprised of n- and p-types legs, synthesis and characterization of p-type nanowires becomes essential to go further in this field.

5.7.5 Thermal conductivity of Sb_2Te_3 nanowires: the p-type leg

The Sb_2Te_3 nanowires were prepared from a solution made of Te 0.01 M, Sb_2O_3 0.0056 M, tartaric acid 0.84 M, HNO_3 1 M and 0.09 $g \cdot L^{-1}$ of sodium lignosulfonate by pulsed electrodeposition at 0.05 V during 1 s and zero current 0.1 s.

Figure 5.48 (a) show the cross section view of the AAO membrane as grown. As the sample has overgrown, a polishing process was carried out until the green dash line is reached, so that the empty region is completely removed. A higher magnification is displayed in Figure 5.48 (b) where a cross section of the nanowires embedded into the alumina matrix is showed. The nanowires diameter is found to measure approximately 40 nm as the porous of the AAO membranes used as template or even have a lower diameter. This can be explained in terms of walls wetting since the Sb_2Te_3 is not able to wet the surfaces of the alumina membrane and in most cases a nanometric air gap is observed between the template and the nanowire. In addition, the EDS analysis showed a composition of $Sb_{2.2}Te_{2.8}$.

The X-ray diffractogram is shown in Figure 5.49. A polycrystalline character can be assumed since many different reflections, like (0 1 5), (1 1 0), (2 0 5), (1 2 5) and (3 0 0) appear in the diffractogram.

Finally, the thermal conductivity of the nanowire was measured, finding a value of 1.42 ± 0.73 $W \cdot m^{-1} \cdot K^{-1}$ for $Sb_{2.2}Te_{2.8}$.

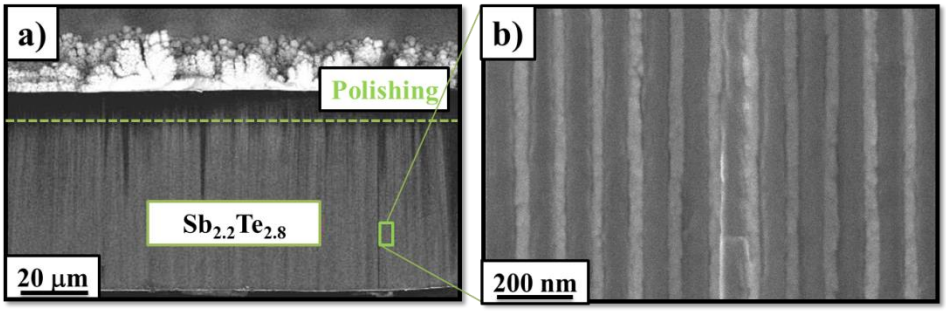

Figure 5.48. (a) SEM picture of the whole template where the Sb-Te overgrowth is observed and (b) higher magnification of the cross-section view of the $Sb_{2.2}Te_{2.8}$ nanowires embedded in the AAO membrane. In the picture a small air gap is observed between the wire and the template.

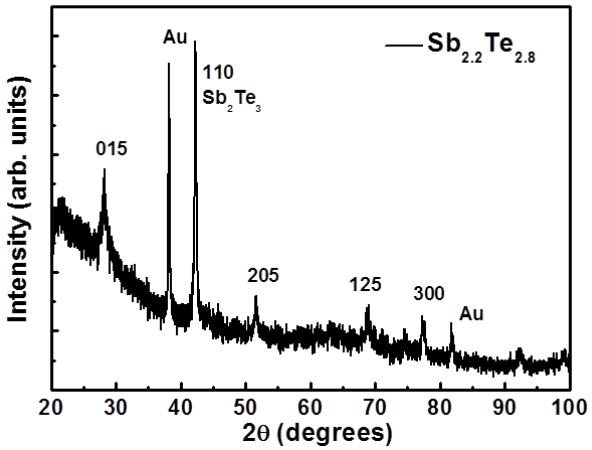

Figure 5.49. X-Ray diffractogram of the $Sb_{2.2}Te_{2.8}$ nanowires embedded into alumina matrix

Table 5.XXII. Sample composition, porosity, nanowire diameter, composite thermal conductivity along with the nanowire thermal conductivity calculated by means of the effective medium theory for both samples.

Sample	Porosity	Nanowire diameter (nm)	Composite thermal conductivity ($W \cdot m^{-1} \cdot K^{-1}$)	NW thermal conductivity ($W \cdot m^{-1} \cdot K^{-1}$)
$Sb_{2.2}Te_{2.8}$	13	40	1.33 ± 0.09	1.42 ± 0.73

The thermal conductivity is ~ 4.4 times lower than the value reported by Jacquot *et al.*[17] for the bulk single crystal perpendicular to the *c-axis*, 6.25 $W \cdot m^{-1}K^{-1}$. This reduction factor similar to the one observed in the thermal conductivity of Bi_2Te_3 nanowires, ~ 3.4, (See Section 5.7.4.1). Saci *et al.*[107] measured the thermal conductivity of Sb_2Te_3 nanowires along the *c-axis*, showing a reduction of 2.3 when compared with the reported values by Jacquot *et al.*[17] in that direction. Therefore, we can conclude that the thermal transport of Sb_2Te_3 nanowires is greatly affected by going into the 40 nm range in a similar manner as in the case of Bi_2Te_3.

5.7.6 P-n junction nanowires: a Bi_2Te_3/Sb_2Te_3 bilayer

In order to understand if the thermal properties of the Bi_2Te_3 and the Sb_2Te_3 are affected by the formation of a p-n junction, we have also initiated the study of Bi_2Te_3/Sb_2Te_3 bilayers of nanowires arrays. They were fabricated also via electrodeposition by alternating the two solutions and conditions previously used. Firstly, the empty AAO membrane was plunged in the same solution as the used to prepared Bi_2Te_3 nanowires plus 0.09 $g \cdot L^{-1}$ of sodium lignosulfonate. The growth was carried out at -0.1 V during 0.1 s and 1 s at zero current density during 1 hour. Then, the solution used was substituted by a solution of Te 0.01 M, Sb_2O_3 0.0056 M, tartaric acid 0.84 M, HNO_3 1 M and 0.09 $g \cdot L^{-1}$ of sodium lignosulfonate. In this case a potential of 1 s at -0.18 V and 0.25 s at zero current density was employed to grow the antimony telluride nanowires.

Figure 5.50 (a) shows the SEM image of the cross section of the nanowires embedded into the AAO membrane showing the two different layers. The chemical analysis performed by EDX points out that a composition of 36 % Bi and 64 % Te ($Bi_{1.8}Te_{3.2}$) and 38.8% Sb and 61.2% Te ($Sb_{1.9}Te_{3.1}$) were found. Figure 5.50 (b) shows a TEM image of the clear interface between both materials for a nanowire with a diameter of 200 nm, as an example. According with the linear analysis done along the wire no interfusion is observed between the two layers.

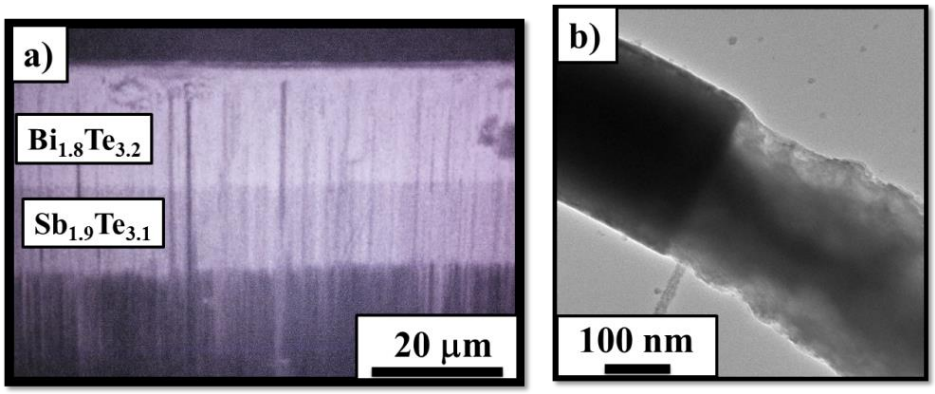

Figure 5.50. Bilayer SEM images of (a) cross-section of a 40 nm $Bi_{1.8}Te_{3.22}/Sb_{1.9}Te_{3.1}$ bilayer and (b) Transmission electron microcopy (TEM) image of the nanowire with a diameter of 200 nm showing the $Bi_{1.8}Te_{3.22}/Sb_{1.9}Te_{3.1}$ interface.

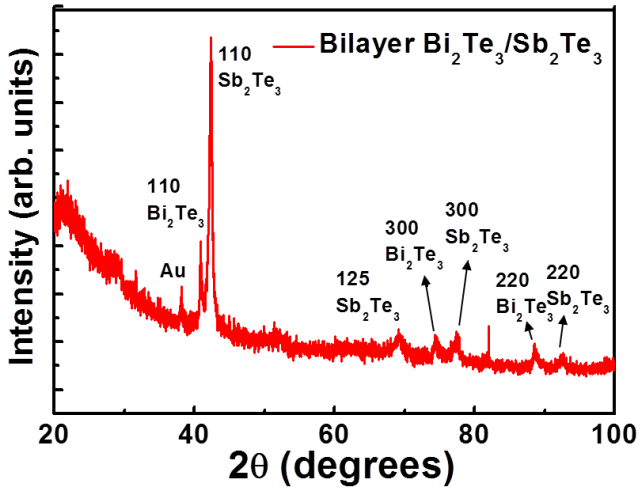

Figure 5.51. X-ray diffractogram of the nanowires bilayer embedded into alumina matrix.

Regarding the crystal orientation, Figure 5.51 shows a preferential orientation of the wires along the [1 1 0] direction since the diffraction peak found at 2θ = 40.82 ° and 2θ = 42.34 ° for $Bi_{1.8}Te_{3.2}$ and $Sb_{1.9}Te_{3.1}$, respectively, are the strongest for both materials. Less intense diffraction peak is also found at 2θ = 74.39 ° and 2θ = 77.54 ° for $Bi_{1.8}Te_{3.2}$ and $Sb_{1.9}Te_{3.1}$, respectively, indicating the presence of [1 0 0] direction additionally for these wires. Therefore, the nanowires are preferred oriented along the basal plane of the hexagonal structure, i.e., perpendicular to the *c-axis*.

The thermal conductivity was extracted in this case by assuming three different layers apart from the titanium layer, $Bi_{1.8}Te_{3.2}$, $Sb_{1.9}Te_{3.1}$ and an empty AAO region whose properties are shown in Table 5.XXIII.

Table 5.XXIII. Thickness, density, specific heat and thermal conductivity of each of the layers used in the PA model for the bilayer sample. The italic letters indicate that those are the thermal conductivity values extracted from the fitting.

Layer	Thickness (μm)	Density ($kg \cdot m^{-3}$)	Specific heat ($J \cdot kg^{-1} \cdot K^{-1}$)	Thermal conductivity ($W \cdot m^{-1} \cdot K^{-1}$)
AAO/Air	3.1	1632 ±71	885 ±69	0.70 ± 0.09
AAO/ $Sb_{1.9}Te_{3.1}$	19	4303 ±84	460 ±60	*1.35 ± 0.14*
AAO/ $Bi_{1.8}Te_{3.2}$	10	4796 ±87	433 ±60	*0.91 ± 0.09*
Ti	0.08	4500	522	21.9
Air	0	1.176	1007	0.026

Figure 5.52 shows the experimental phase shift as a function of the frequency along with the best fitting.

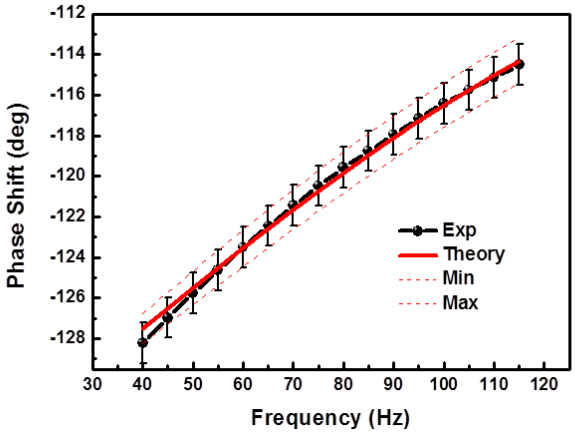

Figure 5.52. Phase shift as a function of the frequency together with the best fitting for the bilayer sample.

Applying the effective medium theory and taking account both a porosity of 41 % and the thermal conductivity of the alumina, a thermal conductivity values of 0.64 ± 0.28 $W \cdot m^{-1}K^{-1}$ for $Bi_{1.8}Te_{3.2}$ and 1.71 ± 0.38 $W \cdot m^{-1}K^{-1}$ for $Sb_{1.9}Te_{3.1}$ were obtained. The thermal conductivity of the $Bi_{1.8}Te_{3.2}$ nanowires is similar to the $Bi_{1.8}Te_{3.2}$ nanowires value previously measured, which allows us to validate the accuracy of the measurement.

The $Sb_{1.9}Te_{3.1}$ nanowire was found to be 1.71 ± 0.38 $W \cdot m^{-1} \cdot K^{-1}$, which is a factor ~3.7 lower than the bulk value in the same direction (perpendicular to the *c-axis*), as occur in the case of Bi_2Te_3 nanowires. The effect of the stoichiometry on the thermal conductivity of Sb_2Te_3 nanowires can be studied by the value previously shown in Section 5.7.5. The properties of both nanowires are summarized in Table XXIV.

Table 5.XXIV. Comparison between the composite and nanowire thermal conductivity of two different antimony telluride stoichiometries.

Sample	Porosity	Nanowire diameter (nm)	Composite thermal conductivity ($W \cdot m^{-1} \cdot K^{-1}$)	NW thermal conductivity ($W \cdot m^{-1} \cdot K^{-1}$)
$Sb_{1.9}Te_{3.1}$	41	44	1.35 ± 0.14	1.71 ± 0.38
$Sb_{2.2}Te_{2.8}$	13	40	1.33 ± 0.09	1.42 ± 0.73

Despite the large uncertainties for the $Sb_{2.2}Te_{2.8}$ due mainly to the low porosity of the template, a difference between both thermal conductivity values can be appreciated. The main explanation of this difference can be found in the difference in stoichiometry of both samples. In any case, more samples should be measured to extract further conclusions for this material.

In summary, the thermal conductivity of Sb_2Te_3 nanowires is highly affected by composition; even more than it seems to be affected the Bi_2Te_3 nanowires. The nanostructuration of Sb_2Te_3 plays an important role in the reduction of the thermal conductivity.

Finally, it must be point out that the viability of measuring the thermal conductivity of two different materials forming a bilayer embedded into an alumina by the photoacoustic technique has been clearly stayed.

5.8 Summary

In this chapter the ability of measuring of thick and thin films, porous structures and nanowires is proved. Many different types of samples have been studied.

- Reference samples have been satisfactorily measured by the multilayered model. From references with well-known thermal parameters, like SiO_2, to different samples which k values were cross-checked by measuring the samples by other techniques such as TDTR or SThM. Finally, additional films like: 298 nm SiO_2 film, 1.2 µm thick PCDTBT film and a 3.46 µm Bi_2Te_3 layer were used to check the reliability of the technique and the model showing values with a mean deviation from the expected values of around 10 %.

- The influence of the addition of sodium lignosulfonate (SLS), on the thermoelectric properties of tellurium films grown by electrodeposition was investigated. The growth mechanism is found to play an important role in the thermoelectric properties given that the grain size of the films is dramatically reduced when the SLS is added to the solution. Therefore, the electrical resistivity of the tellurium films when SLS is not added is 229 µΩ·m, which is lower than the value with SLS, 798 µΩ·m. The Seebeck coefficient values are not affected, with values of approximately 285 µV/K for both solutions. Power factors of 280 $\mu W \cdot m^{-1} \cdot K^{-2}$ (without SLS)

and 82 $\mu W \cdot m^{-1} \cdot K^{-2}$ (with SLS) at room temperature were found. Moreover, the thermal conductivity values were of the order of 1 $W \cdot m^{-1} \cdot K^{-1}$for both solutions, which is a factor of 3 less than the tellurium bulk value. Both the power factor and the thermal conductivity values of electrodeposited tellurium films are of the same order of magnitude of bismuth telluride films grown by electrodeposition. The figure of merit is calculated to be approximately one order of magnitude higher than the bulk value, 0.09 without SLS and 0.03 with SLS, both at room temperature.

- The effect on the thermal properties of SiGe thin films produced by two routes of metal induced crystallization were studied. Values of thermal conductivity as low as 1.13 ± 0.13 $W \cdot m^{-1} \cdot K^{-1}$ and 1.23 ± 0.12 $W \cdot m^{-1} \cdot K^{-1}$ for the *in-situ* and *ex-situ* thermal treatments, respectively, were measured. This values are lower than those of SiGe bulk (4-5 $W \cdot m^{-1} \cdot K^{-1}$) and can be ascribed to the cluster presence formed inside the film during the crystallization process.

- The influence of the fabrication conditions on the thermal conductivity of AAO templates has been thorough studied. To this end, the porosity, specific heat and density of each membrane were characterized. The composite density and thermal conductivity as a function of the porosity follow the rule of mixtures and the effective medium theory, respectively, so that the skeletal density and skeletal thermal conductivity could be obtained depending on the preparation conditions. Two equations were obtained for the density and the thermal conductivity in such a way that both magnitudes could be calculated by determining the percentage of porosity of any AAO membrane. Thermal conductivity values of 1.07 $W \cdot m^{-1} \cdot K^{-1}$ and 1.32 $W \cdot m^{-1} \cdot K^{-1}$ have been found for the AAO membranes fabricated in sulfuric and oxalic and phosphoric acid electrolyte, respectively. These values are common for amorphous alumina. There is no variation of the thermal conductivity as a function of the pore diameter since the heat conduction takes place in the direction parallel to the pores and the phonon mean free path is on the order of the interatomic distance in amorphous alumina so that no phonon scattering would influence the heat transfer. However, a reduction in the value is observed when using sulfuric acid, due to the incorporation of SO_4^{-2} to the alumina structure.

- The effective thermal conductivity of a non-filled 3D anodic aluminum oxide membrane was extracted. The values of the density, specific heat and porosity of the sample were characterized in order to perform the thermal conductivity fitting. A value of the composite thermal conductivity of 0.38 $W \cdot m^{-1} \cdot K^{-1}$ was obtained In order to determine the skeletal thermal conductivity, a 3D thermal model based on a combination of a parallel and series thermal resistances was developed which provided a value of 1.25 ± 0.25 $W \cdot m^{-1} \cdot K^{-1}$. This model was also utilized to study the influence of the number of transversal nanochannels as

well as the thickness of the 3D-AAO structure for both empty and filled with different materials, showing the capability of tuning the effective thermal conductivity by manipulating the geometric parameters. Finally, a thermal conductivity measurement of 3D-AAO filled with a reference sample was carried out. The result was found to be in good agreement with the theoretical prediction, thus, corroborating the validity of the thermal model.

- The versatility of PA technique to measure individual NWs was also proved by measuring the nanowires embedded into the alumina matrix and the subsequent application of the effective medium theory. With a future thermoelectric device in mind, both n- (Bi_2Te_3) and p-type (Sb_2Te_3) nanowires were study. Regarding the Bi_2Te_3 nanowires, highly oriented samples along the [1 1 0] direction with diameters ranging from 30 nm to 52 nm were examined. The obtained values showed a great reduction of the thermal conductivity of Bi_2Te_3 of a factor in the vicinity of 3.4 in comparison with the bulk value along the same crystal orientation. Although very similar values were found in all the cases were found, 0.6 $W \cdot m^{-1} \cdot K^{-1}$, a thermal conductivity reduction could be elucidate when considering the reduction occurred in nanowires with higher diameters studied in our group. Moreover, a study about the influence of the stoichiometry was also carried out for nanowires with diameters around 40 nm. A slight reduction when the Te content increases can be appreciated which can be ascribed to the Te clusters in the nanowire and the reduction that a high tellurium can cause. The effect of the sodium lignosulfonate presence in the solution used for the depositions was also investigated, showing no dependence as previously found for Bi_2Te_3 films.
- Conversely, the thermal conductivity of Sb_2Te_3 nanowires was also measured. Again, a reduction in a factor of around 3.5 in comparison with the bulk value along the same crystal orientation was found.
- Finally, a nanowire bilayer composed of both materials was also measured, proving the capability of the technique to determine two thermal conductivity values in a sample.

5.9 References

1. Wang, X.; Hu, H.; Xu, X., Photo-Acoustic Measurement of Thermal Conductivity of Thin Films and Bulk Materials. *Journal of Heat Transfer* **2000,** *123*, 138-144.
2. http://www.cidraprecisionservices.com/products-services-glass-fused-silica-glass.html Fused Silica Glass Machining & Grinding.
3. Lide, D. R., CRC Handbook of Chemistry and Physics. In Press, C., Ed. Boca Raton, 2005.
4. Ghosh, S.; Ghosh, A.; Mukherjee, J.; Banerjee, R., Improved thermal properties of borosilicate glass composite containing single walled carbon nanotube bundles. *RSC Advances* **2015,** *5*, 51116-51121.
5. Maiz, J.; Rojo, M. M.; Abad, B.; Wilson, A.; Nogales, A.; Borca-Tasciuc, D.-A.; Borca-Tasciuc, T.; Martin-Gonzalez, M. S., Enhancement of thermoelectric efficiency of doped PCDTBT polymer films. *RSC Advances* **2015**.
6. Choy, C. L., Thermal conductivity of polymers. *Polymer* **1977,** *18*, 984-1004.
7. Hu, M.; Yu, D.; Wei, J., Thermal conductivity determination of small polymer samples by differential scanning calorimetry. *Polymer Testing* **2007,** *26*, 333-337.
8. Snyder, G. J.; Toberer, E. S., Complex thermoelectric materials. *Nat Mater* **2008,** *7*, 105-114.
9. Greenaway, D. L.; Harbeke, G., Band structure of bismuth telluride, bismuth selenide and their respective alloys. *Journal of Physics and Chemistry of Solids* **1965,** *26*, 1585-1604.
10. Manzano, C. V.; Abad, B.; Muñoz-Rojo, M.; Koh, Y. R.; Hodson, S. L.; Martinez, A. M. L.; Xu, X.; Shakouri, A.; Sands, T. D.; Borca-Tasciuc, T.; Martín-González, M., Anisotropy effect on the thermoelectric properties of highly oriented electrodeposited Bi2Te3 films. *Scientific Reports* **2015,** *accepted*.
11. Tritt, T. M.; Subramanian, M. A., Thermoelectric Materials, Phenomena, and Applications: A Bird's Eye View. *MRS Bulletin* **2006,** *31*, 188-198.
12. Delves, R. T.; Bowley, A. E.; Hazelden, D. W.; Goldsmid, H. J., Anisotropy of the Electrical Conductivity in Bismuth Telluride. *Proceedings of the Physical Society* **1961,** *78*, 838.
13. Goldsmid, H. J., Recent Studies of Bismuth Telluride and Its Alloys. *Journal of Applied Physics* **1961,** *32*, 2198-2202.
14. Rowe, R. M., Materials, preparation, and characterization in thermoelectrics. *CRC Press* **2012**.
15. Ziman, J. M., *Electrons and Phonons-The Theory of Transport Phenomena in Solids*. Oxford university press, : 1960.
16. Fleurial, J. P.; Gailliard, L.; Triboulet, R.; Scherrer, H.; Scherrer, S., Thermal properties of high quality single crystals of bismuth telluride—Part I: Experimental characterization. *Journal of Physics and Chemistry of Solids* **1988,** *49*, 1237-1247.
17. Jacquot, A.; Farag, N.; Jaegle, M.; Bobeth, M.; Schmidt, J.; Ebling, D.; Böttner, H., Thermoelectric Properties as a Function of Electronic Band Structure and Microstructure of Textured Materials. *Journal of Electronic Materials* **2010,** *39*, 1861-1868.
18. Manzano, C. V.; Rojas, A. A.; Decepida, M.; Abad, B.; Feliz, Y.; Caballero-Calero, O.; Borca-Tasciuc, D. A.; Martin-Gonzalez, M., Thermoelectric properties of Bi2Te3 films by constant and pulsed electrodeposition. *Journal of Solid State Electrochemistry* **2013,** *17*, 2071-2078.
19. Bolling, G. F., Some thermal data for Bi_2Te_3 [14]. *The Journal of Chemical Physics* **1960,** *33*, 305-306.
20. Epstein, A. S.; Fritzsche, H.; Lark-Horovitz, K., Electrical Properties of Tellurium at the Melting Point and in the Liquid State. *Physical Review* **1957,** *107*, 412-419.
21. Tsiulyanu, D.; Mocreac, O., Concentration induced damping of gas sensitivity in ultrathin tellurium films. *Sensors and Actuators B: Chemical* **2013,** *177*, 1128-1133.
22. Royer, D.; Dieulesaint, E., Elastic and piezoelectric constants of trigonal selenium and tellurium crystals. *Journal of Applied Physics* **1979,** *50*, 4042-4045.
23. Li, H. H.; Zhang, P.; Liang, C. L.; Yang, J.; Zhou, M.; Lu, X. H.; Hope, G. A., Facile electrochemical synthesis of tellurium nanorods and their photoconductive properties. *Crystal Research and Technology* **2012,** *47*, 1069-1074.
24. Pan, T.; Zhuang, F.; Li, Z.-Y., Absolute photonic band gaps in a two-dimensional photonic crystal with hollow anisotropic rods. *Solid State Communications* **2004,** *129*, 501-506.

25. Görtz, W.; Gerstenhauer, E.; Grosse, P., Photoconducting tellurium for submillimeterwave detectors. *Appl Phys A* **1982,** *27*, 35-38.
26. Bodiul, P.; Bondarchuk, N.; Huber, T.; Konopko, L.; Nikolaeva, A.; Botnari, O. In *Thermoelectric Properties of Films and Monocrystalline Whiskers of Tellurium*, Thermoelectrics, 2006. ICT '06. 25th International Conference on, 6-10 Aug. 2006, 2006; 2006; pp 607-610.
27. Fischer, G.; White, G. K.; Woods, S. B., Thermal and Electrical Resistivity of Tellurium at Low Temperatures. *Physical Review* **1957,** *106*, 480-483.
28. Bottom, V. E., The Hall Effect and Electrical Resistivity of Tellurium. *Science* **1952,** *115*, 570-571.
29. Perron, J. C., Thermal conductivity of Selenium-Tellurium liquid alloys. *Physics Letters A* **1970,** *32*, 169-170.
30. C.Y. Ho, R. W. P., P.E. Liley, Thermal Conductivity of the Elements: A Comprehensive Review. *Journal of Physical and Chemical reference data* **1974,** *3*.
31. Abad, B.; Rull-Bravo, M.; Hodson, S. L.; Xu, X.; Martin-Gonzalez, M., Thermoelectric properties of electrodeposited tellurium films and the sodium lignosulfonate effect. *Electrochimica Acta* **2015,** *169*, 37-45.
32. Capers, M. J.; White, M., Structure, growth and orientation of vacuum deposited tellurium films. *Thin Solid Films* **1971,** *8*, 317-331.
33. Dinno, M. A.; Schwartz, M.; Giammara, B., Structural dependence of electrical conductivity of thin tellurium films. *Journal of Applied Physics* **1974,** *45*, 3328-3331.
34. Okuyama, K., Mobility studies of evaporated tellurium films. *Thin Solid Films* **1976,** *33*, 165-171.
35. Capers, M. J.; White, M., The electrical properties of vacuum deposited tellurium films. *Thin Solid Films* **1973,** *15*, 5-14.
36. Phahle, A. M., Electrical properties of thermally evaporated tellurium films. *Thin Solid Films* **1977,** *41*, 235-241.
37. Goswami, A.; Ojha, S. M., Semiconducting properties of tellurium films. *Thin Solid Films* **1973,** *16*, 187-197.
38. Damodara Das, V.; Jayaprakash, N.; Soundararajan, N., Thermoelectric power of tellurium thin films and its thickness and temperature dependence. *J Mater Sci* **1981,** *16*, 3331-3334.
39. Jiang, C. H.; Wei, W.; Yang, Z. M.; Tian, C.; Zhang, J. S., Electrodeposition of tellurium film on polyaniline-coated macroporous phenolic foam and its thermopower. *J Porous Mater* **2012,** *19*, 819-823.
40. Wu, J. J.; Wu, H. C.; Zhao, C. Z., CdTe Solar Cells on Flexible Metallic Substrates. *Advanced Materials Research* **2012,** *535*, 2075-2078.
41. Fauzi, F.; Diso, D. G.; Echendu, O. K.; Patel, V.; Purandare, Y.; Burton, R.; Dharmadasa, I. M., Development of ZnTe layers using an electrochemical technique for applications in thin-film solar cells. *Semiconductor Science and Technology* **2013,** *28*, 045005.
42. Ivanova, Y. A.; Ivanou, D. K.; Streltsov, E. A., Electrochemical deposition of PbTe onto n-Si(100) wafers. *Electrochemistry Communications* **2007,** *9*, 599-604.
43. Heremans, J. P.; Thrush, C. M.; Morelli, D. T., Thermopower enhancement in PbTe with Pb precipitates. *Journal of Applied Physics* **2005,** *98*, 063703-6.
44. Martín-González, M. S.; Prieto, A. L.; Gronsky, R.; Sands, T.; Stacy, A. M., Insights into the Electrodeposition of Bi2Te3. *Journal of The Electrochemical Society* **2002,** *149*, C546-C554.
45. Manzano, C.; Rojas, A.; Decepida, M.; Abad, B.; Feliz, Y.; Caballero-Calero, O.; Borca-Tasciuc, D.-A.; Martin-Gonzalez, M., Thermoelectric properties of Bi2Te3 films by constant and pulsed electrodeposition. *Journal of Solid State Electrochemistry* **2013,** *17*, 2071-2078.
46. Martín-González, M.; Caballero-Calero, O.; Díaz-Chao, P., Nanoengineering thermoelectrics for 21st century: Energy harvesting and other trends in the field. *Renewable and Sustainable Energy Reviews* **2013,** *24*, 288-305.
47. Mishra, K. K.; Rajeshwar, K., A re-examination of the mechanisms of electrodeposition of CdX and ZnX (X = Se, Te) semiconductors by the cyclic photovoltammetric technique. *Journal of Electroanalytical Chemistry* **1989,** *273*, 169-182.
48. Xiao, F.; Yoo, B.; Ryan, M. A.; Lee, K. H.; Myung, N. V., Electrodeposition of PbTe thin films from acidic nitrate baths. *Electrochimica Acta* **2006,** *52*, 1101-1107.

49. Caballero-Calero, O.; Díaz-Chao, P.; Abad, B.; Manzano, C. V.; Ynsa, M. D.; Romero, J. J.; Rojo, M. M.; Martín-González, M. S., Improvement of Bismuth Telluride electrodeposited films by the addition of Sodium Lignosulfonate. *Electrochimica Acta* **2014,** *123*, 117-126.
50. She, G.; Shi, W.; Zhang, X.; Wong, T.; Cai, Y.; Wang, N., Template-Free Electrodeposition of One-Dimensional Nanostructures of Tellurium. *Crystal Growth & Design* **2008,** *9*, 663-666.
51. Szymczak, J.; Legeai, S.; Diliberto, S.; Migot, S.; Stein, N.; Boulanger, C.; Chatel, G.; Draye, M., Template-free electrodeposition of tellurium nanostructures in a room-temperature ionic liquid. *Electrochemistry Communications* **2012,** *24*, 57-60.
52. Pichanusakorn, P.; Bandaru, P., Nanostructured thermoelectrics. *Materials Science and Engineering: R: Reports* **2010,** *67*, 19-63.
53. Takashiri, M.; Miyazaki, K.; Tanaka, S.; Kurosaki, J.; Nagai, D.; Tsukamoto, H., Effect of grain size on thermoelectric properties of n-type nanocrystalline bismuth-telluride based thin films. *Journal of Applied Physics* **2008,** *104*, -.
54. Schumacher, C.; Reinsberg, K. G.; Rostek, R.; Akinsinde, L.; Baessler, S.; Zastrow, S.; Rampelberg, G.; Woias, P.; Detavernier, C.; Broekaert, J. A. C.; Bachmann, J.; Nielsch, K., Optimizations of Pulsed Plated p and n-type Bi2Te3-Based Ternary Compounds by Annealing in Different Ambient Atmospheres. *Advanced Energy Materials* **2013,** *3*, 95-104.
55. Rowe, D. M., CRC Thermoelectrics Handbook: Macro to Nano. In *CRC Press*, Rowe, D. M., Ed. 2005.
56. Shiraki, Y.; Usami, N., *Silicon-Germanium (SiGe) Nanostructures*. 2011; p 1-627.
57. Shin, W.; Ishikawa, M.; Nishibori, M.; Izu, N.; Itoh, T.; Matsubara, I., High-temperature thermoelectric measurement of B-Doped SiGe and Si thin films. *Materials Transactions* **2009,** *50*, 1596-1602.
58. Borca-Tasciuc, T.; Liu, W.; Liu, J.; Zeng, T.; Song, D. W.; Moore, C. D.; Chen, G.; Wang, K. L.; Goorsky, M. S.; Radetic, T.; Gronsky, R.; Koga, T.; Dresselhaus, M. S., Thermal conductivity of symmetrically strained Si/Ge superlattices. *Superlattices and Microstructures* **2000,** *28*, 199-206.
59. Handbook, T., Macro to Nano, ed. DM Rowe. In CRC Press, Taylor& Francis: 2006.
60. Prakash, C., Thermal conductivity variation of silicon with temperature. *Microelectronics Reliability* **1978,** *18*, 333.
61. Schaffler, F., Properties of Advanced Semiconductor Materials GaN, AlN, InN, BN, SiC, SiGe. *Eds. Levinshtein ME, Rumyantsev SL, Shur MS, John Wiley & Sons, Inc., New York* **2001**, 149-188.
62. Basu, R.; Bhattacharya, S.; Bhatt, R.; Roy, M.; Ahmad, S.; Singh, A.; Navaneethan, M.; Hayakawa, Y.; Aswal, D.; Gupta, S., Improved thermoelectric performance of hot pressed nanostructured n-type SiGe bulk alloys. *Journal of Materials Chemistry A* **2014,** *2*, 6922-6930.
63. Takashiri, M.; Borca-Tasciuc, T.; Jacquot, A.; Miyazaki, K.; Chen, G., Structure and thermoelectric properties of boron doped nanocrystalline Si0.8Ge0.2 thin film. *J. Appl. Phys.* **2006,** *100*, -.
64. Rowe, D. M., *Thermoelectrics handbook: macro to nano*. CRC press: 2005.
65. Martín-González, M.; Prieto, A. L.; Gronsky, R.; Sands, T.; Stacy, A. M., High-Density 40 nm Diameter Sb-Rich Bi2–xSbxTe3 Nanowire Arrays. *Advanced Materials* **2003,** *15*, 1003-1006.
66. Martín-González, M.; Snyder, G. J.; Prieto, A. L.; Gronsky, R.; Sands, T.; Stacy, A. M., Direct Electrodeposition of Highly Dense 50 nm Bi2Te3-ySey Nanowire Arrays. *Nano Letters* **2003,** *3*, 973-977.
67. Masuda, H.; Fukuda, K., Ordered Metal Nanohole Arrays Made by a Two-Step Replication of Honeycomb Structures of Anodic Alumina. *Science* **1995,** *268*, 1466-1468.
68. Manzano, C. V.; Martín, J.; Martín-González, M. S., Ultra-narrow 12 nm pore diameter self-ordered anodic alumina templates. *Microporous and Mesoporous Materials* **2014,** *184*, 177-183.
69. Martín, J.; Manzano, C. V.; Caballero-Calero, O.; Martín-González, M., High-Aspect-Ratio and Highly Ordered 15-nm Porous Alumina Templates. *ACS Applied Materials & Interfaces* **2012,** *5*, 72-79.
70. Sun, C.; Luo, J.; Wu, L.; Zhang, J., Self-ordered anodic alumina with continuously tunable pore intervals from 410 to 530 nm. *ACS Applied Materials and Interfaces* **2010,** *2*, 1299-1302.

71. Pashchanka, M.; Schneider, J. J., Uniform contraction of high-aspect-ratio nanochannels in hexagonally patterned anodic alumina films by pulsed voltage oxidation. *Electrochemistry Communications* **2013,** *34*, 263-265.
72. Dresselhaus, M.; Lin, Y.-M.; Rabin, O.; Black, M.; Kong, J.; Dresselhaus, G., Nanowires. In *Springer Handbook of Nanotechnology*, Bhushan, B., Ed. Springer Berlin Heidelberg: 2010; pp 119-167.
73. Martín, J.; Maiz, J.; Sacristan, J.; Mijangos, C., Tailored polymer-based nanorods and nanotubes by "template synthesis": From preparation to applications. *Polymer* **2012,** *53*, 1149-1166.
74. Poudel, B.; Hao, Q.; Ma, Y.; Lan, Y.; Minnich, A.; Yu, B.; Yan, X.; Wang, D.; Muto, A.; Vashaee, D.; Chen, X.; Liu, J.; Dresselhaus, M. S.; Chen, G.; Ren, Z., High-Thermoelectric Performance of Nanostructured Bismuth Antimony Telluride Bulk Alloys. *Science* **2008,** *320*, 634-638.
75. Caballero-Calero, O.; Martín-González, M., Thermoelectric nanowires: A brief prospective. *Scripta Materialia* **2015**.
76. Rojo, M. M.; Martín, J.; Grauby, S.; Borca-Tasciuc, T.; Dilhaire, S.; Martin-Gonzalez, M., Decrease in thermal conductivity in polymeric P3HT nanowires by size-reduction induced by crystal orientation: New approaches towards thermal transport engineering of organic materials. *Nanoscale* **2014,** *6*, 7858-7865.
77. Hochbaum, A. I.; Chen, R.; Delgado, R. D.; Liang, W.; Garnett, E. C.; Najarian, M.; Majumdar, A.; Yang, P., Enhanced thermoelectric performance of rough silicon nanowires. *Nature* **2008,** *451*, 163-167.
78. Doerk, G. S.; Carraro, C.; Maboudian, R., Single Nanowire Thermal Conductivity Measurements by Raman Thermography. *ACS Nano* **2010,** *4*, 4908-4914.
79. Feser, J. P.; Sadhu, J. S.; Azeredo, B. P.; Hsu, K. H.; Ma, J.; Kim, J.; Seong, M.; Fang, N. X.; Li, X.; Ferreira, P. M.; Sinha, S.; Cahill, D. G., Thermal conductivity of silicon nanowire arrays with controlled roughness. *Journal of Applied Physics* **2012,** *112*, -.
80. Chen, C.-L.; Chen, Y.-Y.; Lin, S.-J.; Ho, J. C.; Lee, P.-C.; Chen, C.-D.; Harutyunyan, S. R., Fabrication and Characterization of Electrodeposited Bismuth Telluride Films and Nanowires. *The Journal of Physical Chemistry C* **2010,** *114*, 3385-3389.
81. Muñoz Rojo, M.; Grauby, S.; Rampnoux, J.-M.; Caballero-Calero, O.; Martin-Gonzalez, M.; Dilhaire, S., Fabrication of Bi2Te3 nanowire arrays and thermal conductivity measurement by 3ω-scanning thermal microscopy. *Journal of Applied Physics* **2013,** *113*, -.
82. Biswas, K. G.; Sands, T. D.; Cola, B. A.; Xu, X., Thermal conductivity of bismuth telluride nanowire array-epoxy composite. *Applied Physics Letters* **2009,** *94*, 223116-3.
83. Persson, A. I.; Koh, Y. K.; Cahill, D. G.; Samuelson, L.; Linke, H., Thermal Conductance of InAs Nanowire Composites. *Nano Letters* **2009,** *9*, 4484-4488.
84. Stark, I.; Stordeur, M.; Syrowatka, F., Thermal conductivity of thin amorphous alumina films. *Thin Solid Films* **1993,** *226*, 185-190.
85. Borca-Tasciuc, D.-A.; Chen, G., Anisotropic thermal properties of nanochanneled alumina templates. *Journal of Applied Physics* **2005,** *97*, -.
86. Lee, J.; Kim, Y.; Jung, U.; Chung, W., Thermal conductivity of anodized aluminum oxide layer: The effect of electrolyte and temperature. *Materials Chemistry and Physics* **2013,** *141*, 680-685.
87. Cai, A.; Yang, L.-p.; Chen, J.-p.; Xi, T.-g.; Xin, S.-g.; Wu, W., Thermal Conductivity of Anodic Alumina Film at (220 to 480) K by Laser Flash Technique. *Journal of Chemical & Engineering Data* **2010,** *55*, 4840-4843.
88. Auerkari, P., Mechanical and physical properties of engineering alumina ceramics. In *VTT Tiedotteita - Valtion Teknillinen Tutkimuskeskus*, 1996; pp X-26.
89. Tritt, T. M., Thermal Conductivity: Theory, properties and applications. In Tritt, T. M., Ed. 233 Spring Street, New York, New York 10013, 2004.
90. Lee, S. M.; Cahill, D. G.; Allen, T. H., Thermal conductivity of sputtered oxide films. *Physical Review B* **1995,** *52*, 253-257.
91. Ogden, T. R.; Rathsam, A. D.; Gilchrist, J. T., Thermal conductivity of thick anodic oxide coatings on aluminum. *Materials Letters* **1987,** *5*, 84-87.
92. Sulka, G. D., Highly Ordered Anodic Porous Alumina Formation by Self-Organized Anodizing. In *Nanostructured Materials in Electrochemistry*, 2008; pp 1-116.

93. González-Rovira, L.; López-Haro, M.; Hungría, A. B.; El Amrani, K.; Sánchez-Amaya, J. M.; Calvino, J. J.; Botana, F. J., Direct sub-nanometer scale electron microscopy analysis of anion incorporation to self-ordered anodic alumina layers. *Corrosion Science* **2010,** *52*, 3763-3773.
94. Göbel, A.; Hemberger, F.; Vidi, S.; Ebert, H. P., A new method for the determination of the specific heat capacity using laser-flash calorimetry down to 77K. *Int J Thermophys* **2013,** *34*, 883-893.
95. Gopal Khan, G.; Singh, A. K.; Mandal, K., Structure dependent photoluminescence of nanoporous amorphous anodic aluminium oxide membranes: Role of F+ center defects. *Journal of Luminescence* **2013,** *134*, 772-777.
96. Quimby, R. S.; Yen, W. M., On the adequacy of one‐dimensional treatments of the photoacoustic effect. *Journal of Applied Physics* **1980,** *51*, 1252-1253.
97. Hu, H.; Wang, X.; Xu, X., Generalized theory of the photoacoustic effect in a multilayer material. *Journal of Applied Physics* **1999,** *86*, 3953-3958.
98. Smith, M. K.; Singh, V.; Kalaitzidou, K.; Cola, B. A., Poly(3-hexylthiophene) nanotube array surfaces with tunable wetting and contact thermal energy transport. *ACS Nano* **2015,** *9*, 1080-1088.
99. Braginsky, L.; Shklover, V.; Hofmann, H.; Bowen, P., High-temperature thermal conductivity of porous Al2O3 nanostructures. *Physical Review B - Condensed Matter and Materials Physics* **2004,** *70*, 134201-1-134201-7.
100. Martín, J.; Martín-González, M.; Francisco Fernández, J.; Caballero-Calero, O., Ordered three-dimensional interconnected nanoarchitectures in anodic porous alumina. *Nat Commun* **2014,** *5*.
101. Sulka, G. D.; Hnida, K., Distributed Bragg reflector based on porous anodic alumina fabricated by pulse anodization. *Nanotechnology* **2012,** *23*.
102. Platschek, B.; Keilbach, A.; Bein, T., Mesoporous structures confined in anodic alumina membranes. *Advanced Materials* **2011,** *23*, 2395-2412.
103. Lee, W.; Park, S.-J., Porous Anodic Aluminum Oxide: Anodization and Templated Synthesis of Functional Nanostructures. *Chemical Reviews* **2014,** *114*, 7487-7556.
104. Abad, B.; Maiz, J.; Martín-González, M., Rules to determine thermal conductivity and density of Anodic Aluminum Oxide (AAO) membranes *Nano Research (under review)* **2016**.
105. Maiz, J.; Muñoz Rojo, M.; Abad, B.; Wilson, A. A.; Nogales, A.; Borca-Tasciuc, D. A.; Borca-Tasciuc, T.; Martín-González, M., Enhancement of thermoelectric efficiency of doped PCDTBT polymer films. *RSC Advances* **2015,** *5*, 66687-66694.
106. Zhang, H.; Liu, C.-X.; Qi, X.-L.; Dai, X.; Fang, Z.; Zhang, S.-C., Topological insulators in Bi2Se3, Bi2Te3 and Sb2Te3 with a single Dirac cone on the surface. *Nat Phys* **2009,** *5*, 438-442.
107. Saci, A.; Battaglia, J.-L.; Kusiak, A.; Fallica, R.; Longo, M., Thermal conductivity measurement of a Sb2Te3 phase change nanowire. *Applied Physics Letters* **2014,** *104*, 263103.
108. Rojo, M. M. Transport Porperty Measurements of Nanostructured Materials. 2015.
109. Rodriguez-Fernandez, C.; manzano, m. c.; Romero, A.; Martin, J.; Martin Gonzalez, M.; Morais de Lima Jr., M.; Cantarero, A., The Fingerprint of Te-rich and stoichiometric Bi2Te3 nanowires by Raman spectroscopy. *accepted in Nanotechnology* **2015**.

Chapter 6:

Conclusions

The **partial conclusions** extracted from this PhD work are summarized in three main blocks:

1. Design and implementation of the photoacoustic system.

The photoacoustic technique has been proved to be valid for measuring different type of materials. From bulk materials, to films, to porous structures, and to nanowires arrays embedded into an alumina matrix. This objective was achieved by an exhaustive study of the different components of the experimental setup which are described below:

1.1 PA experimental setup

The implementation of the experimental setup was carried out by taking into account the following aspects:

- **Photoacoustic cell:** Both the material and the characteristic dimensions of the PA cell were thoroughly studied. PMMA was chosen as the material to build the PA cell since its reflectivity is low enough to avoid parasitic signals. The radius and the length of the PA cavity were established to be 4 mm and 8.4 mm, respectively, since those dimensions allows for 3D effects and acoustic resonances to be avoided. Other important dimensions like the length and diameter of the duct which communicates the PA cavity with the microphone or the distance from the sample to the microphone were also optimized. The former has bene design to avoid Helmholtz resonances as much as possible and the last dimension was found to be uniquely determined by the mechanical feasibility.
- **Laser beam:** the laser beam diameter was characterized and optimized by the knife-edge profiling technique to be 1.4 mm which is small enough to avoid the lateral heat flow in such a way that 1D heat conduction model can be applied.
- **Stability and reproducibility:** The electronic components and their parameters are properly selected so that a variation during a measurement is found to be lower than 0.2 deg and 1 % for the phase shift and the amplitude, respectively. In the case of the deviation among different measurements, these values are lower than 1 deg and 5 %.

1.2 Measurement procedure

- **Bulk materials:** The phase lag method and the tangent discontinuity, which are based on the front and rear configuration measurements, have been demonstrated to be effective for measuring bulk samples. Measurements of reference samples show a deviation from the expected values generally lower than 10 %. Moreover, a high reproducibility was found in all the cases with values which differ in less than 5 %.

- **Multilayer samples:** Samples composed of different layers have been measured by applying a multilayer theoretical model. Different references have been analyzed and compared with values obtained in other labs and other techniques with a mean deviation of 10 %.

1.3 Detection limits

- **Thickness of the sample:** In the case of bulk materials model, the acoustic waves detection becomes difficult in the rear configuration when the thickness of the samples is larger than three times the thermal diffusion length. Moreover, assuming 10 Hz like the lowest operating frequency at which no 3D effects occur, a relation of the maximum sample thickness was found. In the case of the multilayered model, the minimum and maximum thicknesses are limited by the highest and lowest frequency that the microphone is able to detect and their relation with the thermal diffusivity by means of the thermal diffusion length expression.

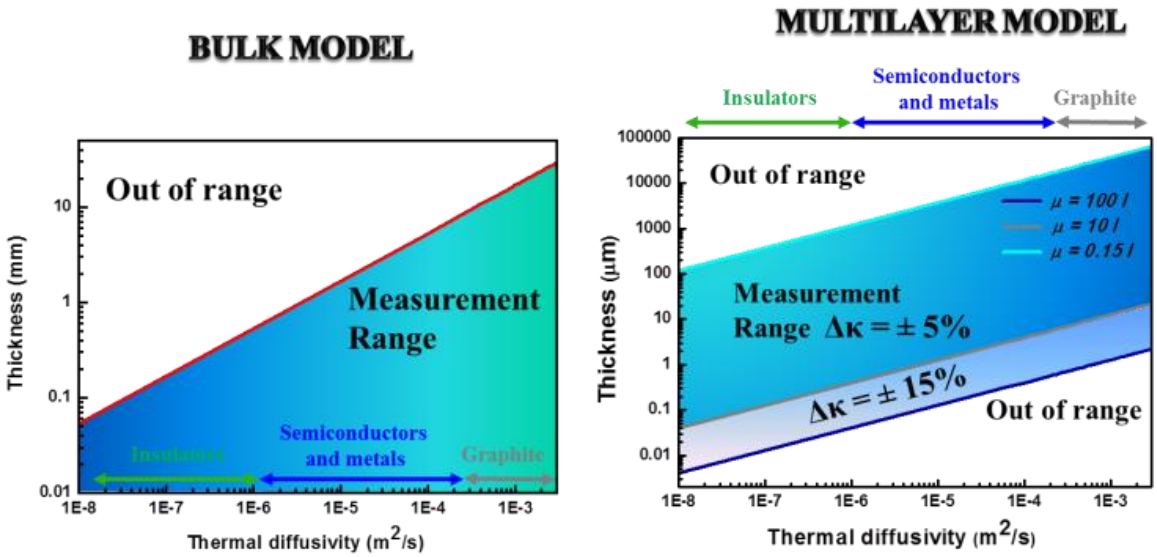

- **Other limitations**: In the case of a two different layers with a low thermal contact resistance between them, the difference between the thermal diffusivity values of the two different layers should be of at least 50 %.

2. Thermal diffusivity measurement of bulk materials.

Front and rear configuration measurements have been demonstrated to be effective for measuring bulk samples. Different reference samples with a wide range of thermal diffusivities have been measured, proving the reliability of the photoacoustic system for this type of measurement.

2.1 Inorganic materials: Thermoelectric properties of Zinc oxide doped with nickel oxide.

A threshold in the NiO quantity produces a power factor of approximately 620 $\mu W \cdot K^{-1} \cdot m^{-2}$ at 65 ºC for regular ZnO powders. Pure nano ZnO samples sintered at 1100 ºC exhibit the highest power factor, 379 $\mu W \cdot K^{-1} \cdot m^{-2}$ at 56 ºC. Regarding the thermal conductivity, the obtained values matched previous works values. Particularly, samples sintered at 850 ºC show the lowest thermal conductivity values. The addition of NiO causes a reduction in the thermal conductivity until a threshold value from which the thermal conductivity at room temperature stays steady, 25 $W \cdot m^{-1}K^{-1}$ and 15 $W \cdot m^{-1}K^{-1}$, for regular and nano powders, respectively. The figure of merit was estimated, exhibiting the maximum value for regular ZnO and 1 wt. % NiO sintered at 1100 ºC, with a value of 7.3 10^{-3} at room temperature.

2.2 Organic materials: Polyaniline/Graphene nanoplatelets nanocompites thermoelectric properties.

The thermoelectric properties of pellets composed of polyaniline blended with graphene nanoplatelets have been studied. The best power factor obtained in this work, 14 $\mu W \cdot m^{-1} \cdot K^{-2}$, was higher than previous investigations based on polyaniline at that time. Regarding the thermal conductivity, the nanocomposite could roughly work as a parallel thermal resistor which indicates that the GNPs are parallelt oriented to the surfaces of the pellets and hence, the highly anisotropy does not allow the figure of merit estimation. The thermal conductivity ranged from 0.46 $W \cdot m^{-1}K^{-1}$ to 3.3 $W \cdot m^{-1}K^{-1}$ for pure PANI and PANI with a GNP content of 50 wt. %, respectively.

3. Thermal conductivity measurement of the multilayers and porous structures.

The standard samples measurements results corroborate the reliability of the photoacoustic system for both thick and thin films, inorganic and organic materials, with different roughness values, reaching values of 300 nm.

3.1 Thick and thin films thermal conductivity.

- **Tellurium films prepared by electrodeposition:** The sodium lignosulfonate addition modifies the tellurium growth mechanism given that the grain size of the films is dramatically reduced. Consequently, the electrical resistivity of the tellurium films without SLS is lower than with SLS. Conversely, the Seebeck coefficient values are not influenced by the SLS addition. Room temperature power factors of 280 $\mu W \cdot m^{-1} \cdot K^{-2}$ and 82 $\mu W \cdot m^{-1} \cdot K^{-2}$ without and with SLS, respectively, were obtained. Finally, the thermal conductivity values were of the

order of 1 $W \cdot m^{-1}K^{-1}$ for both solutions, a factor of 3 less than the tellurium bulk value. In the case of films grown with SLS, a lower thermal conductivity was found due to the lower grain size induced by modification of the growth mechanism. The figure of merit is estimated to be around one order of magnitude higher than the bulk value.

- **Effect of the sodium lignosulfonate on the thermal conductivity of bismuth telluride prepared by electrodeposition:** The thermal conductivity of a Bi_2Te_3 film grown by electrodeposition from a solution with sodium lignosulfonate was studied. No modifications from the Bi_2Te_3 single crystal thermal conductivity was found, thus, indicating the no influence of the surfactant for this material.
- **Silicon Germanium films:** Crystalline SiGe thin films were synthesized by sputtering by metal induced crystallization along with two different thermal treatments, in-situ (heating the chamber during the fabrication process) and ex-situ (a post-annealing in a external RTA equipment). The thermal conductivity values were found to be 1.13 ± 0.13 $W \cdot m^{-1} \cdot K^{-1}$ and 1.23 ± 0.12 $W \cdot m^{-1} \cdot K^{-1}$ for the in-situ and ex-situ thermal treatments, respectively. These values are lower than those found for SiGe bulk (4-5 $W \cdot m^{-1} \cdot K^{-1}$) and they are attributed to the cluster presence created inside the films during the crystallization process.

3.2 Porous structures

- **Anodic aluminum oxide (AAO) membranes:** the skeletal density and skeletal thermal conductivity could be accurately obtained depending on the preparation conditions since the composite density and thermal conductivity as a function of the porosity was found to follow the rule of mixtures and the effective medium theory, respectively. Thermal conductivity values of 1.07 $W \cdot m^{-1} \cdot K^{-1}$ for AAO membranes prepared in sulfuric acid solution and 1.32 $W \cdot m^{-1} \cdot K^{-1}$ for oxalic and phosphoric acid electrolytes were obtained. A reduction in the value obtained when using sulfuric acid can be explained in terms of SO_4^{-2} incorporation to the alumina structure.
- **3D Anodic aluminum oxide membrane:** The effective thermal conductivity of a non-filled 3D AAO membrane was measured by the PA technique, obtaining a value of 0.38 $W \cdot m^{-1} \cdot K^{-1}$. A 3D thermal model was developed which provided a value of the skeletal thermal conductivity of 1.25 ± 0.25 $W \cdot m^{-1} \cdot K^{-1}$. A study of the influence of the number of transversal nanochannels as well as the thickness of the 3D-AAO structure for both empty and filled with different materials was performed with the aid of the new thermal model. Therefore, tuning the effective thermal conductivity by manipulating the geometric parameters is demonstrated. Finally, the 3D-AAO was

filled with a reference sample and the effective thermal conductivity was measured. The result was in accordance with the thermal model predictions, thus, corroborating its validity.

-

3.3 Nanowires embedded in alumina matrix

- **Bi_2Te_3 nanowires:** the thermal conductivity of highly oriented Bi_2Te_3 nanowires of diameters of 30 nm, 45 nm and 65 nm resulted in the vicinity of 0.6 $W \cdot m^{-1} \cdot K^{-1}$ which is a factor of 3.5 lower than the bulk value. NWs with different stoichiometries were studied, showing a slightly reduction of the thermal conductivity when the tellurium content increases due to the presence of Te clusters. Moreover, the effect of the addition of sodium lignosulfonate during the nanowire growth was studied for nanowire diameters of around 40 nm, showing no variation with respect to the highly oriented as the Bi_2Te_3 electrodeposited films.
- **Sb_2Te_3 nanowires:** the thermal conductivity of nanowires of approximately 40 nm was found to be a factor of 3.5 lower than the bulk value.
- **N-p junction bilayer Bi_2Te_3/ Sb_2Te_3:** the thermal conductivity of two different NWs grown in the same AAO template with a clear interface between them was successfully measured by the PA technique, showing the capability of measuring the thermal conductivity of two different layers.

All the partial conclusions extracted from this PhD work can be summarized in four **general conclusion**:

1. The photoacoustic technique has been proved to be valid for thermal property measurements of materials from any type of structure, bulk, thin and thick films, porous structures and nanowires embedded into alumina matrix. Materials of a wide range of thermal conductivities, from 0.2 $W \cdot m^{-1} \cdot K^{-1}$ to 240 $W \cdot m^{-1} \cdot K^{-1}$, have been successfully measured.

2. Thermal transport measurements are extremely complicated since they involved complex processes related to heat transfer phenomena. High quality metrology in this field becomes essential. The selection and measurements of reference samples were critical to calibrate the experimental setup. Moreover, performing round robin experiments was also crucial to determine the accuracy of the measurement technique.

3. Thermal transport of different structures is explained based on morphology, composition or characteristic dimensions which are deeply characterized, allowing an elementary and solid understanding of best tactics to engineer thermal transport. Example of remarkable results include: i) the effect of using NiO nanoparticles in reducing thermal conductivity and increasing electrical conductivity of ZnO; ii) an induced anisotropy in the PANI/GNP pellets created by the graphene positioning in polyaniline matrix; iii) the effect of acid solution used for the fabrication of anodic alumina membranes on their thermal conductivity, density and specific heat; iv) the first heat transfer model developed for a 3D anodic alumina; v) the effect of sodium lignosulfonate on morphology and properties of tellurium films and bismuth telluride films and nanowires; vi) the extraordinary reduction in the thermal conductivity of SiGe films due to phonon scattering induced by clusters presence; and vii) the role of diameter, composition and crystal orientation on the thermal transport of nanowires. In general, a common reduction in the thermal conductivity has been observed when the dimensions are near to the nanoscale due to phonon-boundary scattering, as observed in the reduction of the thermal conductivity of Si-Ge films, Te films, ZnO pellets with NiO nanoparticles, or Bi_2Te_3 and Sb_2Te_3 nanowires.

-

List of publications

During this doctoral thesis, the PhD student has participated in 18 publications. The number of citations of each article has been taken from Scopus the 13^{h} of December of 2015:

Publications as first autor:

1. **"Thermoelectric properties of electrodeposited tellurium films and the sodium lignosulfonate effect"** Authors: **Begoña Abad** , Marta Rull-Bravo, Stephen Hodson, Xianfan Xu, and Marisol Martín-González, Electrochimica Acta **169** (2015) 37-45
   Citations: 3

2. **"Improved power factor of polyaniline nanocomposites with exfoliated graphene nanoplatelets (GNPs)"** Authors: **Begoña Abad**, Irene Alda, Pablo Díaz-Chao, Hiroshi Kawakami, Albert Almarza, David Amantia, David Gutierrez, Laurent Aubouy and Marisol Martín-González, Journal of Materials Chemistry A, **1**, 2013, 10450-10457
   Citations: 21

3. "**Thermal Diffusivity Measurement System Applied To Polymers",** Authors: **B. Abad**, P. Díaz-Chao, A. Almarza, D. Amantia, S. Vázquez-Campos, Y. Isoda, Y. Shinohara, F. Briones, M.S. Martín-González, 9th European Conference on Thermoelectrics (ECT2011) Proceedings, Tesalónica (Grecia) AIP Conf. Proc., 1449, 2012, 354-357
   Citations: 0

4. **"Rules to determine thermal conductivity and density of Anodic Aluminium Oxide (AAO) membranes"** Authors: Begoña Abad, Jon Maiz, and M.S. Martin-Gonzalez **(To be submitted)**

5. **"Opening the door to engineering material thermal properties by three dimensional porous alumina"** Authors: **Begoña Abad**, Jon Maiz, and M.S. Martin-Gonzalez (20015) Scientific Reports (under review)

6. **"Review of non-contact methods for thermal conductivity measurement"** Authors: **Begoña Abad**, D.-A. Borca-Tasciuc, and M.S. Martin-Gonzalez **(To be submitted)**

7. **"Thermal properties of antimony telluride nanowires"** Authors: **Begoña Abad**, O. Caballero-Calero, and M.S. Martin-Gonzalez **(In preparation)**

8. **"Effect of the sodium lignosulfonate in the thermal properties of Bi_2Te_3 grown by electrodeposition"** Authors: **Begoña Abad**, O. Caballero-Calero, and M.S. Martin-Gonzalez **(In preparation)**

9. **"Thermal conductivity measurement of a nanowire array of a n-p bilayer"** Authors: **Begoña Abad**, O. Caballero-Calero, and M.S. Martin-Gonzalez **(In preparation)**

Publications as co-author related to the work presented in this thesis

10. "**AC Seebeck Coefficient and Thermal Conductivity Measurements of High and Low Thermal Conductivity Materials Using a Scanning Wollaston Hot Probe in the 3ω Method"** Authors: A. A. Wilson, M. M. Rojo, **B. Abad**, J. A. Perez, J. Maiz, J. Schomacker, Marisol. S. Martín-González, D. Borca-Tasciuc and T. Borca-Tasciuc, Nanoscale, 2015, 7, 15404-15412
Citations: 1

11. **"Enhancement of thermoelectrics efficiency of doped PCDTBT polymer films"** Authors: Jon Maiz, Miguel Muñoz-Rojo, **Begoña Abad**, Adam Wilson, Aurora Nogales, Diana-Andra Borca-Tasciuc, Theodorian Borca-Tasciuc, Marisol Martín-González, RSC Advances, 2015, 5 (82), 66687-66694
Citations: 1

12. **"Anisotropy effect on the thermoelectric properties of highly oriented electrodeposited Bi_2Te_3 films"** Authors: Cristina V. Manzano, **Begoña Abad** , Miguel Muñoz-Rojo , Yee Rui Koh , Stephen L. Hodson Hodson, Antonio Lopez , Xianfan Xu , Ali Shakouri , Timothy Sands, Theodorian Borca-Tasciuc, M.S. Martin-Gonzalez, (2015) Scientific Reports **(accepted)**

13. **"Low thermal conductivity and improved thermoelectric performance of nanocrystalline Silicon Germanium films by sputtering"** J. A. Pérez Taborda, J.J. Romero, **B. Abad**, M. Muñoz-Rojo, A. Mello, F. Briones, M.S. Martin-Gonzalez (2015) Nanotechnology **(under review)**

14. **"Decrease in Thermal Conductivity and Increase in Electrical Conductivity in Bi2Te3 nanowires by diameter size reduction induced by phonon scattering and topological insulator effects"** Authors: Miguel Muñoz Rojo, C. V. Manzano**, B. Abad**, Yingjie Zhang,

Alexandre Buyain, J. Maiz, Liliana Vera, X. Alvarez, Miquel Salmeron, Johannes Gooth and M. Martín Gonzalez **(In preparation)**

Other publications as co-author not shown in this thesis

15. **"Improvements on electrodeposited $Bi_2Te_{3-y}Se_y$ films by different additives"** Authors: Olga Caballero-Calero, Melissa Mohner, Marina Casas, **Begoña Abad**, Marta Rull, Diana A. Borca-Tasciuc, Marisol Martín-González, Materials Today Proceedings, 2015, **2**, 620–628

16. **"Improvement of Bismuth Telluride electrodeposited films by the addition of Sodium Lignosulfonate"** Authors: O. Caballero-Calero, P. Diaz-Chao, **B. Abad**, C.V. Manzano, M.D. Ynsa, J. J. Romero, M. M.Rojo and M. Martin-Gonzalez, Electrochimica Acta, 2014, 123, 117-126
Citations: 10

17. **"Thermoelectric properties of Bi_2Te_3 films by constant and pulsed electrodeposition"** Athors: C. V. Manzano, A. A. Rojas, M. Decepida, **B. Abad**, Y. Feliz, O. Caballero-Calero, D. A. Borca-Tasciuc, M.S. Martín-González, Journal of Solid State Electrochemistry, 2013, **17**, 2071 – 2078
Citations: 14

18. **"$SrTiO_3$ thin films as high efficient thermoelectric materials"**, S Bhansali, W Khunsin, JS Reparaz, MR Wagner, J Roqueta, J Santiso, **B. Abad**, P Diaz-Chao, M Martin-Gonzalez, Sotomayor Torres, Thermal Investigations of ICs and Systems (THERMINIC), 2013 19th International Workshop on, IEEE 359-360

19. **"Percolated Skutterudite-oxides nanocomposites: a different approach to decouple electrical and thermal conductivity by functional interfaces"** Authors: M. Rull, A. Moure, **B. Abad**, A. Del Campo, M. Muñoz, A. Jacquot , J. F. Fernandez, M. Martin-Gonzalez **(To be submitted)**

20. **"Influence of powders impurities in the power factor of Bi_2Te_3"** Authors: C. V. Manzano, B. Abad, M. Martín Gonzalez **(In preparation)**

21. **"A new method to obtain in-situ CoSb3 nanocomposite by mechanosynthesis"**
    Authors:M. Rull, A. Moure, A. Del Campo, **B. Abad**, J. F. Fernandez, M. Martin-Gonzalez.
    (**In preparation**)

Patents

INVENTORS: Martínez Crespiera, Sandra, Amantia, David, Pelegrin Rellan, Cesar, M.S. Martín-González, Rull Bravo, Marta, **Abad Mayor, Begoña**, Fernández Lozano, José Francisco, Gutiérrez Tauste, David, Della Pirreiera, Monica, Faccini, Mirko y Aubouy, Laurent.

TITLE: SKUTTERUDITE PREPARATION PROCEDURE TO OBTAIN $COSB_3$. (PROCEDIMIENTO PARA LA PREPARACIÓN DE SKUTTERUDITAS NANOESTRUCTURADAS DEL TIPO $COSB_3$)

APPLICATION NUMBER: P201431385 **PRIORITY COUNTRY**: España

PRIORITY DATE: 23 September 2014 **REFERENCE**: P27484ES00

ENTITY: Centro Tecnológico LEITAT y Consejo Superior de Investigaciones Científicas

APPENDIX

List of Figures

List of Tables

Abbreviations

η = Thermoelectric efficiency

T_H = Hot side temperature

T_C = Cold side temperature

z = Thermoelectric figure of merit

T = Absolute temperature

S = Seebeck coefficient

σ = Electrical conductivity

κ = Thermal conductivity

κ_e = Electronic thermal conductivity

κ_{ph} = Phononic thermal conductivity

PF = Power factor

$\vec{Q}$ = Heat flux vector

$\vec{\nabla}T$ = Temperature gradient vector

C = Heat capacity

v = particle velocity

l = mean free path

α = Thermal diffusivity

C_p = Specific heat

ρ = Density

ΔR = Change in reflectivity

ΔT = Temperature difference

TDTR = Time-Domain Thermoreflectance

d = Thickness

τ = Pulse duration

$V_f(t)$ = TDTR signal

V_0 = TDTR average voltage output

Q = Quality factor

R = Reflectivity

t = Time delay

V_{in} = In-phase TDTR signal component

V_{out} = Out-of-phase TDTR signal component

$t_{1/2}$ = halft time laser flash

t_x = time of the interception with the y-axis

TTG = Transient thermal grating

$g(t)$ = time dependent component of the temperature distribution in TTG

TM = Thermal mirror effect

PTDT = pulsed photothermal displacement technique

μ = thermal penetration length or thermal diffusion length

f = modulation frequency

FDTR = Frequency-domain reflectance method

$\Delta\varphi$ = phase shift

PBD = Photothermal Beam deflection

PA = Photoacoustic

$\overline{\phi(t)}$ = spatially averaged temperature of the gas

θ = complex amplitude of the temperature at the solid gas boundary

ω = angular frequency

t = time

j = imaginary unit

$\delta x(t)$ = gas displacement

T_0 = room temperature

$\delta P(t)$ = pressure variation

l_g = gas column length

P_0= ambient pressure

SPS = Spark plasma sintering

PANI = polyaniline

GNP = Graphene nanoplatelets

AAO = Anodic aluminum oxide

E = reduction potential

E^0 = standard potential

n =

F = Faraday constant

a_M^{n+} = oxidized species

a_M = reduced species

m = mass

M = molecular weight

I = electrical current

CE = counter electrode

WE = working electrode

RE = reference electrode

RTA = Rapid thermal annealing

λ = wavelength

d = interplanar distance

θ = angle between the incident wave and the scattering planes

FE-SEM = Field Emission Scanning electron microscope

EDX = Energy dispersive X-ray spectroscopy

BET = Brunauer-Emmett-Teller technique

P = porosity

V_{pores} = pore volume

V_{solid} = solid volume

DSC = Differential Scanning Calorimetry

W_{air} = weight in air

W_{et} = weight in ethanol

S_{rel} = relative Seebeck coefficient

ΔV = voltage difference

S_{abs} = absolute Seebeck coefficient

S_{Pt} = Platinum Seebeck coefficient

Λ_s = wavelength of the acoustic wave

L_g = PA cavity length

β_{mn} = transversal eigenvalue

q = longitudinal eigenvalue

ϕ_{cell} = cavity diameter

$f_{m,n,q}$ = resonance frequencies

SNR = Signal to noise ratio

ϕ_{front} = phase shift in front configuration

ϕ_{rear} = phase shift in rear configuration

μ_β = optical penetration length

fc = critic frequency

ΔA = amplitude variation

$\Delta\varphi$ = phase shift variation

σ = standard deviation

Φ = normalized phase shift

θ_{N+1} = transient temperature

S_p = sensitivity of the property p

E_{ran} = random error

t_{n-1} = Student-t distribution

E_{sist} = systematic error